
On the development and application of distributed delay
equations to mathematical physiology

TYLER CASSIDY

Department of Mathematics and Statistics
FACULTY OF SCIENCE
McGill University, Montreal

APRIL 2019

A thesis submitted to McGill University
in partial fulfillment of the
requirements for the degree of
Doctor of Philosophy

© Tyler Cassidy 2019

ABSTRACT

Human physiology is filled with examples of time-delayed feedback. In certain cases, such as the hematopoietic system, the time lag between signal and response is variable and distributed around a mean delay. In this dissertation, we derive a physiologically realistic method of modelling these delays and apply the technique to model tumour growth in the presence of immune surveillance.

We begin by deriving a general model of population renewal that includes a maturation period. We initially consider an age structured partial differential equation model of a population with a randomly distributed maturation period and variable maturation rate. We reduce the age structured partial differential equation to a state dependent distributed delay differential equation (DDE) and analyse the resulting model without specifying the maturation density function. This general setting encompasses the common state dependent discrete DDE and generalizes the linear chain technique to include variable transition rates and concatenated ageing processes. To illustrate the utility of the distributed DDE framework, we simplify two published models of hematopoiesis to their equivalent state dependent distributed DDE and analyse their resulting form.

Next, we develop and analyse a mathematical model of tumour-immune interaction that explicitly incorporates heterogeneity in tumour cell cycle duration by using a distributed DDE. Through linear stability analysis, we completely characterise the importance of tumour-immune interaction through a necessary and sufficient condition for disease remission. Consistent with the immunoediting hypothesis, bifurcation analysis of the mathematical model shows that decreasing tumour-immune interaction leads to tumour expansion through a transcritical bifurcation. By incorporating a model of viral therapy, we show that immune involvement is crucial in determining long-term treatment outcomes. Furthermore, to understand the effects of genetic variability in treatment outcome, we perform a virtual clinical trial of viral therapy and immunotherapy. We quantify the synergistic interaction between these two treatment techniques by simulating viral and immunostimulating combination therapy. Finally, we exploit this synergy by using a genetic algorithm to create an optimal dosing regimen that reduces treatment burden and improves virtual prognosis.

ABRÉGÉ

La physiologie humaine regorge d'exemples de dynamiques retardées. Dans certains cas, tels que le système hématopoïétique, le décalage entre un signal et la réponse qu'il induit est variable et distribué autour d'un délai moyen. Pour modéliser ces retards, nous développons une méthode physiologiquement réaliste que nous appliquons à l'étude de la croissance tumorale sujette à l'immunosurveillance.

Nous commençons en considérant une population ayant une vitesse de maturation variable et une durée de maturation aléatoirement distribuée autour d'une valeur moyenne. Les dynamiques de cette population sont régies par une équation aux dérivées partielles (EDP) structurées en âge. Nous réduisons l'EDP structurée en l'âge en une équation différentielle à retard (EDR) variable et distribué. Nous analysons ce dernier modèle sans spécifier la densité de probabilité de la maturation. Ce cadre général englobe les EDR aux délais ponctuels et variables, et généralise la technique de la chaîne linéaire pour inclure des vitesses de transition variables et des processus de vieillissement concaténés. Afin d'illustrer l'utilité du cadre EDR à délai distribué, nous démontrons l'équivalence entre deux modèles d'équations différentielles ordinaires et deux EDRs.

Ensuite, par le biais d'une EDR distribué, nous développons et analysons un modèle mathématique de l'immunité antitumorale incorporant l'hétérogénéité dans la durée du cycle cellulaire des cellules tumorales. Grâce à une analyse de stabilité linéaire, nous caractérisons l'importance de l'immunité antitumorale par l'énoncé d'une condition nécessaire et suffisante pour la rémission du cancer. Conformément à l'hypothèse d'immunoediting, un analyse de bifurcation du modèle démontre que la diminution de l'interaction tumeur-immunitaire induit l'expansion tumorale suite à une bifurcation transcritique. En intégrant un modèle de virothérapie, nous montrons que l'efficacité du traitement à long terme est déterminée par l'implication du système immunitaire. En outre, pour comprendre les effets de la variabilité génétique sur l'efficacité du traitement, nous réalisons un essai clinique virtuel de la thérapie combinée de virothérapie et d'immunothérapie. Nous quantifions les interactions synergiques entre ces deux traitements en simulant la virothérapie en combinaison avec un immunostimulant. Enfin, cette synergie est exploitée pour déterminer un schéma posologique optimal qui réduit le fardeau posologique du traitement tout en améliorant le pronostic virtuel.

STATEMENT OF CONTRIBUTION

This dissertation is a collection of original manuscripts that are either published or submitted for publication and were completed with my advisors, Prof. Morgan Craig and Prof. Antony R. Humphries. The contributions are:

Chp.2 : *Equivalences Between Age Structured Models and State Dependent Distributed Delay Differential Equations* is a reproduction of the same article which will appear in *Mathematical Biosciences and Engineering*, co-authored with Morgan Craig and Antony R. Humphries. This manuscript was accepted for publication on March 27th, 2019 and published June 11th, 2019.

Chp.3 : *A Mathematical Model of Viral Oncology as an Immuno-oncology Instigator* is a reproduction of the same article which will appear in *Mathematical Medicine and Biology- A journal of the IMA*, co-authored with Antony R. Humphries. This manuscript was accepted for publication on March 26th, 2019 and published online April 29th, 2019.

Chp.4 : *Determinants of combination GM-CSF immunotherapy and oncolytic virotherapy success identified through in silico treatment personalization* is a reproduction of the same article, co-authored with Morgan Craig, and is under revision at *PLoS Computational Biology*.

Chapter 2 was developed with Antony R. Humphries and Morgan Craig. I established equivalence between the age structured PDE and distributed DDE formulations in the general and specific cases. I wrote the initial draft of the article, and the final version was produced with input and feedback from both co-authors.

I developed, analysed and simulated the mathematical model of Chapter 3. I wrote the initial draft of the article. The final version was produced with input and feedback from Antony R. Humphries.

The virtual clinical trial in Chapter 4 was developed with Morgan Craig. I performed the parameter fitting, wrote the code to simulate the clinical trial and to optimize therapeutic scheduling, and developed the "maintenance" therapy. The article was written with Morgan Craig.

LIST OF FIGURES

1.1	Illustration of deterministic and random maturation age for individual cells. Cells increase in age along the curves before maturing at the red dots. Solid curves represent cells that mature once reaching a threshold age. Dashed curves represent cells that mature randomly with probability given by the age density shown. The slope of these curves gives the variable ageing rate $V(t)$. Adapted from Metz and Diekmann [1986].	4
1.2	Transit of individuals between consecutive compartments as used in the derivation of (1.1). The figure can be used to understand the concatenation of j ageing processes in Erlang distributed DDEs. Figure from McKendrick [1925]. In the public domain following A.G McKendrick's death in 1943.	5
1.3	Figure (a): The distribution of absolute doubling times of HeLa cells. The doubling time is the difference between the the birth and division time of an individual cell. Taken from Sato et al. [2016] under a Creative Commons Attribution 4.0 International License. Figure (b): Cell cycle duration of daughter cells plotted against parent cells in a population of cyanobacteria. Reproduced from Sandler et al. [2015] with permission of Springer.	7
1.4	The mechanism of action of oncolytic viruses. Infectious virions preferentially infect and reproduce inside malignant tumour cells. Virions reproduce inside the infected cell, leading to tumour cell lysis and the release of viral progeny into the tumour microenvironment.	10
3.1	Pictorial representation of the tumour growth model. Populations are denoted by circles, processes by squares and rates by arrows. Quiescent cells enter G_1 at rate a_1 and undergo apoptosis at rate d_1 . Cells leave G_1 and enter the active phase of the cell cycle at rate a_2 while undergoing apoptosis at a rate d_2 . The active phase death rate is \hat{d}_k and cells re-enter quiescence after mitosis. Phagocytes interact with quiescent and G_1 phase cells at respective rates ψ_Q and ψ_G . Tumour-immune interaction drives cytokine production through the function C_{prod}	64

3.2	A comparison of simulation results for various distributions and immune strengths with $k_{cp} = 2.65$. Figure (a) shows the simulation of (3.1) with a gamma distribution for $j = 6$, a discrete delay, and the Crivelli model from Appendix A. Figure (b) shows the simulation of (3.1) with a gamma distribution for $j = 50$ and the same simulations for the discrete and Crivelli models.	89
3.3	Simulated viral therapy with limited and sufficient immune recruitment. The parameters used in sufficient immune recruitment are given in Table 3.1. Limited immune recruitment occurs with $k_{cp} = 1.63$ and other parameters as given in Table 3.1.	89
3.4	Stability regions for the CFE for various parameter combinations. Fig. (a) shows the relationship between the stability of the CFE and the parameters k_p, a_1 and a_2 . Fig. (b) shows the relationship between stability of the CFE and the parameters k_{cp}, k_p and \hat{d}_g	90
3.5	The bifurcation diagram showing a transcritical bifurcation. Figure (a) shows the transcritical bifurcation as k_p increases past k_p^{crit} for the quiescent population. The dashed lines represent unstable equilibria and the solid lines denote stable equilibria. Figure (b) the dependence of asymptotic behaviour on initial conditions. The quiescent initial populations used are shown in Figure (a) as crosses.	90
4.1	Pictorial representation of the tumour growth model. Quiescent cells activate to begin division by transiting into the G_1 phase of the cell-cycle. Cells exit G_1 to enter the active phase and complete division. Most susceptible cells in the active phase re-enter quiescence after mitosis, however certain dividing cells may mutate into an immuno-resistant lineage (red dotted arrow). Immune interactions are driven by phagocytes who come into contact with quiescent and G_1 phase susceptible cells (dashed yellow lines). Tumour-immune interactions increase pro-inflammatory cytokine concentrations to recruit additional phagocytes to the tumour site (blue dotted line). Cells and cytokine are denoted by circles, processes by squares, and rates by arrows.	108

- 4.2 **Schematic representation of the *in silico* patient creation algorithm.** Individual *in silico* patient parameter values are sampled from a normal distribution of values based on an average parameterization [Cassidy and Humphries, 2019]. The model was then simulated for each individual and tumour growth predictions (tumour doubling time) were tested for physiological relevance. If the *in silico* patient's tumour growth behaviour was considered physiologically realistic, they were cloned n times and each clone was assigned to n separate arms of the *in silico* clinical trial. 111
- 4.3 **Treatment with oncolytic virus provides improves outcomes over immunotherapy in virtual clinical trial.** **A)** Kaplan-Meier curves for patients in the immunotherapy and virotherapy arms of the virtual trial; **B)** The relative survival benefit for identical virtual patients. The ratio of survival time on T-VEC against survival time on GM-CSF for identical virtual patients (line of best fit, slope=0.0035) establishes a causal relationship between treatment type and survival time, indicating that oncolytic virus therapy provided slightly larger survival gains in those with longer doubling times when compared to GM-CSF. 115
- 4.4 **Optimal personalized dose scheduling for each of the 300 virtual patients.** Dose size presented as a multiple of the standard dose with immunotherapy in shades of purple, and virotherapy in shades of green. The n th horizontal row corresponds to the n th virtual patient, while the m -th vertical column corresponds to the dose administered on day m 116
- 4.5 ***In silico* clinical trial predicts improved outcomes for both probabilistic dosing strategies and maintenance therapy versus standard combination therapy.** Kaplan-Meier curves for Arm 1: patients receiving Standard Combination Therapy (dotted turquoise line), Arm 2: Maintenance Treatment (solid light blue line), Arm 3: Probabilistic dosing regimen determined through the *in silico* clinical trial (dashed dark blue line). 119
- 4.6 **Parameter fitting results.** A and B) Data (red circles) from Dingli et al. [2009] for tumour growth in immunocompromised mice compared to model predictions (solid black lines). C) Comparisons of model predictions (solid black lines) and the Toda et al. [2000] data (red circles) for the number of viable cells following the administration of T-VEC. 130

4.7 **Local parameter sensitivity analysis.** Left: dependence of tumour burden on the parameters shown on the y-axis. Right: dependence of tumour doubling time on the parameters shown on the y-axis. In both cases, parameters were varied by $\pm 10\%$. Tumour doubling times of 0 indicate that the tumour did not reach twice the initial size. 133

LIST OF TABLES

3.1	The parameters used to simulate (3.27) in Fig. 3.3. $C_{1/2}$ was calculated from the homeostatic phagocyte production rate and k_p was calculated from the mass-action tumour-immune interaction from Liu et al. [2007]. C_{prod}^{max} was calculated from G-CSF response to infection [Pauksen et al., 1994]. $\eta_{1/2}$ was chosen to ensure a high initial infectivity of viral therapy while $k_{q,s}$ and $\Psi_{1/2}$ were selected to ensure a physiologically realistic tumour doubling time.	88
4.1	Inferred probability distribution for GM-CSF scheduling. The probability of administering immunotherapy ($P_I(\text{Day}_i)$) in each day of the treatment cycle and the conditional probability $P_I(n \text{Day}_i)$ of administering n doses of immunotherapy for $n = 1, 2, 3, 4$	117
4.2	Inferred probability distribution for T-VEC scheduling. The probability of administering virotherapy on each 7th day of the treatment cycle ($P_V(\text{Day}_7)$) and the conditional probability $P_V(n \text{Day}_7)$ of administering n doses of virotherapy for $n = 1, 2, 3, 4$	117
4.3	Mean parameter estimates. The vector \mathbf{p} (see main section <i>Generation of in-silico individuals and patient cohorts</i>) with biological interpretations. See Cassidy and Humphries [2019] for detailed descriptions of each parameter.	132

CONTENTS

Abstract	ii
Abrégé	iii
Statement of contribution	iv
List of Figures	v
List of Tables	ix
Acknowledgements	xii
1 Introduction	1
2 Equivalences Between Age Structured Models and State Dependent Distributed Delay Differential Equations	15
2.1 Introduction	19
2.2 From McKendrick type equations to state dependent delays	21
2.3 Properties of state dependent delay differential equations	25
2.4 Distributed delay differential equations with specific maturation probabilities	30
2.5 Examples from hematopoiesis	41
2.6 Discussion and conclusion	52
Bibliography	53
3 A Mathematical Model of Viral Oncology as an Immuno-oncology Instigator	57
3.1 Introduction	59
3.2 Model development	62
3.3 Model analysis	68
3.4 The gamma distribution and equivalent ODE system	80
3.5 Discussion	91
Bibliography	92
A Reduction to the Crivelli model and the discrete delay case	98
B Number of cells in the cell cycle	100

4	Determinants of combination GM-CSF immunotherapy and oncolytic virotherapy success identified through <i>in silico</i> treatment personalization	103
	Introduction	105
	Methods	107
	Results	114
	Discussion	118
	Bibliography	121
	Supplementary Information	125
5	Conclusion	137
	Bibliography	139

ACKNOWLEDGEMENTS

I have greatly benefited from an exceptional group of mentors during my time at McGill. Tony, Morgan and Michael encouraged me to develop as a scientist and person and ensured our group meetings were a place to exchange questions, ideas, and laughs. I am particularly grateful to Tony for helping shape the ideas that led to this thesis, to Morgan for teaching me to enjoy the journey and to Michael for showing me the human side of science. This acknowledgement is the only part of the thesis that has not benefited from their input and is undoubtedly poorer for it. I look forward to continued collaboration and friendship.

The days (and nights) in Burnside Hall were anything but predictable. Thanks to the running group, my officemates and everyone else who made the department such a lively place to learn– and helped me survive the Part A exam. I am particularly grateful to Annabelle and the Redelmeier family for the breakfasts and adventures we shared.

I was lucky enough to hold a few fellowships throughout my PhD; NSERC, the Alberta Government, FRQNT, the CRM and CAMBAM supplied the funding that supported this work. I am also grateful to the Mittag-Leffler Institute for the opportunity to participate in the Thematic Semester in Mathematical Biology.

This adventure in Montreal would not have been possible without the support of some amazing friends. I am deeply indebted to Ali for the small hot chocolates, to Brady for always signing the back of the crib board and to Kevin and Tyler for being the best friends I could ever ask for. I've learned how to keep a sense of humour in tough times from Dallen and Kristen while Sean taught me how to maintain relationships across time and space.

There are no words to express my gratitude to my family. My parents encouraged me to chase this dream, to ask “what if?”, and have been an inexhaustible source of support and love my entire life. Matt, I am extremely grateful for all our adventures as brothers – especially the roadtrips with Fast Eddy – and am looking forward to making new memories with Andy and Wyatt.

To anyone I've shared a coffee, a beer, or a run with: thanks for the laughs.

To Grandpa
for reminding me to laugh
and teaching me to waste time and money

INTRODUCTION

Human physiology is filled with examples of time delays. These delays describe the time-lag between signal and response, such as in cytokine control of the hematopoietic system [Dale and Mackey, 2015; Mackey and Glass, 1977; Rubinow and Lebowitz, 1975]; in ageing processes, like the progression of a single cell through the cell cycle [Burns and Tannock, 1970; Golubev, 2016; Mackey, 1978; Sandler et al., 2015]; or in systems exhibiting a *cyclic* structure where feedback occurs between the beginning and the end of a chain of sequential steps [Goodwin, 1965; Yildirim et al., 2004]. This dissertation develops a mathematical framework to model both inter-individual heterogeneity and external control of the delay time. We then apply this framework to develop a mathematical model of viral oncology and optimize combination immuno- and viral therapies. As each chapter is a self-contained manuscript, we now provide a higher level discussion of the overall theme of the dissertation.

This dissertation is primarily concerned with the development and analysis of distributed delay differential equations (DDEs) in the context of human physiology. As their name suggests, DDEs are a type of differential equation that explicitly incorporate dependence on the past and current state of the system. When the time delay τ is fixed and constant, a generic discrete DDE can be written as

$$\frac{d}{dt}x(t) = F(x(t), x(t - \tau)).$$

We argue that the assumption of a constant and fixed time delay is overly restrictive in the physiological context. To relax this assumption, we demonstrate how to incorporate population level delay time heterogeneity through a distributed DDE. Informally, distributed DDEs use a delay kernel $K(t)$ to weigh the influence of the history of the system and, generically, take the form

$$\frac{d}{dt}x(t) = F\left(x(t), \int_0^\infty x(t - \phi)K(\phi)d\phi\right).$$

As we demonstrate in Chapter 3, replacing a discrete DDE by a distributed DDE increases physiological relevance when modelling tumour cell reproduction. Through numerical simulation, we show that the form of the delay kernel $K(t)$ drastically changes model

predictions. Thus, appropriately incorporating tumour heterogeneity in mathematical models can aid in making accurate predictions.

However, heterogeneity is not limited to reproduction in malignant tumours. Rather, it is reasonable to expect that every physiological process exhibits some form of random delay time. It follows that mathematical models should properly account for this heterogeneity in delay time. The development of appropriate modelling techniques to account for these heterogeneous delay times is one of the main contributions of this dissertation.

FROM AGE STRUCTURE TO DELAYS

We begin by establishing the relationship between age structured partial differential equations (PDEs) and DDEs in Chapter 2. Age structured models made their first appearance in mathematical biology in McKendrick's modelling of infectious diseases [McKendrick, 1925]. By considering transition between two adjacent states and a mortality rate $\mu(t)$, McKendrick [1925] derived the McKendrick age structured PDE

$$\partial_t n(t, a) + \partial_a n(t, a) = -\mu(t)n(t, a). \quad (1.1)$$

Equation (1.1) models the density of individuals¹, $n(t, a)$, with state a at time t (see the thorough reviews by Gyllenberg [2007] and Metz and Diekmann [1986]). While the variable a is often understood to be age, many authors have generalized the idea of physiological state to include maturity, size, temperature or other measures of physiological age [Fredrickson et al., 1967; Sinko and Streifer, 1967, 1971]. The McKendrick equation naturally describes the progression of individuals through an ageing process that can, in certain cases, be solved along the characteristic curves to yield a DDE. [Bélair et al., 1994; Craig et al., 2016; Otto and Radons, 2017; Smith, 1993]. If individuals exit the ageing process after achieving a threshold age (or size, maturity, temperature, etc.), the age structured PDE can be reduced to a discrete DDE, where the fixed delay represents the time required for individuals to reach the threshold.

Discrete DDEs have been used extensively in mathematical physiology, especially in the models of hematopoiesis produced by Mackey and co-workers [Bélair et al., 1994; Bernard et al., 2003; Colijn and Mackey, 2005a,b; Hearn et al., 1998a; Mackey and Glass, 1977]. These discrete delays represent a fixed time-lag between signal and response in blood cell production. The use of a fixed delay implicitly assumes that progenitor cells progress through the ageing and maturation process at a constant rate and ties physiological

¹These individuals could be humans, insects, single cells, or a host of other organisms. In what follows, it may be helpful to consider a single cell progressing through the cell cycle.

age to chronological age. For example, in two consecutive papers, Colijn and Mackey developed a discrete DDE model of hematopoiesis, or the production of blood cells, that includes hematopoietic stem cells (HSCs), the red and white blood cell lineages and the platelet lineage [Colijn and Mackey, 2005a,b]. HSCs, multipotent progenitor cells that drive hematopoiesis, differentiate into a specific lineage and undergo a series of divisions during a proliferative process. This proliferative process is responsible for a lineage dependent delay between differentiation from the HSCs and appearance in circulation. By fitting the model to patient data from periodic myeloid leukemia and cyclic neutropenia, Colijn and Mackey hypothesised that these so-called “dynamical” diseases result from dysregulation of apoptosis in HSCs. In the second of these papers, Colijn and Mackey [2005b] fit their model to data from patients receiving treatment of cyclic neutropenia with a cytokine, granulocyte colony stimulating factor (G-CSF). To replicate the well-known G-CSF dependent increase in maturation speed, Colijn and Mackey [2005b] included the neutrophil lineage delay time as a parameter to be fit to treated data. This G-CSF-mediated increase in maturation speed illustrates a limitation of discrete DDEs: maturation delays are often variable and subject to external control. This is clearly incompatible with the fixed and constant delay length of discrete DDEs.

In fact, the physiological age of an individual is only weakly linked to the chronological age. Further, the physiological age is often dynamically controlled by environmental factors such as the availability of resources. It is possible to include this dynamic control of the ageing process by adapting the McKendrick equation to include a variable ageing velocity, $V(t)$. This ageing velocity modulates how individuals accrue physiological age, and the modified McKendrick equation becomes

$$\partial_t n(t, a) + V(t) \partial_a n(t, a) = -\mu(t) n(t, a). \quad (1.2)$$

Once again, it is possible to solve (1.2) along the characteristics to yield a DDE. However, as the ageing velocity is now variable, the time required to reach the maturity threshold is also variable and depends on external control. As a result, the delay time in the resulting DDE is no longer fixed. Thus, age structured PDEs such as (1.2) are reduced to state dependent DDEs [Craig et al., 2016, 2015; Mahaffy et al., 1998]. In state dependent DDEs arising from an age structured PDE such as (1.2), the delay time is sometimes determined implicitly through an integral condition that generalises the maturation threshold of discrete DDEs. While state dependent DDEs incorporate the external control of ageing that is present in many physiological systems, their analysis is considerably more complicated than that of a constant delay DDE [Câmara De Souza et al., 2018; Cooke and Huang, 1996].

Moreover, typical applications of state dependent DDEs and discrete DDEs implic-

itly assume that individuals mature, or leave the ageing process, immediately once the maturation threshold is reached. Given differences between individuals, it seems overly restrictive to assume that maturation occurs in this completely deterministic manner. Rather, intraspecies heterogeneity is likely reflected through a randomly distributed maturation age, i.e. the individual maturation age is not fixed but rather follows a stochastic process and is described by a positive random variable. This random variable has a corresponding probability density function (PDF), or delay kernel, $K(t)$ that distributes the maturation age of individuals across an interval of physiologically relevant delay times. Thus, the use of this PDF generalises the deterministic maturation age to the randomly distributed maturation age. DDEs that use these distributions of delays are called distributed DDEs.

In Figure 1.1, we illustrate the progression of a hypothetical cell towards division. The accumulation of age is variable, and the ageing rate $V(t)$ in (1.2) is given by the slope curves at any point in time. If cells mature upon reaching the threshold age, as in the solid curves, then the delay between birth and reproduction could be modelled as a state dependent discrete DDE. However, if maturation were to occur randomly with the maturation density as shown, then individual cells may mature following the dashed lines.

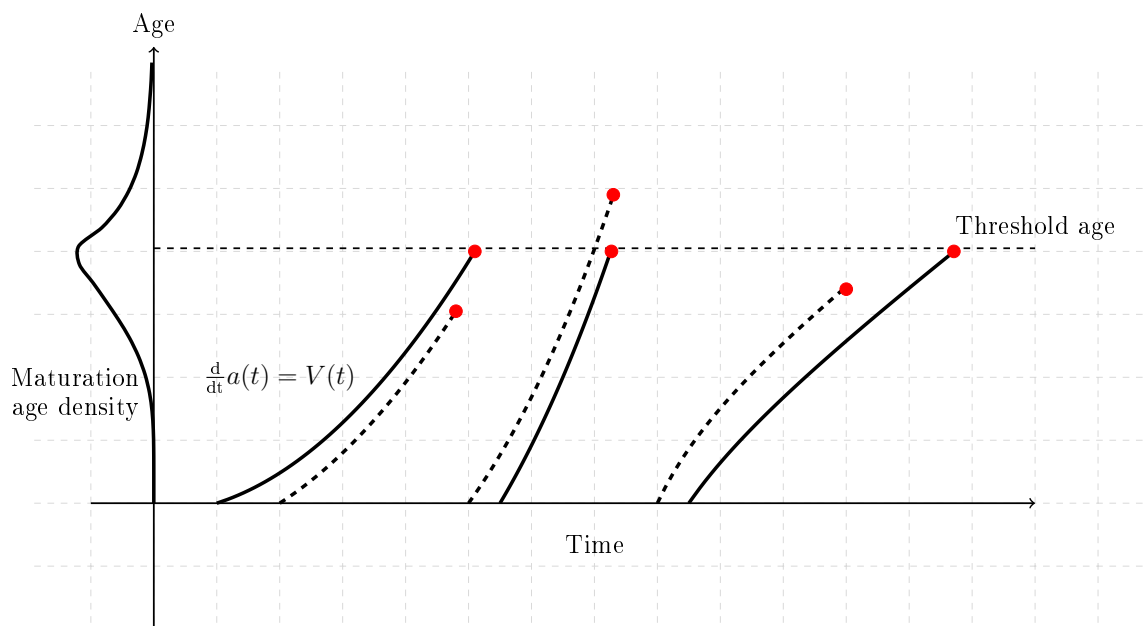


Figure 1.1: Illustration of deterministic and random maturation age for individual cells. Cells increase in age along the curves before maturing at the red dots. Solid curves represent cells that mature once reaching a threshold age. Dashed curves represent cells that mature randomly with probability given by the age density shown. The slope of these curves gives the variable ageing rate $V(t)$. Adapted from [Metz and Diekmann \[1986\]](#).

Typical examples of distributed DDEs employ a Erlang random variable for both the simple biological interpretation and convenient mathematical formulation. Erlang distributions, or gamma distributions with integer shape parameter j , have a simple interpretation: the concatenation of j processes with exponentially distributed waiting times. The biological interpretation of this maturation age distribution corresponds to individuals progressing through j stages before reaching maturation. This interpretation recalls McKendrick's derivation of (1.1) by considering the instantaneous transit of individuals from one compartment to the next as illustrated in Figure 1.2

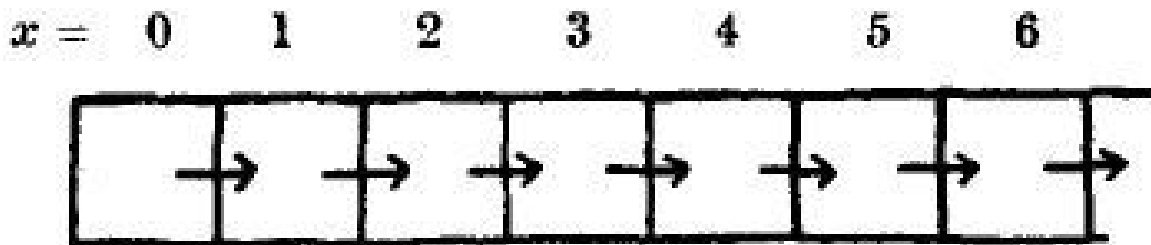


Figure 1.2: Transit of individuals between consecutive compartments as used in the derivation of (1.1). The figure can be used to understand the concatenation of j ageing processes in Erlang distributed DDEs. Figure from McKendrick [1925]. In the public domain following A.G McKendrick's death in 1943.

These gamma distributed DDEs are also mathematically convenient, as they are equivalent to a finite dimensional transit compartment system of ordinary differential equations (ODEs) through the linear chain technique [Diekmann et al., 2018; MacDonald, 1978; Smith, 2011; Vogel, 1961]. These finite dimensional ODEs model the transit of individuals through a series of compartments which corresponds to the concatenation of processes with exponential waiting times. In traditional applications of the linear chain technique, transit between the compartments must occur at a constant rate that is fixed throughout the chain. ODE models demonstrating this chain like structure are common in the pharmaceutical sciences; however, the direct link between these transit compartment ODEs and distributed DDEs is not always established. Câmara De Souza et al. [2018] demonstrated the equivalence of the Friberg model of granulopoiesis with a distributed DDE [Friberg et al., 2002].

Similar to the variable ageing rate of (1.2), it is possible to conceive of transit compartment models with a variable transit rate between compartments. In fact, the Friberg model was extended by Quartino et al. [2014] to include the effect of G-CSF on the development of neutrophil cells through a variable transit rate. Câmara De Souza et al. [2018] established the equivalence of the Quartino model with a distributed DDE by performing a non-linear time rescaling to account for this variable transit rate. However, this time rescaling must

be performed on a model-by-model basis and is not generalisable to transit compartment models with multiple ageing processes. Transit compartment ODE models with multiple ageing processes have been used extensively to study the administration of exogenous cytokines on the production of blood cells [Pérez-Ruixo et al., 2008; Roskos et al., 2006], and have not previously been amenable to the linear chain technique, even after time rescaling.

In Chapter 2, we show how to incorporate both external control of ageing processes and the maturation heterogeneity in an ageing process by deriving a generic state dependent distributed DDE. To derive the state dependent distributed DDE, we calculate the *hazard rate*, or the rate at which individuals will leave the non-deterministic ageing process from first principles. A similar expression was obtained through heuristic arguments by Gurney et al. [1986] without considering the underlying maturation process.

Careful consideration of the maturation rate leads naturally to the “correction factor” obtained by Craig et al. [2016] for a state dependent DDE. This correction factor ensures that individuals are not erroneously created or destroyed upon crossing the maturation threshold in a state dependent DDE. However, Craig et al. [2016] relied on the presence of this deterministic maturation threshold to derive the correction factor. We generalise their result to all state dependent distributed DDEs and elucidate the biological interpretation of the correction factor. Finally, by specifying the PDF $K(t)$, we obtain discrete state dependent distributed DDEs, uniformly distributed DDEs and state dependent gamma distributed DDEs. We show how to reduce these state dependent gamma distributed DDEs to a variable rate transit compartment ODE models. Through two examples, we show how our technique generalises to transit compartment models with multiple ageing processes.

MODELLING TUMOUR HETEROGENEITY

Having developed a more general framework for distributed DDEs in Chapter 2, we consider a more concrete example of heterogeneity in ageing processes. Specifically, malignant tumours are composed of a multitude of cancerous cells with distinct genotypes and phenotypes [Bell and McFadden, 2014; Grzywa et al., 2017; Lawrence et al., 2013; Lichty et al., 2014]. As with healthy cells, these malignant cells reproduce through mitosis after successfully completing the cell cycle. The cell cycle duration reflects the intratumour heterogeneity, as cells of different pheno- and genotypes will progress through the cell cycle at different rates [Buczacki et al., 2018; Palm et al., 2018; Sandler et al., 2015; Sato et al., 2016].

Sato et al. [2016] measured the absolute doubling time of individual cervical cancer cells from a single cell HeLa3 lineage. The distribution of absolute doubling time recorded by Sato et al. [2016] is presented in Figure 1.3 (a). Sandler et al. [2015] used Fucci marking, a fluorescent marker designed to indicate the presence of proteins that indicate progress through the cell cycle, to study inheritance of the cell cycle duration between mother and daughter cells. These authors demonstrated that this inheritance, and thus the cell cycle duration, is governed by a stochastic process [Sandler et al., 2015]. The resulting heterogeneity in cell cycle duration among parent-daughter pairs is shown in Figure 1.3 (b).

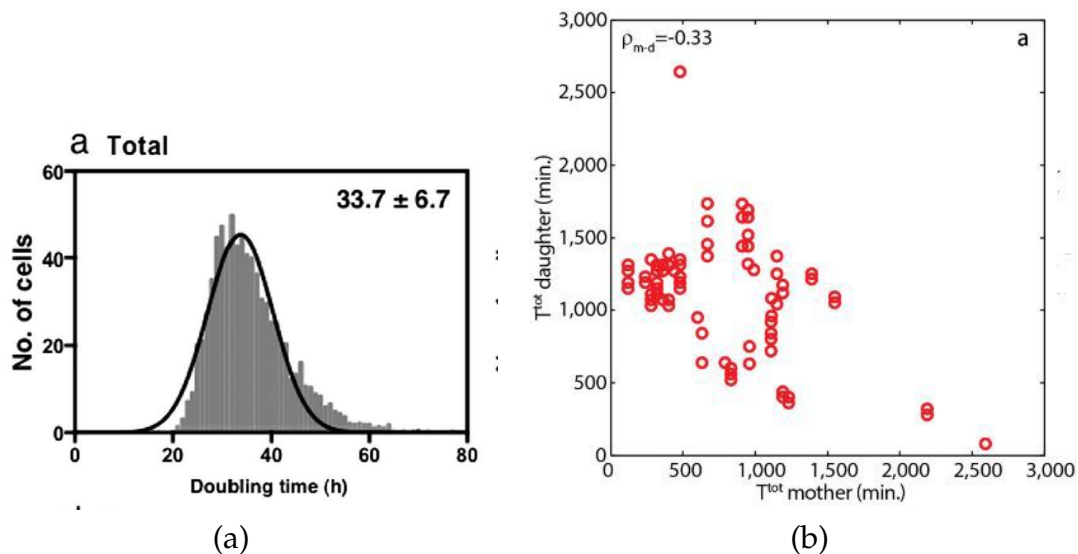


Figure 1.3: Figure (a): The distribution of absolute doubling times of HeLa cells. The doubling time is the difference between the the birth and division time of an individual cell. Taken from Sato et al. [2016] under a Creative Commons Attribution 4.0 International License. Figure (b): Cell cycle duration of daughter cells plotted against parent cells in a population of cyanobacteria. Reproduced from Sandler et al. [2015] with permission of Springer.

Interactions between cancerous and healthy cells are complex, and the immune system has been tied to cancer progression through the immunoediting hypothesis [Dunn et al., 2002; Swann and Smyth, 2007]. The immuno-editing hypothesis comprises of three distinct stages [Dunn et al., 2004]. The first of these stages, the elimination phase, corresponds to the beginning of cancer, where the immune system is able to effectively eliminate malignant cells. This immune surveillance exhibits a selection pressure on tumour cells, as malignant cells that are not susceptible to immune predation gain a fitness advantage [Dunn et al., 2002, 2004]. The directed evolution of the tumour microenvironment leads to the second stage, the equilibrium phase, where the immune system and cancerous cells

co-exist in a delicate balance between immune pressure and selection of immune resistant strains of tumour cells. Finally, in the escape phase, cancerous cells evolve to evade the immune system. Here, tumours that have escaped immune pressure grow rapidly, leading to clinical progression of the disease.

Recent advances in immunotherapy have attempted to reverse the immuno-editing process by directly modifying the tumour microenvironment. Clinically approved immunotherapies include programmed death protein (PD-1) and programmed death ligand (PDL-1) inhibitors [Mahoney et al., 2015; Sunshine and Taube, 2015]. These inhibitors prevent immune evasion by targeting the binding between immune cells expressing PD-1 with tumour cell produced PDL-1. Similarly, recent work has investigated the use of cytotoxic T-lymphocyte antigen 4 (CTLA-4) inhibitors [Ganesh and Massagué, 2018; Rowshanravan et al., 2017; Seidel et al., 2018]. CTLA-4 inhibitors block binding to the CTLA-4 receptor on the surface of T-cells and therefore reduce the immuno-suppressive signalling resulting from the activation of this pathway. An alternative approach is to directly stimulate the immune system through the administration of pro-inflammatory cytokines that signal and activate the immune system [Dranoff, 2004; Mellman et al., 2011].

Given the complexity of tumour-immune interactions, it is unlikely that treatment strategies attacking only one axis will be successful. To this end, recent therapeutic developments include the creation of genetically engineered viruses [Eissa et al., 2018; Marelli et al., 2018]. These viruses are designed to prey upon the high reproductive rate and decreased anti-viral defences characteristic of cancer to preferentially infect malignant cells [Bartlett et al., 2013; Bell and McFadden, 2014; Bommareddy et al., 2017; Breitbach et al., 2016; Marelli et al., 2018].

After infection, oncolytic viruses hijack the cellular machinery to reproduce and eventually kill the host cancerous cell through lysis [Cassady et al., 2016; Chaurasiya et al., 2018]. Lysis releases viral progeny back into the tumour microenvironment, leading to the re-infection of other tumour cells. It was initially thought that lysis would be the primary mechanism of action of oncolytic viruses [Lichty et al., 2014], and that the immune system would hinder their effectiveness through an adaptive anti-viral immune response [Marelli et al., 2018; Russell et al., 2012]. However, oncolytic viruses have been shown to shrink tumours that are uninjected, and therefore uninfected by the virus [Andtbacka et al., 2015; Chesney et al., 2018]. This shrinking of the uninfected tumours indicates a systemic immune response against tumour cells [Bell and McFadden, 2014; Breitbach et al., 2016; Chaurasiya et al., 2018]. The mechanisms of action of oncolytic viruses are summarized in Figure 1.4. Thus, to understand oncolytic viruses, it is crucial to understand the interplay between oncolytic viruses and the in-host immune response.

Mathematical modelling of tumour-immune interactions has a long history (see [Santiago et al. \[2017\]](#); [Walker and Enderling \[2016\]](#) for reviews). In particular, [Kuznetsov et al. \[1994\]](#) established a simplified model of tumour-immune interactions in the presence of activated and de-activated immune cells. They showed that the inactivation of the immune system can allow for small tumours to “sneak through” immune surveillance and lead to the establishment of disease, while larger tumours are effectively cleared. Further, [Kirschner and Panetta \[1998\]](#) modelled the influence of a pro-inflammatory cytokine, interleukin 2 (IL-2), on immune cell function using a simple system of ODEs. Through an in depth bifurcation analysis of the model, [Kirschner and Panetta \[1998\]](#) determined that IL-2 monotherapy cannot change disease progression. Rather, [Kirschner and Panetta \[1998\]](#) proposed that combination therapy of IL-2 and adoptive immune cell therapy, namely the injection of tumour suppressing immune cells, could influence disease progression. Both [Kuznetsov et al. \[1994\]](#) and [Kirschner and Panetta \[1998\]](#) indicate that the activation of the immune system against malignant tumours can improve clinical outcome.

To understand the dynamics of anticancer viral therapy, mathematical models of oncolytic viruses and the immune system have been proposed [[Eftimie and Eftimie, 2018](#); [Jenner et al., 2018](#); [MacNamara and Eftimie, 2015](#)]. Both [MacNamara and Eftimie \[2015\]](#) and [Eftimie and Eftimie \[2018\]](#) use systems of ODEs to model evolution of the immune response following cancer virotherapy. [MacNamara and Eftimie \[2015\]](#) demonstrated the importance of the memory immune cell population in controlling tumour growth, while [Eftimie and Eftimie \[2018\]](#) studied the influence of tumour promoting and tumour suppressing macrophages in the tumour microenvironment.

Further, [Jenner et al. \[2018\]](#) used a simplified mathematical model of cancer virotherapies to study the influence of therapeutic scheduling on disease progression without including the immune response. In a PDE model of oncolytic virus therapy, [Malinzi et al. \[2017\]](#) considered oncolytic virus and chemotherapy combination therapy. However, these models did not explicitly model the subset of cancer cells that are susceptible to viral infection.

Oncolytic viruses rely on the active portion of the cell cycle to successfully infect malignant cells and to complete the viral life cycle [[Bommareddy et al., 2017](#); [Colao et al., 2017](#); [Yamashita and Emerman, 2006](#)]. Thus, to study the effect of oncolytic viruses on tumour cells, it is crucial to know how many cells are actively dividing and are therefore susceptible to infection. [Crivelli et al. \[2012\]](#) developed a mathematical model of a oncolytic virus that explicitly includes the susceptible population of tumour cells by using a discrete DDE. However, as previously mentioned, the use of a discrete DDE implicitly assumes homogeneity in the cell cycle duration of tumour cells. In Chapter 3, we address this

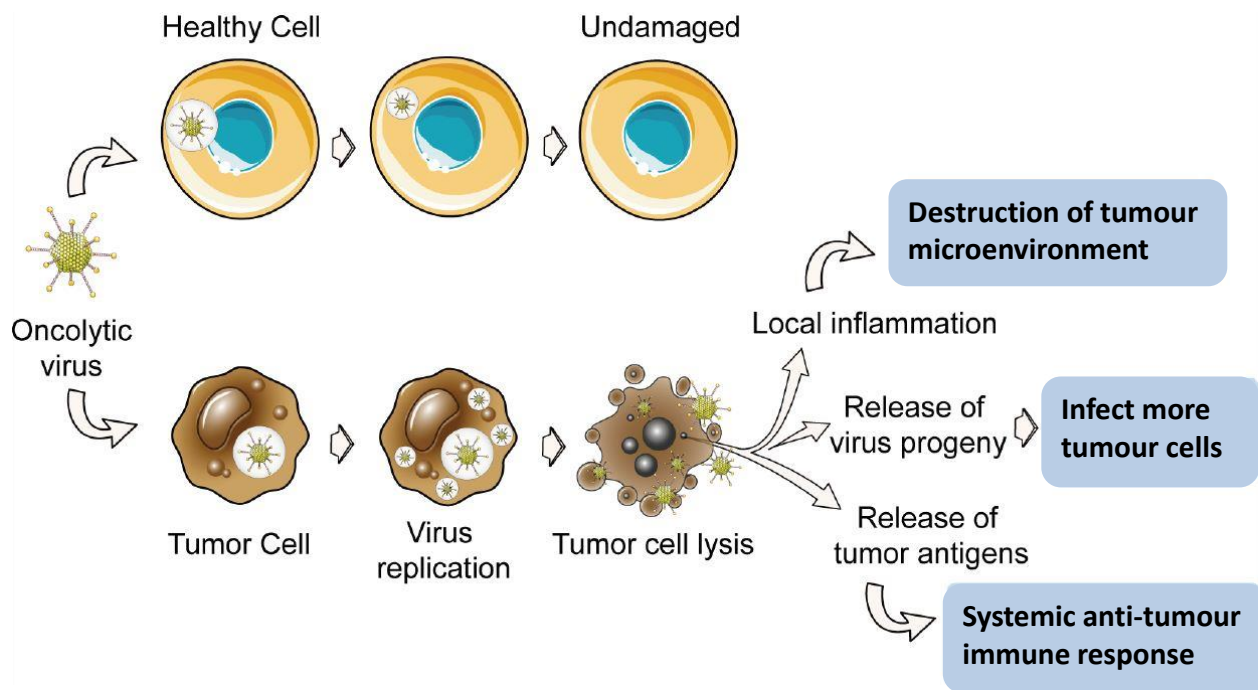


Figure 1.4: The mechanism of action of oncolytic viruses. Infectious virions preferentially infect and reproduce inside malignant tumour cells. Virions reproduce inside the infected cell, leading to tumour cell lysis and the release of viral progeny into the tumour microenvironment.

simplification by using a distributed DDE to model the cell cycle duration heterogeneity inherent to the tumour cell population. We demonstrate that including cell cycle duration heterogeneity drastically changes the model predictions, and quantify the importance of cell cycle duration heterogeneity in disease progression.

Moreover, the Crivelli model does not include the immune system. To replicate the ability of oncolytic viruses to cause disease remission, [Crivelli et al. \[2012\]](#) used a non-differentiable function to model infection of tumour cells. Conversely, we explicitly include the immune system and demonstrate that immune involvement determines the long-term disease outcome. Specifically, by linearising the DDE about the disease free state, we show that the local stability of the cancer free equilibrium is determined by the immune involvement. Further, we establish that the cancer free equilibrium loses stability through

a transcritical bifurcation corresponding to a transient decrease in immune recognition of cancerous cells. Then, by including oncolytic virus therapy, we show that the degree of immune involvement determines treatment success or failure.

USING MATHEMATICAL MODELLING TO OPTIMIZE ONCOLYTIC VIRUS THERAPY

While the use of viruses as a cancer treatment dates back to at least the 1950s [Hoster et al., 1949], the first oncolytic virus, talimogene laherparepvec (T-VEC), was approved by the United States Food and Drug Administration in 2015 for patients with late stage melanoma [Andtbacka et al., 2015; Pol et al., 2016; Rehman et al., 2016]. T-VEC is a genetically modified herpes virus that preferentially infects tumour cells. Cancerous cells typically have defective anti-viral defences due to decreased protein kinase R (PKR) activity. In normal cells, PKR activation terminates viral replication and wild-type herpes viruses have evolved to counteract PKR activity through the infected cell protein 34.5 (ICP 34.5) [Bommareddy et al., 2017; Rehman et al., 2016]. In T-VEC, the genes encoding for ICP 34.5 are replaced by the genes that encode the production of granulocyte-macrophage colony stimulating factor (GM-CSF) [Andtbacka et al., 2015; Bommareddy et al., 2017; Kaufman et al., 2014; Rehman et al., 2016]. Thus, lytic tumour cells release GM-CSF into the tumour microenvironment to recruit and activate immune cells.

The clinical development of T-VEC began with a phase I trial in 2006 and culminated in the OPTiM trial that led to the approval of T-VEC monotherapy in 2015 [Andtbacka et al., 2015; Hu et al., 2006]. This trial compared T-VEC monotherapy against the subcutaneous administration of GM-CSF and involved the recruitment of 437 patients from May 2009 to July 2011 [Clinical Trial Registry: NCT00769704]. The OPTiM trial demonstrated a significantly increased durable response rate –the objective treatment response lasting longer than 6 months– as well as a longer overall survival in patients receiving T-VEC against GM-CSF [Andtbacka et al., 2015]. Further, patients receiving T-VEC demonstrated indications of systemic anti-tumour immunity in the form of reduced uninjected lesions.

Given the mechanism of action of oncolytic viruses, it is reasonable to expect that oncolytic viruses and immunotherapies may act synergistically to engender an anti-tumour immune response [Bell and McFadden, 2014; Guo and Bartlett, 2014; Lawler and Chiocca, 2015]. Thus, recent work has studied possible oncovirus-immunotherapy combination therapies [Chaurasiya et al., 2018; Chesney et al., 2018; Martin and Bell, 2018]. For example, Chesney et al. [2018] investigated the combination of T-VEC with a immune checkpoint inhibitor and showed improved patient outcomes against immunotherapy alone in a phase II trial.

However, these combination therapies can impose high treatment burden on patients and increase overall treatment toxicity [Chesney et al., 2018; Martin and Bell, 2018]. Accordingly, determining a reasonable treatment schedule is extremely important to maximize treatment effect while minimizing therapy burden. However, testing all reasonable combination treatment schedules in humans is prohibitively expensive and optimal scheduling of virotherapies and immunotherapies remains an open problem. *In silico* clinical trials address this problem by using computational biology techniques to perform virtual clinical trials [Agur, 2010; Allen et al., 2016; Schmidt et al., 2013; Walker and Enderling, 2016].

Virtual clinical trials mimic clinical trials by selecting a cohort of virtual patients and studying the effectiveness of a proposed treatment on patient outcome [Allen et al., 2016; Barish et al., 2017; Walker and Enderling, 2016]. The creation of a virtual population attempts to combat uncertainty in parameter estimation in computational biology models [Allen et al., 2016]. As shown in Chapter 4, *in silico* trials also allow researchers to test the impact of different therapy strategies on the same virtual patient. Thus, these virtual clinical trials can be used to investigate alternative treatment schedules, personalise therapy and evaluate the toxicity of combination therapies [Agur, 2010]. However, translating the results of an *in silico* clinical trial to the clinic has been difficult [Walker and Enderling, 2016].

The remarkable success of a simple evolutionary game theory model in deriving an adaptive treatment schedule for patients with metastatic prostate cancer indicates the possible power of mathematical modelling in oncology [Zhang et al., 2017]. Zhang et al. [2017] modelled three separate populations of prostate cancer cells, including a lineage resistant to anti-androgen therapy. Through the use of this model, they adopt a treatment schedule that attempts to limit the development of a resistant population. In short, treatment is suspended when the prostate specific antigen (PSA), a biomarker for prostate cancer, reaches 50% of pretreatment value. Treatment is suspended until PSA once again reaches pre-treatment levels and the cycle is repeated. In an on-going phase I clinical trial, Zhang et al. [2017] report significant improvements when compared to a similar cohort receiving the standard of care.

The success of the Zhang et al. [2017] trial indicates the ability of computational biology models to explore novel treatment schedules. However, no one virtual patient will precisely represent a human being. Rather, by using the insights gained through mathematical modelling, we aim to identify the underlying themes of successful treatment schedules and translate these themes into actionable therapeutic strategies. In Chapter 4, we investigate the synergy between oncolytic viruses and the administration of GM-CSF. We first simulate a *in silico* clinical trial following the same treatment scheduling

as [Andtbacka et al. \[2015\]](#). The cohort of virtual patients was comprised of 300 sets of identical triplets and divided into three arms of 300 identical virtual patients. We then used a genetic algorithm to create optimal treatment schedules for each of the 300 virtual patients. As in reality, an optimal treatment schedule must both be effective and tolerable. Thus, we constrained our treatment schedule to respect the maximum tolerated doses.

These optimized treatment schedules are personalised to each of the 300 virtual patients. To test effectiveness and generalisability of our results, we created 200 new virtual patients and used the optimized treatment schedules to create a predictive treatment schedule for these new patients. This predictive treatment schedule significantly improves survival time, but, as we discuss in [Chapter 4](#), would be ethically questionable to implement in the clinic. However, by investigating the distribution of dose size and frequency, we propose a maintenance type treatment schedule that uses immunotherapy to maintain an immune response between doses of viral therapy. This maintenance schedule has a reduced drug burden and offers comparable survival to the predictive schedule without the ethical considerations. The improved survival offered by the maintenance treatment schedule underlines the ability of mathematical modelling to propose and test rational treatment regimens.

SUMMARY

In short, we address the question of accurately modelling delayed processes that include heterogeneity or stochastic effects through the development of distributed DDE models of physiological processes. The following three chapters, each a distinct publication, describe a method to include both external control and heterogeneity in mathematical models of delayed physiological processes. Through a combination of analytical and numerical techniques, each chapter illustrates the physiological relevance of distributed DDE models. This work provides increased insight into hematopoietic cell production, malignant tumour-immune interaction and the development of improved anti-cancer strategies and indicates the importance of appropriately modelling the heterogeneous and variable nature of physiological delays. Finally, in [Chapter 5](#), we summarise our contributions and indicate directions for future work.

EQUIVALENCES BETWEEN AGE STRUCTURED MODELS AND STATE DEPENDENT DISTRIBUTED DELAY DIFFERENTIAL EQUATIONS

In this chapter, we lay the theoretical framework for the remainder of this thesis and develop a generic mathematical model that includes both heterogeneity in delay times and external control of ageing velocity. Starting from the McKendrick age structured PDE (1.2) and relaxing the assumption of a threshold maturation age, we derive a generic state dependent distributed DDE. We show that the generic state dependent distributed DDE is well defined as a population model and preserves non-negativity of initial data. By performing a linear stability analysis of the scalar DDE, we study the qualitative behaviour of the state dependent distributed DDE near equilibrium.

Finally, for a given maturation density $K_A(t)$, we show that the state dependent distributed DDE can be reduced to an equivalent formulation that is more suitable to numerical simulation. In this sense, we show that modellers can convert between state dependent distributed DDEs, which are amenable to analytical investigation, and equivalent formulations of the same model which are simpler to simulate numerically. To illustrate the benefits of this equivalence, we consider two large systems of ODEs used in the pharmaceutical sciences and convert these models to their equivalent state dependent distributed DDE formulation. This chapter appears in the special issue *Recent Advances in Mathematical Population Dynamics* published in *Mathematical Biosciences and Engineering*.

There are a number of typos that persist in the published version of this chapter. Here, we address these mistakes and show that they have no bearing on the conclusions of this chapter.

1. On page 30, we define the expected delay time as

$$\tau^* = \int_0^\infty tK_A(V_A^*t)dt.$$

This definition confuses time and age and is incorrectly stated. Rather, the random variable A represents the maturation age. Thus, the expected maturation age is

$$\mathcal{T} = \int_0^\infty aK_A(a)da.$$

As we state, the expected time delay τ^* should satisfy $V_a^*\tau^* = \mathcal{T}$. Thus, the proper definition

of τ^* is

$$\tau^* = \frac{1}{V_a^*} \int_0^\infty a K_A(a) da,$$

and using the natural change of variable $a = V_a^* t$ gives

$$\tau^* = \int_0^\infty V_a^* t K_A(V_a^* t) dt.$$

2. The integration variable used in the discussion of the correction factor is misstated. Rather, the equation

$$\int_0^\infty h(a_t(\phi)) n(t, a_t(\phi)) d\phi = \int_0^\infty \beta x(t - \phi) \frac{V_a(t)}{V_a(t - \phi)} \exp \left[- \int_{t-\phi}^t \mu(x(s)) ds \right] K_A(\sigma) d\phi.$$

should read

$$\int_0^\infty h(a_t(\phi)) n(t, a_t(\phi)) d\phi = \int_0^\infty \beta x(t - \phi) \frac{V_a(t)}{V_a(t - \phi)} \exp \left[- \int_{t-\phi}^t \mu(x(s)) ds \right] K_A(a_t(\phi)) d\phi.$$

This typo has no impact on any results or discussion in this chapter.

3. In Section 2.4.3, we scale the ageing velocity $V_a(t)$ by the homeostatic ageing rate to define $\hat{V}_a(t)$. We then use $\hat{V}_a(t)$ in the derivation of $A_g(t)$. The introduction of the homeostatic scaling velocity leads to a series of typos, and is unnecessary.

After scaling, the ageing velocity of immature individuals is $\hat{V}_a(t)$. Therefore, the gamma distributed DDE (2.39) should read

$$\begin{aligned} \frac{d}{dt} x(t) &= F \left[x(t), \hat{V}_a(t) A_g(t) \right] - \gamma(x(t)) x(t) \\ x(s) &= \rho(s), s \in (-\infty, t_0]. \end{aligned}$$

This change should propagate to the finite dimensional representation of $x(t)$. Thus, Theorem 2.4.4 should also include the scaled ageing velocity and the correct differential equation for $x(t)$ is

$$\frac{d}{dt} x(t) = F(x(t), \hat{V}_a(t) x_j(t)) - \gamma(x(t)) x(t).$$

Similarly, the definition of $x_i(t)$ in (2.41) must include the scaled ageing velocity and should read

$$x_i(t) = \int_{-\infty}^t g_{V_a^*}^i(a_t(t - \phi)) \frac{\beta x(\phi)}{\hat{V}_a(\phi)} \exp \left[- \int_{\phi}^t \mu(x(s)) ds \right] d\phi.$$

The corrected definition of x_i ensures that $x_j(t) = A_g(t)$ as claimed. It is important to mention that the neither the results nor the derivations of Section 2.4.3 are impacted by these typos, nor is the age scaling necessary in Theorem 2.4.4.

In fact, we now show it is simple to rederive those results without rescaling the ageing velocity. Consider the generic gamma distributed DDE

$$\frac{d}{dt}x(t) = F(x(t), V_a(t)\Lambda_g(t)) - \gamma(x(t))x(t)$$

where

$$\Lambda_g(t) = \int_0^\infty g_b^j \left(\int_{t-\phi}^t V_a(s) ds \right) \frac{\beta x(t-\phi)}{V_a(t-\phi)} \exp \left[- \int_{t-\phi}^t \mu(x(s)) ds \right] d\phi.$$

By defining

$$\chi_i(t) = \int_0^\infty g_b^i \left(\int_{t-\phi}^t V_a(s) ds \right) \frac{\beta x(t-\phi)}{V_a(t-\phi)} \exp \left[- \int_{t-\phi}^t \mu(x(s)) ds \right] d\phi,$$

we immediately see that $\Lambda_g(t) = \chi_j(t)$. By repeating the proof of Lemma 2.4.3 verbatim, it is clear that that

$$\begin{aligned} \frac{d}{dt}\chi_1(t) &= \frac{\beta x(t)}{V_a(t)} - bV_a(t)\chi_1(t) - \mu(x(t))\chi_1(t) \\ \frac{d}{dt}\chi_i(t) &= bV_a(t) [\chi_{i-1}(t) - \chi_i(t)] - \mu(x(t))\chi_i(t) \quad \text{for } i = 2, 3, \dots, j. \end{aligned}$$

Thus, the scaled ageing velocity $\hat{V}_a(t)$ used in Section 2.4.3.1 is not necessary. However, most transit compartment models with variable transit speed in the literature explicitly write the velocity $V_a(t)$ and not the product $bV_a(t)$. In such cases, including the examples considered in Section 2.5, it is simpler to use the scaled velocity $\hat{V}_a(t)$.

Equivalences Between Age Structured Models and State Dependent Distributed Delay Differential Equations

Tyler Cassidy¹, Morgan Craig^{2,3} and Antony R. Humphries^{1,3}

¹ Department of Mathematics and Statistics, McGill University,
805 Sherbrooke Street West, Montreal, H3A 0B9, Canada.

² Département de mathématiques et de statistique, Université de Montréal,
2920 chemin de la Tour, Montréal, H3T 1J4, Canada

³ Department of Physiology, McGill University,
3655 Promenade Sir-William-Osler, Montreal, H3G 1Y6, Canada.

Submitted: 30 November 2018; revised on 26 March 2019; accepted on 27
March 2019

Abstract

We use the McKendrick equation with variable ageing rate and randomly distributed maturation time to derive a state dependent distributed delay differential equation. We show that the resulting delay differential equation preserves non-negativity of initial conditions and we characterise local stability of equilibria. By specifying the distribution of maturation age, we recover state dependent discrete, uniform and gamma distributed delay differential equations. We show how to reduce the uniform case to a system of state dependent discrete delay equations and the gamma distributed case to a system of ordinary differential equations. To illustrate the benefits of these reductions, we convert previously published transit compartment models into equivalent distributed delay differential equations.

2.1 INTRODUCTION

Age structured population models have been used extensively in mathematical biology throughout the past 90 years [McKendrick, 1925; Trucco, 1965] (see Metz and Diekmann [1986] for a review). These age structured models describe the progression of individuals through an ageing process by using partial differential equations (PDEs), that can, in certain cases, be reduced to a delay differential equation (DDE) [Craig et al., 2016; Metz and Diekmann, 1986; Smith, 1993]. When individuals exit the ageing process in a deterministic manner upon reaching a threshold maturation age, the age structured model is typically reduced to a discrete DDE.

In many populations, the speed at which an individual matures is often only weakly coupled to chronological time and is dynamically controlled by the availability of resources. Consequently, when considering the age of an individual in a population, it is the biological age – and not the chronological age – that is of interest. It is possible to allow for this dynamic accumulation of biological age by including a variable ageing rate in an age structured PDE model. PDE models with variable ageing rates and threshold maturation rates can be reduced to state dependent discrete DDEs. State dependent delays considerably complicate the study of these models, but incorporate external control of the maturation process and increase physiological relevance.

However, imposing a threshold maturation age does not account for population heterogeneity and implicitly assumes a homogeneous maturation age. Given the importance of individual differences in a population, it is important that intraspecies heterogeneity is included in mathematical models. In light of these observations, we develop a technique to explicitly incorporate maturation age heterogeneity and external control of age accumulation by providing a framework for state dependent distributed DDEs. State dependent distributed DDEs account for a measure of population heterogeneity not present in discrete DDE models while retaining external control of the ageing process. Therefore, distributed DDEs offer a physiologically more realistic manner to model ageing processes in populations [Cassidy and Humphries, 2019].

To derive a state dependent distributed DDE, we consider a general age structured model with a variable ageing rate. We eschew a deterministic maturation process (which would lead to state dependent discrete DDEs), and instead assume that maturation age is a positive random variable A . This random variable defines a density function $K_A(t)$ through

$$K_A(t) = \lim_{\Delta t \rightarrow 0} \frac{\mathbb{P}[t \leq A \leq t + \Delta t]}{\Delta t}, \quad (2.1)$$

which satisfies

$$\int_0^{\infty} K_A(t) dt = 1 \quad \text{and} \quad K_A(t) \geq 0 \quad \forall t \geq 0.$$

As shown by [Craig et al. \[2016\]](#), [Otto and Radons \[2017\]](#), and [Bernard \[2016\]](#), replacing existing discrete delays with state dependent delays requires careful attention to how solutions pass across the maturation boundary. [Craig et al. \[2016\]](#) derived a “correction” factor to ensure that individuals are not spuriously created or destroyed during maturation. Our work generalises the correction factor derived by [Craig et al. \[2016\]](#) for state dependent discrete DDEs to any state dependent DDE. Specifically, our derivation does not rely on a smoothness argument, but arises naturally from the age structured PDE after a careful derivation of the maturation rate.

We show how the age structured PDE can be reduced to a state dependent distributed DDE. For specific densities $K_A(t)$, we show equivalence between the state dependent distributed DDE and state-dependent discrete DDEs with one or two delays or a finite dimensional systems of ordinary differential equations (ODEs). These equivalences arise from the explicit consideration of the ageing process modelled by the distributed DDEs. By applying the linear chain technique to the age variable, instead of the time variable, we are able to establish the desired equivalences. As there is not an available all purpose numerical method capable of solving distributed DDEs, these equivalences allow for the model to be analysed as a DDE and simulated using the highly efficient established techniques for discrete DDEs or ODEs. To illustrate the benefits of the techniques developed here, we consider two previously published models of hematopoietic cell production and show how using distributed DDEs can simplify the analysis of the resulting model.

The structure of the article is as follows. In [Section 2.2](#), we study the McKendrick equation for a generic population with a variable ageing rate and random maturation time. By solving the PDE using the method of characteristics, we derive a state-dependent distributed DDE for the general density $K_A(t)$ in [Theorem 2.2.1](#). We discuss the naturally arising correction factor in [Section 2.2.1](#). To illustrate the benefits of reducing age structured models to DDEs, we show that the resulting DDE preserves non-negativity of initial conditions and perform stability analysis to study the local stability of equilibria in [Section 2.3](#). By specifying $K_A(t)$ to be a degenerate distribution, we recover a state-dependent discrete DDE in [Section 2.4.1](#). Next, we consider uniform distributions and the equivalent two delay DDE in [Section 2.4.2](#). In [Section 2.4.3](#), we study a gamma distributed DDE. Through a generalization of the linear chain technique to include a variable transit rate, we show how this gamma distributed DDE can be reduced to a finite dimensional system of transit compartment ODEs in [Section 2.4.3.1](#). In [Section 2.5](#), we formalize the link between variable transit rate compartment models and state dependent delayed processes

by converting two previously published transit compartment models to the corresponding distributed DDEs. Finally, we summarize our results with a brief conclusion.

2.2 FROM MCKENDRICK TYPE EQUATIONS TO STATE DEPENDENT DELAYS

Consider a population divided into immature and mature compartments in which only mature individuals reproduce. Let $n(t, a)$ denote the number of immature individuals at time t with age a and $x(t)$ denote the number of mature members of the population at time t . The purpose of this section is to establish a state dependent distributed DDE model for $x(t)$.

We begin with an age structured PDE for the immature population, $n(t, a)$. Immature individuals progress through maturation with a variable ageing rate $V_a(t)$, where $V_a(t)$ satisfies

$$0 < V_a^{min} \leq V_a(t) \leq V_a^{max} < \infty.$$

Following McKendrick [1925], the PDE describing $n(t, a)$ is

$$\left. \begin{aligned} \partial_t n(t, a) + V_a(t) \partial_a n(t, a) &= -[\mu(x(t)) + h(a)] n(t, a) \\ V_a(t) n(t, 0) &= \beta x(t) \quad t \geq t_0; \quad n(t_0, a) = f(a) \geq 0 \quad \forall a \in (0, \infty). \end{aligned} \right\} \quad (2.2)$$

The boundary condition $V_a(t)n(t, 0) = \beta x(t)$ that we impose links the creation of immature individuals $n(t, 0)$ with the birth rate $\beta x(t)$. The presence of $V_a(t)$ in this boundary term can be understood from the conveyor belt analogy [Bernard, 2016; Mahaffy et al., 1998]. In the following, we assume $\beta > 0$. The initial conditions $n(t_0, a) = f(a) \geq 0$, describes immature individuals with non-zero age at time t_0 .

The death rate of immature individuals is given by $\mu(x(t))$ while transition from the immature state to the mature state is modelled by $h(a)$. It is important to note that the transition rate is a function of the age of individuals at time t . Since we expect a link between time and physiological age, we will write $a(t)$. Later, we formalize the weakly coupled relationship between biological and chronological age and justify this notation by finding the characteristics of (2.2).

We begin by deriving the transition rate from immaturity to maturity, $h(a(t))$. As mentioned, we assume that the age at which an individual matures is a non-negative random variable A with density function $K_A(t)$. The transition rate, $h(a(t))$, is the instantaneous change in probability that an individual matures at age $a(t + \Delta t)$, given that the individual has not matured at age $a(t)$. Formally, using the definition of conditional probability,

$$h(a(t)) = \lim_{\Delta t \rightarrow 0} \frac{\mathbb{P}[a(t) \leq A \leq a(t + \Delta t) \mid A \geq a(t)]}{\Delta t} = \lim_{\Delta t \rightarrow 0} \frac{\mathbb{P}[a(t) \leq A \leq a(t + \Delta t)]}{\mathbb{P}[A \geq a(t)] \Delta t}.$$

Multiplying by unity gives

$$h(a(t)) = \frac{1}{\mathbb{P}[A \geq a(t)]} \lim_{\Delta t \rightarrow 0} \frac{\mathbb{P}[a(t) \leq A \leq a(t + \Delta t)] [a(t + \Delta t) - a(t)]}{[a(t + \Delta t) - a(t)] \Delta t}.$$

By (2.1) and the derivative of $a(t)$, we obtain

$$h(a(t)) = \frac{K_A(a(t))}{1 - \int_0^{a(t)} K_A(\sigma) d\sigma} \frac{d}{dt} a(t). \quad (2.3)$$

The transition (or maturation) rate, $h(a(t))$, is known as the hazard rate of the random variable A and has applications in modelling failure rates [Cox, 1972; Kaplan and Meier, 1958]. The identical expression for $h(a(t))$ without considering the conditional maturation probability was derived by Metz and Diekmann [1986].

It is possible that immature individuals create multiple mature individuals upon transitioning to the mature compartment (i.e mitosis), so we model the influx rate into the mature compartment as a function

$$F \left(x(t), \int_0^\infty h(s)n(t, s) ds \right),$$

where the integral term

$$\int_0^\infty h(s)n(t, s) ds \quad (2.4)$$

is the number of immature individuals that reach maturity at time t . If mature individuals are cleared at a population dependent rate $\gamma(x(t))$, then the mature population satisfies

$$\left. \begin{aligned} \frac{d}{dt} x(t) &= F \left(x(t), \int_0^\infty h(s)n(t, s) ds \right) - \gamma(x(t))x(t) \\ x(0) &= x_0. \end{aligned} \right\} \quad (2.5)$$

We are now able to establish equivalence between the system of equations describing the populations $x(t)$ and $n(t, a)$ and a distributed DDE. To do this, we partially solve the PDE (2.2) using the method of characteristics.

Theorem 2.2.1 (State-Dependent Distributed DDE). *Let the immature population $n(t, a)$ satisfy the McKendrick age structured PDE (2.2) with the distribution dependent transition rate $h(a(t))$ (2.3). Assume that the mature population $x(t)$ is given by (2.5).*

Then, the mature population $x(t)$ satisfies the initial value problem (IVP)

$$\begin{aligned} \frac{d}{dt}x(t) = & F\left(x(t), \int_0^\infty \beta x(t-\phi) \frac{V_a(t)}{V_a(t-\phi)} \exp\left[-\int_{t-\phi}^t \mu(x(s))ds\right] K_A\left(\int_{t-\phi}^t V_a(s)ds\right) d\phi\right) \\ & - \gamma(x(t))x(t) \end{aligned} \quad (2.6)$$

with initial data

$$x(s) = \rho(s) \quad \forall s \in (-\infty, t_0].$$

Proof. The characteristics of equation (2.2) satisfy

$$\frac{d}{d\phi}t(\phi) = 1, \quad \text{and} \quad \frac{d}{dt}a(t) = V_a(t), \quad (2.7)$$

and hence are given by

$$t = \phi + T_0 \quad \text{and} \quad a(t) = \int_{T_0}^t V_a(x)dx + a_0.$$

Along the characteristics, the age structured PDE (2.2) becomes

$$\frac{d}{dt}n(t, a(t)) = - \left[\mu(x(t)) + \frac{K_A(a(t))}{1 - \int_0^{a(t)} K_A(\sigma)d\sigma} V_a(t) \right] n(t, a(t)). \quad (2.8)$$

Equation (2.8) has solution

$$n(t, a(t)) = n(T_0, a_0) \exp\left[-\int_{T_0}^t \mu(x(s))ds\right] \left(1 - \int_0^{a(t)} K_A(\sigma)d\sigma\right).$$

If $a_0 = 0$, we use the boundary condition of (2.2) to find

$$n(t, a(t)) = \frac{\beta x(T_0)}{V_a(T_0)} \exp\left[-\int_{T_0}^t \mu(x(s))ds\right] \left(1 - \int_0^{a(t)} K_A(\sigma)d\sigma\right), \quad (2.9)$$

while, if $a_0 > 0$, the initial condition of (2.2) gives

$$n(t, a(t)) = f(a_0) \exp\left[-\int_{t_0}^t \mu(x(s))ds\right] \left(1 - \int_0^{a(t)} K_A(\sigma)d\sigma\right).$$

To establish an equivalence between the PDE (2.2) and the distributed DDE (2.6), it is necessary to define suitable initial data $x(s) = \rho(s)$ for $s < t_0$ for the DDE. To do this, it is natural to assume that an immature individual with positive age $a > 0$ at time t_0 was born at sometime $s < t_0$. Since the PDE (2.2) is not defined for $s < t_0$, we are free to prescribe fixed values for $V_a(s) = V_a^*$ and $\mu(x(s)) = \mu^*$ for $s < t_0$. Then, imposing that individuals born at time $s < t_0$ evolved according to the McKendrick Equation, we have

$a = V_a^*(t_0 - s)$, or $s = t_0 - a/V_a^*$. Hence, the initial condition $f(a)$ defines the history function ρ through

$$f(a) = \frac{\beta}{V_a^*} \rho(t_0 - a/V_a^*) \exp \left[\int_{t_0 - a/V_a^*}^{t_0} -\mu^* ds \right]. \quad (2.10)$$

Therefore defining $x(s) = \rho(s)$ this way, for $s < t_0$, the solution (2.9) applies.

Now, we finalize the link between the age structured PDE and the distributed DDE by following the characteristic curves until they intersect with the $a = 0$ axis. Along the characteristic curves, at time t , individuals born at time $T_0 = t - \phi$ have age

$$a_t(\phi) = \int_{T_0}^t V_a(x) dx = \int_{t-\phi}^t V_a(x) dx$$

for $\phi > 0$. So we have

$$n(t, a_t(\phi)) = \frac{\beta x(t - \phi)}{V_a(t - \phi)} \exp \left[- \int_{t-\phi}^t \mu(x(s)) ds \right] \left(1 - \int_0^{a_t(\phi)} K_A(\sigma) d\sigma \right).$$

At time t , the rate at which individuals mature is

$$\int_0^\infty h(a_t(\phi)) n(t, a_t(\phi)) d\phi = \int_0^\infty K_A(a_t(\phi)) \beta x(t - \phi) \frac{V_a(t)}{V_a(t - \phi)} \exp \left[- \int_{t-\phi}^t \mu(x(s)) ds \right] d\phi. \quad (2.11)$$

By defining, for any density $K_A(t)$,

$$A_K(x(t)) := \int_0^\infty K_A(a_t(\phi)) \frac{\beta x(t - \phi)}{V_a(t - \phi)} \exp \left[- \int_{t-\phi}^t \mu(x(s)) ds \right] d\phi, \quad (2.12)$$

we have

$$\int_0^\infty h(a_t(\phi)) n(t, a_t(\phi)) d\phi = V_a(t) A_K(x(t)).$$

Consequently, using (2.12) and defining the history $\rho(s)$ according to (2.10), we have established the equivalence between the system of (2.2) and (2.5) with the distributed DDE (2.6). \square

2.2.1 Accounting for the Random Maturation Threshold

Further inspection of equation (2.11) reveals a ratio of ageing speeds $V_a(t)/V_a(t - \phi)$ in the integral term

$$\int_0^\infty h(a_t(\phi)) n(t, a_t(\phi)) d\phi = \int_0^\infty \beta x(t - \phi) \frac{V_a(t)}{V_a(t - \phi)} \exp \left[- \int_{t-\phi}^t \mu(x(s)) ds \right] K_A(\sigma) d\phi.$$

The ratio of ageing velocities at the entrance and exit of the ageing process acts as a correction factor. As shown by [Bernard \[2016\]](#) and [Craig et al. \[2016\]](#), models without the correction factor allow for spurious creation of individuals during maturation and some state-dependent DDEs have missed this important correction factor. Solutions of models without this correction factor do not necessarily preserve nonnegativity of initial data [Bernard \[2016\]](#).

[Craig et al. \[2016\]](#) derived the correction factor by carefully accounting for the number of cells crossing the maturation threshold in a discrete state-dependent DDE. In discrete DDEs, individuals mature following a deterministic process after accruing a specific threshold age, so the maturation boundary is well-defined. The derivation of the correction factor was based on the smoothness of the solution crossing the fixed maturation boundary. However, the idea of a fixed maturation boundary does not extend to random maturation ages. Consequently, the derivation of the correction factor by [Craig et al. \[2016\]](#) does not generalise to generic distributed DDEs.

Our derivation of the state-dependent distributed DDE produces the same correction factor through the instantaneous maturation probability, $h(a(t))$. The derivation of $h(a(t))$ in equation (2.3) produces the term $V_a(t)$ by accounting for the change of maturation probability due to the variable accumulation of age at time t . For a degenerate distribution, as shown in Section 2.4.1, we obtain precisely the same ratio as [Craig et al. \[2016\]](#).

2.3 PROPERTIES OF STATE DEPENDENT DELAY DIFFERENTIAL EQUATIONS

Replacing an age structured PDE by a DDE eliminates the need to explicitly model the ageing populations, which can be difficult to measure experimentally. DDEs offer a natural framework that explicitly incorporates delays and identifies the relationship between the current and past states. This can facilitate communication between mathematical biologists and biologists and physiologists. In particular, the explicit presence of the delay term allows for simple calculation of mean delay time. As shown [Câmara De Souza et al. \[2018\]](#), models of delayed processes without DDEs do not always accurately calculate the mean delay time. However, DDEs typically define infinite dimensional semi-dynamical systems, which can introduce mathematical difficulties.

As we have seen in Theorem 2.2.1, partially solving an age structured PDE may lead to a DDE. As such, analysing these partially solved systems can be simpler than studying the corresponding PDE. As an example, we analyse the state-dependent distributed DDE in

equation (2.6). Define

$$\bar{x}(t) = V_a(t)A_K(t) = V_a(t) \int_0^\infty K_A(a_t(\phi)) \frac{\beta x(t-\phi)}{V_a(t-\phi)} \exp \left[- \int_{t-\phi}^t \mu(x(s)) ds \right] d\phi, \quad (2.13)$$

and consider the IVP

$$\left. \begin{aligned} \frac{d}{dt}x(t) &= F[x(t), \bar{x}(t)] - \gamma(x(t))x(t) & t > t_0 \\ x(s) &= \rho(s) & s \in (-\infty, t_0], \end{aligned} \right\} \quad (2.14)$$

where $F(x, y) \in C^1(\mathbb{R}^2, \mathbb{R})$ and $\gamma(x(t)) \in C^1(\mathbb{R}, \mathbb{R})$ with

$$F(x, y) > 0 \quad \text{if } x > 0 \text{ or } y > 0, \quad F(0, 0) = 0, \quad \text{and} \quad \gamma(x(t)) < \gamma_{max} < \infty. \quad (2.15)$$

We recall that A is the random variable representing the maturation age of immature individuals. The history function, $\rho(s)$, is chosen to belong to the space $L_1(A)$ where

$$K_A(t) = \frac{dA}{d\lambda},$$

and λ is the Lebesgue measure on \mathbb{R} . $L_1(A)$ satisfies the axioms for a phase space given by Hale and Verduyn Lunel [1993] and Hino et al. [1991], so the solution of the IVP (2.14) exists and is unique in $L_1(A)$. In population modelling, it is likely that any realistic history is uniformly continuous and bounded. The space of bounded and uniformly continuous functions is a subspace of $L_1(A)$ and is a suitable phase space.

The age structured PDE (2.2) describes population dynamics in the presence of a maturation time. Consequently, solutions of (2.14) must represent a population, and in particular, remain non-negative. However, the presence of delays in other models may lead to solutions that do not remain non-negative, as noted by Liu et al. [2007]. We begin our analysis by showing that the solution of the IVP (2.14), $x(t)$, evolving from non-negative initial conditions remains non-negative. This property is a natural requirement for models of population dynamics.

Proposition 2.3.1. *Let $F(x, y)$ and $\gamma(x(t))$ satisfy equations (2.15). Moreover, assume that the history function satisfies*

$$\rho(s) \geq 0 \quad \forall s \in (-\infty, t_0].$$

Then, the solution of the IVP (2.14) remains non-negative for all time $t > t_0$.

Proof. As $\rho(s) \geq 0$, it is simple to see that

$$\bar{x}(t_0) = V_a(t_0) \int_0^\infty K_A(a_{t_0}(\phi)) \frac{\beta \rho[t_0 - \phi]}{V_a(t_0 - \phi)} \exp \left[- \int_{t_0 - \phi}^{t_0} \mu(x(s)) ds \right] d\phi \geq 0.$$

We have a series of cases.

1) If $\rho(t_0) = x(t_0) > 0$ then $F(x(t_0), \bar{x}(t_0)) > 0$. Therefore,

$$\frac{d}{dt}x(t) = F(x(t), \bar{x}(t)) - \gamma(x(t))x(t) \geq -\gamma(x(t))x(t) > -\gamma_{max}x(t)$$

and using Gronwall's inequality, we have

$$x(t) \geq \rho(t_0) \exp(-\gamma_{max}[t - t_0]) > 0.$$

2) If $\rho(t_0) = 0$ and $\rho(s) = 0$ A -almost everywhere in $(-\infty, t_0)$, then $x(t) = 0$ is the solution of the IVP.

3) Finally, if $\rho(t_0) = 0$ and $\rho(s) > 0$ on a set of A -positive measure in $(-\infty, t_0)$ then $\bar{x}(t_0) > 0$ and

$$\left. \frac{d}{dt}x(t) \right|_{t=t_0} = F(x(t_0), \bar{x}(t_0)) - \gamma(t_0)x(t_0) = F(0, \bar{x}(t_0)) > 0.$$

Consequently, $x(t)$ becomes positive immediately and Case 3 reduces to Case 1.

Therefore, solutions of the IVP (2.14) remain non-negative for all time $t > t_0$. \square

2.3.1 Linearisation of the DDE

We continue the analysis of equation (2.6) by studying the local stability of equilibrium solutions. To do this, let $x^*(t) = x^* \in L_1(A)$ be an equilibrium of the IVP (2.14), so

$$F(x^*, \bar{x}^*) = \gamma(x^*)x^*. \quad (2.16)$$

At the equilibrium $x(t) = x^*$, $V_a(t) = V_a^*$, so

$$a_t(\phi) = \int_{t-\phi}^t V_a(s) ds = V_a^* \phi \quad \text{and} \quad \frac{V_a(t)}{V_a(t-\phi)} = 1$$

then, by evaluating (2.13) with $x(t) = x^*$, the homeostatic delayed term \bar{x}^* in (2.16) satisfies

$$\bar{x}^* = \int_0^\infty \beta x^* K_A(V_a^* \phi) \exp[-\mu^* \phi] d\phi = \frac{\beta}{V_a^*} x^* \mathcal{L}[K_A](\mu^*/V_a^*),$$

where $\mathcal{L}[f](s)$ is the Laplace transform of $f(x)$ evaluated at s .

Hence, \bar{x}^* is a function of the density $K_A(t)$. However, if desired, it is possible to vary the homeostatic death rate μ^* to ensure that the equilibria value x^* does not change for different densities $K_A(t)$ as shown by Cassidy and Humphries [2019].

Set $z(t) = x(t) - x^*$, and for $z(t)$ small– similar to the discrete state dependent delay

case considered by [Hartung et al. \[2006\]](#)– freeze the ageing and clearance rates at their homeostatic values, so $V_a(t) = V_a^*$ and $\mu(s) = \mu^*$. By expanding exponential integral to leading order following [Cassidy and Humphries \[2019\]](#), it is possible to relax the assumption that $\mu(s) = \mu^*$. Now, define $\bar{z}(t) = \bar{x}(t) - \bar{x}^*$ so that

$$\begin{aligned}\bar{z}(t) &= \int_0^\infty K_A(V_a^* \phi) \beta x[t - \phi] \exp[-\mu^* \phi] - \beta x^* K_A(V_a^* \phi) \exp[-\mu^* \phi] \, d\phi \\ &= \int_0^\infty K_A(V_a^* \phi) \beta z[t - \phi] \exp[-\mu^* \phi] \, d\phi,\end{aligned}\tag{2.17}$$

and the equilibrium is translated to the origin. Then, the differential equation for $z(t)$ is

$$\frac{d}{dt} z(t) = F(z(t) + x^*, \bar{z}(t) + \bar{x}^*) - \gamma(x(t))z(t) - \gamma(x(t))x^*.$$

By making the ansatz

$$z(t) = C e^{\lambda t},$$

we compute the expression for $\bar{z}(t)$ from [\(2.17\)](#)

$$\begin{aligned}\bar{z}(t) &= C z(t) \int_0^\infty K_A(V_a^* \phi) \beta e^{-\lambda \phi} [\exp[-\mu^* \phi]] \, d\phi \\ &= C z(t) \frac{\beta}{V_a^*} \mathcal{L}[K_A](\mu^* + \lambda / V_a^*).\end{aligned}$$

Therefore

$$\frac{d}{dt} z(t) = k_1 z(t) + k_2 \frac{\beta}{V_a^*} \mathcal{L}[K_A](\mu^* + \lambda / V_a^*) z(t) - \gamma^* z(t) + \mathcal{O}(z^2)$$

where $\gamma^* = \partial_x \gamma(x(t))|_{x=x^*}$, $k_1 = \partial_a F(a, b)|_{(x, \bar{x})}$ and $k_2 = \partial_b F(a, b)|_{(x, \bar{x})}$. Dropping nonlinear terms, the linearised equation is

$$\frac{d}{dt} z(t) = (k_1 - \gamma^*) z(t) + k_2 \frac{\beta}{V_a^*} \mathcal{L}[K_A](\mu^* + \lambda / V_a^*) z(t).\tag{2.18}$$

The characteristic equation corresponding to [\(2.18\)](#) is

$$0 = \lambda - (k_1 - \gamma^*) - k_2 \frac{\beta}{V_a^*} \mathcal{L}[K_A](\mu^* + \lambda / V_a^*).\tag{2.19}$$

Through a standard analysis, we study the local stability of the equilibrium x^* for a density $K_A(t)$.

Proposition 2.3.2. 1) If

$$|k_2| \frac{\beta}{V_a^*} \mathcal{L}[K_A](\mu^* / V_a^*) < \gamma^* - k_1,$$

the equilibrium point x^* is locally asymptotically stable.

2) If

$$k_2 \frac{\beta}{V_a^*} \mathcal{L}[K_A](\mu^*/V_a^*) > \gamma^* - k_1,$$

the equilibrium point x^* is unstable.

Proof. 1) Let λ^* be a root of (2.19) and assume for contradiction that $\Re(\lambda^*) \geq 0$. We necessarily have

$$\lambda^* = (k_1 - \gamma^*) + k_2 \frac{\beta}{V_a^*} \mathcal{L}[K_A](\mu^*/V_a^*),$$

and we calculate

$$\Re(\lambda^*) = (k_1 - \gamma^*) + k_2 \frac{\beta}{V_a^*} \Re[\mathcal{L}[K_A](\mu^*/V_a^*)].$$

We note that

$$k_2 \frac{\beta}{V_a^*} \Re[\mathcal{L}[K_A](\mu^*/V_a^*)] \leq \left| k_2 \frac{\beta}{V_a^*} \mathcal{L}[K_A](\mu^*/V_a^*) \right|.$$

While, for arbitrary $\nu = \nu_r + i\nu_i \in \mathbb{C}$,

$$\begin{aligned} \left| k_2 \frac{\beta}{V_a^*} \mathcal{L}[K_A](\nu/V_a^*) \right| &= \left| k_2 \frac{\beta}{V_a^*} \int_0^\infty \exp[-(\mu^* + \nu_r + i\nu_i)\phi] K_A(V_a^*\phi) \mathbf{d}\phi \right| \\ &\leq \left| k_2 \frac{\beta}{V_a^*} \int_0^\infty \exp[-(\mu^* + \nu_r)\phi] K_A(V_a^*\phi) \left| e^{-i\nu_i\phi} \right| \mathbf{d}\phi \right| \\ &= \left| k_2 \frac{\beta}{V_a^*} \mathcal{L}[K_A](\nu_r/V_a^*) \right|. \end{aligned}$$

Moreover, if $\nu_r \geq 0$,

$$\left| k_2 \frac{\beta}{V_a^*} \mathcal{L}[K_A](\nu_r/V_a^*) \right| \leq \left| k_2 \frac{\beta}{V_a^*} \mathcal{L}[K_A](\mu^*/V_a^*) \right|.$$

Therefore, using the assumption in 1), we find

$$\Re(\lambda^*) = (k_1 - \gamma^*) + k_2 \frac{\beta}{V_a^*} \Re[\mathcal{L}[K_A](\mu^*/V_a^*)] \leq (k_1 - \gamma^*) + \left| k_2 \frac{\beta}{V_a^*} \mathcal{L}[K_A](\mu^*/V_a^*) \right| < 0,$$

which is a contradiction, so no such λ^* can exist. Therefore, all roots of the characteristic equation have negative real part and the equilibrium is stable.

2) To show instability, we will prove that there must be one characteristic root with

positive real part. Define

$$g(\lambda) := k_1 - \gamma - \lambda + k_2 \frac{\beta}{V_a^*} \mathcal{L}[K_A](\lambda + \mu^*/V_a^*),$$

and note that $g(\lambda)$ is continuous with

$$g(0) = k_1 - \gamma + k_2 \frac{\beta}{V_a^*} \mathcal{L}[K_A](\mu^*/V_a^*) > 0 \quad \text{and} \quad \lim_{\lambda \rightarrow \infty} g(\lambda) = -\infty.$$

Then, there must be a real $\lambda^* > 0$ such that $g(\lambda^*) = 0$. The equilibrium is therefore unstable. \square

We note that if $k_2 > 0$, i.e. the production of mature individuals is controlled through positive feedback with the number of maturing individuals at time t , then Proposition 2.3.2 completely characterizes the local stability of x^* . If $k_2 < 0$, it seems likely that x^* would lose stability through a Hopf bifurcation, similar to the discrete delay case. A similar analysis was done in the constant ageing rate by Yuan and Bélair [2011]. However, Yuan and Bélair [2011] did not consider death of immature individuals, nor the linear clearance of mature individuals which corresponds to $\mu = \gamma = 0$.

2.4 DISTRIBUTED DELAY DIFFERENTIAL EQUATIONS WITH SPECIFIC MATURATION PROBABILITIES

Next, we study the DDE found in Theorem 2.2.1 for various density functions. By first considering the characteristic equation (2.19) for specific densities $K_A(t)$, we motivate the reduction of these population models to familiar discrete DDEs and transit compartment ODEs. In the discussion that follows, we once again assume that $x^* \in L_1(A)$ is an equilibrium point so that $\mu(x^*) = \mu^*$ and $V_a(t) = V_a^*$. Denote the homeostatic maturation time as the first moment of the random variable A with constant ageing rate V_a^* ,

$$\tau^* = \int_0^\infty t K_A(V_a^* t) dt.$$

Consequently, the expected homeostatic maturation age is given by $\mathcal{T} = V_a^* \tau^*$.

We first consider the degenerate distribution concentrated at \mathcal{T} and recover the familiar state dependent discrete DDE. Next, we use a linear chain-type technique to reduce state dependent uniformly distributed DDEs to a system involving two state dependent delays. Finally, we show how to reduce a gamma distributed DDE to a transit compartment system of ODEs.

However, true equivalence between the distributed DDE and the reduced form does not follow directly. We must take care when prescribing initial conditions and history functions so that solutions of the different formulations are in fact equivalent. Only then do these reductions allow for the use of the highly efficient numerical methods available for discrete DDEs and ODEs available in most programming languages.

2.4.1 Deterministic maturation

Assuming that maturation is a deterministic process and occurs after achieving the threshold age \mathcal{T} implies that $K_A(t)$ is the degenerate distribution concentrated at \mathcal{T} with

$$K_A \left(\int_{t-\phi}^t V_a(s) ds \right) = \delta \left(\int_{t-\phi}^t V_a(s) ds - \mathcal{T} \right). \quad (2.20)$$

where $\delta(x)$ is the Dirac delta function. In the deterministic case, all individuals mature at precisely the same age \mathcal{T} . At the equilibrium x^* , using (2.19), the characteristic equation is

$$0 = \lambda - (k_1 - \gamma^*) - k_2 \frac{\beta}{V_a^*} \exp[-(\mu^* + \lambda)\mathcal{T}/V_a^*] = \lambda - (k_1 - \gamma^*) - k_2 \frac{\beta}{V_a^*} \exp[-(\mu^* + \lambda)\tau^*], \quad (2.21)$$

which is exactly the characteristic equation of a discrete DDE. This is unsurprising, since it is well known that threshold conditions lead to discrete DDEs [Otto and Radons, 2017; Smith, 1993].

Returning to the DDE (2.6) with $K_A(t)$ given by (2.20), the threshold maturation age \mathcal{T} allows us to calculate when an individual that matures at time t began maturation. The maturation time, $\tau(x(t))$, must satisfy the implicit threshold condition

$$\mathcal{T} = \int_{t-\tau(x(t))}^t V_a(s) ds. \quad (2.22)$$

We use the definition of $\tau(x(t))$ to evaluate the convolution integral given in (2.12) to find

$$\begin{aligned} A_\delta(t) &= \int_0^\infty \delta \left(\int_{t-\phi}^t V_a(s) ds - \mathcal{T} \right) \frac{\beta x(t-\phi)}{V_a(t-\phi)} \exp \left[- \int_{t-\phi}^t \mu(x(s)) ds \right] d\phi \\ &= \frac{\beta x[t - \tau(x(t))]}{V_a(t - \tau(x(t)))} \exp \left[- \int_{t-\tau(x(t))}^t \mu(x(s)) ds \right]. \end{aligned}$$

Consequently, the corresponding IVP to (2.6) with state dependent discrete delay is

$$\left. \begin{aligned} \frac{d}{dt} x(t) &= F \left(x(t), \beta x[t - \tau(x(t))] \exp \left[- \int_{t-\tau(t)}^t \mu(x(s)) ds \right] \frac{V_a(t)}{V_a(t - \tau(t))} \right) - \gamma x(t) \\ x(s) &= \rho(s) \quad s \in (-\infty, t_0]. \end{aligned} \right\} \quad (2.23)$$

To implement (2.23) numerically, it is necessary to solve (2.22) to find the maturation time $\tau(x(t))$. This can be done by differentiating (2.22) to find

$$\frac{d}{dt}\tau(x(t)) = 1 - \frac{V_a(t)}{V_a(t - \tau(x(t)))}, \quad (2.24)$$

and imposing the correct initial condition so that the solution of (2.24) also solves (2.22).

In the case that $\rho(s) = x^*$, then it is simple to set $\tau(0) = \tau^*$. However, for more general initial data $\rho(s)$, choosing an appropriate initial condition for (2.24) can be delicate [Otto and Radons, 2017].

Then, we can solve the discrete state dependent DDE by solving the system of equations given by (2.23) and (2.24). Hence the age structured PDE framework in Section 2.2 offers an alternative to the “moving threshold” method to derive state dependent DDEs as described by Otto and Radons [2017].

2.4.2 Uniformly Distributed Maturation

We consider uniformly distributed DDEs centered about the expected homeostatic maturation age \mathcal{T} . In the simplest case, the uniform distribution defines lower and upper threshold ages and assigns equal weight to each age falling between the thresholds. The probability density function corresponding to a uniform distribution centred at \mathcal{T} is

$$K_U(a) = \begin{cases} \frac{1}{2V_a^*\delta} & \text{if } a \in [\mathcal{T} - V_a^*\delta, \mathcal{T} + V_a^*\delta] \\ 0 & \text{otherwise.} \end{cases} \quad (2.25)$$

At the equilibrium x^* , with $K_A(t)$ given by the uniform density (2.25), the characteristic equation (2.19) is

$$\begin{aligned} 0 &= \lambda - (k_1 - \gamma^*) - k_2 \left(\frac{\beta}{V_a^*} \right) \left(\frac{1}{2\delta V_a^* [\lambda + \mu^*] / V_a^*} \right) \left[e^{-(\lambda + \mu^*)(\mathcal{T} - V_a^*\delta) / V_a^*} - e^{-(\lambda + \mu^*)(\mathcal{T} + V_a^*\delta) / V_a^*} \right] \\ &= \lambda - (k_1 - \gamma^*) - k_2 \left(\frac{\beta}{V_a^*} \right) \left(\frac{1}{2\delta(\lambda + \mu^*)} \right) \left[e^{-(\lambda + \mu^*)(\tau^* - \delta)} - e^{-(\lambda + \mu^*)(\tau^* + \delta)} \right]. \end{aligned} \quad (2.26)$$

$\mathcal{T} - V_a^*\delta$ and $\mathcal{T} + V_a^*\delta$ represent the minimal and the maximal ages at which an individual can mature. Due to the variable ageing rate, the minimal and maximal delay times, $\tau_{min}(x(t))$ and $\tau_{max}(x(t))$, are state dependent, and implicitly defined by

$$\mathcal{T} - V_a^*\delta = \int_{t - \tau_{min}(x(t))}^t V_a(s) ds \quad \text{and} \quad \mathcal{T} + V_a^*\delta = \int_{t - \tau_{max}(x(t))}^t V_a(s) ds.$$

We note that, at homeostasis, $V_a(s) = V_a^*$ so

$$\mathcal{T} - V_a^* \delta = \tau_{min}(x^*) V_a^* \quad \text{and} \quad \mathcal{T} + V_a^* \delta = \tau_{max}(x^*) V_a^*.$$

Recalling that $\mathcal{T} = V_a^* \tau^*$, the terms $\tau^* - \delta$ and $\tau^* + \delta$ in (2.26) correspond to the minimal and maximal homeostatic delay times.

The presence of minimal and maximal delay terms in (2.26) hints that a uniformly distributed DDE may be reducible to a discrete DDE with two distinct delays.

Inserting the uniform density (2.25) into the convolution integral (2.12) gives

$$\begin{aligned} A_U(t) &= \int_0^\infty K_U \left(\int_{t-\phi}^t V_a(s) ds \right) \frac{\beta x(t-\phi)}{V_a(t-\phi)} \exp \left[- \int_{t-\phi}^t \mu(x(s)) ds \right] d\phi \\ &= \int_{\tau_{min}(t)}^{\tau_{max}(t)} \frac{1}{2V_a^* \delta} \frac{\beta x(t-\phi)}{V_a(t-\phi)} \exp \left[- \int_{t-\phi}^t \mu(x(s)) ds \right] d\phi. \end{aligned}$$

Thus the state dependent uniform distributed DDE is

$$\left. \begin{aligned} \frac{d}{dt} x(t) &= F(x(t), A_U(t) V_a(t)) - \gamma(x(t)) x(t) \\ x(s) &= \rho(s), \quad s \in (-\infty, t_0]. \end{aligned} \right\} \quad (2.27)$$

2.4.2.1 Reduction to Discrete DDE

Next, we show that (2.27) can be reduced to an IVP with two state dependent discrete delays. Once again, this is advantageous, as numerical algorithms for systems of state dependent discrete DDEs are available in most programming languages.

We begin by formalizing the link between uniformly distributed DDEs and discrete DDEs that was hinted at in (2.26). To do this, we show to write the delay kernel as the solution of a differential equation. This strategy is also used in the well known linear chain technique (see Smith [2011]), which we generalise in Section 2.4.3.1. However, unlike the linear chain technique, we will not recover a system of ODEs, but rather a system of differential equations with two state dependent discrete delays. The technique here can also be adapted to ‘‘tent’’ like distributions (see Teslya [2015]).

Lemma 2.4.1. $A_U(t)$ satisfies the differential equation

$$\begin{aligned} \frac{d}{dt} A_U(t) &= \frac{1}{2V_a^* \delta} \left[\frac{\beta x[t - \tau_{min}(t)]}{V_a(t - \tau_{min}(t))} \exp \left[- \int_{t-\tau_{min}(t)}^t \mu(x(s)) ds \right] \frac{V_a(t)}{V_a(t - \tau_{min}(t))} \right. \\ &\quad \left. - \frac{\beta x[t - \tau_{max}(t)]}{V_a(t - \tau_{max}(t))} \exp \left[- \int_{t-\tau_{max}(t)}^t \mu(x(s)) ds \right] \frac{V_a(t)}{V_a(t - \tau_{max}(t))} \right] - \mu(x(t)) A_U(t). \end{aligned} \quad (2.28)$$

Proof. Similar to the linear chain technique, we differentiate $A_U(t)$ using Leibniz's rule to find

$$\begin{aligned} \frac{d}{dt} A_U(t) &= \frac{1}{2V_a^* \delta} \left[\frac{\beta x[t - \tau_{max}(t)]}{V_a(t - \tau_{max}(t))} \exp \left[- \int_{t - \tau_{max}(t)}^t \mu(x(s)) ds \right] \frac{d}{dt} \tau_{max}(t) \right. \\ &\quad \left. - \frac{\beta x[t - \tau_{min}(t)]}{V_a(t - \tau_{min}(t))} \exp \left[- \int_{t - \tau_{min}(t)}^t \mu(x(s)) ds \right] \frac{d}{dt} \tau_{min}(t) \right] \\ &\quad + \frac{1}{2\delta} \int_{\tau_{min}(t)}^{\tau_{max}(t)} \frac{d}{dt} \left(\frac{\beta x(t - \phi)}{V_a(t - \phi)} \exp \left[- \int_{t - \phi}^t \mu(x(s)) ds \right] \right) d\phi. \end{aligned}$$

We note that

$$\begin{aligned} \frac{d}{dt} \left(\frac{\beta x(t - \phi)}{V_a(t - \phi)} \exp \left[- \int_{t - \phi}^t \mu(x(s)) ds \right] d\phi \right) &= - \frac{d}{d\phi} \left(\frac{\beta x(t - \phi)}{V_a(t - \phi)} \exp \left[- \int_{t - \phi}^t \mu(x(s)) ds \right] \right) \\ &\quad - \mu(x(t)) \frac{\beta x(t - \phi)}{V_a(t - \phi)} \exp \left[- \int_{t - \phi}^t \mu(x(s)) ds \right], \end{aligned}$$

so that, integrating by parts,

$$\begin{aligned} \int_{\tau_{min}(t)}^{\tau_{max}(t)} \frac{d}{dt} \left(\frac{\beta x(t - \phi)}{V_a(t - \phi)} \exp \left[- \int_{t - \phi}^t \mu(x(s)) ds \right] \right) d\phi \\ = \left(- \frac{1}{2\delta} \frac{\beta x(t - \phi)}{V_a(t - \phi)} \exp \left[- \int_{t - \phi}^t \mu(x(s)) ds \right] \right) \Big|_{\phi = \tau_{min}(t)}^{\tau_{max}(t)} - \mu(x(t)) A_U(t). \end{aligned}$$

Consequently, the derivative of $A_U(t)$ is

$$\begin{aligned} \frac{d}{dt} A_U(t) &= \frac{1}{2V_a^* \delta} \left[\frac{\beta x[t - \tau_{max}(t)]}{V_a(t - \tau_{max}(t))} \exp \left[- \int_{t - \tau_{max}(t)}^t \mu(x(s)) ds \right] \left(\frac{d}{dt} \tau_{max}(t) - 1 \right) \right. \\ &\quad \left. - \frac{\beta x[t - \tau_{min}(t)]}{V_a(t - \tau_{min}(t))} \exp \left[- \int_{t - \tau_{min}(t)}^t \mu(x(s)) ds \right] \left(\frac{d}{dt} \tau_{min}(t) - 1 \right) \right] - \mu(x(t)) A_U(t). \end{aligned}$$

To finish the proof, we note that, similar to (2.24), $\tau_{min}(x(t))$ and $\tau_{max}(x(t))$ solve the following differential equations

$$\frac{d}{dt} \tau_{min}(x(t)) - 1 = - \frac{V_a(t)}{V_a(t - \tau_{min}(x(t)))} \quad \text{and} \quad \frac{d}{dt} \tau_{max}(x(t)) - 1 = - \frac{V_a(t)}{V_a(t - \tau_{max}(x(t)))}. \quad (2.29)$$

The identities in equation (2.29) give (2.28). \square

By writing the delay term $A_U(t)$ as a solution of a differential equation, we are able to reduce the distributed DDE to a system with state dependent discrete delays. Once again, this allows for simulation of the distributed DDE (2.27) using existing techniques. This relationship is formalized in the following theorem.

Theorem 2.4.2. *The IVP (2.27) is equivalent to the IVP with the following system of discrete delay differential equations*

$$\left. \begin{aligned} \frac{d}{dt}x(t) &= F(x(t), y(t)V_a(t)) - \gamma(x(t))x(t) \\ \frac{d}{dt}y(t) &= \frac{1}{2\delta} \left[\frac{\beta x[t - \tau_{min}(t)]}{\hat{V}_a(t - \tau_{min}(t))} \exp \left[- \int_{t-\tau_{min}(t)}^t \mu(x(s))ds \right] \frac{V_a(t)}{V_a(t - \tau_{min}(t))} \right. \\ &\quad \left. - \frac{\beta x[t - \tau_{max}(t)]}{\hat{V}_a(t - \tau_{max}(t))} \exp \left[- \int_{t-\tau_{max}(t)}^t \mu(x(s))ds \right] \frac{V_a(t)}{V_a(t - \tau_{max}(t))} \right] - \mu(x(t))y(t). \end{aligned} \right\} \quad (2.30)$$

with suitably chosen initial data.

Proof. Using Lemma 2.4.1, it is simple to see that

$$y(t)V_a(t) = A_U(t)V_a(t), \quad (2.31)$$

and the other terms in the differential equations are identical if the initial data are equivalent. It therefore remains to show that we can choose suitable history functions for the distributed and discrete DDEs. For the history function of the distributed DDE (2.27), $\rho(s)$, setting the initial data of (2.30) to be

$$x(s) = \rho(s)$$

and

$$y(t_0) = \int_{\tau_{min}(t_0)}^{\tau_{max}(t_0)} \frac{1}{2\delta} \frac{\beta \rho(t_0 - \phi)}{\hat{V}_a(t_0 - \phi)} \exp \left[- \int_{t_0 - \phi}^{t_0} \mu(\rho(s))ds \right] d\phi.$$

gives the desired equivalence [Teslya, 2015]. To convert from (2.30) with history function $x(s) = \eta(s)$ to (2.27), $y(t_0)$ must satisfy

$$y(t_0) = \int_{\tau_{min}(t_0)}^{\tau_{max}(t_0)} \frac{1}{2\delta} \frac{\beta \eta(t_0 - \phi)}{\hat{V}_a(t_0 - \phi)} \exp \left[- \int_{t_0 - \phi}^{t_0} \mu(\eta(s))ds \right] d\phi. \quad (2.32)$$

By taking the initial data for (2.27) to be $x(s) = \eta(s)$, we see that this condition is sufficient for equivalence of (2.30) and (2.27). Now, if (2.32) does not hold, then (2.31) cannot be satisfied at $t = t_0$, so (2.32) is a necessary and sufficient condition to be able to convert the system of DDEs (2.30) into the distributed DDE (2.27) with $x(s) = \eta(s)$. \square

2.4.3 Gamma distributed maturation and a generalized linear chain technique

Finally, we study gamma distributed DDEs and show how to reduce the state-dependent gamma distributed DDE to a transit chain of ODEs. The probability density function of

the gamma distribution is

$$g_b^j(x) = \frac{b^j x^{j-1} e^{-bx}}{\Gamma(j)}, \quad (2.33)$$

where $j, b \in \mathbb{R}$.

Again, let \mathcal{T} denote the mean maturation age and fix $j > 0$. Then, we have the following relationships

$$\mathcal{T} = j/V_a^*, \quad \sigma^2 = j/(V_a^*)^2, \quad \text{and} \quad K_g(\sigma) = g_{V_a^*}^j(\sigma),$$

where σ^2 is the variance of the gamma distribution and we set $b = V_a^*$.

Calculating (2.19) for the gamma density in (2.33) gives

$$0 = k_1 - \gamma - \lambda + k_2 \left(\frac{\beta}{V_a^*} \right) \left(\frac{(V_a^*)^j}{(V_a^* + [\lambda + \mu^*]/V_a^*)^j} \right). \quad (2.34)$$

Now, we use the relationships $V_a^* = j/\mathcal{T}$ and $\mathcal{T} = \tau^*V_a^*$ to rewrite the characteristic function as

$$\begin{aligned} k_1 - \gamma - \lambda + k_2 \left(\frac{\beta}{V_a^*} \right) \left(\frac{1}{(1 + \frac{\lambda + \mu^*}{V_a^*})^j} \right) &= k_1 - \gamma - \lambda + k_2 \left(\frac{\beta}{V_a^*} \right) \left(\frac{1}{(1 + \frac{\mathcal{T}(\lambda + \mu^*)}{V_a^* j})^j} \right) \\ &= k_1 - \gamma - \lambda + k_2 \left(\frac{\beta}{V_a^*} \right) \left(\frac{1}{(1 + \frac{\tau^*(\lambda + \mu^*)}{j})^j} \right). \end{aligned}$$

Using a common denominator gives

$$0 = (k_1 - \gamma - \lambda) \left(1 + \frac{\tau^*(\lambda + \mu^*)}{j} \right)^j + k_2 \frac{\beta}{V_a^*}. \quad (2.35)$$

Now, we consider multiple cases for the parameter j . If $j \in \mathbb{N}$, then (2.35) is a polynomial of degree $j + 1$, with $j + 1$ roots. This is markedly different than the generic distributed DDE, as the characteristic equation (2.19) is typically a transcendental function of λ with infinitely many characteristic values. Now, with $j = n/m \in \mathbb{Q}$, we can rearrange (2.35) to

$$(k_1 - \gamma - \lambda) \left(1 + \frac{\tau^*(\lambda + \mu^*)}{j} \right)^j = -k_2 \frac{\beta}{V_a^*},$$

and raising both sides of the equality to the power m gives

$$0 = (k_1 - \gamma - \lambda)^m \left(1 + \frac{\tau^*(\lambda + \mu^*)}{j} \right)^n + \left(-k_2 \frac{\beta}{V_a^*} \right)^m. \quad (2.36)$$

Not all solutions of (2.36) will necessarily satisfy (2.34). However, every solution of (2.34) will satisfy (2.36). Moreover, (2.36) is a polynomial with $m + n$ roots, so (2.34) with

$j = n/m \in \mathbb{Q}$ has at most $m + n$ roots. However, if the parameter j is not rational, then (2.35) is once again a transcendental equation with possibly infinitely many roots.

The relationship between the number of characteristic values and the parameter j leads to interesting questions. If $j \in \mathbb{N}$ increases by unit steps, then the characteristic equation gains precisely one root. However, if j increases smoothly between j and $j + 1$, do characteristic values spring in and out of existence depending on the rationality of j ? This question, while important, is outside the scope of the current work.

Having studied the characteristic equation of gamma distributed DDEs, we proceed to write down the gamma distributed DDE. We have parametrized the gamma distribution so that at homeostasis, the mean delay time is τ^* . The variable ageing velocity must then be scaled so that at homeostasis, individuals age chronologically. Therefore, we define the scaled ageing velocity

$$\hat{V}_a(t) = \frac{V_a(t)}{V_a^*}, \quad (2.37)$$

and will use $\hat{V}_a(t)$ throughout the remainder of our study. The scaled density function $g_{V_a^*}^j(a_t(\phi))$ is given by

$$g_{V_a^*}^j \left(\int_{t-\phi}^t \hat{V}_a(s) ds \right) = \frac{(V_a^*)^j}{\Gamma(j)} \left[\int_{t-\phi}^t \hat{V}_a(s) ds \right]^{j-1} \exp \left[-V_a^* \int_{t-\phi}^t \hat{V}_a(s) ds \right].$$

By inserting $g_{V_a^*}^j(a_t(\phi))$ into equation (2.12), we define

$$A_g(t) = \int_0^\infty g_{V_a^*}^j \left(\int_{t-\phi}^t \hat{V}_a(s) ds \right) \frac{\beta x(t-\phi)}{\hat{V}_a(t-\phi)} \exp \left[- \int_{t-\phi}^t \mu(x(s)) ds \right] d\phi. \quad (2.38)$$

Then, the IVP with a state-dependent distributed DDE corresponding to equation (2.6) is

$$\left. \begin{aligned} \frac{d}{dt} x(t) &= F[x(t), V_a(t) A_g(t)] - \gamma(x(t)) x(t) \\ x(s) &= \rho(s), s \in (-\infty, t_0]. \end{aligned} \right\} \quad (2.39)$$

As we show in Section 2.5, equivalent models to (2.39) have been used in pharmacokinetic modelling. However, these models typically take the form of finite dimensional systems of ODEs and the direct link between these ODEs with variable transit rates and (2.39) has not been established previously.

2.4.3.1 A Generalized linear chain technique

The finitely many roots of equation (2.34) for integer $j \in \mathbb{N}$ suggest that there is a finite dimensional representation of the DDE (2.39). The link between gamma distributed DDEs

and transit chain ODEs with constant transit rates has been known since at least 1961 [Vogel, 1961]. The method entered into the English literature in the works of MacDonald [1978] as the linear chain trick or the linear chain technique.

Just as in Section 2.4.2, the linear chain technique consists of replacing the convolution integral (2.38) by the solution of a system of differential equations. To do this, we will exploit the fact that, for $j \in \mathbb{N}$,

$$\frac{d}{dx}g_b^1(x) = -bg_b^1(x) \quad \text{and} \quad \frac{d}{dx}g_b^j(x) = b[g_b^{j-1}(x) - g_b^j(x)]. \quad (2.40)$$

The linear chain technique has been used extensively in pharmacology to model delayed drug absorption and action. However, typical applications of the technique require that transition rates between compartments are constant and identical. Câmara De Souza et al. [2018] developed an adapted linear chain technique that allows for variable transition rates by rescaling time in a non-linear way. This non-linear time rescaling leads to difficulties in establishing a link between time rescaled simulations and time series patient data [Câmara De Souza et al., 2018]. Here, we provide an alternative technique that allows for variable transition rates between compartments without rescaling time.

We first show how to write (2.38) as the solution of a system of ordinary differential equations.

Lemma 2.4.3. For $j \in \mathbb{N}$, $A_g(t) = x_j(t)$ where $\{x_i(t)\}_{i=1}^j$ satisfies

$$\begin{aligned} \frac{d}{dt}x_1(t) &= \frac{\beta x(t)}{\hat{V}_a(t)} - V_a(t)x_1(t) - \mu(x(t))x_1(t) \\ \frac{d}{dt}x_i(t) &= V_a(t)[x_{i-1}(t) - x_i(t)] - \mu(x(t))x_i(t) \quad \text{for } i = 2, 3, \dots, j. \end{aligned}$$

Proof. We first note that

$$g_{V_a^*}^i \left(\int_t^t \hat{V}_a(s) ds \right) = \begin{cases} V_a^* & \text{if } i = 1 \\ 0 & \text{if } i = 2, 3, \dots, j. \end{cases}$$

Then using (2.40) and (2.7), the chain and Leibniz rules show that

$$\frac{d}{dt}g_{V_a^*}^1 \left(\int_\phi^t \hat{V}_a(s) ds \right) = -V_a^* \hat{V}_a(t) g_{V_a^*}^1 \left(\int_\phi^t \hat{V}_a(s) ds \right) = -V_a(t) g_{V_a^*}^1 \left(\int_\phi^t \hat{V}_a(s) ds \right)$$

while, for $i = 2, 3, 4, \dots$,

$$\begin{aligned} \frac{d}{dt} g_{V_a^*}^i \left(\int_{\phi}^t \hat{V}_a(s) ds \right) &= V_a^* \hat{V}_a(t) \left[g_{V_a^*}^{i-1} \left(\int_{\phi}^t \hat{V}_a(s) ds \right) - g_{V_a^*}^i \left(\int_{\phi}^t \hat{V}_a(s) ds \right) \right] \\ &= V_a(t) \left[g_{V_a^*}^{i-1} \left(\int_{\phi}^t \hat{V}_a(s) ds \right) - g_{V_a^*}^i \left(\int_{\phi}^t \hat{V}_a(s) ds \right) \right]. \end{aligned}$$

Now we define,

$$a_t(x) = \int_{t-x}^t \hat{V}_a(s) ds$$

and, for $i = 1, 2, \dots, j$,

$$x_i(t) = \int_{-\infty}^t g_{V_a^*}^i(a_t(t-\phi)) \frac{\beta x(\phi)}{V_a(\phi)} \exp \left[- \int_{\phi}^t \mu(x(s)) ds \right] d\phi, \quad (2.41)$$

and note that, after making the change of variable $u = t - \phi$ in $A_g(t)$,

$$x_j(t) = \int_{-\infty}^t g_{V_a^*}^j(a_t(t-\phi)) \frac{\beta x[\phi]}{V_a(\phi)} \exp \left[- \int_{\phi}^t \mu(x(s)) ds \right] d\phi = A_g(t).$$

Now, by differentiating (2.41) using the Leibniz rule, the transit chain $x_i(t)$ satisfies the system of equations

$$\begin{aligned} \frac{d}{dt} x_1(t) &= \frac{\beta x(t)}{\hat{V}_a(t)} - V_a(t) x_1(t) - \mu(x(t)) x_1(t) \\ \frac{d}{dt} x_i(t) &= V_a(t) [x_{i-1}(t) - x_i(t)] - \mu(x(t)) x_i(t) \quad \text{for } i = 2, 3, \dots, j. \quad \square \end{aligned}$$

Importantly, Lemma 2.4.3 ensures that

$$V_a(t) A_g(t) = V_a(t) x_j(t). \quad (2.42)$$

Now, we can use the relationship between equations (2.41) and (2.42) to establish the following theorem:

Theorem 2.4.4 (Finite Dimensional Representation). *The distributed state dependent DDE (2.39) with $j \in \mathbb{N}$ is equivalent to the finite dimensional transit compartment ODE system given by*

$$\left. \begin{aligned} \frac{d}{dt} x(t) &= F(x(t), V_a(t) x_j(t)) - \gamma(x(t)) x(t) \\ \frac{d}{dt} x_1(t) &= \frac{\beta x(t)}{\hat{V}_a(t)} - V_a(t) x_1(t) - \mu(x(t)) x_1(t) \\ \frac{d}{dt} x_i(t) &= V_a(t) [x_{i-1}(t) - x_i(t)] - \mu(x(t)) x_i(t) \quad \text{for } i = 2, 3, \dots, j. \end{aligned} \right\} \quad (2.43)$$

Proof. Lemma 2.4.3 ensures that the differential equations are equivalent. Therefore, we need only construct appropriate initial data for the distributed DDE and ODE formulation. For a history function $\rho(s)$ of (2.39), we set, for $i = 1, 2, \dots, j$,

$$x_i(0) = \int_{-\infty}^0 g_{V_a^*}^i(a(-\phi)) \frac{\beta \rho(\phi)}{V_a(\phi)} \exp \left[- \int_{\phi}^t \mu(\rho(s)) ds \right] d\phi. \quad (2.44)$$

If $\mu(s) = \mu^*$ is constant and the initial conditions satisfy

$$x_i(0) = \left(\frac{V_a^*}{V_a^* + \mu^*} \right)^i x_1(0),$$

it is simple to choose $\rho(s) = x_1(0)$. However, in the more general case with $\mu(t) \neq \mu^*$ and arbitrary ODE initial conditions $x_i(0) = \alpha_i$ of (2.41), we can use a similar method to Cassidy and Humphries [2019] to construct one of the infinitely many appropriate history functions. \square

A form of the expression for the variable age transit chain in equation (2.41) was derived Krzyzanski [2011] to study the equivalence between lifespan and transit compartment models in pharmacodynamics. However, the derivation did not include the underlying age structured PDE and was specific to the gamma distribution. Gurney et al. [1986] derived a similar expression for the density of individuals progressing through a specific stage of maturation from a balance equation. However, they did not explicitly formulate the underlying DDE nor did they derive the correct initial conditions for each of the transit compartments. Consequently, they did not show equivalence between the transit compartment formulation and the DDE.

Remark 2.1 (Recipe for equivalency between ODEs and gamma distributed DDEs). We note that the finite dimensional representation of (2.39) with $j \in \mathbb{N}$ includes a transit compartment chain. Due to the equivalence between (2.39) and (2.43), we are able to identify the ingredients needed to transform a transit compartment ODE such as (2.43) into a DDE such as (2.39). We first consider

$$\frac{d}{dt} x_1(t) = \frac{\beta x(t)}{\hat{V}_a(t)} - V_a(t) x_1(t) - \mu(x(t)) x_1(t).$$

From the equation for $x_1(t)$, we can easily identify the ratio $\beta x(t)/\hat{V}_a(t)$ as the rate at which individuals in the 1st compartment are created. Next, by considering the rate at which

individuals enter the second compartment,

$$\begin{aligned}\frac{d}{dt}x_1(t) &= \frac{\beta x(t)}{\hat{V}_a(t)} - V_a(t)x_1(t) - \mu(x(t))x_1(t) \\ \frac{d}{dt}x_2(t) &= V_a(t)x_1(t) - V_a(t)x_2(t) - \mu(x(t))x_2(t),\end{aligned}\tag{2.45}$$

we find the (possibly variable) transit rate between compartments. Then, a process of elimination immediately yields the mortality rate $\mu(x(t))$ (if $\mu(x(t)) < 0$, then population growth rather than decay is occurring through the transit chain). The creation and transit rates also yield the homeostatic ageing rate via (2.37). Further inspection of (2.38) shows that these rates are all that are needed to transform the transit chain ODE to a distributed DDE.

We note that the classic linear chain technique (see [Smith \[2011\]](#)) is a special case of Remark 2.1 where the ageing velocity, $V_a(t)$, is constant.

2.5 EXAMPLES FROM HEMATOPOIESIS

Sometimes, analysis of distributed DDEs is more tractable and simpler than that of a high dimensional equivalent ODE system. For example, by rescaling time, [[Câmara De Souza et al., 2018](#)] converted Quartino's ODE transit compartment model of granulopoiesis into a distributed DDE [[Quartino et al., 2014](#)]. The distributed DDE formulation proved to be much more analytically tractable than the ODE case, and was used to show the positivity of solutions and establish the local stability of equilibrium solutions.

However, due to the lack of a general numerical algorithm, simulation of distributed DDEs must be handled on a case by case basis. Simulation of transit compartment ODEs is routine in many programming languages and can be used for the calibration of models to existing data. Once calibrated, mathematical models can be simulated and used in a predictive manner. Consequently, by converting models between the equivalent distributed DDE or ODE formulations, researchers can use the form of the model that is most suitable to their needs.

The hematopoietic system controls blood cell production and, through tight cytokine control, is able to quickly respond to challenges, including infection and blood loss. Cytokines control hematopoietic output by varying effective proliferation and maturation rates in each hematopoietic lineage. As cells are not produced instantaneously, there is necessarily a delay between cytokine signal and production response. Mathematical models have been used to understand the complex dynamics observed in so-called dy-

namical diseases since the 1970s [Glass, 2015; Mackey, 1978; Rubinow and Lebowitz, 1975]. Existing mathematical models of hematopoiesis have included discrete, distributed and state-dependent DDEs [Colijn and Mackey, 2005a; Craig et al., 2016; Crauste and Adimy, 2007; Hearn et al., 1998b; Mahaffy et al., 1998] as well as transit compartment models [Friberg et al., 2002; Krzyzanski et al., 2010; von Schulthess and Mazer, 1982].

Here, we use the equivalence between state dependent distributed DDEs and ODE transit compartment models derived in Section 2.4.3.1 to convert two previously published ODE models of hematopoietic cell production to their equivalent state-dependent distributed DDEs. The ODE models specify the entrance rate of individuals into the maturation compartment and the maturation speed, $V_a(t)$, which allows for the calculation the birth rate β of immature individuals. As these models involve more than one population, the birth rate β is no longer constant but is a function of other populations in the model.

In the first example, we show how a model of reticulocyte production can be reduced to a renewal equation whose dynamics are completely characterized by a simple system of ordinary differential equations.

In the second example, we extend the framework of Section 2.4.3.1 to include non-identical transitions between ageing populations and a variable transition rate. This example shows how the state dependent distributed DDE framework addresses the inability of the linear chain technique to model dynamic ageing processes.

2.5.1 Pérez-Ruixo model of reticulocyte production

Pérez-Ruixo et al. [2008] studied the effect of recombinant human erythropoietin (EPO) on red blood cell precursors using a mathematical model. EPO is the protein responsible for controlling production of red blood cells and their precursors. The model arises from pharmacokinetic and pharmacodynamic data from patients receiving one dose of exogenous EPO. EPO was modelled through an open two compartment model of exogenous dose absorption and homoeostatic endogenous production rate, k_{EPO} , and the blood serum level (*BSL*). The bioavailable exogenous EPO was modelled as a dose dependent hyperbolic function satisfying

$$F = F_0 + \frac{E_{max}Dose}{ED_{50} + Dose},$$

where Dose is the amount of EPO administered. Exogenous EPO was absorbed through a dual absorption model into the depot and central compartments. The duration of first order absorption into the depot and central compartments are given by D_1 and D_2 , respectively. A fraction of the bioavailable exogenous EPO, f_r , was absorbed into the depot

compartment before entering the central compartment at rate k_a . The depot concentration of EPO follows

$$\frac{d}{dt}A_1(t) = \begin{cases} \frac{\text{Dose}f_rF}{D_1} - k_aA_1 & \text{if } t \leq D_1 \\ -k_aA_1 & \text{if } t > D_1, \end{cases} \quad (2.46)$$

The remaining exogenous EPO, $(1 - f_r)F$ enters the central compartment following a lag time $t_{\text{lag}2}$ and is cleared linearly at the rate k_{20} . The volume of the central compartment is V_1 . The dynamics of exogenous EPO in the central compartment are given by

$$\frac{d}{dt}A_2(t) = \begin{cases} \frac{\text{Dose}(1-f_r)F}{D_2} + k_aA_1(t) + k_{32}A_3(t) - k_{23}A_2(t) \\ \quad - k_{20}A_2(t) + k_{epo} - \frac{V_{max}A_2(t)/V_2}{K_M + A_2(t)/V_2} & \text{if } t_{\text{lag}2} \leq t \leq D_2 \\ k_{epo} - \frac{V_{max}A_2(t)/V_1}{K_M + A_2(t)/V_1} & \text{if } t > D_2, t < t_{\text{lag}2}, \end{cases} \quad (2.47)$$

Finally, EPO enters the peripheral compartment from -and returns to- the central compartment linearly, so

$$\frac{d}{dt}A_3(t) = k_{23}A_2(t) - k_{32}A_3(t). \quad (2.48)$$

The total bioavailable EPO is given by

$$C(t) = BSL + A_2(t)/V_1.$$

[Pérez-Ruixo et al. \[2008\]](#) considered 4 different pharmacodynamics models of erythrocyte response to exogenous EPO (titled the A,B,C and D models). In each of the 4 different pharmacodynamic models, the EPO dynamics are unchanged and described by equations (2.46), (2.47) and (2.48).

Here, we describe the ‘‘B’’ model from [Pérez-Ruixo et al. \[2008\]](#). Model B divides the erythrocyte progenitors, $P(t)$, into N_P compartments further subdivided into two distinct populations; EPO only affects the growth rate of the first population. Thus, the first $N_P/2$ compartments constitute the EPO sensitive population. Progression through these N_P compartments represents the ageing process of the progenitor cells. Once erythrocyte progenitors have reached maturity, they progress into the reticulocyte population. Once again, the maturation process of reticulocytes is modelled through a series of N_R transit compartments that are not sensitive to EPO. In this manner, the [Pérez-Ruixo et al. \[2008\]](#) model uses a concatenation of transit compartments to model the separate ageing processes of reticulocytes.

The Pérez-Ruixo B model of erythrocyte progenitor and reticulocyte production is

$$\left. \begin{aligned}
 \frac{d}{dt}P_1(t) &= k_{in} - \frac{S_{max}C(t)}{SC_{50} + C(t)} \frac{N_P}{T_P} P_1(t) \\
 \frac{d}{dt}P_i(t) &= \frac{S_{max}C(t)}{SC_{50} + C(t)} \frac{N_P}{T_P} [P_{i-1}(t) - P_i(t)] \quad \text{for } i = 2, 3, \dots, N_P/2 \\
 \frac{d}{dt}P_{N_P/2+1}(t) &= \frac{S_{max}C(t)}{SC_{50} + C(t)} \frac{N_P}{T_P} P_{N_P/2}(t) - \frac{N_P}{T_P} P_{N_P/2+1}(t) \\
 \frac{d}{dt}P_i(t) &= \frac{N_P}{T_P} [P_{i-1}(t) - P_i(t)] \quad \text{for } i = N_P/2 + 2, \dots, N_P. \\
 \frac{d}{dt}R_1(t) &= \frac{N_P}{T_P} P_{N_P}(t) - \frac{N_R}{T_R} R_1(t) \\
 \frac{d}{dt}R_i(t) &= \frac{N_R}{T_R} [R_{i-1}(t) - R_i(t)] \quad \text{for } i = 2, 3, \dots, N_R.
 \end{aligned} \right\} \quad (2.49)$$

By identifying the ingredients necessary from Remark 2.1, we will show how the distributed DDE framework from Section 2.4.3.1 can account for these separate ageing processes with distinct ageing velocities. Accounting for multiple ageing processes is not possible by rescaling time so the approach of Câmara De Souza et al. [2018] cannot be generalized to this case.

The most immature erythrocyte progenitors are modelled by $P_1(t)$ and are created from multipotent progenitors differentiating into the erythrocyte lineage at a constant rate k_{in} . Transit between the first $N_P/2$ compartments occurs at the variable rate

$$V_e(t) = \frac{S_{max}C(t)}{SC_{50} + C(t)} \frac{N_P}{T_P} \quad \text{with} \quad V_e^* = \frac{S_{max}BSL}{SC_{50} + BSL} \frac{N_P}{T_P}.$$

Using (2.41), we define $\hat{V}_e(t) = V_e(t)/V_e^*$, so the birth rate of precursor cells into $P_2(t)$ is

$$V_e(t)P_1(t) = \frac{\beta_e(t)}{\hat{V}_e(t)}.$$

Further, we see that the only removal of cells from the compartment model is due to transition to later compartments. Therefore, $\mu(t) = 0$, and we have identified all the ingredients necessary in Remark 2.1. Therefore, for $i = 2, 3, \dots, N_P/2$,

$$P_i(t) = \int_{-\infty}^t \frac{V_e(\phi)}{V_e^*} P_1(\phi) g_{V_e^*}^i \left[\int_{\phi}^t \hat{V}_e(s) ds \right] d\phi. \quad (2.50)$$

The $N_P/2 + 1$ st compartment satisfies

$$\frac{d}{dt}P_{N_P/2+1}(t) = V_e(t)P_{N_P/2}(t) - \frac{N_P}{T_P}P_{N_P/2+1}(t).$$

Erythrocyte progenitors enter the first non-EPO sensitive ageing compartment, $P_{N_P/2+1}(t)$, with appearance rate

$$\frac{\tilde{\beta}_e(t)}{V_p(t)} = V_e(t)P_{N_P/2}(t),$$

and then progress through the remaining $N_P/2$ compartments at a constant rate $V_p(t) = V_p^* = N_P/T_P$. Once again, we note that there is no removal of cells in any of the $N_P/2$ compartments, so $\mu(t) = 0$. Further, since the ageing velocity is constant, $\hat{V}_p^* = 1$. Therefore, a simple application of Remark 2.1 for constant ageing velocity, and using (2.50) gives

$$\begin{aligned} P_{N_P}(t) &= \int_0^\infty \frac{\tilde{\beta}_e(t-\theta)}{N_P/T_P} g_{N_P/T_P}^{N_P/2}(\theta) d\theta = \int_{-\infty}^t \frac{\tilde{\beta}_e(\theta)}{N_P/T_P} g_{N_P/T_P}^{N_P/2}(t-\theta) d\theta \\ &= \int_{-\infty}^t \left[\frac{V_e(\theta)}{N_P/T_P} \int_{-\infty}^\theta V_e(\phi) P_1(\phi) g_{V_e^*}^{i-1} \left(\int_\phi^\theta \hat{V}_e(s) ds \right) d\phi \right] g_{N_P/T_P}^{N_P/2}(t-\theta) d\theta. \end{aligned} \quad (2.51)$$

Mature erythrocyte precursors enter into the most immature reticulocyte compartment, $R_1(t)$. Given (2.51), the differential equation for $R_1(t)$ becomes

$$\begin{aligned} \frac{d}{dt}R_1(t) &= \frac{N_P}{T_P} \int_{-\infty}^t \underbrace{\left[\frac{V_e(\theta)}{N_P/T_P} \int_{-\infty}^\theta V_e(\phi) P_1(\phi) g_{V_e^*}^{i-1} \left(\int_\phi^\theta \hat{V}_e(s) ds \right) d\phi \right] g_{N_P/T_P}^{N_P/2}(t-\theta) d\theta}_{P_{N_P}(t)} \\ &\quad - \frac{N_R}{T_R} R_1. \end{aligned}$$

Hence, the Pérez-Ruixo B model of reticulocyte production is equivalent to

$$\begin{aligned} C(t) &= BSL + A_2(t)/V_1 \\ \frac{d}{dt}P_1(t) &= k_{in} - \frac{S_{max}C(t)}{SC_{50} + C(t)} \frac{N_P}{T_P} P_1(t) \\ \frac{d}{dt}R_1(t) &= \frac{N_P}{T_P} \int_{-\infty}^t \left[\frac{V_e(\theta)}{N_P/T_P} \int_{-\infty}^\theta V_e(\phi) P_1(\phi) g_{V_e^*}^{N_P/2} \left(\int_\phi^\theta \hat{V}_e(s) ds \right) d\phi \right] g_{N_P/T_P}^{N_P/2}(t-\theta) d\theta \\ &\quad - \frac{N_R}{T_R} R_1 \\ \frac{d}{dt}R_i(t) &= \frac{N_R}{T_R} [R_{i-1}(t) - R_i(t)] \quad \text{for } i = 2, 3, \dots, N_R. \end{aligned}$$

Finally, we can use Remark 2.1 with the constant ageing velocity $V_r(t) = V_r^* = N_R/T_R$ to

solve the transit compartment system for $R_i(t)$ to find

$$R_i(t) = \int_0^\infty \frac{T_R}{N_R} \beta_R(\sigma) g_{N_R/T_R}^i(\sigma) d\sigma, \quad (2.52)$$

where

$$\beta_R(\sigma) = \frac{N_P}{T_P} \int_{-\infty}^\sigma \left[\frac{V_e(\theta)}{N_P/T_P} \int_{-\infty}^\theta V_e(\phi) P_1(\phi) g_{V_e^*}^{N_P/2} \left(\int_\phi^\theta \hat{V}_e(s) ds \right) d\phi \right] g_{N_P/T_P}^{N_P/2}(t - \theta) d\theta.$$

Using the techniques developed in Section 2.4.3.1, we have transformed the differential equations for the transit compartments for the erythrocyte progenitors and the reticulocytes into renewal type equations given by (2.51) and (2.52) [Diekmann et al., 2018]. Since Pérez-Ruixo et al. [2008] did not model reticulocyte mediated clearance of EPO, the cytokine and early progenitor dynamics are independent of the $P_{N_P}(t)$ and $R_{N_R}(t)$ concentrations. Consequently, the dynamics of equation (2.49) are completely determined by the dynamics of

$$\begin{aligned} C(t) &= BSL + A_2(t)/V_1 \\ \frac{d}{dt} P_1(t) &= k_{in} - \frac{S_{max} C(t)}{SC_{50} + C(t)} \frac{N_P}{T_P} P_1(t), \end{aligned}$$

and the EPO concentrations given by equations (2.46), (2.47), and (2.48). We are now able to completely characterise the homeostatic behaviour of erythropoiesis by studying

$$\left. \begin{aligned} \frac{d}{dt} A_1(t) &= -k_a A_1(t) \\ \frac{d}{dt} A_2(t) &= k_{epo} - \frac{V_{max} A_2/V_1}{K_M + A_2/V_1} \\ \frac{d}{dt} A_3(t) &= k_{23} A_2(t) - k_{32} A_3(t) \\ \frac{d}{dt} P_1(t) &= k_{in} - \frac{S_{max} C(t)}{SC_{50} + C(t)} \frac{N_P}{T_P} P_1(t), \end{aligned} \right\} \quad (2.53)$$

To ensure that the initial value problem (2.53) is equivalent to the Pérez-Ruixo et al. [2008], we re-use the initial conditions for $A_1(0)$, $A_2(0)$, and $A_3(0)$. Since $\mu = 0$ and the initial conditions $P_1(0) = P_i(0)$ are constant, we can set the history function for the progenitors, $\rho_p(s)$, to be $\rho_p(s) = P_1(0)$. The same can be done for the reticulocytes with $\rho_r(s) = R_1(0)$.

We find the homeostatic concentration of EPO in the depot, central and peripheral compartments by solving

$$\frac{d}{dt} A_1(t) = 0, \quad \frac{d}{dt} A_2(t) = 0, \quad \frac{d}{dt} A_3(t) = 0, \quad \text{and} \quad \frac{d}{dt} P_1(t) = 0.$$

This yields the following homeostatic EPO concentrations

$$A_1^* = 0, \quad A_2^* = \frac{V_1 k_{epo} k_M}{V_{max} - k_{epo}}, \quad A_3^* = \frac{k_{23}}{k_{32}} A_2^*, \quad \text{and} \quad C^* = BSL + A_2^*,$$

while the homeostatic progenitor concentration is

$$P_1^* = \frac{k_{in}(SC_{50} + C^*) T_P}{S_{max} C^* N_P}.$$

The simplified erythropoiesis dynamics (2.53) and homeostatic concentrations lead to the following proposition:

Proposition 2.5.1. *For positive parameter values, the homeostatic equilibrium point of equation (2.49) is locally asymptotically stable.*

Proof. The linearisation matrix of equation (2.53) about the equilibrium $x^* = (A_1^*, A_2^*, A_3^*, P_1^*)$ is

$$\mathbb{J}(x^*) = \begin{bmatrix} -k_a & 0 & 0 & 0 \\ 0 & \frac{-V_{max}/V_1 k_M}{(k_M + A_2^*/V_1)^2} & 0 & 0 \\ 0 & k_{23} & -k_{32} & 0 \\ 0 & \frac{1}{V_1} \frac{S_{max} C^*}{(SC_{50} + C^*)^2} & 0 & -\frac{S_{max} C^*}{SC_{50} + C^*} \frac{N_P}{T_P} \end{bmatrix}.$$

The matrix $\mathbb{J}(x^*)$ is lower triangular with strictly negative diagonal entries, so the eigenvalues are strictly negative and the equilibrium is locally asymptotically stable. \square

This example illustrates how Remark 2.1 can be adapted to include a series of concatenated ageing processes. In the age structured PDE interpretation, each ageing process corresponds to a unique random variable modelling the transition between distinct stages. As we do not *a priori* expect the transition ages to be independent, interpreting the resulting ageing processes requires some care. The final renewal equation (2.53) includes a joint multivariate distribution representing the concatenation of distinct ageing processes.

Further, Pérez-Ruixo et al. [2008] did not show that the homeostatic equilibrium is locally asymptotically stable. For the ODE system (2.49), the Jacobian would be a $(3 + N_P + N_R) \times (3 + N_P + N_R)$ matrix with a degree $(3 + N_P + N_R)$ characteristic polynomial. In general, analytically finding the roots of a large degree polynomial is difficult. Hence, while the ODE (2.49) is obviously finite dimensional, it is analytically intractable.

Conversely, the equivalent renewal equation (2.53) is simple to analyse and a similar argument to Proposition 2.3.1 shows that solutions of the renewal equation (2.53) evolving from non-negative initial conditions remain non-negative. The “A”, “C” and “D” models

can also be modelled as renewal equations through a simple application of the classical linear chain technique and the technique shown here.

2.5.2 Roskos's model of granulocyte production

Roskos et al. [2006] modelled the impact of exogenous administration of granulocyte colony stimulating factor (G-CSF) on neutrophil proliferation and maturation speed. G-CSF is a proinflammatory cytokine that binds to G-CSF specific receptors on mature neutrophil cells and controls neutrophil kinetics through a negative feedback loop [Roberts, 2005; Shochat et al., 2007]. G-CSF governs neutrophil production by increasing the effective proliferation of neutrophil precursors, reducing the maturation time of non-mitotic neutrophil precursors, and increasing release of neutrophil cells from the bone marrow into the blood. The dynamics of neutrophil production have been well-studied from both a mathematical and a pharmacometric point of view [Câmara De Souza et al., 2018; Craig et al., 2016; Quartino et al., 2014]. These models have used different techniques to incorporate the delays intrinsic to the system, such as discrete DDEs or transit compartment ODEs. Roskos et al. [2006] model distinct stages of granulocyte production such as the bone marrow concentrations of metamyelocytes, $M(t)$; band cells, $B(t)$; and segmented neutrophil cells, $S(t)$. The ageing and maturation processes for each of these cell types is modelled through a series of three transit chains with N_M , N_B and N_S compartments, respectively. Moreover, band and segmented neutrophil cells can be shunted into circulation following the administration of G-CSF. We denote the metamyelocyte, band and segmented neutrophil cell shunting rates as $\mu_m(t)$, $\mu_b(t)$ and $\mu_s(t)$

Administration of G-CSF is modelled in a similar way to the EPO model of Section 2.5.1 using a first order delayed absorption model. However, Roskos et al. [2006] do not give the differential equations for exogenous administration of G-CSF other than to state that the clearance of G-CSF includes neutrophil receptor mediated clearance through the term

$$CL_N/F = \frac{k_{cat}/F(B_p(t) + S_p(t))}{K_M + C(t)},$$

where $B_p(t)$ and $S_p(t)$ are the number of circulating band and segmented neutrophil cells, respectively. Due to the feedback between the circulating neutrophil precursors and the cytokine $C(t)$, we are unable to completely reduce the Roskos model to a renewal type equation as was done in Section 2.5.1.

The Roskos model for granulocyte production is

$$\frac{d}{dt}M_1(t) = S_0 + \frac{E_{mit}C(t)}{EC_{50} + C(t)} - \frac{N_M}{\tau_{meta} \left(1 - \frac{f_{mmt}C(t)}{EC_{50} + C(t)}\right)} M_1(t)$$

$$\begin{aligned}
\frac{d}{dt}M_i(t) &= \frac{N_M}{\tau_{meta} \left(1 - \frac{f_{mmt}C(t)}{EC_{50}+C(t)}\right)} (M_{i-1}(t) - M_i(t)) \quad \text{for } i = 2, \dots, N_M \\
\frac{d}{dt}B_1(t) &= \frac{N_M}{\tau_{meta} \left(1 - \frac{f_{mmt}C(t)}{EC_{50}+C(t)}\right)} M_{N_M}(t) - \frac{N_B}{\tau_{band} \left(1 - \frac{f_{mmt}C(t)}{EC_{50}+C(t)}\right)} B_1(t) \\
&\quad - \frac{E_{band}C(t)}{EC_{50} + C(t)} B_1(t) \\
\frac{d}{dt}B_i(t) &= \frac{N_B}{\tau_{band} \left(1 - \frac{f_{mmt}C(t)}{EC_{50}+C(t)}\right)} [B_{i-1}(t) - B_i(t)] - \frac{E_{band}C(t)}{EC_{50} + C(t)} B_i(t); \quad i = 2, \dots, N_B \\
\frac{d}{dt}B_p(t) &= \sum_{i=1}^{N_B} \frac{E_{band}C(t)}{EC_{50} + C(t)} B_i(t) - (k_\lambda + k_{bp\text{mat}}) B_p(t) \\
\frac{d}{dt}S_1(t) &= \frac{N_B}{\tau_{band} \left(1 - \frac{f_{mmt}C(t)}{EC_{50}+C(t)}\right)} B_{N_B}(t) - \left(\frac{N_S}{\tau_{seg} \left(1 - \frac{f_{mmt}C(t)}{EC_{50}+C(t)}\right)} + \frac{E_{seg}C(t)}{EC_{50} + C(t)} \right) S_1(t) \\
\frac{d}{dt}S_i(t) &= \frac{N_S}{\tau_{seg} \left(1 - \frac{f_{mmt}C(t)}{EC_{50}+C(t)}\right)} [S_{i-1}(t) - S_i(t)] - \frac{E_{seg}C(t)}{EC_{50} + C(t)} S_i(t); \quad i = 2, \dots, N_S. \\
\frac{d}{dt}S_p(t) &= \sum_{i=1}^{N_S} \frac{E_{band}C(t)}{EC_{50} + C(t)} S_i(t) - (k_\lambda + k_{bp\text{mat}}) S_p(t),
\end{aligned}$$

and is an example of a transit compartment model with variable ageing speed and linear clearance. The linear clearance terms are Hill type functions with a maximal clearance rate E_j given by

$$\mu_j(t) = \frac{E_j C(t)}{EC_{50} + C(t)}.$$

Including these linear clearance terms in a transit compartment model is uncommon, but allows for the direct modelling of G-CSF mediated shunting of immature cells into circulation.

By converting the model into a distributed DDE, we underline the link between clearance of cells in a transit compartment to the exponential decay present in the distributed DDE. Once again, we will proceed by identifying the ingredients discussed in Remark 2.1.

As in Section 2.5.1, the most immature metamyelocytes ($M_1(t)$) are produced from the earlier progenitors at a constant baseline rate S_0 with the G-CSF dependent recruitment rate

$$\frac{\beta_m(t)}{V_m(t)} = S_0 + \frac{E_{mit}C(t)}{EC_{50} + C(t)}.$$

Metamyelocytes progress through maturation at a G-CSF dependent rate

$$V_m(t) = \frac{N_M}{\tau_{meta} \left(1 - \frac{f_{mmt}C(t)}{EC_{50}+C(t)}\right)}.$$

Metamyelocytes are not shunted into circulation following the administration of G-CSF, so $\mu_m(t) = 0$. Therefore, the metamyelocyte transit compartment model can be reduced to a distributed DDE using Remark 2.1 in an identical procedure to the Pérez-Ruixo model in Section 2.5.1. The most mature metamyelocyte population is given by

$$M_{N_M}(t) = \int_{-\infty}^t \frac{\beta_m(t)}{V_m(t)} g_{V_m^*}^{N_M} \left[\int_{\phi}^t \hat{V}_m(s) ds \right] d\phi. \quad (2.54)$$

Immature neutrophil band cells, $B_1(t)$, are created at the birth rate

$$\frac{\beta_b(t)}{\hat{V}_b(t)} = \frac{N_M}{\tau_{meta} \left(1 - \frac{f_{mmt}C(t)}{EC_{50}+C(t)}\right)} M_{N_M}(t).$$

These band cells progress through the maturation compartments at the G-CSF dependent ageing rate

$$V_b(t) = \frac{N_B}{\tau_{band} \left(1 - \frac{f_{mmt}C(t)}{EC_{50}+C(t)}\right)} \quad \text{with} \quad V_b^* = \frac{N_B}{\tau_{band} \left(1 - \frac{f_{mmt}C^*}{EC_{50}+C^*}\right)},$$

so the scaled ageing rate is $\hat{V}_b(t) = V_b(t)/V_b^*$. Inspecting the remaining terms in the equation for $B_1(t)$ gives

$$\mu_b(t) = \frac{E_{band}C(t)}{EC_{50} + C(t)}.$$

Therefore, using Remark 2.1, we find that the i -th band compartment satisfies

$$B_i(t) = \int_{-\infty}^t \frac{\beta_b(\phi)}{V_b(\phi)} \exp \left[- \int_{\phi}^t \mu_b(s) ds \right] g_{V_b^*}^i \left(\int_{\phi}^t \hat{V}_b(s) ds \right) d\phi \quad (2.55)$$

for $i = 1, 2, \dots, N_B$.

Mature band cells, given by (2.55) with $i = N_B$, transition into the first segmented neutrophil cell compartment $S_1(t)$ with creation rate

$$\frac{\beta_s(t)}{\hat{V}_s(t)} = \frac{N_B}{\tau_{band} \left(1 - \frac{f_{mmt}C(t)}{EC_{50}+C(t)}\right)} B_{N_B}(t) = V_b(t) B_{N_B}(t).$$

These cells transit through the segmented neutrophil population with G-CSF dependent

ageing ($V_s(t)$) and clearance ($\mu_s(t)$) rates

$$V_s(t) = \frac{N_S}{\tau_{seg} \left(1 - \frac{f_{mmt}C(t)}{EC_{50} + C(t)}\right)} \quad \text{and} \quad \mu_s(t) = \frac{E_{seg}C(t)}{EC_{50} + C(t)}.$$

Therefore, we have identified all the ingredients in Remark 2.1 for the segmented neutrophil precursors, $S(t)$. The first segmented neutrophil cell compartment satisfies

$$\begin{aligned} \frac{d}{dt} S_1(t) = & \overbrace{V_b(t) \int_{-\infty}^t \frac{\beta_b(\phi)}{V_b(\phi)} \exp \left[- \int_{\phi}^t \mu_b(s) ds \right] g_{V_B^*}^{N_b} \left(\int_{\phi}^t \hat{V}_b(s) ds \right) d\phi}^{\beta_s(t)/\hat{V}_s(t)} \\ & - V_s(t) S_1(t) - \mu_s(t) S_1(t). \end{aligned}$$

Therefore, it is possible to replace the transit compartment system of ODEs for $S_i(t)$ using Remark 2.1 to find

$$\begin{aligned} S_i(t) = & \int_{-\infty}^t \overbrace{V_b(\theta) \left[\int_{-\infty}^{\theta} \frac{\beta_b(\phi)}{V_b(\phi)} \exp \left[- \int_{\phi}^{\theta} \mu_b(s) ds \right] g_{V_B^*}^{N_b} \left(\int_{\phi}^{\theta} \hat{V}_b(s) ds \right) d\phi \right]}^{\beta_s(\theta)/\hat{V}_s(\theta)} \\ & \times \exp \left[- \int_{\theta}^t \mu_s(x) dx \right] g_{V_s^*}^i \left(\int_{\theta}^t \hat{V}_s(s) ds \right) d\theta \quad \text{for } i = 1, 2, \dots, N_s. \end{aligned} \quad (2.56)$$

The initial value problem studied by Roskos et al. [2006] was equipped with initial conditions for the cytokine equations as well as the $N_M + N_S + N_B + 2$ compartments. Since $\mu \neq 0$ in general, to create an equivalent renewal type equation, we use the same initial conditions as Roskos et al. [2006] for the cytokine differential equations and follow Cassidy and Humphries [2019] to construct appropriate history functions for $M(t)$, $B(t)$ and $S(t)$.

Therefore, we can reduce the ODE model of granulopoiesis to a renewal-type equation with unchanged cytokine dynamics from Roskos et al. [2006] using the resulting DDEs for $B_p(t)$ and $S_p(t)$. The resulting renewal equation is given by the equations describing the cytokine dynamics and the system of distributed DDEs

$$\begin{aligned} \frac{d}{dt} B_p(t) &= \sum_{i=1}^{N_B} \frac{E_{band}C(t)}{EC_{50} + C(t)} B_i(t) - (k_{\lambda} + k_{bpmat}) B_p(t) \\ \frac{d}{dt} S_p(t) &= \sum_{i=1}^{N_S} \frac{E_{band}C(t)}{EC_{50} + C(t)} S_i(t) - (k_{\lambda} + k_{bpmat}) S_p(t), \end{aligned}$$

where $B_i(t)$ and $S_i(t)$ are given by (2.55) and (2.56), respectively.

In this example, we have shown how to concatenate multiple ageing processes with distinct ageing velocities, as well as how to include the loss of cells throughout the ageing

process. Once again, we can use a similar argument to Proposition 2.3.1 to ensure that the solutions evolving from non-negative initial data remain non-negative.

2.6 DISCUSSION AND CONCLUSION

In this work, we have shown how to reduce age structured PDEs to possibly state-dependent DDEs. Our derivation shows how the correction factor discussed in Section 2.2.1 results naturally from considering the hazard rate at which cells exit maturation, and generalises the derivation of Craig et al. [2016] to the non-deterministic case.

In Section 2.3, we analysed the general distributed DDE that arises from the age structured population model. We showed, in Proposition 2.3.1, that populations evolving from non-negative initial conditions remain non-negative, regardless of the density $K_A(t)$. By linearising the distributed DDE, we showed, in Proposition 2.3.2, that stability analysis of the general DDE is analytically tractable. We characterized the stability of a generic equilibrium solution as a function of the linearisation of the growth function $F(x^*, \bar{x}^*)$.

Next, we considered the state-dependent DDE in the case of the degenerate, uniform and gamma distributions. Choosing a degenerate distribution leads to the familiar state-dependent discrete DDE, while uniformly distributed DDEs are reducible to discrete DDEs with two state dependent delays. Finally, in the case of gamma distributed DDEs, we explicitly related transit compartment models that include variable transit rates with gamma distributed DDEs in Theorem 2.4.4. As shown by Câmara De Souza et al. [2018], it can be simpler to analyse stability of equilibria and positivity of solutions of a distributed DDE than the corresponding ODE. However, the ODE models may be simpler to simulate numerically. The equivalence between the differential equations allows for the resulting model to be analysed in the more convenient setting.

By the means of two examples, we showed how to express transit compartment models as an equivalent DDE or renewal equation. First, we showed how to incorporate a variable transit rate into a distributed DDE using a simple application of Theorem 2.4.4. Next, we demonstrated that our method is capable of including multiple distinct ageing processes in the form of a multivariate distributed DDE. Lastly, we showed how a linear clearance term in each of the transit compartments can be included in the equivalent DDE model. Analysis of the renewal equation was shown to be simpler than the corresponding ODE system, and we were able to easily characterise the stability of the homeostatic equilibria.

This work emphasizes the link between transit compartment ODEs and delay differential equations. While this link has been known for over 50 years, we explicitly establish it for compartment models with variable transit rates. We demonstrated that these transit

compartment models are equivalent to state dependent distributed DDEs. The equivalence between easy-to-simulate ODE models and the simpler to analyse distributed DDEs allows modellers to use the formulation that is most convenient for their purposes. Consequently, the framework developed in this article allows for researchers to incorporate both external control of ageing rates and heterogeneous, non-deterministic maturation age into models of physiological maturation processes.

ACKNOWLEDGMENTS

TC would like to thank the Natural Sciences and Engineering Research Council of Canada (NSERC) for funding through the PGS-D program and the Alberta Government for funding through the Sir James Lougheed award of distinction. MC and ARH are grateful for funding through the NSERC Discovery Grant program.

CONFLICT OF INTEREST

All authors declare no conflicts of interest in this paper.

BIBLIOGRAPHY

- Bernard, S. (2016). Moving the boundaries of granulopoiesis modelling. *Bull. Math. Biol.*, 78(12):2358–2363.
- Câmara De Souza, D., Craig, M., Cassidy, T., Li, J., Nekka, F., Bélair, J., and Humphries, A. R. (2018). Transit and lifespan in neutrophil production: implications for drug intervention. *J. Pharmacokinet. Pharmacodyn.*, 45(1):59–77.
- T. Cassidy and A. R. Humphries, A mathematical model of viral oncology as an immunology instigator, *Math. Med. Biol.*, Online First (2019), dqz008. Available from: <https://doi.org/10.1093/imammb/dqz008>.
- Colijn, C. and Mackey, M. (2005). A mathematical model of hematopoiesis - I. Periodic chronic myelogenous leukemia. *J. Theor. Biol.*, 237(2):117–132.
- Cox, D. R. (1972). Regression models and life-tables. *J. R. Stat. Soc.*, 34(2):187–220.
- Craig, M., Humphries, A. R., and Mackey, M. C. (2016). A mathematical model of granulopoiesis incorporating the negative feedback dynamics and kinetics of G-CSF/neutrophil binding and internalization. *Bull. Math. Biol.*, 78(12):2304–2357.

- Crauste, F. and Adimy, M. (2007). Modeling and asymptotic stability of a growth factor-dependent stem cell dynamics model with distributed delay. *Discret. Contin. Dyn. Syst. - Ser. B*, 8(1):19–38.
- Diekmann, O., Gyllenberg, M., and Metz, J. A. J. (2018). Finite dimensional state representation of linear and nonlinear delay systems. *J. Dyn. Differ. Equations*, 30(4):1439–1467.
- Friberg, L. E., Henningson, A., Maas, H., Nguyen, L., and Karlsson, M. O. (2002). Model of chemotherapy-induced myelosuppression with parameter consistency across drugs. *J. Clin. Oncol.*, 20(24):4713–4721.
- Glass, L. (2015). Dynamical disease: Challenges for nonlinear dynamics and medicine. *Chaos An Interdiscip. J. Nonlinear Sci.*, 25(9):097603.
- Gurney, W., Nisbet, R., and Blythe, S. (1986). The systematic formulation of models of stage-structured populations. In Metz, J. A. J. and Diekmann, O., editors, *Dyn. Physiol. Struct. Popul.*, chapter 11, pages 474–493. Springer Berlin Heidelberg, Berlin, Heidelberg, 3 edition.
- Hale, J. K. and Verduyn Lunel, S. M. (1993). *Introduction to Functional Differential Equations*, volume 99 of *Applied Mathematical Sciences*. Springer New York, New York, NY.
- Hartung, F., Krisztin, T., Walther, H.-O., and Wu, J. (2006). Chapter 5 Functional Differential Equations with State-Dependent Delays: Theory and Applications. In Canada, A., Drabek, P., and Fonda, A., editors, *Handb. Differ. Equations*, chapter 5, pages 435–545. Elsevier, North Holland 2004, 3rd edition.
- Hearn, T., Haurie, C., and Mackey, M. C. (1998). Cyclical neutropenia and the peripheral control of white blood cell production. *J. Theor. Biol.*, 192:167–181.
- Hino, Y., Murakami, S., and Naito, T. (1991). *Functional Differential Equations with Infinite Delay*, volume 1473 of *Lecture Notes in Mathematics*. Springer Berlin Heidelberg, Berlin, Heidelberg.
- Kaplan, E. L. and Meier, P. (1958). Nonparametric estimation from incomplete observations. *J. Am. Stat. Assoc.*, 53(282):457.
- Krzyzanski, W. (2011). Interpretation of transit compartments pharmacodynamic models as lifespan based indirect response models. *J. Pharmacokinet. Pharmacodyn.*, 38(2):179–204.

- Krzyzanski, W., Wiczling, P., Lowe, P., Pigeolet, E., Fink, M., Berghout, A., and Balsler, S. (2010). Population modeling of filgrastim PK-PD in healthy adults following intravenous and subcutaneous administrations. *J. Clin. Pharmacol.*, 50(S9):101S–112S.
- Liu, W., Hillen, T., and Freedman, H. I. (2007). A mathematical model for M-phase specific chemotherapy including the G₀-phase and immunoresponse. *Math. Biosci. Eng.*, 4(2):239–59.
- MacDonald, N. (1978). *Time Lags in Biological Models*. Springer, Berlin, 1 edition.
- Mackey, M. (1978). Unified hypothesis for the origin of aplastic anemia and periodic hematopoiesis. *Blood*, 51(5):941–956.
- Mahaffy, J. M., Bélair, J., and Mackey, M. C. (1998). Hematopoietic model with moving boundary condition and state dependent delay: application in erythropoiesis. *J. Theor. Biol.*, 190(2):135–146.
- McKendrick, A. G. (1925). Applications of mathematics to medical problems. *Proc. Edinburgh Math. Soc.*, 44:98–130.
- Metz, J. and Diekmann, O., editors (1986). *The Dynamics of Physiologically Structured Populations*, volume 68 of *Lecture Notes in Biomathematics*. Springer Berlin Heidelberg, Berlin, Heidelberg, 3 edition.
- Otto, A. and Radons, G. (2017). Transformations from variable delays to constant delays with applications in engineering and biology. In Insperger, T., Ersal, T., and Orosz, G., editors, *Time Delay Syst.*, volume 7 of *Advances in Delays and Dynamics*, pages 169–183. Springer International Publishing, Cham.
- Pérez-Ruixo, J. J., Krzyzanski, W., and Hing, J. (2008). Pharmacodynamic analysis of recombinant human erythropoietin effect on reticulocyte production rate and age distribution in healthy subjects. *Clin. Pharmacokinet.*, 47(6):399–415.
- Quartino, A. L., Karlsson, M. O., Lindman, H., and Friberg, L. E. (2014). Characterization of endogenous G-CSF and the inverse correlation to chemotherapy-induced neutropenia in patients with breast cancer using population modeling. *Pharm. Res.*, 31(12):3390–3403.
- Roberts, A. (2005). G-CSF: A key regulator of neutrophil production, but that’s not all! *Growth Factors*, 23(1):33–41.

- Roskos, L. K., Lum, P., Lockbaum, P., Schwab, G., and Yang, B.-B. (2006). Pharmacokinetic/pharmacodynamic modeling of pegfilgrastim in healthy subjects. *J. Clin. Pharmacol.*, 46(7):747–757.
- Rubinow, S. and Lebowitz, J. (1975). A mathematical model of neutrophil production and control in normal man. *J. Math. Biol.*, 225:187–225.
- Shochat, E., Rom-Kedar, V., and Segel, L. (2007). G-CSF control of neutrophils dynamics in the blood. *Bull. Math. Biol.*, 69:299–338.
- Smith, H. (2011). *An Introduction to Delay Differential Equations with Applications to the Life Sciences*, volume 57 of *Texts in Applied Mathematics*. Springer New York, New York, NY.
- Smith, H. L. (1993). Reduction of structured population models to threshold-type delay equations and functional differential equations: a case study. *Math. Biosci.*, 113(1):1–23.
- Teslya, A. (2015). *Predator-Prey Models With Distributed Time Delay*. Doctoral dissertation, McMaster University.
- Trucco, E. (1965). Mathematical models for cellular systems. The Von Foerster equation. Part II. *Bull. Math. Biophys.*, 27(4):449–471.
- Vogel, T. (1961). Systèmes Déferlants, Systèmes Héritaires, Systèmes Dynamiques. In *Proc. Int. Symp. Nonlinear Vib.*, pages 123–130, Kiev. Academy of Sciences USSR.
- von Schulthess, G. and Mazer, N. (1982). Cyclic neutropenia (CN): A clue to the control of granulopoiesis. *Blood*, 59:27–37.
- Yuan, Y. and Bélair, J. (2011). Stability and Hopf Bifurcation Analysis for Functional Differential Equation with Distributed Delay. *SIAM J. Appl. Dyn. Syst.*, 10(2):551–581.

A MATHEMATICAL MODEL OF VIRAL ONCOLOGY AS AN
IMMUNO-ONCOLOGY INSTIGATOR

Having demonstrated how to derive a distributed DDE from a physiological understanding of an ageing processes in the previous chapter, we apply this technique to cellular reproduction in malignant tumours. Specifically, we show that the mathematical formalism of the previous chapter can be used to address a practical problem: cell cycle duration heterogeneity in solid tumours. In this chapter, we develop and analyse a physiologically realistic mathematical model of tumour-immune interaction that explicitly incorporates the heterogeneity in reproductive speed present in solid tumours. Finally, we include oncolytic viral therapy in our mathematical model.

We show that solutions of our mathematical model evolving from non-negative initial data remain non-negative and completely characterise the importance of tumour-immune involvement in tumour growth. Further, we show, both analytically and numerically, that heterogeneity in malignant cell cycle duration increases tumour robustness against therapy. This result implies that the common assumption of a constant cell cycle duration can overestimate the impact of therapy and argues for the inclusion of more biologically realistic delay kernels in mathematical models. This work will appear in *Mathematical Medicine and Biology*.

This chapter is a reproduction of the published version. However, some small typos persist. These typos do not impact the content of this article.

1. Equation (3.15) is missing the $a_2G_1(t - \sigma)K(\sigma)$ term and should read

$$A_R(t) = 2 \int_0^\infty \exp(-[\hat{d}_K + \psi_G^*]\sigma) a_2G_1(t - \sigma)K(\sigma)d\sigma + \mathcal{O}(|U(t) - U^*|^2).$$

This typo is corrected in (3.16) and does not impact the linearisation.

2. In the proof of Lemma 3.3.1, we argue that $Q(t) \geq 0$. We begin by considering the case where $Q(0) = 0$ and $\phi_G(s) = 0$ K -almost everywhere in $(-\infty, 0]$. Here, $\phi_G(s) = 0$ K -almost everywhere is understood as

$$\int_{-\infty}^0 \phi_G(s)d\mu = 0$$

where μ is a probability measure with corresponding Radon-Nikodym derivative $K(s)$.

Next, we consider the case when $\phi_G(s)K(-s) > 0$ on some set of positive measure in $(-\infty, 0]$. However, it is possible that $\phi_G(s)K(-s) = 0$ K -almost everywhere in $(-\infty, 0]$ while

$$\int_{-\infty}^0 \phi_G(s) \mathbf{d}\mu > 0.$$

Therefore, the second case should be that

$$\int_{-\infty}^0 \phi_G(s) \mathbf{d}\mu > 0.$$

In this case, $Q(t)$ eventually becomes positive and the rest of the proof follows without any change.

3. In Theorem 3.3.5, we show the existence of a positive equilibrium. On page 77, we incorrectly state that this unstable equilibrium, or critical tumour size, acts as a separatrix between tumour growth and extinction. In fact, it is the stable manifold of the equilibrium acts as the separatrix, not only the equilibrium itself. The biological interpretation of Theorem 3.3.5 does not change, and this misstatement does not impact our conclusions.

4. The Crivelli model given in (37) is missing an integral term and should read

$$\begin{aligned} \frac{\mathbf{d}}{\mathbf{d}t}Q(t) &= 2 \int_0^\infty \exp\left[-\int_{t-\sigma}^t d_3 + \eta(U(x)) \mathbf{d}x\right] a_2 G_1(t-\sigma) \delta_\tau(t-\sigma) \mathbf{d}\sigma - a_1 Q(t) - d_1 Q(t) \\ \frac{\mathbf{d}}{\mathbf{d}t}G_1(t) &= a_1 Q(t) - a_2 G_1(t) - d_2 G_1(t) - \eta(U(t)) G_1(t) \\ \frac{\mathbf{d}}{\mathbf{d}t}I(t) &= -\delta I(t) + \eta(U(t)) [G_1(t) + \int_0^\tau G_1(\sigma) \exp[-d_3 \sigma] \mathbf{d}\sigma] \\ \frac{\mathbf{d}}{\mathbf{d}t}V(t) &= \alpha I(t) - \omega V(t) - \eta(U(t)) [G_1(t) + \int_0^\tau a_2 G_1(\sigma) \exp[-d_3 \sigma] \mathbf{d}\sigma]. \end{aligned}$$

Evaluating the convolution integral against the degenerate distribution gives

$$\begin{aligned} \frac{\mathbf{d}}{\mathbf{d}t}Q(t) &= 2 \exp\left[-d_3 \tau - \int_{t-\tau}^t \eta(U(x)) \mathbf{d}x\right] a_2 G_1(t-\tau) - a_1 Q(t) - d_1 Q(t) \\ \frac{\mathbf{d}}{\mathbf{d}t}G_1(t) &= a_1 Q(t) - a_2 G_1(t) - d_2 G_1(t) - \eta(U(t)) G_1(t) \\ \frac{\mathbf{d}}{\mathbf{d}t}I(t) &= -\delta I(t) + \eta(U(t)) [G_1(t) + \int_0^\tau G_1(\sigma) \exp[-d_3 \sigma] \mathbf{d}\sigma] \\ \frac{\mathbf{d}}{\mathbf{d}t}V(t) &= \alpha I(t) - \omega V(t) - \eta(U(t)) [G_1(t) + \int_0^\tau a_2 G_1(\sigma) \exp[-d_3 \sigma] \mathbf{d}\sigma]. \end{aligned}$$

This typo does not impact the discussion of the Crivelli model in Appendix A.

A mathematical model of viral oncology as an immuno-oncology instigator

Tyler Cassidy¹ and Antony R. Humphries^{1,2}

¹ Department of Mathematics and Statistics, McGill University,
805 Sherbrooke Street West, Montreal, H3A 0B9, Canada.

² Department of Physiology, McGill University,
3655 Promenade Sir-William-Osler, Montreal, H3G 1Y6, Canada.

[Received: 27 September 2018; revised on 15 February 2019; accepted on 26
March 2019]

Abstract

We develop and analyse a mathematical model of tumour-immune interaction that explicitly incorporates heterogeneity in tumour cell cycle duration by using a distributed delay differential equation. We derive a necessary and sufficient condition for local stability of the cancer free equilibrium in which the amount of tumour-immune interaction completely characterises disease progression. Consistent with the immunoediting hypothesis, we show that decreasing tumour-immune interaction leads to tumour expansion. Finally, by simulating the mathematical model, we show that the strength of tumour-immune interaction determines the long-term success or failure of viral therapy. viral oncology, mathematical biology, delay differential equations, cancer

3.1 INTRODUCTION

Malignant tumours contain a highly heterogeneous population of cells that have distinct genotypes and reproductive abilities [Bell and McFadden, 2014; Lichty et al., 2014]. The heterogeneous nature of tumours is mirrored in the reproduction speed of malignant

cells. Most existing mathematical models greatly simplify the impact of heterogeneity in cell cycle times by either neglecting the cell cycle or assuming that all tumour cells have identical cell cycle durations. We will account for the range of cell cycle durations by deriving a mathematical model of tumour growth using a delay differential equation (DDE) with a distribution of delays. This is, to our knowledge, a novel way of considering the heterogeneity present in malignant tumours and presents a physiologically realistic model of tumour expansion.

Distributed DDEs model a continuum of cell cycle durations that belong to an interval of physiologically realistic values, with durations distributed according to a probability density function (PDF). This contrasts with discrete DDEs, where the discrete delay represents the cell cycle duration which is taken to be the same for all tumour cells. Thus discrete delays implicitly assume homogeneity of the tumour cell cycle duration which limits the physiological relevance of such models.

The human immune system attempts to eradicate malignant cells and inhibit tumour establishment [Hallam et al., 2009; Hoos et al., 2011]. We study this phenomenon by explicitly including tumour-immune interaction in our mathematical model. Analysis of this model shows that there is a threshold tumour size below which the immune system successfully prevents tumour establishment and quantifies the role of immune surveillance in tumour establishment and growth.

Therapeutic strategies under development attempt to exploit the immune system to eradicate malignant tumours via immuno-oncology and genetically engineered oncolytic viruses [Cassady et al., 2016; Chiocca and Rabkin, 2015; Hoos et al., 2011; Lawler and Chiocca, 2015]. Oncolytic viruses are designed to exploit the high reproductive rate characteristic of malignant tumours and preferentially infect cancerous cells. Immune regulated death of infected tumour cells releases tumour specific antigens that signal the immune system [Breitbach et al., 2016]. We incorporate oncolytic viral therapy into our mathematical model to study how these viruses can prime the immune system to eliminate tumours.

The release of tumour specific antigens induces a long-lasting immune response that causes tumour regression that persists after resolution of the infection [Bourgeois-Daigneault et al., 2016]. Consequently, oncolytic viruses have recently been recast as instigators of immuno-oncology and are being engineered to induce immune recruitment. For example, in 2015, the United States Food and Drug Administration approved a modified herpes virus that promotes granulocyte-macrophage colony-stimulating factor production and resulting anti-tumour immunity for treatment of melanoma [Bommareddy et al., 2017].

Mathematical models have been used extensively to understand and predict tumour growth and tumour-immune interactions (see [Santiago et al. \[2017\]](#); [Walker and Enderling \[2016\]](#); [Wodarz \[2016\]](#) for reviews). Existing models range from formulations as ordinary differential equations (ODEs) [[Idema et al., 2010](#); [Kim et al., 2015](#); [Kirschner and Panetta, 1998](#); [MacNamara and Eftimie, 2015](#)], to partial differential equations [[Hillen et al., 2013](#); [Malinzi et al., 2017](#)] and discrete DDEs [[Liu et al., 2007](#); [Mahasa et al., 2017](#); [Villasana and Radunskaya, 2003](#)].

[Crivelli et al. \[2012\]](#) developed and analysed a discrete DDE model of tumour growth and viral oncology. The Crivelli model is simple enough to be analytically tractable while retaining important physiological aspects of tumour growth and oncolytic viral therapy, but neglects the role of the immune system in tumour eradication. [Crivelli et al. \[2012\]](#) model the interaction of virions and tumour cells by using a non-differentiable function which significantly complicates the analysis of the model. This contact function allows for viral therapy alone to drive tumour remission in their model, without interaction with the immune system.

We develop a novel tumour growth and viral oncology model which incorporates immune recruitment to drive tumour clearance. Our model is partly based on the Crivelli model but augments and generalises it in very significant ways. We explicitly model phagocytosis of the tumour cells, and cytokine driven phagocyte recruitment. As mentioned, we also include a distribution of cell cycle times for the tumour cells which results in a DDE with distributed delays. We show the explicit link between our work and [Crivelli et al. \[2012\]](#) in Appendix A.

The duration of the cell cycle is crucial to the life cycle of many oncolytic viruses [[Bommareddy et al., 2017](#); [Colao et al., 2017](#)], and only actively dividing tumour cells can be infected by the oncolytic virus. Therefore, in a model of viral therapy, it is crucial to explicitly include the cell cycle duration of tumour cells. The inclusion of a heterogeneous cell cycle duration is more realistic than models with a discrete delay, because a discrete delay is equivalent to assuming that every cell in the tumour has a constant and identical cell cycle duration.

The distributed DDE tumour-immune model is developed in full generality in Section 3.2. In Section 3.3, we prove that solutions of the initial value problem evolving from non-negative initial data remain non-negative. Next, in Theorem 3.3.3, we determine a condition for treatment free extinction of the tumour that quantifies the link between immune involvement and disease progression. Our results show that immune involvement is crucial in controlling tumour growth. As a direct consequence, we show in Corollary 3.3.4 that homogeneous tumours are less robust than tumours with heterogeneous cell cycle

durations. Finally, by showing the existence of a cancer-immune co-existence equilibrium in Theorem 3.3.5, we establish a direct link between the minimal viable number of tumour cells and the immune killing capacity that is consistent with the immunoeediting hypothesis of tumour progression [Mittal et al., 2014]. Our analytical results are derived independently of the delay kernel chosen. In Section 3.4, by deriving a variant of the linear chain technique, we prove that the distributed DDE is equivalent to a finite dimensional ODE. We end Section 3.4 by simulating viral oncology treatment and illustrating the previously derived stability results. Our simulations show the existence of a transcritical bifurcation where the unstable nonzero equilibrium acts as a separatrix between tumour extinction and growth. Biologically, this result implies that treatment strategies that force the malignant tumour across the separatrix will eradicate the tumour. Moreover, we show that sufficiently strong immune involvement can counteract aggressive tumour growth and lead to tumour extinction without treatment. Finally, we discuss our results in Section 3.5.

3.2 MODEL DEVELOPMENT

Our model of tumour-immune interaction is given by the system of differential equations

$$\left. \begin{aligned} \frac{d}{dt}Q(t) &= 2 \int_{-\infty}^t \exp \left[- \int_{\sigma}^t \hat{d}_K + \eta(U(x)) + \psi_G(U(x)) dx \right] a_2 G_1(\sigma) K(t - \sigma) d\sigma \\ &\quad - a_1 Q(t) - d_1 Q(t) - \psi_Q(U(t)) Q(t) \\ \frac{d}{dt}G_1(t) &= a_1 Q(t) - a_2 G_1(t) - d_2 G_1(t) - \eta(U(t)) G_1(t) - \psi_G(U(t)) G_1(t) \\ \frac{d}{dt}I(t) &= \eta(U(t)) [G_1(t) + N(t)] - \delta I(t) \\ \frac{d}{dt}V(t) &= -\eta(U(t)) [G_1(t) + N(t)] + \alpha [\delta I(t)] - \omega V(t) \\ \frac{d}{dt}C(t) &= C_{prod}(U(t)) - k_{elim} C(t). \\ \frac{d}{dt}P(t) &= \varphi(C(t)) - \gamma_p P(t) \end{aligned} \right\} (3.1)$$

In (3.1), $Q(t)$ and $G_1(t)$ denote the quiescent and proliferative phase tumour cells. The cytokine concentration is denoted by $C(t)$, and the phagocyte concentration in the tumour microenvironment by $P(t)$. Finally, $V(t)$ is the concentration of oncolytic virions and $I(t)$ is the number of infected tumour cells.

In (3.1), $Q(t)$ corresponds to cells in the G_0 phase of the Burns and Tannock [1970] model of the cell cycle while $G_1(t)$ corresponds to the G_1 phase. We model the active phases of the cell cycle (S , G_2 and M) as an ageing process that yields the integral term in (3.1).

We denote by $N(t)$ the total number of cells in the active portion (the S , G_2 and M phases) of the cell cycle, given by

$$N(t) = \int_0^\infty a_2 G_1(t - \xi) \exp \left[- \int_{t-\xi}^t \hat{d}_K + \psi_G(U(x)) + \eta(U(x)) dx \right] \left(1 - \int_0^\xi K(\sigma) d\sigma \right) d\xi, \quad (3.2)$$

as derived in Appendix B. In equations (3.1) and (3.2) the distribution of the duration of the active phase of the cell cycle is described by the PDF $K(t)$. We do not choose a specific distribution in our model but rather derive our analytic results independently of $K(t)$; see Section 3.2.1 for a discussion of the properties of $K(t)$.

The functions $\eta(U(t))$, $\psi_Q(U(t))$, $\psi_G(U(t))$, $\varphi(C(t))$, and $C_{prod}(U(t))$ in (3.1) are defined in equations (3.8), (3.10), (3.11) and (3.13). To simplify notation, we denote the vector

$$U(t) = [Q(t), G_1(t), I(t), V(t), C(t), P(t)].$$

The distributed DDE (3.1) is given initial data $Q(t_0)$, $I(t_0)$, $C(t_0)$ and $[G_1(s), V(s), P(s)] = [\phi_G(s), \phi_V(s), \phi_P(s)]$ for $s \in (-\infty, t_0]$ for integrable functions $\phi_G(s)$, $\phi_V(s)$, $\phi_P(s)$ to create an initial value problem. The time t_0 can be thought of as the beginning of treatment; for simplicity, we take $t_0 = 0$.

We derive equation (3.1) in three steps. First, we consider tumour growth in the absence of immune interaction and viral therapy in Section 3.2.1. Tumour heterogeneity is explicitly accounted for by using a distributed cell cycle time length. The tumour growth equations are derived keeping in mind the eventual use of the model to describe the impact of an RNA oncolytic virus on tumour growth. Next, in Section 3.2.2, we derive the tumour-immune interaction and incorporate immunosurveillance into the tumour growth model. The graphical representation of the tumour-immune growth model is given in Fig. 3.1. Finally, by including viral therapy and immune recruitment in Section 3.2.3, we arrive at equation (3.1).

3.2.1 Tumour growth model development

RNA viruses replicate in infected cells during stages G_1 through M of the Burns and Tannock [1970] model of the cell cycle. As previously noted, we separately model the quiescent ($Q(t)$) and G_1 phase ($G_1(t)$) tumour cell populations. Quiescent tumour cells undergo apoptosis at a rate d_1 . We denote the transit rate between the quiescent and G_1 population as a_1 . Cells in G_1 undergo apoptosis at a rate d_2 , and enter into the active phase of the cell cycle at a rate a_2 . We define the cell cycle duration as the time length of the active portion of the cell cycle, calculated as the time a cell takes between exiting G_1 and

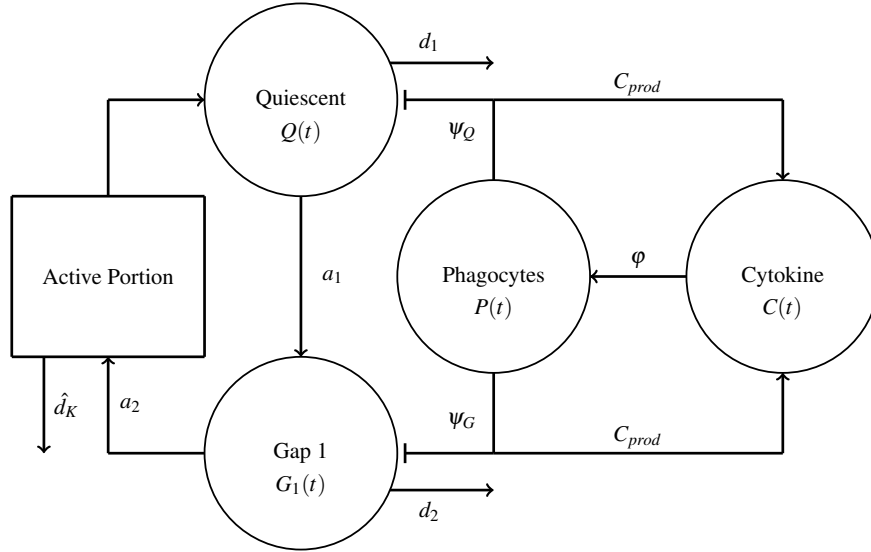


Figure 3.1: Pictorial representation of the tumour growth model. Populations are denoted by circles, processes by squares and rates by arrows. Quiescent cells enter G_1 at rate a_1 and undergo apoptosis at rate d_1 . Cells leave G_1 and enter the active phase of the cell cycle at rate a_2 while undergoing apoptosis at a rate d_2 . The active phase death rate is \hat{d}_k and cells re-enter quiescence after mitosis. Phagocytes interact with quiescent and G_1 phase cells at respective rates ψ_Q and ψ_G . Tumour-immune interaction drives cytokine production through the function C_{prod} .

re-entering Q .

We assume that the cell cycle time of tumour cells is a positive random variable with PDF $K(t)$ satisfying

$$K(t) \geq 0 \quad \forall t \in [0, \infty), \quad \int_0^\infty K(t) dt = 1.$$

We assume that cells have an expected mean cell cycle duration of τ , so the expected value of $K(t)$ satisfies

$$\mathbb{E}_K(t) := \int_0^\infty tK(t) dt = \tau < \infty. \quad (3.3)$$

We will also use that

$$\mathbb{E}_K(f(t)) = \int_0^\infty f(t)K(t) dt, \quad (3.4)$$

where in particular we note that the Laplace transform $\mathcal{L}[K](\lambda)$ of the PDF $K(t)$ is equivalent to $\mathbb{E}_K(e^{-\lambda t})$ since

$$\mathcal{L}[K](\lambda) := \int_0^\infty e^{-\lambda t} K(t) dt = \mathbb{E}_K(e^{-\lambda t}). \quad (3.5)$$

Let $A_R(t)$ denote the rate that successfully dividing cells re-enter quiescence at time t . Such cells began the active portion of the cell cycle some time σ in the past at rate $a_2G_1(\sigma)$. The likelihood that these cells complete the cell cycle at time t is given by $K(t - \sigma)$. Disregarding immune interaction for now, cells in the active portion of the cell cycle undergo apoptosis at a constant, distribution specific, rate \hat{d}_K . Consequently, cells that spend more time in the active phase of the cell cycle are more likely to undergo apoptosis instead of completing the cell cycle and returning to quiescence. Thus

$$A_R(t) = 2 \int_{-\infty}^t \exp \left[- \int_{\sigma}^t \hat{d}_K dx \right] a_2G_1(\sigma)K(t - \sigma)d\sigma. \quad (3.6)$$

Later, we will update $A_R(t)$ to include tumour-immune interaction and viral therapy. The distributed delay expression $A_R(t)$ is a novel model of tumour cell reproduction that is more physiologically appropriate than a discrete delay.

The discrete delay model considered by [Crivelli et al. \[2012\]](#) corresponds to $K(t) = \delta(t - \tau)$ and $d_\delta = d_3$. The explicit link between (3.1) and the Crivelli model is shown in Appendix A. The expected cellular output of the cell cycle with a discrete and fixed duration is

$$\mathbb{E}_\delta[te^{-d_3t}] = \tau e^{-d_3\tau}.$$

To ensure a consistent cellular output from the cell cycle for different distributions $K(t)$, we define $\hat{d}_K > 0$ as the distribution dependent unique positive value that solves

$$\mathbb{E}_K[te^{-\hat{d}_K t}] = \tau e^{-d_3\tau}. \quad (3.7)$$

The parameter \hat{d}_K must exist for a given distribution K as the function

$$f_K(\zeta) = \mathbb{E}_K[te^{-\zeta t}] - \tau e^{-d_3\tau}$$

is continuous and satisfies

$$f_K(0) = \tau(1 - e^{-d_3\tau}) > 0 \quad \text{and} \quad \lim_{\zeta \rightarrow \infty} f_K(\zeta) = -\tau e^{-d_3\tau} < 0.$$

The intermediate value theorem along with the fact that $f(\zeta)$ is strictly decreasing for $\zeta > 0$ guarantees the existence and uniqueness of \hat{d}_K .

The resulting model of tumour growth without immunosurveillance is then

$$\begin{aligned} \frac{d}{dt}Q(t) &= A_R(t) - a_1Q(t) - d_1Q(t) \\ \frac{d}{dt}G_1(t) &= a_1Q(t) - a_2G_1(t) - d_2G_1(t), \end{aligned}$$

where $A_R(t)$ is given by (3.6).

3.2.2 Immune model development

The tumour microenvironment is complex and contains a multitude of cytokines and cell types [Bartlett et al., 2013; Cassady et al., 2016; Grivennikov and Karin, 2011; Hallam et al., 2009]. To avoid overcomplicating the model by adding variables and creating equations corresponding to each cytokine and signalling pathway, we instead model a general local proinflammatory cytokine compartment $C(t)$. We assume the cytokine is produced at a variable rate $C_{prod}(U(t))$ with the homeostatic production rate C_{prod}^* . The viral and immune mediated destruction of tumour cells results in increased cytokine production by releasing tumour specific antigens [Bartlett et al., 2013; Bell and McFadden, 2014]. Conversely, we do not consider apoptosis of tumour cells to be immunogenic [Bartlett et al., 2013]. Therefore, $C_{prod}(U(t))$ is an increasing function of viral and immune destruction of tumour cells. The resulting positive feedback loop is consistent with self activation of immune cells observed experimentally [Mosser, 2003]. Finally, we assume that the cytokine is cleared linearly at rate k_{elim} , mimicking the dynamics of many endogenous cytokines [Craig et al., 2016; Krzyzanski et al., 2010; Piscitelli et al., 1997]. The simplified cytokine dynamics are thus given by

$$\frac{d}{dt}C(t) = C_{prod}(U(t)) - k_{elim}C(t).$$

We assume that phagocytes can undergo phagocytosis multiple times, so phagocyte clearance is linear, and we do not include a phagocytosis related death term. Inflammatory cytokines drive phagocyte recruitment and activation [Bartlett et al., 2013; Cassady et al., 2016; Hallam et al., 2009]. Consequently, we model the local phagocyte population in a similar cytokine driven manner to Schirm et al. [2016] by using a Michaelis–Menten growth function $\varphi(C(t))$ with maximal production rate k_{cp} and half effect concentration of cytokine $C_{1/2}$. The phagocyte dynamics are therefore given by

$$\frac{d}{dt}P(t) = \varphi(C(t)) - \gamma_p P(t), \quad \text{where} \quad \varphi(C(t)) = \frac{k_{cp}C(t)}{C_{1/2} + C(t)}. \quad (3.8)$$

The disease free equilibrium concentrations of $(C(t), P(t))$ represent the tumour-free tissue concentrations of cytokine and phagocytes and are given by

$$C^* = \frac{C_{prod}^*}{k_{elim}} \quad \text{and} \quad P^* = \frac{1}{\gamma_p} \frac{k_{cp}C^*}{C_{1/2} + C^*}. \quad (3.9)$$

We describe phagocyte-tumour cell interaction by

$$\psi_Q(U(t))Q(t) = \frac{k_p P(t)}{1 + k_q Q(t)} Q(t), \quad \text{and} \quad \psi_G(U(t))G_1(t) = \frac{k_p P(t)}{1 + k_s G_1(t)} G_1(t). \quad (3.10)$$

For small tumour cell populations, the tumour-immune interaction follows mass-action kinetics, while for large tumour cell populations, the phagocytosis rate is limited by the phagocyte concentration as would be expected. We assume that cells in the active portion of the cell cycle interact with the immune system in the same way as cells in the G_1 phase.

The total immune mediated death is then

$$\Psi(U(t)) = \psi_Q(U(t))Q(t) + \psi_G(U(t))(N(t) + G_1(t)).$$

Contact rates similar to (3.10) were derived by [Imran and Smith \[2007\]](#) using a handling time argument.

3.2.3 Viral therapy model development

Viral infections are caused by virus specific particles, called virions, that infect and replicate in host cells. Infected host cells die after undergoing lysis and releasing virions into the surrounding tissue. To model the effect of oncolytic virus treatment, we consider the virion population, $V(t)$, and the number of infected malignant cells, $I(t)$.

Infection occurs following contact of a virion and a susceptible cell. Susceptible cells are cells in the G_1, S, G_2 and M phases of the cell cycle. We model the infection rate between virions and susceptible cells by $\eta(U(t))$. Infection due to virion and susceptible cell contact occurs in a similar manner to tumour-immune interactions. Consequently, $\eta(U(t))$ is structured similarly to equation (3.10), with half effect concentration $\eta_{1/2}$ and maximal infectious rate κ , so

$$\eta(U(t)) = \kappa \frac{V(t)}{\eta_{1/2} + V(t)}. \quad (3.11)$$

As previously noted, disease remission following viral therapy is thought to result from activation of the immune system against the tumour and increased antitumour immunity [[Bartlett et al., 2013](#); [Bell and McFadden, 2014](#); [Cassady et al., 2016](#); [Fukuhara et al., 2016](#); [Rehman et al., 2016](#)]. Therefore, introduction of viral therapy alone should not impact the stability of the disease free equilibrium but rather immune response to viral therapy may change the quantitative behaviour of solutions. This is in contrast to [Crivelli et al. \[2012\]](#), who modelled contact between virions and susceptible cells using a non-differentiable contact function. Their choice of contact function was motivated by noting that viral

therapy has driven cancer into remission, which implicitly assumed that the virus alone drives disease remission.

Infected tumour cells are produced following infection and undergo lysis at a rate δ . Lysis of infected tumour cells releases α virions. Virions are only produced during lysis and lose infectivity at a rate ω , leading to the differential equations for $I(t)$ and $V(t)$

$$\begin{aligned}\frac{d}{dt}I(t) &= \eta(U(t)) [G_1(t) + N(t)] - \delta I(t) \\ \frac{d}{dt}V(t) &= -\eta(U(t)) [G_1(t) + N(t)] + \alpha \delta I(t) - \omega V(t).\end{aligned}$$

Clearance of proliferating cells leads to exponential loss as the cleared cells no longer divide nor return to quiescence. This is accounted for by updating (3.6) to include the loss of mitotic cells due to immune and viral mediated death, giving

$$A_R(t) = 2 \int_{-\infty}^t \exp \left[- \int_{\sigma}^t \hat{d}_K + \eta(U(x)) + \psi_G(U(x)) dx \right] a_2 G_1(\sigma) K(t - \sigma) d\sigma. \quad (3.12)$$

Finally, the link between the oncolytic virus and the immune system is cytokine production, modelled by $C_{prod}(U(t))$. Both lysis of infected cells and immune killing are immunogenic, leading to an increase in immune signalling. Therefore, we link virus and immune mediated cell death by the cytokine production rate $C_{prod}(U(t))$, given by

$$C_{prod}(U(t)) = C_{prod}^* + (C_{prod}^{max} - C_{prod}^*) \frac{[\delta I(t) + \Psi(U(t))]}{\Psi_{1/2} + [\delta I(t) + \Psi(U(t))]} \quad (3.13)$$

We note that $C_{prod}(U(t)) \geq C_{prod}^* > 0$ for nonnegative cell populations; the homeostatic cytokine production rate is effectively the minimal cytokine production rate.

Combining the differential equations for each population with the PDF $K(t)$ gives the complete model in equation (3.1).

3.3 MODEL ANALYSIS

The mathematical model in (3.1) represents cell populations that are non-negative quantities. Consequently, we begin our analysis by showing that solutions of (3.1) evolving from non-negative initial data remain non-negative.

Lemma 3.3.1. *Assume that the parameters in (3.1) are strictly positive and that the initial conditions are componentwise non-negative. Moreover, assume that $G_1(s) = \phi_G(s) \geq 0$ for $s \in (-\infty, 0]$. Then solutions of the initial value problem corresponding to (3.1) are non-negative for all time $t \geq 0$.*

Proof. By the assumption on the initial conditions, $C_{prod}(U(0)) \geq C_{prod}^* > 0$, so

$$\frac{d}{dt}C(t) > -k_{elim}C(t)$$

in a neighbourhood $t \in [0, \varepsilon_C]$. Gronwall's inequality ensures that $C(t) \geq C(0)e^{-k_{elim}t} \geq 0$ for $t \in [0, \varepsilon_C]$. In this interval,

$$-\gamma_p P(t) \leq \frac{d}{dt}P(t) \leq k_{cp} - \gamma_p P(t),$$

therefore

$$0 \leq P(0)e^{-\gamma_p t} \leq P(t) \leq \frac{k_{cp}}{\gamma_p}(1 - e^{-\gamma_p t}) + P(0)e^{-\gamma_p t} \leq \max\left\{\frac{k_{cp}}{\gamma_p}, P(0)\right\} = P^{max}.$$

We now investigate the populations $Q(t)$ and $G_1(t)$. If $Q(0) = G_1(0) = 0$ and $\phi_G(s) = 0$ K -almost everywhere in $(-\infty, 0]$, $Q(t)$ and $G_1(t)$ remain identically zero for all time $t > 0$. If $Q(0) = 0$ and $\phi(s)K(-s) > 0$ on some set of positive measure in $(-\infty, 0]$, then $Q(t)$ eventually becomes positive for some $t > 0$. Therefore, we only need to consider the case where $Q(0) > 0$ and $\phi(s) \geq 0$ for $s \in (-\infty, 0]$.

Now, let $t_g \in [0, \varepsilon_C]$ be the first time that $G_1(t_g) = 0$. Then $A_R(t)$ defined by equation (3.12) satisfies $A_R(t) \geq 0$ for all $t \in [0, t_g]$.

It follows from (3.1) that

$$\frac{d}{dt}Q(t) \geq -(a_1 + d_1 + k_p P^{max})Q(t) \quad \text{for } t \in [0, t_g].$$

Then $Q(t) > 0$ for $t \in [0, t_g]$ and

$$\left. \frac{d}{dt}G_1(t) \right|_{t=t_g} = a_1 Q(t_g) - a_2 G_1(t_g) - d_2 G_1(t_g) - \eta(U(t_g))G_1(t_g) - \psi_G(U(t_g))G_1(t_g) = a_1 Q(t_g) > 0. \quad (3.14)$$

Thus $G_1(t)$ is strictly increasing at t_g . If $t_g = 0$, then $G_1(t) > 0$ immediately. Conversely, if $t_g > 0$, then $G_1(t)$ must be nonincreasing at t_g . This contradicts (3.14), so no such $t_g > 0$ can exist and $G_1(t) > 0$ for $t \in (0, \varepsilon_C]$. Since $A_R(t) \geq 0$ while $G_1(t) \geq 0$, it follows from the arguments above that $Q(t) > 0$ while $G_1(t) \geq 0$. Finally, it is simple to see that $G_1(t) > 0$ for $t \in (0, \varepsilon_C]$ implies that $N(t)$ defined by (3.2) satisfies $N(t) > 0$ for all $t \in (0, \varepsilon_C]$.

If $V(0) = I(0) = 0$, then the $I(t), V(t)$ populations remain identically zero for all time. Therefore, we consider $V(0) + I(0) > 0$ and we have three cases:

Case I If $V(0) = 0$ then $I(0) > 0$ and it is simple to calculate that

$$\left. \frac{d}{dt}V(t) \right|_{t=0} = \alpha \delta I(0) > 0,$$

so $V(t)$ becomes strictly positive immediately.

Case II If $I(0) = 0$

If $Q(0) = 0$ and $\phi(s) = 0$ almost everywhere in $(-\infty, 0]$, the tumour free case, then $Q(t), G_1(t)$ and $I(t)$ remain identically zero for all time $t > 0$ and $V(t)$ decays exponentially to 0.

Thus, as above, we need only consider $Q(0) > 0$ and $G_1(t) > 0$ in $(0, \varepsilon_C]$. Now, $I(0) = 0$ so $V(0) > 0$ and for all $t \in (0, \varepsilon_C]$, if $I(t) = 0$ then

$$\frac{d}{dt}I(t) = \eta(U(t)) [G_1(t) + N(t)] > 0$$

and $I(t) > 0$ for all $t \in (0, \varepsilon_C]$, otherwise a contradiction ensues.

Case III Thus, it only remains to consider the case where $V(t)$ and $I(t)$ are both strictly positive immediately and remain positive in some neighbourhood of $t = 0$. While $I(t)$ and $V(t)$ are non-negative, we compute

$$\frac{d}{dt}(I(t) + V(t)) = -(\delta - \alpha\delta)I(t) - \omega V(t) \geq -\max[(\delta - \alpha\delta), \omega](I(t) + V(t)),$$

so

$$V(t) + I(t) \geq [V(0) + I(0)] \exp(-\max[(\delta - \alpha\delta), \omega]t) > 0.$$

If there exists a time t_v such that $V(t_v) = 0$ then $I(t_v) > 0$ and $\frac{d}{dt}V(t)|_{t=t_v} \leq 0$, but arguing as in Case I, we see that $\frac{d}{dt}V(t)|_{t=t_v} > 0$, and hence no such time t_v can exist. Similarly, if there exists a time t_I such that $I(t_I) = 0$ then $V(t_I) > 0$ and $\frac{d}{dt}I(t)|_{t=t_I} \leq 0$, but arguing as in Case II, we see that $\frac{d}{dt}I(t)|_{t=t_I} > 0$, so no such t_I can exist. Therefore, $V(t) > 0$ and $I(t) > 0$ for all $t \in [0, \varepsilon_C]$.

Finally, for $Q(t), G_1(t), I(t), V(t), P(t)$ strictly positive, the cytokine production rate satisfies $C_{prod}(U(t)) \geq C_{prod}^*$ so

$$\frac{d}{dt}C(t) \geq C_{prod}^* - k_{elim}C(t),$$

and $C(t) \geq \left(\frac{C_{prod}^*}{k_{elim}}(1 - e^{-k_{elim}t}) + C(0)e^{-k_{elim}t} \right) > 0$ for all $t \in [0, \varepsilon_C]$. Then, each component is positive at $t = \varepsilon_C$ and the above argument extends from $[0, \varepsilon_C]$ to $[0, \infty)$. \square

3.3.1 Linearisation of the distributed DDE

The system (3.1) has the cancer free equilibrium (CFE), $U^* = (0, 0, 0, 0, C^*, P^*)$. Although it is often convenient to regard a trajectory $U(t)$ of the system (3.1) as a parameterised curve with $U(t) \in \mathcal{C}(\mathbb{R}, \mathbb{R}^6)$, it is important to realise that the DDE system (3.1) defines an

infinite dimensional dynamical system. The infinite-dimensional phase space is

$$L^1((-\infty, 0], \mathbb{R}^6, \mu) = \left\{ f : (-\infty, 0] \rightarrow \mathbb{R}^6 \mid \int_0^\infty |f(-s)| d\mu(s) < \infty \right\}$$

where $|\cdot|$ is the ℓ_1 norm in \mathbb{R}^6 , and μ is a probability measure whose Radon-Nikodym derivative with respect to the Lebesgue measure is $K(t)$. When $K(t)$ is Riemann integrable (such as in the case of the Gamma distribution that we will consider in Section 3.4) this implies that

$$\mu(t) = \int_0^t K(\xi) d\xi.$$

This space satisfies the axioms given by [Hale and Verduyn Lunel \[1993\]](#); [Hino et al. \[1991\]](#), so there exists a unique solution to the corresponding initial value problem.

To investigate the long term behaviour of the model, we linearise the system around the CFE in $L_1(\mu)$. In a similar procedure to [Câmara De Souza et al. \[2018\]](#), we first linearise the function $A_R(t)$, given in (3.12) around the CFE. Using the Taylor expansions of $\eta(U(x))$ and $\psi_G(U(x))$, with $\eta(U^*) = 0$, we approximate the inner integral

$$\begin{aligned} I &= - \int_{t-\sigma}^t \hat{d}_K + \eta(U(x)) + \psi_G(U(x)) dx \\ &= - \int_{t-\sigma}^t \hat{d}_K + \psi_G^* + \eta'(U^*)(U(x) - U^*) + \psi_G'(U^*)(U(x) - U^*) + \mathcal{O}(|U(x) - U^*|^2) dx. \end{aligned}$$

The full expansion of e^I is

$$\begin{aligned} e^I &= e^{-[\hat{d}_K + \psi_G^*]\sigma} \exp \left(- \int_0^\sigma \eta'(U^*)(U(t-x) - U^*) + \psi_G'(U^*)(U(t-x) - U^*) + \mathcal{O}(|U(t-x) - U^*|^2) dx \right) \\ &= e^{-[\hat{d}_K + \psi_G^*]\sigma} \left[1 - \int_0^\sigma \eta'(U^*)(U(t-x) - U^*) + \psi_G'(U^*)(U(t-x) - U^*) dx + \mathcal{O}(|U(t-x) - U^*|^2) \right]. \end{aligned}$$

Importantly, e^I is multiplied by $G_1(t - \sigma)$ in $A_R(t)$ and any non-constant terms of $U(t)$ in the expansion of e^I are consequently nonlinear. So we obtain

$$A_R(t) = 2 \int_0^\infty \exp \left(-[\hat{d}_K + \psi_G^*]\sigma \right) d\sigma + \mathcal{O}(|U(t) - U^*|^2) \quad (3.15)$$

We translate the CFE of (3.1) to zero by setting $\bar{C}(t) = C(t) - C^*$ and $\bar{P}(t) = P(t) - P^*$ with C^* and P^* given by (3.9). Then, noting that $\eta(U^*) = 0$ and using (3.15), the $N(t)$ terms in

the $I(t)$ and $V(t)$ equations are also nonlinear. Equation (3.1) becomes

$$\left. \begin{aligned}
 \frac{d}{dt}Q(t) &= 2 \int_0^\infty \exp\left(-[\hat{d}_K + \psi_G^*]\sigma\right) a_2 G_1(t - \sigma) K(\sigma) d\sigma \\
 &\quad - (a_1 + d_1 + k_p P^*)Q(t) + \mathcal{O}(|U(t) - U^*|^2). \\
 \frac{d}{dt}G_1(t) &= a_1 Q(t) - (a_2 + d_2 + k_p P^*)G_1(t) + \mathcal{O}(|U(t) - U^*|^2) \\
 \frac{d}{dt}I(t) &= -\delta I(t) + \mathcal{O}(|U(t) - U^*|^2) \\
 \frac{d}{dt}V(t) &= \alpha \delta I(t) - \omega V(t) + \mathcal{O}(|U(t) - U^*|^2) \\
 \frac{d}{dt}\bar{C}(t) &= \left(\frac{C_{prod}^{max} - C_{prod}^*}{\Psi_{1/2} + k_p P^*}\right) [\delta I(t) + k_p P^* (G_1(t) + Q(t))] - k_{elim}(\bar{C}(t)) + \mathcal{O}(|U(t) - U^*|^2) \\
 \frac{d}{dt}\bar{P}(t) &= \frac{k_{cp}}{C_{1/2} + C^*} \bar{C}(t) - \gamma_p \bar{P}(t) + \mathcal{O}(|U(t) - U^*|^2).
 \end{aligned} \right\} \tag{3.16}$$

We follow [Smith \[2011\]](#) to complete the linearisation. We define $\mathbf{X}(t) := U(t) - U^*$ and use \mathbf{X}_τ to denote the linear delayed terms via

$$\mathbf{X}_\tau(t) := \int_0^\infty e^{-[\hat{d}_K + \psi_G^*]\sigma} \mathbf{X}(t - \sigma) K(\sigma) d\sigma.$$

By making the ansatz $\mathbf{X}(t) = \mathbf{C}e^{\lambda t}$, we see that $\mathbf{X}_\tau(t)$ satisfies

$$\begin{aligned}
 \mathbf{X}_\tau(t) &= \int_0^\infty e^{-[\hat{d}_K + \psi_G^*]\sigma} \mathbf{X}(t - \sigma) K(\sigma) d\sigma = \mathbf{C}e^{\lambda t} \int_0^\infty e^{-(\lambda + \hat{d}_K + \psi_G^*)\sigma} K(\sigma) d\sigma \\
 &= \mathbf{X}(t) \mathcal{L}[K](\lambda + \hat{d}_K + \psi_G^*),
 \end{aligned}$$

where $\mathcal{L}[K](\lambda)$ is the Laplace transform of $K(\sigma)$ defined by (3.5).

Dropping the nonlinear terms in equation (3.16) and setting

$$\xi_c = \frac{(C_{prod}^{max} - C_{prod}^*)}{\Psi_{1/2} + k_p P^*},$$

we obtain the linearised infinite dimensional DDE

$$\frac{d}{dt}\mathbf{X}(t) = \mathbb{A}\mathbf{X}(t) + \mathbb{B}\mathbf{X}_\tau(t) = (\mathbb{A} + \mathcal{L}[K](\lambda + \hat{d}_K + \psi_G^*)\mathbb{B})\mathbf{X}(t), \tag{3.17}$$

where

$$\mathbb{A} + \mathcal{L}[K](\lambda + \hat{d}_K + \psi_G^*)\mathbb{B} = \left[\begin{array}{cc|cccc} -(a_1 + d_1 + k_p P^*) & 2a_2 \mathcal{L}[K](\lambda + \hat{d}_K + \psi_G^*) & 0 & 0 & 0 & 0 \\ a_1 & -(a_2 + d_2 + k_p P^*) & 0 & 0 & 0 & 0 \\ \hline 0 & 0 & -\delta & 0 & 0 & 0 \\ 0 & 0 & \alpha\delta & -\omega & 0 & 0 \\ \xi_c k_p P^* & \xi_c k_p P^* & \xi_c \delta & 0 & -k_{elim} & 0 \\ 0 & 0 & 0 & 0 & \frac{k_{ep}}{C_{1/2} + C^*} & -\gamma_p \end{array} \right].$$

Hence (3.17) becomes

$$C\lambda e^{\lambda t} = (\mathbb{A} + \mathcal{L}[K](\lambda + \hat{d}_K + \psi_G^*)\mathbb{B})C e^{\lambda t}, \quad (3.18)$$

From (3.18), the characteristic equation is

$$q(\lambda) := \det [\mathbb{A} + \mathcal{L}[K](\lambda + \hat{d}_K + \psi_G^*)\mathbb{B} - \lambda I] = 0.$$

Using the block nature of the linearisation matrix gives

$$q(\lambda) = \rho(\lambda)p(\lambda) = 0,$$

where

$$\left. \begin{aligned} \rho(\lambda) &= (\delta + \lambda)(\omega + \lambda)(k_{elim} + \lambda)(\gamma_p + \lambda), \\ p(\lambda) &= 2a_1 a_2 \mathcal{L}[K](\lambda + \hat{d}_K + \psi_G^*) - (a_1 + d_1 + k_p P^* + \lambda)(a_2 + d_2 + k_p P^* + \lambda). \end{aligned} \right\} \quad (3.19)$$

Here $\rho(\lambda)$ is the determinant of the lower triangular block and has strictly negative real roots. The explicit roots of $\rho(\lambda)$ imply that the stability of the CFE is determined by the roots of $p(\lambda)$.

To study the persistence of small tumours, we characterise the stability of the disease free steady state. Typically, for DDEs, this involves solving a transcendental equation with infinitely many roots. To simplify the following analysis, we first show that the rightmost root of the characteristic equation is real. This result is unsurprising, as a complex rightmost eigenvalue would give rise to spiralling solutions around the CFE, which would become negative, contradicting Lemma 3.3.1.

Lemma 3.3.2. *For strictly positive parameters, the rightmost root of $q(\lambda)$ is real.*

Proof. First, we note from (3.5) that the Laplace transform of a non-negative function f , is

a decreasing function of λ . Similarly,

$$\mathcal{L}[K](\lambda + \hat{d}_K + \psi_G^*) = \int_0^\infty e^{-(\lambda + \hat{d}_K + \psi_G^*)\sigma} K(\sigma) d\sigma$$

is decreasing for real λ where it converges. Therefore, as a function of a real variable, $p(\lambda)$ is continuous and $p(\lambda)$ is strictly decreasing for

$$\lambda > \max[-(a_1 + d_1 + k_p P^*), -(a_2 + d_2 + k_p P^*)] := -\Theta.$$

Moreover,

$$p(-\Theta) = 2a_1 a_2 \mathcal{L}[K](-\Theta + \hat{d}_K + \psi_G^*) > 0 \quad \text{and} \quad \lim_{\lambda \rightarrow \infty} p(\lambda) = -\infty,$$

so there is exactly one real root λ^* of $p(\lambda)$ that satisfies $\lambda^* > -\Theta$.

Since $\rho(\lambda)$ has strictly negative real roots, any complex roots, $\nu = \nu_r + i\nu_i$ with $\nu_r \in (-\Theta, \infty)$ and $\nu_i \neq 0$, of the characteristic equation $q(\lambda)$ must solve $p(\nu) = 0$, which we may rewrite as

$$(a_1 + d_1 + k_p P^* + \nu)(a_2 + d_2 + k_p P^* + \nu) = 2a_1 a_2 \mathcal{L}[K](\nu + \hat{d}_K + \psi_G^*). \quad (3.20)$$

Taking the magnitude of the equality (3.20) gives

$$\left[(a_1 + d_1 + k_p P^* + \nu_r)^2 + \nu_i^2 \right] \left[(a_2 + d_2 + k_p P^* + \nu_r)^2 + \nu_i^2 \right]^{1/2} = 2a_1 a_2 \left| \mathcal{L}[K](\nu + \hat{d}_K + \psi_G^*) \right|. \quad (3.21)$$

However,

$$\begin{aligned} & (a_1 + d_1 + k_p P^* + \nu_r)(a_2 + d_2 + k_p P^* + \nu_r) \\ & < \left[(a_1 + d_1 + k_p P^* + \nu_r)^2 + \nu_i^2 \right] \left[(a_2 + d_2 + k_p P^* + \nu_r)^2 + \nu_i^2 \right]^{1/2} \end{aligned}$$

and

$$\begin{aligned} 2a_1 a_2 \left| \mathcal{L}[K](\nu + \hat{d}_K + \psi_G^*) \right| &= 2a_1 a_2 \left| \int_0^\infty \exp[-(\nu_r + i\nu_i + \hat{d}_K + \psi_G^*)\sigma] K(\sigma) d\sigma \right| \\ &\leq 2a_1 a_2 \int_0^\infty \left| \exp[-(\nu_r + \hat{d}_K + \psi_G^*)\sigma] K(\sigma) \right| e^{-i\nu_i \sigma} d\sigma \\ &= 2a_1 a_2 \int_0^\infty \left| \exp[-(\nu_r + \hat{d}_K + \psi_G^*)\sigma] K(\sigma) \right| d\sigma \\ &= 2a_1 a_2 \mathcal{L}[K](\nu_r + \hat{d}_K + \psi_G^*) \end{aligned}$$

where the last equality comes from the nonnegativity of the integrand. Substituting these

bounds into (3.21) gives

$$(a_1 + d_1 + k_p P^* + \nu_r)(a_2 + d_2 + k_p P^* + \nu_r) < 2a_1 a_2 \mathcal{L}[K](\nu_r + \hat{d}_K + \psi_G^*),$$

from which we obtain

$$0 = p(\nu_r + i\nu_i) < p(\nu_r).$$

Since $p(\lambda)$ is strictly decreasing for $\lambda > -\Theta$, we must have $\nu_r < \lambda^*$. Then, the rightmost root of $q(\lambda)$ is either λ^* or a root of $\rho(\lambda)$ and is real. \square

The preceding result simplifies the analysis of the transcendental characteristic equation by ensuring that the critical characteristic root is real. Therefore, the stability of the CFE, and consequently, the persistence of small tumours, can be characterised using the intermediate value theorem.

Theorem 3.3.3. *The CFE U^* of equation (3.1) is locally asymptotically stable if*

$$2a_1 a_2 \mathcal{L}[K](\hat{d}_K + \psi_G^*) < (a_1 + d_1 + k_p P^*)(a_2 + d_2 + k_p P^*) \quad (3.22)$$

and unstable if

$$2a_1 a_2 \mathcal{L}[K](\hat{d}_K + \psi_G^*) > (a_1 + d_1 + k_p P^*)(a_2 + d_2 + k_p P^*).$$

Proof. The condition for stability is equivalent to $p(0) < 0$. In this case, since $p(\lambda)$ is strictly decreasing for $\lambda > \max[-(a_1 + d_1 + k_p P^*), -(a_2 + d_2 + k_p P^*)]$, there can be no real root of the characteristic equation with non-negative real part. Since the rightmost root must be real, all roots of the characteristic equation must have negative real part and the CFE is stable.

The condition for instability is equivalent to $p(0) > 0$. Since

$$\lim_{\lambda \rightarrow \infty} p(\lambda) = -\infty,$$

the intermediate value theorem ensures that there is a root of the characteristic equation in the positive half plane and the CFE is unstable. \square

Using (3.5) we can rewrite the stability condition (3.22) as

$$2a_1 a_2 \mathbb{E}_K(\exp(-[\hat{d}_K + \psi_G^*]t)) < (a_1 + d_1 + k_p P^*)(a_2 + d_2 + k_p P^*). \quad (3.23)$$

This can be rearranged as a basic reproduction number type condition

$$\underbrace{\left[\frac{2a_2 \mathbb{E}_K(\exp(-[\hat{d}_K + \psi_G^*]t))}{a_1 + d_1 + k_p P^*} \right]}_{\text{Rate out of quiescence}} \underbrace{\left[\frac{a_1}{a_2 + d_2 + k_p P^*} \right]}_{\text{Rate out of } G_1} < 1.$$

Hence, the CFE is locally attracting if the product of the ratios of expected transit rates into and out of the quiescent and G_1 phases is less than one. Biologically, this corresponds to each cell that transits out of either the quiescence or G_1 phase not replacing itself through mitosis. Clinically, while the CFE is unreachable in finite time, the local stability of the CFE is crucial in determining treatment success or failure. If the CFE is locally asymptotically stable, an effective treatment need only drive the tumour into the CFE basin of attraction to be effective. Conversely, if the CFE is unstable, then the disease free state is repelling and all treatments will ultimately be unsuccessful.

Finally, we can characterise the importance of heterogeneity in cell cycle duration as a determining factor of disease progression. Let \mathcal{P} be the parameter space of the distributed DDE (3.1). Following [Campbell and Jessop \[2009\]](#), for each PDF $K(t)$, we define the stability region as

$$\Omega_K = \{ \mathbf{p} \in \mathcal{P} \mid \text{The CFE of (3.1) is locally asymptotically stable} \}.$$

Then, we are able to define the stability region of the homogeneous cell cycle duration case. The homogeneous cell cycle duration case corresponds to $K(t) = \delta(t - \tau)$ with stability region:

$$\Omega_\delta = \{ \mathbf{p} \in \mathcal{P} \mid 2a_1 a_2 \exp(-[\hat{d}_K + \psi_G^*]\tau) < (a_1 + d_1 + k_p P^*)(a_2 + d_2 + k_p P^*) \}.$$

Then, we are able to characterise the stability regions for certain PDFs with respect to the discrete DDE. For these PDFs, the tumour heterogeneity in cell cycle duration acts to destabilise the CFE and leads to more a robust tumour. We formalise this relationship in the following corollary.

Corollary 3.3.4. *For any PDF $K(t)$ which satisfies (3.3) and $\hat{d}_K \leq d_3$ we have the inclusion $\Omega_K \subseteq \Omega_\delta$.*

Proof. Take $\mathbf{p} \in \Omega_K$ so that (3.23) is satisfied and the CFE is locally stable. Now, we define

$$h_K(x) = \exp(-[\hat{d}_K + \psi_G^*]x).$$

It is simple to see that $h_K(x)$ is convex. Jensen's inequality gives

$$\begin{aligned} \exp\left(-[\hat{d}_K + \psi_G^*]\tau\right) &= h_K\left(\int_0^\infty xK(x)\mathbf{d}x\right) \\ &\leq \int_0^\infty \exp\left(-[\hat{d}_K + \psi_G^*]x\right) K(x)\mathbf{d}x = \mathbb{E}_K(\exp(-(\hat{d}_K + \psi_G^*)t)). \end{aligned}$$

Now, using $\hat{d}_K \leq d_3$, we have

$$\mathbb{E}_\delta(\exp(-(\hat{d}_K + \psi_G^*)t)) = \exp(-[d_3 + \psi_G^*]\tau) \leq \exp(-[\hat{d}_K + \psi_G^*]\tau) \leq \mathbb{E}_K(\exp(-(\hat{d}_K + \psi_G^*)t)).$$

It follows that

$$\mathbb{E}_\delta(\exp(-(\hat{d}_K + \psi_G^*)t)) - (a_1 + d_1 + k_p P^*)(a_2 + d_2 + k_p P^*) < 0,$$

so the CFE is stable in the discrete DDE case and $\mathbf{p} \in \Omega_\delta$. □

The condition $\hat{d}_K \leq d_3$ corresponds to

$$\int_0^\infty t e^{-d_3 t} K(t) \mathbf{d}t - \tau e^{-d_3 \tau} \leq 0,$$

which can be viewed as a measure of the skewness of the PDF $K(t)$. Using (3.3), this condition is satisfied if

$$\int_0^\tau t (e^{-d_3 t} - e^{-d_3 \tau}) K(t) \mathbf{d}t \leq \left| \int_\tau^\infty t (e^{-d_3 t} - e^{-d_3 \tau}) K(t) \mathbf{d}t \right| = \int_\tau^\infty t (e^{-d_3 \tau} - e^{-d_3 t}) K(t) \mathbf{d}t.$$

It is important to note that the linearisation only determines local stability. So, while small tumours may not grow, large tumours do not necessarily disappear. In fact, for a given level of immune recognition of tumour cells, k_p , there is a critical tumour size above which the tumour grows unboundedly. The critical tumour size acts as a separatrix between tumour extinction and growth and takes the form of a nonzero equilibrium point where tumour growth and immune surveillance are balanced. In Theorem 3.3.5, we show that such an equilibrium must exist. Transition across this equilibrium has been hypothesised to occur as part of the cancer immunoediting process that allows tumours to grow and corresponds to a transient decrease of k_p [Bhatia and Kumar, 2011; Mittal et al., 2014; Swann and Smyth, 2007].

To emphasise the biological interpretation of Theorem 3.3.5, we use the stability condition as written in (3.23) to characterise the existence of the non-zero equilibrium.

Theorem 3.3.5. *Assume that the parameters in (3.1) are nonnegative. Let k_p^{crit} solve*

$$2a_1a_2\mathbb{E}_K[\exp(-[\hat{d}_k + k_p^{crit}P^*]\sigma)] - (a_1 + d_1 + k_p^{crit}P^*)(a_2 + d_2 + k_p^{crit}P^*) = 0.$$

Then, for $k_p > k_p^{crit}$, there exists a strictly positive untreated equilibrium solution $\bar{Y}_1^ = (\bar{Q}, \bar{G}_1, 0, 0, \bar{C}, \bar{P})$ of (3.1) with Q_1 and G_1 strictly positive.*

Proof. First, in the absence of viral treatment, $V(0) = 0$ and $I(0) = 0$, so $(V^*, I^*) = (0, 0)$.

To simplify notation in the proof, we set $\xi_i = a_i + d_i + k_p P^*$ for $i = 1, 2$. We consider the differential equation for $G_1(t)$ at equilibrium, so $\frac{d}{dt}G_1(t) = 0$ and

$$a_1Q^* = G_1^* \left(a_2 + d_2 + \frac{k_p P^*}{1 + k_s G_1^*} \right).$$

This can be rearranged as a quadratic equation in G_1^* ,

$$(a_2 + d_2)k_s(G_1^*)^2 + (\xi_2 - k_s a_1 Q^*)G_1^* - a_1 Q^* = 0,$$

whose positive root is a function of Q^* defined by

$$G_1^*(Q^*) = \frac{k_s a_1 Q^* - \xi_2 + \sqrt{(k_s a_1 Q^*)^2 + 2(a_2 + d_2 - k_p P^*)k_s a_1 Q^* + \xi_2^2}}{2(a_2 + d_2)k_s}. \quad (3.24)$$

Now, inserting $G_1^*(Q^*)$ into $\frac{d}{dt}Q(t) = 0$ gives

$$0 = 2a_2 G_1^*(Q^*) \int_0^\infty \exp[-(\hat{d}_K + \eta(U^*)) + \psi_G(U^*)] \sigma dx] K(\sigma) d\sigma - (a_1 + d_1 + \psi_Q(U^*))Q^*.$$

Using (3.4) gives

$$F(Q^*) = 2a_2 G_1^*(Q^*) \mathbb{E}_K[\exp(-(\hat{d}_k + \psi_G(U^*))\sigma)] - \left(a_1 + d_1 + \frac{k_p P^*}{1 + k_q Q^*} \right) Q^* = 0.$$

We write

$$F(Q^*) = \frac{f(Q^*)}{1 + k_q Q^*}$$

where

$$\begin{aligned}
f(Q^*) &= k_q \left(\frac{a_1 a_2 \mathbb{E}_K[\exp(-(\hat{d}_k + \psi_G(U^*))\sigma)]}{a_2 + d_2} - (a_1 + d_1) \right) (Q^*)^2 \\
&+ \frac{a_1 a_2 \mathbb{E}_K[\exp(-(\hat{d}_k + \psi_G(U^*))\sigma)]}{a_2 + d_2} Q^* - \xi_1 Q^* \\
&+ \frac{a_2 \mathbb{E}_K[\exp(-(\hat{d}_k + \psi_G(U^*))\sigma)]}{k_s(a_2 + d_2)} \left(-\xi_2 + \sqrt{(k_s a_1 Q^*)^2 + 2(a_2 + d_2 - k_p P^*) k_s a_1 Q^* + \xi_2^2} \right) k_q Q^* \\
&+ \frac{a_2 \mathbb{E}_K[\exp(-(\hat{d}_k + \psi_G(U^*))\sigma)]}{k_s(a_2 + d_2)} \left(-\xi_2 + \sqrt{(k_s a_1 Q^*)^2 + 2(a_2 + d_2 - k_p P^*) k_s a_1 Q^* + \xi_2^2} \right).
\end{aligned}$$

The equilibrium concentration Q_1 must therefore solve $f(Q_1) = 0$. A simple calculation shows that $f(0) = 0$, so we search for Q_1 positive. Now, as $Q^* \rightarrow \infty$,

$$\begin{aligned}
f(Q^*) &= \left(\frac{a_1 a_2 \mathbb{E}_K[\exp(-(\hat{d}_k + \psi_G(U^*))\sigma)]}{a_2 + d_2} - (a_1 + d_1) \right) k_q (Q^*)^2 \\
&+ k_q Q^* \frac{a_2 \mathbb{E}_K[\exp(-(\hat{d}_k + \psi_G(U^*))\sigma)]}{k_s(a_2 + d_2)} \sqrt{(k_s a_1 Q^*)^2 + 2(a_2 + d_2 - k_p P^*) k_s a_1 Q^* + \xi_2^2} \\
&+ \mathcal{O}([Q^*]^{3/2}).
\end{aligned}$$

This is equivalent to

$$\begin{aligned}
f(Q^*) &= \left[2a_1 a_2 \mathbb{E}_K[\exp(-(\hat{d}_k + \psi_G(U^*))\sigma)] - (a_1 + d_1)(a_2 + d_2) \right] \frac{k_q (Q^*)^2}{(a_2 + d_2)} \\
&+ \mathcal{O}([Q^*]^{3/2}) \quad \text{as } Q^* \rightarrow \infty,
\end{aligned}$$

so the sign of $\left[2a_1 a_2 \mathbb{E}_K[\exp(-(\hat{d}_k + \psi_G(U^*))\sigma)] - (a_1 + d_1)(a_2 + d_2) \right]$ determines the sign of $f(Q^*)$ as Q^* grows infinitely large. Now,

$$\begin{aligned}
&2a_1 a_2 \mathbb{E}_K[e^{-(\hat{d}_k + \psi_G(U^*))\sigma}] - (a_1 + d_1)(a_2 + d_2) \\
&> 2a_1 a_2 \mathbb{E}_K[e^{-(\hat{d}_k + k_p^{crit} P^*)\sigma}] - (a_1 + d_1 + k_p^{crit} P^*)(a_2 + d_2 + k_p^{crit} P^*) = 0,
\end{aligned}$$

so $f(Q^*)$ grows infinitely large with Q^* and must be positive for large values of Q^* .

Next, as $Q^* \rightarrow 0$,

$$\begin{aligned}
f(Q^*) &= \frac{a_1 a_2 \mathbb{E}_K[\exp(-(\hat{d}_k + \psi_G(U^*))\sigma)]}{k_s(a_2 + d_2)} \left(-\xi_2 + \sqrt{(k_s a_1 Q^*)^2 + 2(a_2 + d_2 - k_p P^*) k_s a_1 Q^* + \xi_2^2} \right) \\
&+ \frac{a_1 a_2 \mathbb{E}_K[\exp(-(\hat{d}_k + \psi_G(U^*))\sigma)]}{a_2 + d_2} Q^* - \xi_1 Q^* + \mathcal{O}([Q^*]^{3/2}).
\end{aligned}$$

Taylor expanding the square root about the point $Q^* = 0$ gives

$$\begin{aligned} -\xi_2 + \sqrt{(k_s a_1 Q^*)^2 + 2(a_2 + d_2 - k_p P^*) k_s a_1 Q^* + \xi_2^2} \\ = -\xi_2 + \sqrt{\xi_2^2} + \frac{(a_2 + d_2 - k_p P^*) k_s a_1 Q^*}{\xi_2} + \mathcal{O}([Q^*]^2), \end{aligned}$$

so for Q^* near 0,

$$\begin{aligned} f(Q^*) &= \frac{a_1 a_2 \mathbb{E}_K[\exp(-(\hat{d}_k + \psi_G(U^*))\sigma)]}{a_2 + d_2} Q^* - \xi_1 Q^* \\ &\quad + \frac{a_2 \mathbb{E}_K[\exp(-(\hat{d}_k + \psi_G(U^*))\sigma)]}{k_s(a_2 + d_2)} \frac{(a_2 + d_2 - k_p P^*)}{\xi_2} k_s a_1 Q^* + \mathcal{O}([Q^*]^{3/2}). \end{aligned}$$

Crucially, $a_2 + d_2 - k_p P^* = 2(a_2 + d_2) - \xi_2$, so with $f(0) = 0$

$$f'(0) = \lim_{Q^* \rightarrow 0} \frac{f(Q^*)}{Q^*} = \frac{1}{\xi_2} \left[2a_1 a_2 \mathbb{E}_K[\exp(-(\hat{d}_k + \psi_G(U^*))\sigma)] - \xi_1 \xi_2 \right].$$

Thus, the sign of $f'(0)$ is determined by the sign of

$$g(k_p) = 2a_1 a_2 \mathbb{E}_K[\exp(-(\hat{d}_k + \psi_G(U^*))\sigma)] - \xi_1 \xi_2.$$

The function $g(k_p)$ is strictly decreasing with $g(k_p^{crit}) = 0$, therefore, $f'(0) < 0$ for $k_p > k_p^{crit}$.

Consequently, $f(Q^*)$ is negative for Q^* small and positive, and positive for large Q^* , so there must be a positive root \bar{Q} with $f(\bar{Q}) = 0$. This root defines a solution $\bar{G}_1 = G_1^*(Q_1)$ of (3.24).

Finally, we can write an equilibrium solution of $\frac{d}{dt}P(t) = 0$ as a function of $C(t)$ via

$$\bar{P} = \frac{\varphi(C(t))}{\gamma_p} \leq \frac{k_{cp}}{\gamma_p}.$$

Given the upper bound of \bar{P} and the pair (\bar{Q}, \bar{G}_1) , the function $\Psi(U(t))$ is bounded. Therefore, there must exist a solution $\bar{C} > 0$ to

$$0 = C_{prod}(\bar{Q}, \bar{G}_1, \varphi(\bar{C})/\gamma_p) - k_{elim}\bar{C}.$$

Finally, using the value of \bar{C} , we can calculate the corresponding equilibrium \bar{P} . \square

3.4 THE GAMMA DISTRIBUTION AND EQUIVALENT ODE SYSTEM

In this section we illustrate our previous results through numerical simulation. We will show how (3.1) can be reformulated as a larger system of ordinary differential equations,

and use numerical simulations of these to provide insight into the biological mechanisms underlying the success or failure of viral therapy.

To translate our analytical results for a generic distribution into predictions of tumour growth, we must specify a distribution of cell cycle durations, corresponding PDF $K(t)$, and death rate \hat{d}_K . The form of the PDF $K(t)$ for a specific cancer patient could be estimated from clinical data. In the absence of such data, we assume that cell cycle durations follow a gamma distribution, so $K(t) = g_a^j(t)$. The function $g_a^j(t)$ is the PDF of the gamma distribution with

$$g_a^j(t) = \frac{a^j t^{j-1} e^{-at}}{\Gamma(j)} \quad \text{with} \quad \frac{d}{dt} g_a^1(t) = -a g_a^1(t) \quad \text{and} \quad \frac{d}{dt} g_a^j(t) = a[g_a^{j-1}(t) - g_a^j(t)], \quad j \geq 2. \quad (3.25)$$

Gamma distributions have been shown to be appropriate models of the heterogeneity in cell cycle duration [Golubev, 2016; Yates et al., 2017].

The real positive parameters a and j in (3.25) define the shape of the gamma distribution. The expected cell cycle duration is $\tau = j/a$. For given τ we take j to be a strictly positive integer and determine a by $a = j/\tau$. The standard deviation, s^2 , of the gamma distribution is given by $s^2 = \tau^2/j$. For fixed τ , larger values of j result in a more concentrated distribution about τ . In Appendix A we demonstrate that in the limit as $j \rightarrow \infty$ (with fixed τ) the gamma distributed model converges in distribution to a delta distributed model with discrete delay τ .

To calculate \hat{d}_g , we note that the expected cellular output of the cell cycle is

$$\begin{aligned} \mathbb{E}_g(\sigma) &= \int_0^\infty \sigma e^{-\int_{t-\sigma}^t \hat{d}_g dx} g_a^j(\sigma) d\sigma = \frac{a^j}{\Gamma(j)} \int_0^\infty \sigma^{j+1-1} e^{-(a+\hat{d}_g)\sigma} d\sigma \\ &= \frac{a^j}{(a+\hat{d}_g)^{j+1}} j = \left[\frac{a}{a+\hat{d}_g} \right]^{j+1} \frac{j}{a}. \end{aligned}$$

Imposing the equality (3.7) and $\tau = j/a$ gives

$$\left(\frac{1}{1 + \hat{d}_g \tau / j} \right)^{j+1} \tau = \tau e^{-d_3 \tau}.$$

Therefore, \hat{d}_g is given by

$$\hat{d}_g = \frac{j}{\tau} \left[(e^{d_3 \tau})^{1/j+1} - 1 \right]. \quad (3.26)$$

3.4.1 Equivalent ODE formulation

The link between gamma distributed DDEs and transit chain ODEs has been known since at least the 1960s [Vogel, 1961]. The equivalence between infinite dimensional DDEs and

ODEs is typically established through the linear chain technique. Among many other areas, the linear chain technique has recently been used in the pharmaceutical sciences [Câmara De Souza et al., 2018; Hu et al., 2018]. More generally, the equivalence between distributed DDEs and ODEs was studied by Diekmann et al. [2018].

Typical applications of the linear chain technique involve a transit chain type ODE without growth or loss throughout the chain. Here, we derive a variant of the linear chain technique that accounts for the exponential decay of the mitotic cell population due to apoptosis, immune pressure and lysis as modelled in equation (3.1). The resulting ODE system is a compartment model with linear clearance throughout the transit chain.

By taking $K(t) = g_a^j(t)$ with $j \in \mathbb{N}$ and $a = k_{tr} = j/\tau$ and setting

$$A_i(t) = \int_{-\infty}^t \frac{a_2}{k_{tr}} e^{-\int_{\sigma}^t \hat{d}_g + \eta(U(x)) + \psi_G(U(x)) dx} G_1(\sigma) g_{k_{tr}}^i(t - \sigma) d\sigma \quad \text{for } i = 1, 2, \dots, j,$$

we can reduce the distributed DDE model to a system of $6 + j$ ODEs. We show in Theorem 3.4.2 that (3.1) is equivalent to the system of ODEs

$$\left. \begin{aligned} \frac{d}{dt} Q(t) &= 2k_{tr}A_j(t) - a_1Q(t) - d_1Q - \psi_Q(U(t))Q(t) \\ \frac{d}{dt} G_1(t) &= a_1Q(t) - a_2G_1(t) - d_2G_1(t) - \psi_G(U(t))G_1(t) - \eta(U(t))G_1(t) \\ \frac{d}{dt} A_1(t) &= a_2G_1(t) - k_{tr}A_1(t) - [\hat{d}_g + \eta(U(t)) + \psi_G(U(t))]A_1(t) \\ \frac{d}{dt} A_i(t) &= k_{tr}(A_{i-1}(t) - A_i(t)) - [\hat{d}_g + \eta(U(t)) + \psi_G(U(t))]A_i(t) \quad \text{for } i = 2, 3, \dots, j \\ \frac{d}{dt} I(t) &= -\delta I(t) + \eta(U(t)) [G_1(t) + N(t)] \\ \frac{d}{dt} V(t) &= \alpha\delta I(t) - \omega V(t) - \eta(U(t)) [G_1(t) + N(t)] \\ \frac{d}{dt} C(t) &= C_{prod}(U(t)) - k_{elim}C(t) \\ \frac{d}{dt} P(t) &= \varphi(C(t)) - \gamma_p P(t) \end{aligned} \right\} \quad (3.27)$$

with identical initial conditions to the distributed DDE for $Q(0), V(0), I(0), P(0), C(0)$ and

$$G_1(0) = \phi(0), \quad A_i(0) = \int_0^{\infty} \frac{a_2}{k_{tr}} e^{-\int_{-\sigma}^0 \hat{d}_g + \eta(U(x)) + \psi_G(U(x)) dx} \phi(-\sigma) g_{k_{tr}}^i(\sigma) d\sigma,$$

where $\phi(s)$ is the history function of (3.1).

Lemma 3.4.1. *For an integrable function $G_1(t)$ and $j \in \mathbb{N}$ with $a = k_{tr} = j/\tau$, the vector with i -th component given by*

$$A_i(t) = \int_{-\infty}^t e^{-\int_{\sigma}^t \hat{d}_g + \eta(U(x)) + \psi_G(U(x)) dx} \frac{a_2}{k_{tr}} G_1(\sigma) g_{k_{tr}}^i(t - \sigma) d\sigma \quad \text{for } i = 1, 2, \dots, j, \quad (3.28)$$

is the solution of the system of differential equations given by

$$\left. \begin{aligned} \frac{d}{dt}A_1(t) &= a_2G_1(t) - k_{tr}A_1(t) - [\hat{d}_g + \eta(U(t)) + \psi_G(U(t))]A_1(t) \\ \frac{d}{dt}A_i(t) &= k_{tr}(A_{i-1}(t) - A_i(t)) - [\hat{d}_g + \eta(U(t)) + \psi_G(U(t))]A_i(t) \quad \text{for } i = 2, 3, \dots, j \end{aligned} \right\} \quad (3.29)$$

Proof. Using the Leibniz and product rules, we differentiate $A_1(t)$ to obtain

$$\begin{aligned} \frac{d}{dt}A_1(t) &= a_2G_1(t) - k_{tr} \int_{-\infty}^t \frac{a_2}{k_{tr}} e^{-\int_{\sigma}^t \hat{d}_g + \eta(U(x)) + \psi_G(U(x)) dx} G_1(\sigma) g_{k_{tr}}^1(t - \sigma) d\sigma \\ &\quad + \int_{-\infty}^t \frac{d}{dt} e^{-\int_{\sigma}^t \hat{d}_g + \eta(U(x)) + \psi_G(U(x)) dx} \frac{a_2}{k_{tr}} G_1(\sigma) g_{k_{tr}}^1(t - \sigma) d\sigma. \end{aligned} \quad (3.30)$$

Computing the derivative of the exponential then gives

$$\frac{d}{dt}A_1(t) = a_2G_1(t) - k_{tr}A_1(t) - [\hat{d}_g + \eta(U(t)) + \psi_G(U(t))]A_1. \quad (3.31)$$

Similarly for general i , differentiating the expression for $A_i(t)$ from (3.28) gives

$$\begin{aligned} \frac{d}{dt}A_i(t) &= \frac{a_2}{k_{tr}} e^0 G_1(t) g_a^i(0) + \int_{-\infty}^t \frac{a_2}{k_{tr}} \frac{d}{dt} [e^{-\int_{\sigma}^t \hat{d}_g + \eta(U(x)) + \psi_G(U(x)) dx} G_1(\sigma) g_{k_{tr}}^i(t - \sigma)] d\sigma \\ &= k_{tr}(A_{i-1}(t) - A_i(t)) - [\hat{d}_g + \eta(U(t)) + \psi_G(U(t))]A_i(t). \end{aligned}$$

Thus, the vector $\mathbf{A}(t) = [A_1(t), A_2(t), \dots, A_j(t)]$ satisfies (3.29). \square

Comparing equations (3.30) and (3.31) shows that the exponential loss of cells during the cell cycle in equation (3.1) corresponds to linear clearance in the equivalent transit compartment system of ODEs.

We now show the equivalence of the ODE and DDE models by using Lemma 3.4.1 to replace the integral terms in equation (3.1).

Theorem 3.4.2. *The system of distributed DDEs (3.1) with $K(\sigma) = g_a^j(\sigma)$, \hat{d}_g as given in (3.26) and initial conditions $Q(0) = Q_0$, $I(0) = I_0$, $C(0) = C_0$ and history functions $V(s) = \phi_V(s)$, $P(s) = \phi_P(s)$ and $G_1(s) = \phi_G(s)$ for $s \in (-\infty, 0]$ is equivalent to the system of ODEs (3.27) with initial conditions $Q(0) = Q_0$, $I(0) = I_0$, $C(0) = C_0$, $V(0) = \phi_V(0)$, $P(0) = \phi_P(0)$, $G_1(0) = \phi_G(0)$ and*

$$A_i(0) = \int_0^{\infty} \frac{a_2}{k_{tr}} \exp \left[- \int_{-\sigma}^0 \hat{d}_g + \eta(U(x)) + \psi_G(U(x)) dx \right] \phi_G(-\sigma) g_{k_{tr}}^i(\sigma) d\sigma. \quad (3.32)$$

Proof. Using Lemma 3.4.1, we see that

$$2k_{tr}A_j(t) = 2 \int_{-\infty}^t a_2 \exp \left[- \int_{\sigma}^t \hat{d}_g + \eta(U(x)) + \psi_G(U(x)) dx \right] G_1(\sigma) g_{ktr}^j(t - \sigma) d\sigma = A_R(t).$$

Thus, the differential equations for $Q(t)$ in (3.1) and (3.27) are equivalent.

The remaining terms in (3.27) are exactly those in (3.1). To finish the conversion from the DDE (3.1) to the ODE (3.27), we must specify the initial conditions. Given the history functions $[\phi_G(s), \phi_V(s), \phi_P(s)]$ from the DDE model, we chose the initial conditions $A_i(0)$ of (3.27) according to equation (3.32). This ensures that the solution of (3.27) is equivalent to the solution of (3.1) [Smith, 2011].

To convert from the ODE (3.27) to the DDE (3.1), we must take care with the construction of the history functions $(\phi_G(s), \phi_V(s), \phi_P(s))$. The ODE is equipped with initial conditions $V(0)$ and $P(0)$. For simplicity, we set $\phi_V(s) = V(0)$ and $\phi_P(s) = P(0)$.

The j initial conditions for each $A_i(0)$ define j constraints on $\phi_G(s)$. There are many history function that satisfy these constraints and the ODE reduction of the DDE defines the same solution for each such history function. We show how to construct one such history function $\phi_G \in L^1((-\infty, 0], \mathbb{R}, \mu)$. Let the ODE system have initial conditions

$$\alpha_i = A_i(0) \quad \text{for } i = 1, 2, \dots, j \quad \text{and} \quad \alpha_i \in \mathbb{R},$$

and chose a sequence of points

$$0 < x_1 < \dots < x_j < \infty.$$

Now, we make the following ansatz for $\phi_G(s)$

$$\phi_G(s) = \sum_{n=1}^j b_n \delta(s + x_n), \quad (3.33)$$

where $\delta(x)$ is the Dirac function. We will show that is possible to chose the $\{b_n\}_{n=1}^j$ such that

$$\int_0^{\infty} \frac{a_2}{k_{tr}} g_{ktr}^i(\sigma) \exp \left[- \int_{-\sigma}^0 \hat{d}_g + \eta(U(s)) + \psi_G(U(s)) ds \right] \phi(-\sigma) d\sigma = \alpha_i. \quad (3.34)$$

However, the histories $\phi_V(s), \phi_P(s)$ and $\phi_G(s)$ appear in the integral term

$$I = \int_{-\sigma}^0 \hat{d}_g + \eta(U(s)) + \psi_G(U(s)) ds,$$

so some care is needed. We have already set $\phi_V(s) = V(0)$ so $\eta(U(s))$ is defined on $(-\infty, 0]$,

so we need only consider

$$\psi_G(U(s)) = \frac{k_p P(0)}{1 + \phi_G(s)} \quad \text{for } s < 0$$

with $\phi_P(s) = P(0)$. Inserting (3.33) for $\phi_G(s)$ gives

$$\psi_G(U(s)) = \frac{k_p P(0)}{1 + \sum_{n=1}^j b_n \delta(s + x_n)} = \begin{cases} k_p P(0) & \text{if } s \notin \{-x_i\}_{i=1}^j \\ 0 & \text{if } s \in \{-x_i\}_{i=1}^j. \end{cases}$$

Since ψ_G only appears in a Lebesgue integral and differs from $k_p P(0)$ on a set of measure 0, the following holds

$$\int_{-\sigma}^0 \hat{d}_g + \eta(U(s)) + \psi_G(U(s)) \, ds = \int_{-\sigma}^0 \hat{d}_g + \eta(U(s)) + k_p P(0) \, ds.$$

Therefore, finding $\{b_n\}_{n=1}^j$ such that (3.34) holds is equivalent to finding $\{b_n\}_{n=1}^j$ such that

$$\int_0^\infty \frac{a_2}{k_{tr}} g_{k_{tr}}^i(\sigma) \exp \left[- \int_{-\sigma}^0 \hat{d}_g + \eta(U(s)) + k_p P(0) \, ds \right] \phi_G(-\sigma) \, d\sigma = \alpha_i. \quad (3.35)$$

Using the ansatz for ϕ_G in (3.35) gives the following system of equations for $i = 1, 2, \dots, j$

$$\alpha_i = \sum_{n=1}^j b_n \frac{a_2}{k_{tr}} g_{k_{tr}}^i(x_n) \exp \left[- \int_{-x_n}^0 \hat{d}_g + \eta(U(s)) + k_p P(0) \, ds \right]. \quad (3.36)$$

To simplify notation, set

$$\mu_n = \int_{-x_n}^0 \hat{d}_g + \eta(U(s)) + k_p P(0) \, ds$$

and note μ_n is independent of the unknowns $\{b_n\}_{n=1}^j$.

Equation (3.36) defines a linear system of equations for the unknowns $\{b_n\}_{n=1}^j$. Consequently, there exists a unique solution to (3.36) if the matrix

$$A = \begin{bmatrix} \frac{a_2}{k_{tr}} g_{k_{tr}}^1(-x_1) \exp[-\mu_1] & \cdots & \frac{a_2}{k_{tr}} g_{k_{tr}}^1(-x_j) \exp[-\mu_j] \\ \frac{a_2}{k_{tr}} g_{k_{tr}}^2(-x_1) \exp[-\mu_1] & \cdots & \frac{a_2}{k_{tr}} g_{k_{tr}}^2(-x_j) \exp[-\mu_j] \\ \vdots & \ddots & \vdots \\ \frac{a_2}{k_{tr}} g_{k_{tr}}^j(-x_1) \exp[-\mu_1] & \cdots & \frac{a_2}{k_{tr}} g_{k_{tr}}^j(-x_j) \exp[-\mu_j] \end{bmatrix}$$

is invertible. To show this matrix is invertible, we will show that $\det(A) \neq 0$. Using the

definition of $g_{k_{tr}}^j(x_i)$, the m -th column has a common factor of

$$\frac{a_2}{k_{tr}} e^{-k_{tr}x_m} \exp[-\mu_m] > 0$$

while, the n -th row has a common factor of $k_{tr}^n/(n-1)! > 0$ for $n, m = 1, 2, \dots, j$. Thus

$$\det(A) = \left[\prod_{n,m=1}^j \frac{a_2}{k_{tr}} e^{-k_{tr}x_m} \exp[-\mu_m] \frac{k_{tr}^n}{(n-1)!} \right] \det(V),$$

where

$$V = \begin{bmatrix} 1 & 1 & \cdots & 1 \\ x_1 & x_2 & \cdots & x_j \\ \vdots & \vdots & \ddots & \vdots \\ x_1^{j-1} & x_2^{j-1} & \cdots & x_j^{j-1} \end{bmatrix}$$

Since V is a Vandermonde Matrix and the $\{x_i\}_{i=1}^j$ are distinct, $\det(V) \neq 0$. Consequently, $\det(A) \neq 0$ so A is invertible and we can uniquely determine the $\{b_n\}_{n=1}^j$. \square

The equivalence between ODEs and gamma distributed DDEs has been used extensively since Vogel [1961]. Some authors have shown how to convert ODE transit compartment models to distributed DDE for specific initial conditions [Câmara De Souza et al., 2018; Cooke and Grossman, 1982]. However, to the author's knowledge this is the first proof of direct equivalence between an ODE and a distributed DDE for arbitrary ODE initial conditions established by explicitly constructing a suitable history function.

3.4.2 Numerical results

For the purpose of numerical simulation, the system of finite dimensional ODEs derived in Section 3.4.1 is much more tractable than the distributed DDE. Numerically solving the distributed DDE requires the development and implementation of a numerical differential equation solver capable of accurately computing the semi-infinite convolution integral, while there are numerous existing methods for solving systems of ODEs. To solve the DDE given in (3.1), we simulate the equivalent ODE in (3.27) and calculate $N(t)$ as shown in Appendix B to illustrate the analytical results of Section 3.3.

For simplicity, we only present the dynamics of $Q(t)$, as these dynamics are representative of the full model's behaviour. The parameters used in these simulations are given in Table 3.1. These simulations illustrate the analytical results of Section 3 and provide insight into the mechanism by which viral therapy leads to disease remission. However, the simulations are not meant to be representative of individual cancer patients.

The smallest clinically detectable tumour size has been estimated to be roughly $2^{30} \approx 1 \times 10^9$ cells [Carlson, 2003; Schwartz, 1961]. As viral oncology has only been approved for advanced melanoma, we consider tumours with approximately 10^{10} cells. (This corresponds to viral treatment starting 4 tumour doublings after diagnosis.) To ensure that our numerical computations involve numbers of similar magnitude, we measure the number of tumour cells in units of 10^{10} cells. Given the homeostatic approximation of leukocytes ($\approx 6 \times 10^9$ cells/L) and roughly 7 litres of blood, we measure the phagocyte concentration in identical units, namely 10^{10} cells.

To illustrate the difference between distributed and discrete delays in the cell cycle duration, we simulate (3.27) without viral therapy for $j = 6$ and the discrete delay case in Figure 3.2 a). In Fig. 3.2 b), we show the discrete case and the gamma distributed case when $j = 50$. These simulations show that the discrete delay case has a larger basin of attraction than the distributed delay case. This is unsurprising, since for both $j = 6$ and $j = 50$, the condition of Corollary 3.3.4 holds, so all parameter regimes leading to stability of the CFE for the gamma distributed DDE also lead to stability of the CFE in the discrete delay case. Biologically, this corresponds to increased cell cycle duration heterogeneity leading to more robust tumours.

In Fig. 3.2, we also show the impact of including tumour-immune interaction by comparing our model with that of Crivelli et al. [2012]. We compare the results of our simulation with tumour-immune interaction ($k_p = 0.065$) with the Crivelli model ($k_p = 0$) as written in Appendix A. This simulation underlies the importance of tumour-immune interaction in determining disease progression.

In Appendix A, we show that the gamma distribution converges to the degenerate distribution as j grows infinitely large, with $\tau > 0$ held constant. The case $j = 1$ corresponds to an exponential distribution of cell cycle durations. In what follows, we assume that the distribution of cell cycle durations is neither exponential nor degenerate, so $1 < j < \infty$. In the numerical simulations that follow, we illustrate a representative case of our results with $j = 6$.

In Fig. 3.3, we simulate the finite dimensional representation of the distributed DDE (3.1) for different levels of immune recruitment, k_{cp} , during viral therapy. Fig. 3.3 shows that changing k_{cp} changes the long-term success or failure of viral treatment. Sufficiently large values of k_{cp} induce long-lasting remission while smaller values of k_{cp} lead to eventual tumour progression after oncolytic virus treatment.

Fig. 3.4 shows the impact of parameter variability on stability of the CFE. Fig. 3.4 (a) shows that increased immune interaction (k_p) can counteract fast transit between quiescence and mitosis (a_1 and a_2 respectively) to ensure stability of the CFE. Moreover,

Parameter	Value	Biological Interpretation (Unit)	Reference
a_1	0.9	Quiescent to interphase rate (1/day)	Crivelli et al. [2012]
d_1	1×10^{-5}	Quiescent death rate (1/day)	Crivelli et al. [2012]
a_2	0.7	Interphase to active phase rate (1/day)	Crivelli et al. [2012]
d_2	0.19	Interphase death rate (1/day)	Crivelli et al. [2012]
d_3	0.19	Active phase death rate (1/day)	Crivelli et al. [2012]
\hat{d}_g	0.167	Active phase death rate (1/day)	Calculated from (3.26)
κ	1.15	Virion contact rate (1/day)	Crivelli et al. [2012]
$\eta_{1/2}$	$V(0)/10$	Virion half effect concentration (virions)	See caption
δ	1.119	Lysis rate (1/day)	Crivelli et al. [2012]
α	1.65	Lytic virion release rate (virions/cell)	Crivelli et al. [2012]
ω	0.75	Virion death rate (1/day)	Crivelli et al. [2012]
k_{cp}	6.63	Maximal phagocyte production rate (10^{10} cells/day)	Schirm et al. [2016]
$C_{1/2}$	0.87743	Phagocyte production half effect (ng/mL/day)	Liu et al. [2007]
$\Psi_{1/2}$	7	Cytokine production half effect (10^{10} cells/day)	See caption
γ_p	1	Phagocyte death rate (1/day)	Liu et al. [2007]
C_{prod}^*	0.014161	Homeostatic cytokine production rate (ng/mL/day)	Craig et al. [2016]
C_{prod}^{max}	1.4161	Maximal cytokine production rate (ng/mL/day)	See caption
k_{elim}	0.16139	Cytokine elimination rate (1/day)	Craig et al. [2016]
k_p	0.065	Phagocyte-tumour cell contact rate (1/day)	Liu et al. [2007]
$k_{q,s}$	1.75	Phagocyte cell digestion constant	See caption
τ	2.13285	Expected cell cycle duration (day)	Crivelli et al. [2012]

Table 3.1: The parameters used to simulate (3.27) in Fig. 3.3. $C_{1/2}$ was calculated from the homeostatic phagocyte production rate and k_p was calculated from the mass-action tumour-immune interaction from Liu et al. [2007]. C_{prod}^{max} was calculated from G-CSF response to infection [Pauksen et al., 1994]. $\eta_{1/2}$ was chosen to ensure a high initial infectivity of viral therapy while $k_{q,s}$ and $\Psi_{1/2}$ were selected to ensure a physiologically realistic tumour doubling time.

sufficiently slow entrance into the active phase of the cell cycle (small a_2) also stabilises the CFE. Fig. 3.4 (b) shows that immune recruitment (k_{cp}) must grow infinitely large to account for less efficient immune-tumour interaction (k_p), while a large death rate during the cell cycle (\hat{d}_g) can ensure stability of the CFE regardless of immune involvement. These investigations confirm the impact of immune recruitment and clearance of tumour cells. This result indicates that increasing immune involvement is important in developing therapeutic strategies.

Finally, Fig. 3.5 shows the relationship between the nonzero equilibrium found in Theorem 3.3.5 and the parameter k_p . The diagram indicates that the CFE gains stability through a transcritical bifurcation as k_p increases. For $k_p > k_p^{crit}$ and initial conditions straddling the unstable equilibrium, we see the dependence of asymptotic behaviour on initial conditions. A similar relationship exists between the stability of the CFE and k_{cp} .

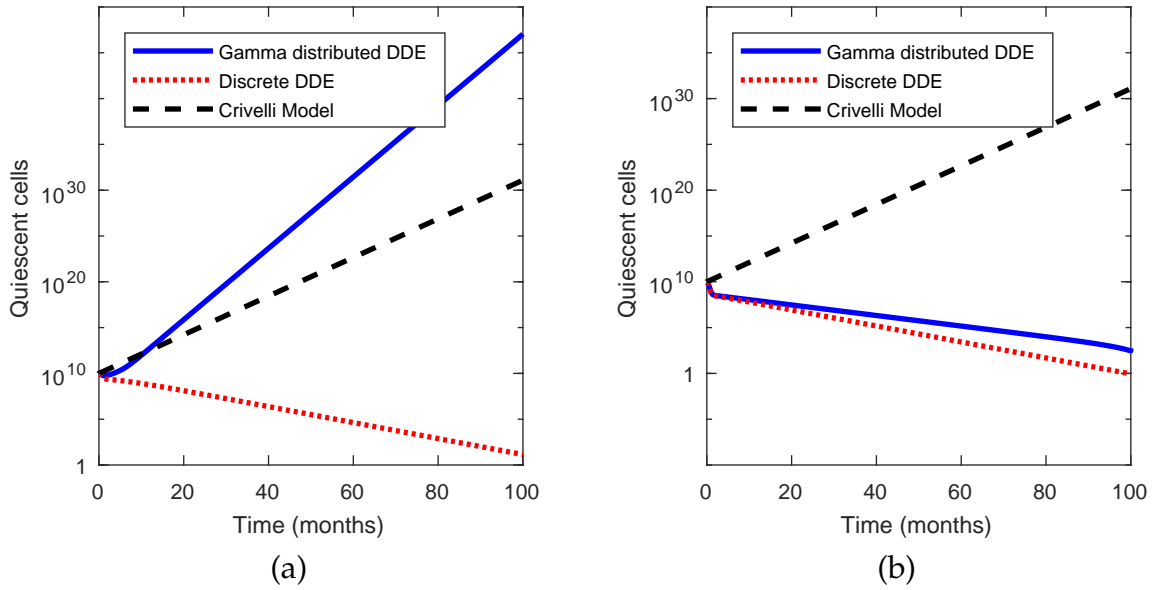


Figure 3.2: A comparison of simulation results for various distributions and immune strengths with $k_{cp} = 2.65$. Figure (a) shows the simulation of (3.1) with a gamma distribution for $j = 6$, a discrete delay, and the Crivelli model from Appendix A. Figure (b) shows the simulation of (3.1) with a gamma distribution for $j = 50$ and the same simulations for the discrete and Crivelli models.

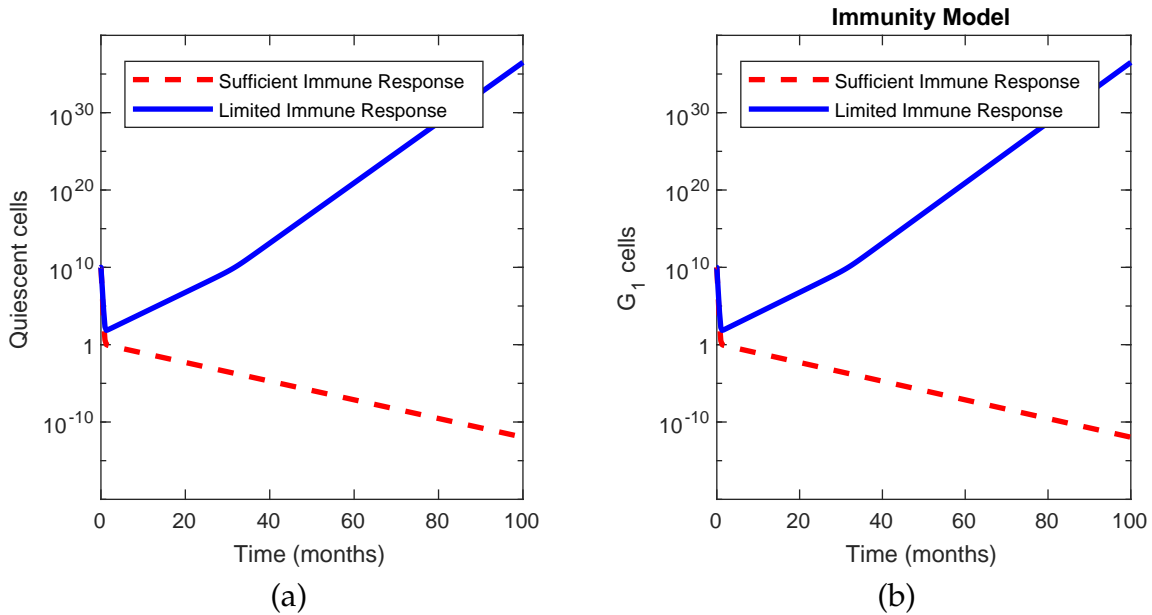


Figure 3.3: Simulated viral therapy with limited and sufficient immune recruitment. The parameters used in sufficient immune recruitment are given in Table 3.1. Limited immune recruitment occurs with $k_{cp} = 1.63$ and other parameters as given in Table 3.1.

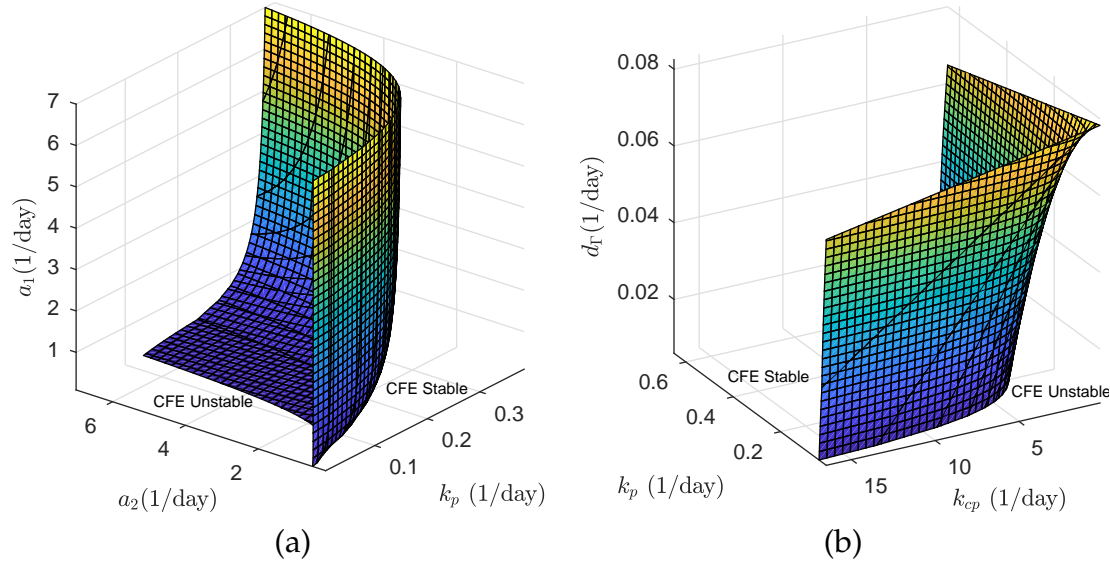


Figure 3.4: Stability regions for the CFE for various parameter combinations. Fig. (a) shows the relationship between the stability of the CFE and the parameters k_p , a_1 and a_2 . Fig. (b) shows the relationship between stability of the CFE and the parameters k_{cp} , k_p and \hat{d}_g .

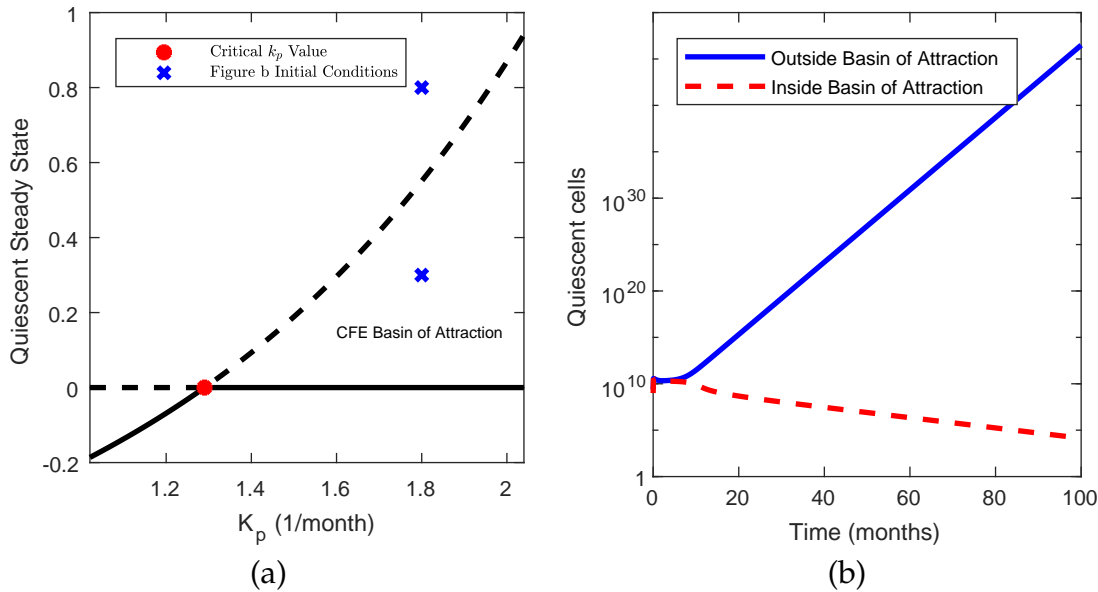


Figure 3.5: The bifurcation diagram showing a transcritical bifurcation. Figure (a) shows the transcritical bifurcation as k_p increases past k_p^{crit} for the quiescent population. The dashed lines represent unstable equilibria and the solid lines denote stable equilibria. Figure (b) the dependence of asymptotic behaviour on initial conditions. The quiescent initial populations used are shown in Figure (a) as crosses.

Biologically, Fig. 3.5 (b) shows that the same immune system can control small tumours while large established tumours grow unboundedly.

3.5 DISCUSSION

Malignant tumours are comprised of an extremely heterogeneous population of malignant cells. Oncolytic viruses combat this heterogeneity by exploiting two common characteristics of malignant cells: weakened antiviral immunity and explosive growth rates. Once an oncolytic virus has infiltrated a tumour, lysis of infected cells and immune recruitment combine to eliminate the tumour. Past models of tumour growth and viral oncology have used discrete DDEs to model the cell cycle duration and infection of susceptible cells. However, discrete DDEs enforce a uniform and constant tumour cell cycle time and do not incorporate any aspect of the inherent heterogeneity of malignant cells inside the tumour microenvironment.

In this work, we produced a mathematical model of tumour cell growth that incorporates the heterogeneity of tumour reproduction speed by modelling cell cycle duration as a random variable following a PDF $K(t)$. This framework is a novel representation of tumour growth and is more physiologically realistic than the discrete delay case. Specifically, variation in tumour cell cycle duration can be seen as a measure of tumour cell heterogeneity. Using linear stability analysis, we established the relationship between the expected number of cells surviving the cell cycle and tumour remission. As we assumed a constant death rate throughout the cell cycle, the expected number of cells surviving the cell cycle is directly related to the distribution of cell cycle durations. The distribution of cell cycle durations and disease progression are explicitly linked in our stability threshold. The stability threshold determines the minimal anti-tumour immune response that ensures that nascent tumours do not persist. This result shows that increasing immune involvement can stabilise the tumour free state regardless of the cancer growth rate.

Our results indicate that lysis of infected cells and increased immune recruitment act synergistically to eliminate tumour cells during viral therapy. Our simulations show that the combination of viral therapy and the resulting immune recruitment function by driving solutions across a separatrix into the basin of attraction of the tumour free equilibrium. If immune recruitment is insufficient to control tumour growth, we predict that viral therapy will drive initial tumour remission that is followed by disease recurrence. Moreover, our results show that viral therapy can act as the external force required to shrink tumours to a size manageable by the immune system, leading to long-term remission. These observations are consistent with clinical results and suggest that oncolytic viruses designed to maximise immune response may have clinical benefits.

Finally, our modelling techniques develop a novel mathematical treatment of tumour cell growth by using a distributed DDE. The distributed DDE considered in this work

incorporates the discrete delay case studied by [Crivelli et al. \[2012\]](#) and others for a suitable choice of $K(t)$ and k_p . In the specific case of a gamma distribution, we derive a novel linear chain technique that incorporates cellular loss throughout the cell cycle. Using this technique, we reduce the infinite dimensional distributed DDE to an equivalent finite dimensional ODE. Our derivation of the equivalent ODE formulation is easily generalisable to physiological processes with exponential growth or decay. The reduction of the distributed DDE to an ODE offers a method whereby models using discrete DDEs can include more physiologically realistic distributed delays without losing the ability to easily simulate the model.

Our modelling framework has certain limitations. The mathematical model greatly simplifies immune recruitment and tumour-immune interactions in favour of an analytically tractable model. The interactions between the legion of cytokines and immune cell types in the tumour micro-environment are not considered in this work, nor have we studied the effect of immune system selection of cancer cells.

This modelling work raises the interesting question of which distribution best models tumour cell cycle durations. Most existing models either use the discrete or gamma distribution to exploit the existing numerical methods to simulate these models. Without data, it is difficult to determine which distribution most accurately models tumour cell cycle durations. Nevertheless, our analytic results are valid for any distribution describing tumour cell cycle durations. In summary, our model incorporates an aspect of tumour cell heterogeneity, makes predictions that are consistent with clinical observations and indicates future avenues of oncolytic virus development.

ACKNOWLEDGEMENTS

TC would like to thank the Natural Sciences and Engineering Research Council of Canada (NSERC) for funding through the Postgraduate Scholarship-Doctoral programme and the Alberta Government for funding through the Sir James Lougheed award of distinction. ARH is grateful to NSERC, Canada for funding through the Discovery Grant programme. Both authors thank Morgan Craig for many helpful discussions.

BIBLIOGRAPHY

Bartlett, D. L., Liu, Z., Sathaiyah, M., Ravindranathan, R., Guo, Z., He, Y., and Guo, Z. S. (2013). Oncolytic viruses as therapeutic cancer vaccines. *Mol. Cancer*, 12(1):103.

- Bell, J. and McFadden, G. (2014). Viruses for tumor therapy. *Cell Host Microbe*, 15(3):260–265.
- Bhatia, A. and Kumar, Y. (2011). Cancer-immune equilibrium: Questions unanswered. *Cancer Microenviron.*, 4(2):209–217.
- Bommareddy, P. K., Patel, A., Hossain, S., and Kaufman, H. L. (2017). Talimogene Laherparepvec (T-VEC) and Other Oncolytic Viruses for the Treatment of Melanoma. *Am. J. Clin. Dermatol.*, 18(1):1–15.
- Bourgeois-Daigneault, M. C., Roy, D. G., Falls, T., Twumasi-Boateng, K., St-Germain, L. E., Marguerie, M., Garcia, V., Selman, M., Jennings, V. A., Pettigrew, J., Amos, S., Diallo, J. S., Nelson, B., and Bell, J. C. (2016). Oncolytic vesicular stomatitis virus expressing interferon-gamma has enhanced therapeutic activity. *Mol. Ther. - Oncolytics*, 3:16001.
- Breitbach, C. J., Lichty, B. D., and Bell, J. C. (2016). Oncolytic viruses: Therapeutics with an identity crisis. *EBioMedicine*, 9:31–36.
- Burns, F. J. and Tannock, J. F. (1970). On the existence of a G₀-phase in the cell cycle. *Cell Tissue Kinet.*, 3(4):321–334.
- Câmara De Souza, D., Craig, M., Cassidy, T., Li, J., Nekka, F., Bélair, J., and Humphries, A. R. (2018). Transit and lifespan in neutrophil production: implications for drug intervention. *J. Pharmacokinet. Pharmacodyn.*, 45(1):59–77.
- Campbell, S. A. and Jessop, R. (2009). Approximating the Stability Region for a Differential Equation with a Distributed Delay. *Math. Model. Nat. Phenom.*, 4(2):1–27.
- Carlson, J. A. (2003). Tumor doubling time of cutaneous melanoma and its metastasis. *Am. J. Dermatopathol.*, 25(4):291–299.
- Cassady, K., Haworth, K., Jackson, J., Markert, J., and Cripe, T. (2016). To infection and beyond: The multi-pronged anti-cancer mechanisms of oncolytic viruses. *Viruses*, 8(2):43.
- Chiocca, E. A. and Rabkin, S. D. (2015). Oncolytic viruses and their application to cancer immunotherapy. *Cancer Immunol. Res.*, 2(4):295–300.
- Colao, I., Pennisi, R., Venuti, A., Nygårdas, M., Heikkilä, O., Hukkanen, V., and Sciortino, M. T. (2017). The ERK-1 function is required for HSV-1-mediated G₁/S progression in HEP-2 cells and contributes to virus growth. *Sci. Rep.*, 7(1):9176.

- Cooke, K. L. and Grossman, Z. (1982). Discrete delay, distributed delay and stability switches. *J. Math. Anal. Appl.*, 86(2):592–627.
- Craig, M., Humphries, A. R., and Mackey, M. C. (2016). A mathematical model of granulopoiesis incorporating the negative feedback dynamics and kinetics of G-CSF/neutrophil binding and internalization. *Bull. Math. Biol.*, 78(12):2304–2357.
- Crivelli, J. J., Földes, J., Kim, P. S., and Wares, J. R. (2012). A mathematical model for cell cycle-specific cancer virotherapy. *J. Biol. Dyn.*, 6(sup1):104–120.
- Diekmann, O., Gyllenberg, M., and Metz, J. A. J. (2018). Finite dimensional state representation of linear and nonlinear delay systems. *J. Dyn. Differ. Equ.*, 30(4):1439–1467.
- Fukuhara, H., Ino, Y., and Todo, T. (2016). Oncolytic virus therapy: A new era of cancer treatment at dawn. *Cancer Sci.*, 107(10):1373–1379.
- Golubev, A. (2016). Applications and implications of the exponentially modified gamma distribution as a model for time variabilities related to cell proliferation and gene expression. *J. Theor. Biol.*, 393:203–217.
- Grivennikov, S. I. and Karin, M. (2011). Inflammatory cytokines in cancer: tumour necrosis factor and interleukin 6 take the stage. *Ann. Rheum. Dis.*, 70(Suppl 1):i104–i108.
- Hale, J. K. and Verduyn Lunel, S. M. (1993). *Introduction to Functional Differential Equations*, vol. 99 of *Applied Mathematical Sciences*. Springer New York, New York, NY.
- Hallam, S., Escorcio-Correia, M., Soper, R., and Schultheiss, A. (2009). Activated macrophages in the tumour microenvironment - dancing to the tune of TLR and NF- κ B. *J. Pathol.*, 219(2):143–152.
- Hillen, T., Enderling, H., and Hahnfeldt, P. (2013). The tumor growth paradox and immune system-mediated selection for cancer stem cells. *Bull. Math. Biol.*, 75(1):161–184.
- Hino, Y., Murakami, S., and Naito, T. (1991). *Functional Differential Equations with Infinite Delay*, vol. 1473 of *Lecture Notes in Mathematics*. Springer Berlin Heidelberg, Berlin, Heidelberg.
- Hoos, A., Britten, C. M., Huber, C., and O'Donnell-Tormey, J. (2011). A methodological framework to enhance the clinical success of cancer immunotherapy. *Nat. Biotechnol.*, 29(10):867–870.

- Hu, S., Dunlavey, M., Guzy, S., and Teuscher, N. (2018). A distributed delay approach for modeling delayed outcomes in pharmacokinetics and pharmacodynamics studies. *J. Pharmacokinet. Pharmacodyn.*, 45(2):1–24.
- Idema, S., Dirven, C. M. F., van Beusechem, V., Carette, J., Planqué, R., Noske, D. P., Lamfers, M. L. M., and Vandertop, W. P. (2010). Objective determination of the oncolytic potency of conditionally-replicating adenoviruses using mathematical modeling. *J. Gene Med.*, 12(7):564–571.
- Imran, M. and Smith, H. L. (2007). The dynamics of bacterial infection, innate immune response, and antibiotic treatment. *Discret. Contin. Dyn. Syst. B*, 8(1):127–143.
- Kim, P. S., Crivelli, J. J., Choi, I., Yun, C., and Wares, J. R. (2015). Quantitative impact of immunomodulation versus oncolysis with cytokine-expressing virus therapeutics. *Math. Biosci. Eng.*, 12(4):841–58.
- Kirschner, D. and Panetta, J. C. (1998). Modeling immunotherapy of the tumor - immune interaction. *J. Math. Biol.*, 37(3):235–252.
- Krzyzanski, W., Wiczling, P., Lowe, P., Pigeolet, E., Fink, M., Berghout, A., and Balsler, S. (2010). Population modeling of filgrastim PK-PD in healthy adults following intravenous and subcutaneous administrations. *J. Clin. Pharmacol.*, 50(S9):101S–112S.
- Lawler, S. E. and Chiocca, E. A. (2015). Oncolytic virus-mediated immunotherapy: A combinatorial approach for cancer treatment. *J. Clin. Oncol.*, 33(25):2812–2814.
- Lichty, B. D., Breitbach, C. J., Stojdl, D. F., and Bell, J. C. (2014). Going viral with cancer immunotherapy. *Nat. Rev. Cancer*, 14(8):559–567.
- Liu, W., Hillen, T., and Freedman, H. I. (2007). A mathematical model for M-phase specific chemotherapy including the G0-phase and immunoresponse. *Math. Biosci. Eng.*, 4(2):239–59.
- MacNamara, C. and Eftimie, R. (2015). Memory versus effector immune responses in oncolytic virotherapies. *J. Theor. Biol.*, 377:1–9.
- Mahasa, K. J., Eladdadi, A., de Pillis, L., and Ouifki, R. (2017). Oncolytic potency and reduced virus tumor- specificity in oncolytic virotherapy. A mathematical modelling approach. *PLoS One*, 12(9):1–25.
- Malinzi, J., Eladdadi, A., and Sibanda, P. (2017). Modelling the spatiotemporal dynamics of chemovirotherapy cancer treatment. *J. Biol. Dyn.*, 11:244–274.

- Mittal, D., Gubin, M. M., Schreiber, R. D., and Smyth, M. J. (2014). New insights into cancer immunoediting and its three component phases-elimination, equilibrium and escape. *Curr. Opin. Immunol.*, 27:16–25.
- Mosser, D. M. (2003). The many faces of macrophage activation. *J. Leukoc. Biol.*, 73(2):209–212.
- Pauksen, K., Elfman, L., Ulfgren, A., and Venge, P. (1994). Serum levels of granulocyte-colony stimulating factor (G-CSF) in bacterial and viral infections, and in atypical pneumonia. *Br J Haematol*, 88(2):256–260.
- Piscitelli, S., Reiss, W., Figg, W., and Petros, W. (1997). Pharmacokinetic studies with recombinant cytokines. Scientific issues and practical considerations. *Clin. Pharmacokinet.*, 32(5):368–81.
- Rehman, H., Silk, A. W., Kane, M. P., and Kaufman, H. L. (2016). Into the clinic: Talimogene laherparepvec (T-VEC), a first-in-class intratumoral oncolytic viral therapy. *J. Immunother. Cancer*, 4:1–8.
- Santiago, D. N., Heidbuechel, J. P. W., Kandell, W. M., Walker, R., Djeu, J., Engeland, C. E., Abate-Daga, D., and Enderling, H. (2017). Fighting cancer with mathematics and viruses. *Viruses*, 9(9):1–26.
- Schirm, S., Ahnert, P., Wienhold, S., Mueller-Redetzky, H., Nouailles-Kursar, G., Loeffler, M., Witzenrath, M., and Scholz, M. (2016). A biomathematical model of pneumococcal lung infection and antibiotic treatment in mice. *PLoS One*, 11(5):1–22.
- Schwartz, M. (1961). A biomathematical approach to clinical tumor growth. *Cancer*, 14(6):1272–1294.
- Smith, H. (2011). *An Introduction to Delay Differential Equations with Applications to the Life Sciences*. Springer, New York, New York, USA.
- Swann, J. B. and Smyth, M. J. (2007). Immune surveillance of tumors. *J. Clin. Invest.*, 117(5):1137–1146.
- Villasana, M. and Radunskaya, A. (2003). A delay differential equation model for tumor growth. *J. Math. Biol.*, 47(3):270–294.
- Vogel, T. (1961). Systèmes Déferlants, Systèmes Héritaires, Systèmes Dynamiques. In *Proc. Int. Symp. Nonlinear Vib.*, pages 123–130, Kiev. Academy of Sciences USSR.

Walker, R. and Enderling, H. (2016). From concept to clinic: Mathematically informed immunotherapy. *Curr. Probl. Cancer*, 40(1):68–83.

Wodarz, D. (2016). Computational modeling approaches to the dynamics of oncolytic viruses. *Wiley Interdiscip. Rev. Syst. Biol. Med.*, 8(3):242–252.

Yates, C. A., Ford, M. J., and Mort, R. L. (2017). A Multi-stage Representation of Cell Proliferation as a Markov Process. *Bull. Math. Biol.*, 79(12):2905–2928.

A REDUCTION TO THE CRIVELLI MODEL AND THE DISCRETE DELAY CASE

We show that the Crivelli model [Crivelli et al., 2012] is a special case of the general distributed DDE model (3.1) developed in Section 3.2 without immune recruitment. We do this two ways: first by showing that the discrete DDE model corresponds to the distributed DDE model with a degenerate distribution, then alternatively by showing that the discrete DDE model can be recovered from the distributed DDE model in a suitable limit when $K(t)$ is taken to be a Gamma distribution.

Crivelli et al. [2012] do not consider tumour-immune involvement, so we take $k_p = 0$ in (3.1). Then, the immune recruitment has no impact on the tumour model, so we drop the differential equations for $P(t)$ and $C(t)$. Crivelli et al. [2012] use a discrete DDE to model the cell cycle duration. The simplest way to recover a discrete DDE from a distributed DDE is to let $K(t) = \delta(t - \tau)$. Then, (3.7) gives $d_\delta = d_3$. Thus the model (3.1) becomes

$$\left. \begin{aligned} \frac{d}{dt}Q(t) &= 2 \exp[-d_3\tau] a_2 G_1(t - \tau) \delta_\tau(t - \sigma) - a_1 Q(t) - d_1 Q(t) \\ \frac{d}{dt}G_1(t) &= a_1 Q(t) - a_2 G_1(t) - d_2 G_1(t) - \eta(U(t)) G_1(t) \\ \frac{d}{dt}I(t) &= -\delta I(t) + \eta(U(t)) [G_1(t) + \int_0^\tau G_1(\sigma) \exp[-d_3\sigma] d\sigma] \\ \frac{d}{dt}V(t) &= \alpha I(t) - \omega V(t) - \eta(U(t)) [G_1(t) + \int_0^\tau a_2 G_1(\sigma) \exp[-d_3\sigma] d\sigma]. \end{aligned} \right\} \quad (37)$$

Finally, evaluating (3.2) with $K(t) = \delta(t - \tau)$ gives

$$\begin{aligned} N(t) &= \int_0^\infty a_2 G_1(t - \xi) \exp \left[- \int_{t-\xi}^t \hat{d}_K + \psi_G(U(x)) + \eta(U(x)) dx \right] \left(1 - \int_0^\xi \delta(\sigma - \tau) d\sigma \right) d\xi \\ &= \int_0^\tau a_2 G_1(t - \xi) \exp \left[- \int_{t-\xi}^t \hat{d}_K + \psi_G(U(x)) + \eta(U(x)) dx \right] d\xi, \end{aligned}$$

and taking $\eta(U(t))$ to be the non-differentiable contact rate

$$\eta(U(t)) = \kappa \frac{V(t)}{V(t) + I(t) + G_1(t) + N(t) + Q(t)},$$

returns the mathematical model in Crivelli et al. [2012]. To illustrate that their results are a special case of ours, we use Theorem 3.3.3 to determine the stability of the CFE for the Crivelli model. With $k_p = 0$ and $K(t) = \delta(t - \tau)$, it is simple to calculate that $\Psi_{G_1} = 0$ and

$$\mathcal{L}[\delta(t - \tau)](d_3) = e^{-d_3\tau}.$$

Then the stability condition (3.22) becomes

$$2a_1 a_2 e^{-d_3\tau} - (a_1 + d_1)(a_2 + d_2) < 0, \quad (38)$$

which is exactly the same as found by [Crivelli et al. \[2012\]](#).

We have shown that discrete DDEs can be modelled as degenerate distributed DDEs. Next, we show a distinct method of reducing the general distributed DDE to a discrete DDE by considering a gamma distributed DDE, i.e. $K(t) = g_{k_{tr}}^j(t)$, in the limit as $j \rightarrow \infty$. We parameterise the gamma distribution by choosing $j \in \mathbb{N}$ and setting $a_j = \tau/j$. Then, for each integer j , the expected duration of the cell cycle is τ . Moreover, the standard deviation is given by $s_j^2 = \tau^2/j$ with

$$\lim_{j \rightarrow \infty} s_j^2 = 0.$$

Heuristically, as j increases, $g_a^j(t)$ becomes increasingly concentrated about the expected value, τ . Formally, the characteristic function of the gamma distribution converges in distribution to the characteristic function of the $\delta(t - \tau)$ distribution with

$$\int_0^\infty y(t - \sigma) g_{j/\tau}^j(\sigma) d\sigma \rightarrow y(t - \tau) \quad \text{as } j \rightarrow \infty$$

for any test function $y(t)$. From equation (3.26), \hat{d}_g is dependent on the parameter j via

$$\hat{d}_g^j = \frac{j}{\tau} \left[(e^{d_3 \tau})^{1/j+1} - 1 \right].$$

To compute the limit of \hat{d}_g^j as $j \rightarrow \infty$, we first note that

$$\lim_{n \rightarrow \infty} n(a^{1/n} - 1) = \lim_{n \rightarrow \infty} \frac{a^{1/n} - 1}{1/n} = \frac{d}{dt} a^t \Big|_{t=0} = \ln(a). \quad (39)$$

Therefore,

$$\lim_{j \rightarrow \infty} \hat{d}_g^j = \lim_{j \rightarrow \infty} \frac{j}{\tau} \left[(e^{d_3 \tau})^{1/j+1} - 1 \right] = \frac{1}{\tau} \ln(e^{d_3 \tau}) = d_3,$$

so \hat{d}_g^j converges to the death rate of the discrete DDE as $j \rightarrow \infty$.

Finally, we compute the linearisation matrix for the linearised DDE (3.17) with $K(t) = g_a^j(t)$:

$$\mathbb{A} + \mathcal{L}[\Gamma](\lambda + \hat{d}_\Gamma^j + k_p P^*) \mathbb{B} = \begin{bmatrix} -(a_1 + d_1 + k_p P^*) & 2a_2 \frac{a^j}{(a + \lambda + \hat{d}_\Gamma^j + k_p P^*)^j} & 0 & 0 & 0 & 0 \\ a_1 & -(a_2 + d_2 + k_p P^*) & 0 & 0 & 0 & 0 \\ 0 & 0 & -\gamma & 0 & 0 & 0 \\ 0 & 0 & \alpha & -\omega & 0 & 0 \\ \xi k_p P^* & \xi k_p P^* & \xi \delta & 0 & -k_{elim} & 0 \\ 0 & 0 & 0 & 0 & \frac{k_{cp} C_{1/2}}{(C_{1/2} + C^*)^2} & -\gamma_p \end{bmatrix}$$

and the corresponding characteristic function, once again using (3.19),

$$q(\lambda) = \rho(\lambda) \left[2a_1a_2 \frac{a^j}{(a + \lambda + \hat{d}_g + k_p P^*)^j} - (a_1 + d_1 + k_p P^* + \lambda)(a_2 + d_2 + k_p P^* + \lambda) \right].$$

Using Theorem 3.3.3, the condition for stability of the CFE is

$$2a_1a_2 \frac{a^j}{(a + \hat{d}_g + k_p P^*)^j} - (a_1 + d_1 + k_p P^*)(a_2 + d_2 + k_p P^*) < 0. \quad (40)$$

Using $a = j/\tau$, we rearrange this condition to find a cell cycle duration, τ_j , that ensures local stability of the CFE

$$\tau_j > \frac{j}{\hat{d}_g^j + k_p P^*} \left[\left(\frac{2a_1a_2}{(a_1 + d_1 + k_p P^*)(a_2 + d_2 + k_p P^*)} \right)^{1/j} - 1 \right].$$

Then, the minimal cell cycle duration for stability, τ_j^* , is given by

$$\tau_j^* = \frac{j}{\hat{d}_g^j + k_p P^*} \left[\left(\frac{2a_1a_2}{(a_1 + d_1 + k_p P^*)(a_2 + d_2 + k_p P^*)} \right)^{1/j} - 1 \right]$$

and is dependent on the parameter j . Once again, using equation (39), we see that

$$\begin{aligned} \lim_{j \rightarrow \infty} \tau_j^* &= \lim_{j \rightarrow \infty} \frac{j}{\hat{d}_g^j + k_p P^*} \left[\left(\frac{2a_1a_2}{(a_1 + d_1 + k_p P^*)(a_2 + d_2 + k_p P^*)} \right)^{1/j} - 1 \right] \\ &= \frac{1}{\hat{d}_g + k_p P^*} \left[\ln \left(\frac{2a_1a_2}{(a_1 + d_1 + k_p P^*)(a_2 + d_2 + k_p P^*)} \right) \right]. \end{aligned}$$

Thus the critical cell cycle duration when $K(t) = g_a^j(t)$ converges to the critical cell cycle duration time in discrete delay case. Moreover, when $k_p = 0$, τ_j^* converges to the critical delay time found by Crivelli et al. [2012].

Consequently, the discrete DDE model considered by Crivelli et al. [2012] can be considered a degenerate case of the distributed DDE or as a limit of a gamma type distributions.

B NUMBER OF CELLS IN THE CELL CYCLE

Here, we detail the calculation of the number of cells in the active portion of the cell cycle at time t . Fix $\xi > 0$, so the number of cells entering the active portion of the cell cycle at time $t - \xi$ is $a_2 G_1(t - \xi)$.

Then, at time t , the probability that a cell that entered the active portion of the cell cycle at time $t - \xi$ has not completed the cell cycle is

$$\int_{\xi}^{\infty} K(\sigma) d\sigma = 1 - \int_0^{\xi} K(\sigma) d\sigma.$$

Of the cells that have not exited the active portion of the cell cycle, the fraction that have not died by time t is

$$a_2 G_1(t - \xi) \exp \left[- \int_{t-\xi}^t \hat{d}_K + \psi_G(U(x)) + \eta(U(x)) dx \right].$$

Integrating over all previous times ξ gives the total number of cells remaining in the cell cycle. Consequently, the number of cells in the cell cycle at time t is

$$N(t) = \int_0^{\infty} a_2 G_1(t - \xi) \exp \left[- \int_{t-\xi}^t \hat{d}_K + \psi_G(U(x)) + \eta(U(x)) dx \right] \left(1 - \int_0^{\xi} K(\sigma) d\sigma \right) d\xi. \quad (41)$$

By making the change of variable $\nu = t - \xi$, we have the alternative form

$$N(t) = \int_{-\infty}^t a_2 G_1(\nu) \exp \left[- \int_{\nu}^t \hat{d}_K + \psi_G(U(x)) + \eta(U(x)) dx \right] \left(1 - \int_0^{t-\nu} K(\sigma) d\sigma \right) d\nu. \quad (42)$$

Equation (42) is difficult to evaluate numerically. However, differentiating $N(t)$ by using the Leibniz and product rules, we find the distributed DDE for $N(t)$

$$\begin{aligned} \frac{d}{dt} N(t) &= a_2 G_1(t) - \left[\hat{d}_K + \psi_G(U(t)) + \eta(U(t)) \right] N(t) \\ &\quad - \int_0^{\infty} a_2 G_1(t - \xi) \exp \left[- \int_{t-\xi}^t \hat{d}_K + \psi_G(U(x)) + \eta(U(x)) dx \right] K(\xi) d\xi \end{aligned} \quad (43)$$

which can be solved numerically. As we have shown in Proposition 3.4.1, we can replace the distributed DDE (43) with the solution of the transit compartment ODE defined in (3.29) when $K(\sigma) = g_a^j(\sigma)$. Therefore, in our simulations of equation (3.27), we calculate $N(t)$ by solving

$$\frac{d}{dt} N(t) = a_2 G_1(t) - \left[\hat{d}_K + \psi_G(U(t)) + \eta(U(t)) \right] N(t) - \frac{k_{tr}}{a_2} A_j(t), \quad (44)$$

subject to the initial condition from evaluating (41) at $t = 0$ by using the lower incomplete gamma function.

DETERMINANTS OF COMBINATION GM-CSF IMMUNOTHERAPY
AND ONCOLYTIC VIROTHERAPY SUCCESS IDENTIFIED THROUGH
IN SILICO TREATMENT PERSONALIZATION

In this chapter, we combine the theoretical basis developed in Chapter 2 and the practical application to tumour heterogeneity in oncolytic viral therapy in Chapter 3 to develop an *in silico* clinical trial platform. By exploiting the equivalence between the physiologically realistic distributed DDE and the numerically tractable ODE formulation, we systematically explore possible treatment schedules. This chapter demonstrates that distributed DDEs can be applied to address important questions in therapeutic development.

We adapt the mathematical model developed in the previous chapter to include a lineage of immune-resistant cells and use the resulting model to study possible combinations of oncolytic viral therapy and GM-CSF immunotherapy. We begin by parametrizing our mathematical model to experimental data before generating a cohort of 300 virtual patients. By simulating the treatment protocols of the OPTiM clinical trial, we show that our mathematical model can replicate the trial results. We then create optimal and individualized combination treatment protocols for each of the virtual patients. By studying these optimal protocols, we infer a “maintenance” type therapy. Through a second *in silico* clinical trial, we show that this maintenance type therapy outperforms naive combination scheduling in both treatment burden and predicted survival.

Determinants of combination GM-CSF immunotherapy and oncolytic virotherapy success identified through *in silico* treatment personalization

Tyler Cassidy¹ and Morgan Craig^{2,3}

¹ Department of Mathematics and Statistics, McGill University

² Département de mathématiques et de statistique, Université de Montréal

³ Department of Physiology, McGill University,

March 21st, 2019

ABSTRACT

Oncolytic virotherapies, including the modified herpes simplex virus talimogene laherparepvec (T-VEC), have shown great promise as potent instigators of anti-tumour immune effects. The OPTiM trial, in particular, demonstrated the superior anti-cancer effects of T-VEC as compared to more traditional immunotherapy treatment using exogenous administration of granulocyte-macrophage colony-stimulating factor (GM-CSF). Theoretically, a combined approach leveraging exogenous cytokine immunotherapy and oncolytic virotherapy would elicit an even greater immune response and improve patient outcomes. However, regimen scheduling of combination GM-CSF and T-VEC therapy has yet to be established. Here, we calibrate a computational biology model of sensitive and resistant tumour cells and immune interactions for implementation into an *in silico* clinical trial to test and individualize combination immuno- and virotherapy. By personalizing and optimizing combination oncolytic virotherapy and GM-CSF therapy, we show improved simulated patient outcomes for individuals with late-stage melanoma. More crucially,

through evaluation of individualized regimens, we identified determinants of combination GM-CSF and T-VEC therapy that can be translated into clinically-actionable dosing strategies without further personalization. Our results serve as a proof-of-concept for interdisciplinary approaches to determining combination therapy, and suggest promising avenues of investigation towards tailored combination immunotherapy/oncolytic virotherapy.

AUTHOR SUMMARY

The advent of biological therapies for anti-cancer treatment has had a significant impact on patient outcomes. Targeted xenobiotics, including oncolytic viruses, in combination with existing, more general, immunotherapies like exogenous cytokines show great promise for continuing to improve cancer care. However, determining optimal combination regimens can be difficult, given that testing proposed schedules would require large cohorts of patients enrolled in clinical trials. Fortunately, computational biology can help to address treatment scheduling while simultaneously helping to unravel the mechanisms driving therapeutic responses. In this work, we integrate a mathematical model of GM-CSF and talimogene laherparepvec (T-VEC) oncolytic virotherapy into a virtual clinical trial to optimize their administration in combination. Using this platform, we inferred a clinically-actionable combination schedule for patients with late-stage melanoma that significantly improved virtual patient outcome when compared to GM-CSF and T-VEC monotherapies, and a standard combination strategy. Our results outline a rational approach to therapy optimization with meaningful consequences for how we effectively design and implement clinical trials to maximize their success, and how we treat melanoma with combined immuno- and virotherapy.

INTRODUCTION

Modern cancer treatments increasingly incorporate a broad class of biological therapies known as immunotherapies to activate the immune system against cancer cells in a generalized or targeted way [Mellman et al., 2011; Russell et al., 2012]. These therapies seek to exploit existing tumour-immune interactions to more effectively recognize and destroy tumour cells with the goal of minimizing off-target and detrimental side effects. Current and investigational immunotherapies include immune-checkpoint inhibitors, monoclonal antibodies, CAR-T cells, and the exogenous administration of cytokines. One such cytokine, granulocyte-macrophage colony-stimulating factor (GM-CSF), is a white blood cell growth factor responsible for stimulating granulocyte production, and

orchestrating innate inflammatory responses. GM-CSF has been used to increase the efficacy of monoclonal antibodies, and has also been administered during B-cell lymphoma treatment to activate certain immune cell subsets [Mellman et al., 2011].

Another older idea, recently adopted in clinical applications, is to use oncolytic viruses to destroy tumour cells [Fukuhara et al., 2016; Hoster et al., 1949] and activate an immune response. Oncolytic viruses are genetically engineered to preferentially attack and infect cancerous cells [Cassady et al., 2016; Chiocca and Rabkin, 2015], forcing infected cells to undergo lysis and release tumour specific antigens that signal the immune system to mount an anti-tumour response [Breitbach et al., 2016; Marelli et al., 2018]. This double effect against tumour cells has propelled the study of oncolytic viruses as a treatment against a variety of malignant solid tumours. In 2015, the modified herpes simplex virus talimogene laherparepvec (T-VEC) was the first oncolytic virus to be approved by the Food and Drug Administration in the United States for use in patients with non-resectable melanoma [Andtbacka et al., 2015; Bommareddy et al., 2017; Rehman et al., 2016]. T-VEC is specifically engineered to enhance expression of GM-CSF after viral infection of tumour cells [Andtbacka et al., 2015]. However, despite much promise, the efficacy of oncolytic virus monotherapy has been limited [Chesney et al., 2018; Marelli et al., 2018; Mostafa et al., 2018]. As it is reasonable to expect that immunotherapy and virotherapy could act synergistically to instigate an immune response against tumour cells [Bell and McFadden, 2014; Guo and Bartlett, 2014; Lawler and Chiocca, 2015], recent efforts have focused on determining the anticipated benefit to their use in combination with a variety of immunotherapies [Chaurasiya et al., 2018; Martin and Bell, 2018]. To that end, GM-CSF has been considered as an immune stimulant during oncolytic virotherapy [Mellman et al., 2011].

Combination therapy can carry a high therapy burden and may increase overall toxicity [Chesney et al., 2018; Martin and Bell, 2018]. Unfortunately, running clinical trials for all possible (dose,time)-pairs of a proposed combined treatment to determine efficient and safe scheduling is both time and cost prohibitive. As a consequence, regimen scheduling of combination immuno-/oncolytic virotherapy remains an open problem. There is an established history of applications of modelling-based, computational biology approaches to the *in silico* determination of potential therapeutic schedules that concretely improve patient outcomes [Agur, 2010; Allen et al., 2016; Love et al., 2017; Schmidt et al., 2013]. In a closely related recent paper, an *in silico* clinical trial approach to anti-CTLA-4 and anti-PD-L1 scheduling in breast cancer demonstrated how systems pharmacology can be leveraged for therapy individualization, subsequently increasing our understanding of the optimization of combination immunotherapy treatment [Wang et al., 2019]. Similarly,

by employing a straight-forward evolutionary game theory model to determine adaptive treatment schedules, Zhang et al. [Zhang et al., 2017] report significant improvements to prostate specific antigen in comparison to the standard-of-care in an on-going phase I clinical trial. These and other [Gatenby et al., 2009] successes motivate the continued application of interdisciplinary approaches in personalized oncology. Perhaps the most significant impact made by quantitative methodologies is the identification and translation of the underlying determinants of treatment success into actionable therapeutic strategies [Bentele et al., 2004; Craig et al., 2016].

To that end, here we detail the rationalization of combination immuno-/virotherapy scheduling for patients with late-stage melanoma by implementing an *in silico* clinical trial. By integrating our previous computational biology model of sensitive and resistant tumour cells and their interactions with the immune system into our virtual trial platform, we generated identical virtual patient cohorts to determine optimal, individualized treatment regimens for combined GM-CSF immunotherapy and T-VEC. We used the results of the personalization to infer a logical and clinically-actionable dosing scheme that significantly improved overall survival and progression free survival while substantially reducing drug burden. Crucially, we identified key mechanisms that determine therapy success, which allowed us to define a successful regimen in a new cohort of virtual patients. Our results highlight the potential and potency of rational regimen prediction using a computational biology approach, and serve as a proof-of-concept for future quantitative studies in oncology.

METHODS

Computational biology model

To establish the synergistic interactions elicited between immunotherapy (exogenous GM-CSF) and oncolytic virotherapy, we adapted our previous mathematical model [Cassidy and Humphries, 2019] describing the instantaneous change in tumour size, phagocyte numbers and cytokine concentrations over time. The model tracks both immuno-susceptible and immuno-resistant tumour cell populations as they progress through the cell cycle. Quiescent immuno-susceptible tumour cells can be cleared through either random death or immune pressure, or transit into the G_1 phase to begin reproduction. Cells in G_1 are also subject to random death and immune clearance before beginning the mitotic process. After completing division, susceptible cells return to quiescence. Mitotic cells may mutate at rate μ into an immuno-resistant cell type with a low probability. This immuno-resistant lineage maintains the same cell cycle behaviour of non-resistant tumour cells, but evades immune

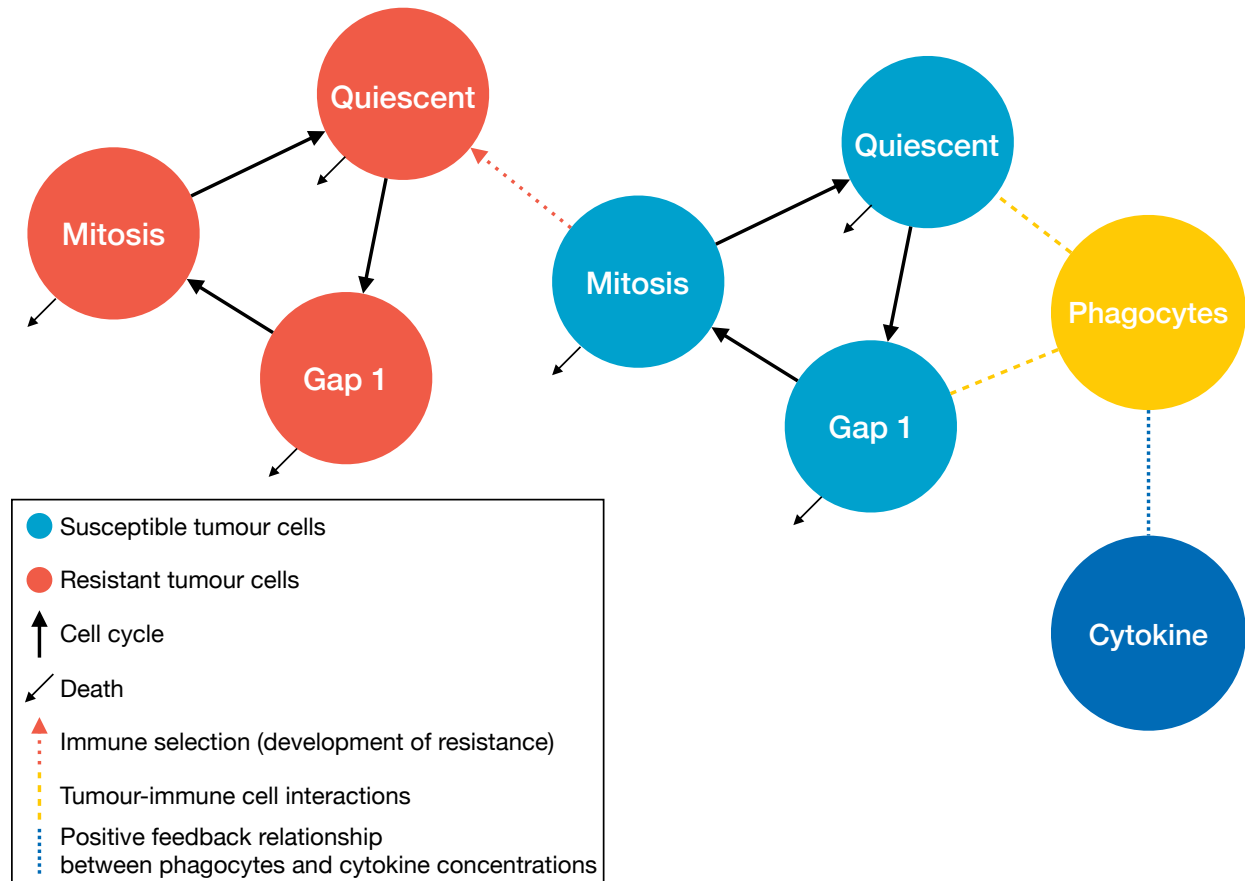


Figure 4.1: **Pictorial representation of the tumour growth model.** Quiescent cells activate to begin division by transiting into the G_1 phase of the cell-cycle. Cells exit G_1 to enter the active phase and complete division. Most susceptible cells in the active phase re-enter quiescence after mitosis, however certain dividing cells may mutate into an immunoresistant lineage (red dotted arrow). Immune interactions are driven by phagocytes who come into contact with quiescent and G_1 phase susceptible cells (dashed yellow lines). Tumour-immune interactions increase pro-inflammatory cytokine concentrations to recruit additional phagocytes to the tumour site (blue dotted line). Cells and cytokine are denoted by circles, processes by squares, and rates by arrows.

pressure and is therefore not subject to any immune interactions. We do not distinguish between different types of immune cells in the tumour microenvironment, but rather model all phagocytes as a single population. These immune cells interact with the susceptible tumour cell population and produce a pro-inflammatory cytokine (e.g. interleukin-12, tumour necrosis factor, interferon gamma, GM-CSF etc.) to recruit other phagocytes to the tumour site. Model predictions are obtained as previously described [Cassidy and Humphries, 2019] (full details are provided in the Supplementary Information). The various interactions described above are schematized in Fig. 4.1.

Generation of in silico individuals and patient cohorts

To calibrate the model of Cassidy and Humphries [Cassidy and Humphries, 2019] to available data, we adopted a sequential fitting procedure to parameterize the mathematical model. Briefly, we used time series data from a number of experimental settings to estimate the different model parameter values. We began by determining the parameters of the delay kernel using data from a cervical cancer cell line [Sato et al., 2016], before fitting the remaining parameters in a sequential manner. First, data from tumour growth in immuno-compromised mice was used to fit the tumour growth parameters a_1 , a_2 , and d_2 [Dingli et al., 2009]. Next, we fit the viral parameters κ , $\eta_{1/2}$, ω , δ , α using a combination of *in vitro* data from Toda et al. and Randazzo et al. [Randazzo et al., 1997; Toda et al., 2000]. Finally, we used data from GM-CSF concentrations following administration of a T-VEC precursor in mice to fit the parameters for the cytokine compartment. In each case, we reduced the mathematical model to replicate the experimental set up, and minimized the least-squares error between simulations and experimental data (for extended details, see the Supplementary Information).

To reflect the interindividual variability and heterogenous nature of patient cohorts, we individualized the model by generating a unique set of parameters to represent single patients. To create individuals in the *in silico* clinical trial, we sampled each of the model's parameters from a generated normal distribution with mean $\hat{\mu}$ determined in the sequential fitting procedure. We then defined \mathbf{p} to be the vector of fitted parameter values [Cassidy and Humphries, 2019] and parametrized the normal distributions so that 99.7% of patients fall within $[\mu - 3\sigma, \mu + 3\sigma] = [0.5\mathbf{p}, 1.5\mathbf{p}]$. If empirical information about a parameter's distribution was available, this measurement was used in lieu of the previously described procedure. Each individual is then created by sampling each model parameter from this distribution. We confirmed that using this methodology created virtual patients with parameter values following an approximately normal distribution about the mean empirical or fitted value, as shown in Fig. 4.2. The distribution of parameters approximates the empirical distribution used to define the virtual population, indicating that this virtual patient generation procedure produces a representative sample of the possible virtual population (and not multiples of the same individual).

To further protect against the creation of nonrealistic virtual patients, we imposed selection and inclusion criteria on each generated individual by verifying that each virtual patient responds in a physiologically-realistic way without and with treatment [Allen et al., 2016]. Specifically, we compared the predicted response of each virtual patient to currently approved oncolytic virotherapy for stage IIIb or IV non-surgically resectable melanoma [Andtbacka et al., 2015; Marelli et al., 2018]. Moreover, we assessed whether

the predicted tumour doubling time of each individual corresponded to clinically relevant tumour doubling times [Carlson, 2003], and used this comparison as the sole inclusion criterion for subsequent enrolment *in silico* clinical trial simulations. To ensure that we were sampling from the entirety of the physiologically realistic portion of parameter space [Allen et al., 2016], we performed a local sensitivity analysis to determine the impact of parameter variation on model output (see the Supplementary Information).

We accepted a total of 300 virtual patients, generated by the parameter sampling and selection processes outlined above. Each virtual patient was then reproduced into n identical clones, and each resulting clone was subsequently assigned to one of n separate cohorts (for example, a treatment free control group, a mono-immunotherapy group, and an oncolytic virotherapy group, for a total of $n = 3$ cohorts). In this way, the total number of participants is 300 times the total number of simulated investigational arms, or $300n$. The *in silico* trial generation process is schematized in Fig. 4.2. As cohorts are identical, we are able to establish a causal relationship between changes in treatment strategy and increased survival time.

Recapitulation of previous trial data

Using three identical cohorts, we evaluated patient outcomes when they received no treatment (Cohort 1), immunotherapy (Cohort 2), or oncolytic virus monotherapy (Cohort 3) to mimic the T-VEC OPTiM trial, where individuals were randomized to receive either intralesional T-VEC or subcutaneous GM-CSF [Andtbacka et al., 2015].

In both the *in silico* immunotherapy and oncolytic virus monotherapy cases, the dosing schedules were identical to the ones used in OPTiM [Andtbacka et al., 2015]: patients in the T-VEC arm received a priming dose of 10^6 plaque forming units pfu/mL, followed by 10^8 pfu/mL doses to a maximal total administration of 4 mL per treatment. T-VEC was administered every 14 days. Patients in the GM-CSF arm received $125 \mu\text{g}/\text{m}^2$ of subcutaneous GM-CSF administered on 14 consecutive days followed by 14 days of no treatment. In both arms, treatment continued for up to 12 months but could be discontinued due to disease progression, intolerability, or the disappearance of injectable lesions. The median treatment length for the T-VEC and GM-CSF arms were 23 and 10 weeks respectively.

We fixed an oncolytic virotherapy dose of 250×10^6 virions – corresponding to roughly 1×10^6 pfu [Klasse, 2015]– as the amount of virus administered the original trial varied based on both patients and physicians [Andtbacka et al., 2015]. Note that the units between the OPTiM trial [Andtbacka et al., 2015] and our *in silico* trial differ owing only to the units of the mathematical model’s parameters and the conversion of pfu to infectious virions. Individuals receiving GM-CSF immunotherapy in the *in silico* trial were administered 125

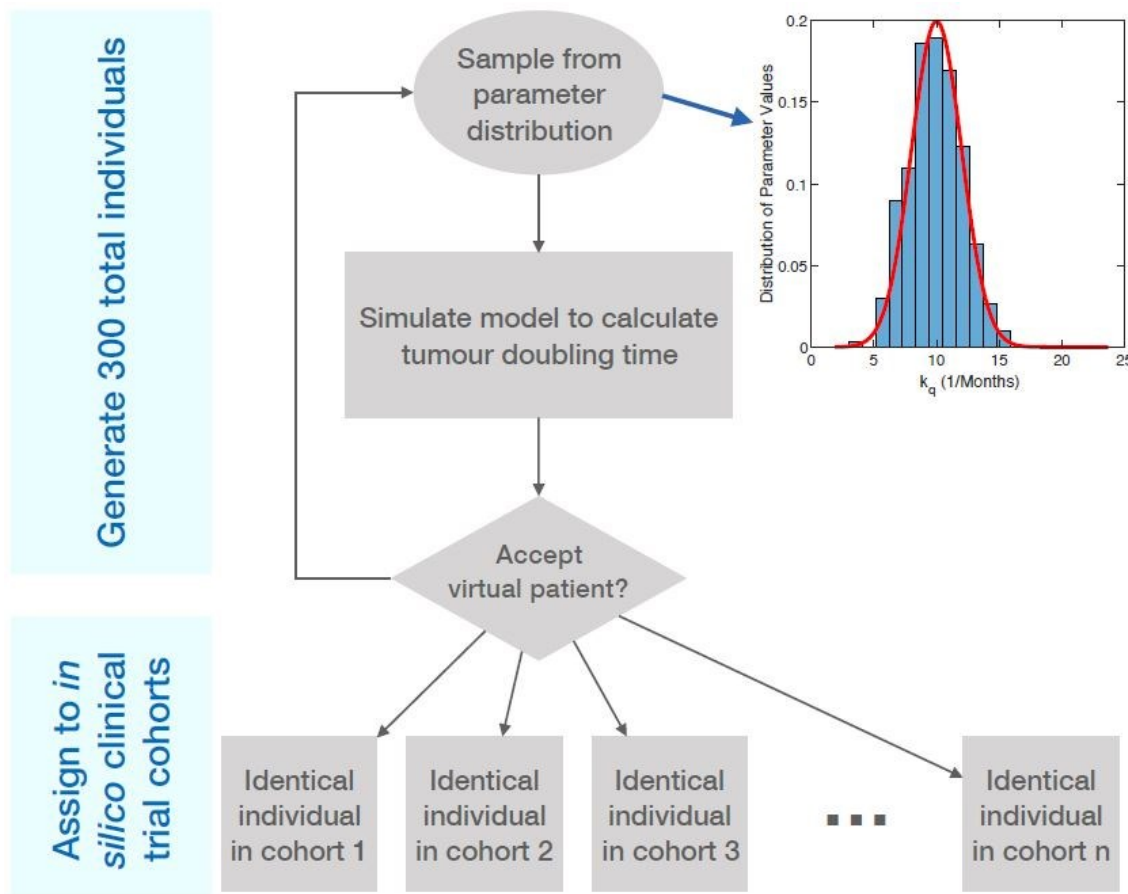


Figure 4.2: **Schematic representation of the *in silico* patient creation algorithm.** Individual *in silico* patient parameter values are sampled from a normal distribution of values based on an average parameterization [Cassidy and Humphries, 2019]. The model was then simulated for each individual and tumour growth predictions (tumour doubling time) were tested for physiological relevance. If the *in silico* patient’s tumour growth behaviour was considered physiologically realistic, they were cloned n times and each clone was assigned to n separate arms of the *in silico* clinical trial.

$\mu\text{g}/\text{m}^2$ of GM-CSF daily for 14 days in 28 day cycles. For both arms, we simulated the model over a fixed treatment time of 6 months.

Late stage melanoma has a low survival rate [Stadler et al., 2006]. Mortality as a function of tumour doublings has been estimated to occur between 40 and 45 tumour doublings [Carlson, 2003; Collins et al., 1956; Schwartz, 1961]. Given that roughly 30 doublings occur before clinical presentation [Schwartz, 1961], we estimated that there are approximately 10 and 15 tumour doublings between diagnosis and death. *In silico* patients were therefore removed from the simulated trial after their predicted tumour size reached 2^λ , where λ denotes the removal number of tumour doublings for each individual. For

each individual, λ was obtained by sampling uniformly from $[10, 15]$, or the set of possible tumour doubling values between diagnosis and death. The incorporation of different disease stages within the OPTiM cohorts in our population approach is discussed in further detail in the Supplementary Information.

Optimization routine for combined immuno- and oncolytic virotherapies

Adverse effects reported in the OPTiM trial including fatigue, chills and other flu like symptoms. Grade 3 adverse effects occurred in 36% and 21% of patients receiving T-VEC and GM-CSF, respectively. To provide maximal therapeutic benefit with the lowest possible treatment burden, we defined individualized dosing regimens to be the schedule that minimizes the cumulative tumour burden (the area under the total tumour curve) over an individualization period of ten week and the cumulative dose (the total amount of therapy administered over the treatment time). Thus, we sought to minimize the objective function

$$F(\text{Dose}) = \text{Cumulative Tumour Burden} + \alpha \text{Cumulative Dose},$$

where the positive scaling coefficient α weights the importance of maximizing the therapeutic effect versus the need to minimize treatment burden. This weighting values takes the need for a treatment to be simultaneously effective and tolerable into account.

Tolerability of combined therapy was attained by bounding the permissible dose size to be four times the standard dose amount, consistent with the maximum dose for T-VEC in the OPTiM trial. As it is only possible to administer discrete amounts of a drug, typically limited to be some multiple of the available vial size, we constrained the dose size to be 1 – 4-times the standard dose size for both immunotherapy and virotherapy. We allowed for daily immunotherapy dosing and restricted virotherapy administration to days 7, 14, 21, 28, 35, 42, 49, 56, 63, 70 so that virotherapy defined the beginning of a week-long treatment cycle. In total, 300 virtual patients underwent ten treatment cycles meaning there are 3000 total possible treatment cycles. Note that the schedule described above is potentially denser than what was administered by Andtbacka et al. [[Andtbacka et al., 2015](#)]. We allowed for increased treatment frequency to measure its impact on improved clinical outcomes, under the constraint that the cumulative dose administered in the optimal treatment regimen must be less than the cumulative dose administered during the OPTiM trial [[Andtbacka et al., 2015](#)].

To determine personalized dosing regimens, the optimal function $F(\text{Dose})$ was minimized over a ten-week treatment period using Matlab's genetic algorithm function *ga* [[MATLAB, 2017](#)]. Genetic algorithms are heuristic global optimization routines inspired

by natural selection [Holland, 1975, 1992; McCall, 2005] that are frequently employed to estimate parameters in computational biology models. They have also previously been applied to study optimal dosing routines in immunology [McCall, 2005].

We then generated personalized schedules for each of the 300 individuals in the optimal combination cohort. These schedules determined an empirical distribution of the probability of administering a dose of either immuno- or virotherapy on a given day of the treatment period. Sampling from this empirical distribution, we next determined the probability that immunotherapy, $P_I(\text{Day}_i)$, or virotherapy, $P_V(\text{Day}_i)$, is administered on Day i of therapy to determine a probabilistic treatment schedule that replicated the results of the treatment optimization on the population-level.

Inference and validation of optimal treatment schedule

We first determined whether a dose of immunotherapy was to be administered on the i -th day of treatment by sampling from a Bernoulli distribution with probability given by $P_I(\text{Day}_i)$ (see Table 4.1). If a dose was administered, we sampled from the empirical distribution of dose sizes determined from the individualization (see previous section). (i.e. the probability of giving a dose of size n given that immunotherapy is administered on day i) to determine the size of the immunotherapy dose. If the i -th day is the beginning of a new treatment cycle, virotherapy may be administered. If so, the same series of steps determined whether virotherapy was administered, and if so, the size of dose, based on $P_V(\text{Day}_i)$.

To test the effectiveness of the probabilistic dosing schedule, we created and cloned 200 new virtual patients, and separated them into three trial arms. The first cohort received the combined immuno- and virotherapy of $125 \mu\text{g}/\text{m}^2$ of GM-CSF daily for 14 days in 28 day cycles and 1 dose of virotherapy every 14 days corresponding to a combination of the standard of care reported in the OPTiM trial [Andtbacka et al., 2015]. A maintenance therapy schedule was derived from the results of the therapy optimization and was followed for the second cohort (see *Results*). Finally, the probabilistic dosing regimen determined from the population optimization was applied to the third arm. In the all three arms, virtual patients received treatment for the median treatment duration of the OPTiM trial. Mortality and removal from the trial followed the same procedure described in the *Model Calibration* section above.

RESULTS

Computational biology model successfully predicts existing therapy results

We first compared the model predictions to the OPTiM results [Andtbacka et al., 2015] to evaluate the computational biology model's ability to accurately represent the outcomes for patients receiving either GM-CSF or the oncolytic virus monotherapy T-VEC (Fig. 3A) [Andtbacka et al., 2015; Rehman et al., 2016]. Unsurprisingly, no untreated virtual patient survived to the end of the trial (not shown) and both of the treated cohorts display increased survival when compared to no treatment. Patients receiving virotherapy were the most likely to survive until the end of the *in silico* trial. The median survival time for patients in the T-VEC cohort of the *in silico* trial was 39.0 months, as compared to the reported median overall survival time of 41.1 months for patients with stage IIIB, IIIC, or IVM1a melanoma in the OPTiM trial. The median survival time for patients in the GM-CSF arm of the *in silico* clinical trial was 31.3 months, just outside of the 95% confidence interval of 17.4 to 29.6 months of the OPTiM trial. The null hypothesis that T-VEC and GM-CSF have the same efficacy was rejected with $p < 0.001$ using a log-rank test.

To measure the time from treatment initiation to failure, we considered the time from beginning of treatment until the tumour contains twice the initial number of tumour cells. The median time to treatment failure was then predicted to be 2.9 (OPTiM trial: 2.9 with 95% confidence interval of 2.8-4.0) and 13.9 months (OPTiM trial: 8.2 with 95% confidence interval of 6.5-9.9) in the GM-CSF and T-VEC arms, respectively.

The relative treatment benefit of virotherapy vs. immunotherapy was established by ordering virtual patients according to their untreated tumour doubling time (Fig. 3B), with longer doubling time indicating slower disease progression and less aggressive disease. A line of best fit with positive slope suggests that oncolytic virus therapy provided larger survival gains in those with longer doubling times when compared to GM-CSF, consistent with the increased survival fraction of patients with stage 3 melanoma in Figure 4(f) of Andtbacka et al. [Andtbacka et al., 2015].

"All or nothing" virotherapy dosing strategy

We expected that treatment with GM-CSF would be used to either prime the immune system before virotherapy, or to support the immune response directly following administration of the oncolytic virus. However, as seen in Fig. 4.4, no structure is easily discerned. To better understand the underlying distribution structure of the individualized treatment schedules, we calculated the probability that any immunotherapy should be administered on each of the seven treatment cycle days of the optimized therapy regimen, as described

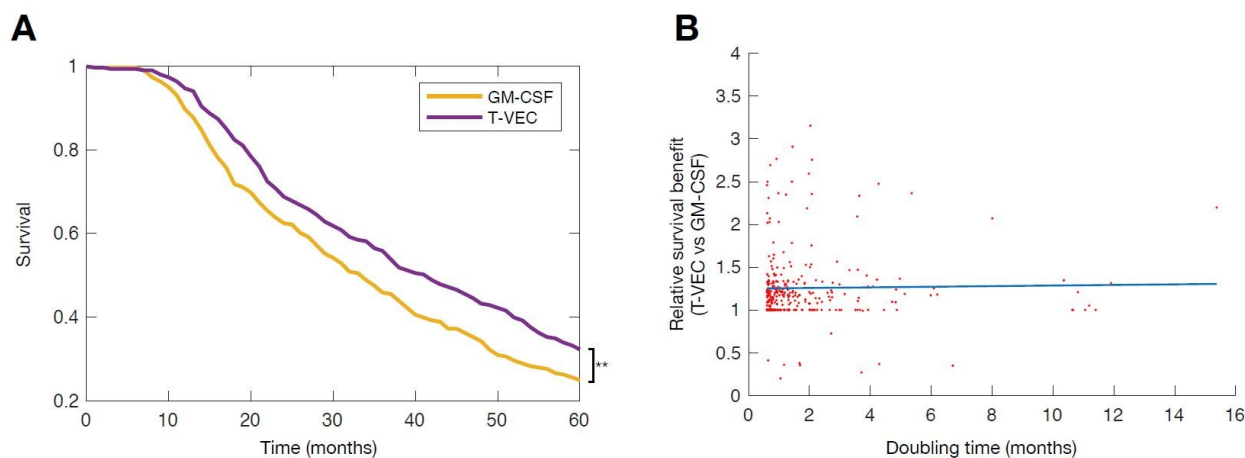


Figure 4.3: Treatment with oncolytic virus provides improves outcomes over immunotherapy in virtual clinical trial. **A)** Kaplan-Meier curves for patients in the immunotherapy and virotherapy arms of the virtual trial; **B)** The relative survival benefit for identical virtual patients. The ratio of survival time on T-VEC against survival time on GM-CSF for identical virtual patients (line of best fit, slope=0.0035) establishes a causal relationship between treatment type and survival time, indicating that oncolytic virus therapy provided slightly larger survival gains in those with with longer doubling times when compared to GM-CSF.

in the Methods section (*Optimization Routine for Combined Immuno- and Oncolytic Virotherapy*). If a dose was given, we computed the conditional probability of administering a dose of one, two, three or four multiples of the standard dose (Table 4.1). We found that the probability of administering a dose of immunotherapy for a given treatment day is roughly constant at 20% throughout the treatment cycle. Interestingly, our results indicate that the immunotherapy dose given is expected to be either the smallest or the largest permitted, suggesting that immunotherapy is most useful as an additional instigator of immune recruitment when virotherapy does not elicit a sufficient immune response, or to otherwise maintain the immune response initiated by successful viral infection and lysis.

Contrary to the mono-immunotherapy dosing schedule, the conditional probabilities $P_V(\text{Day}_i)$ for viral dose size reported in Table 4.2 are heavily skewed to the maximal tolerable dose. Given the mechanism of action of virotherapy (namely, infecting tumour cells), it is unsurprising that administering a larger dose of oncolytic virus should improve clinical outcomes. Put differently, an “all or nothing” approach of dosing infrequently, but for maximal therapeutic benefit, is optimal, in contrast to the logic of the immunotherapy case.

These results suggest that administering immunotherapy between administrations of

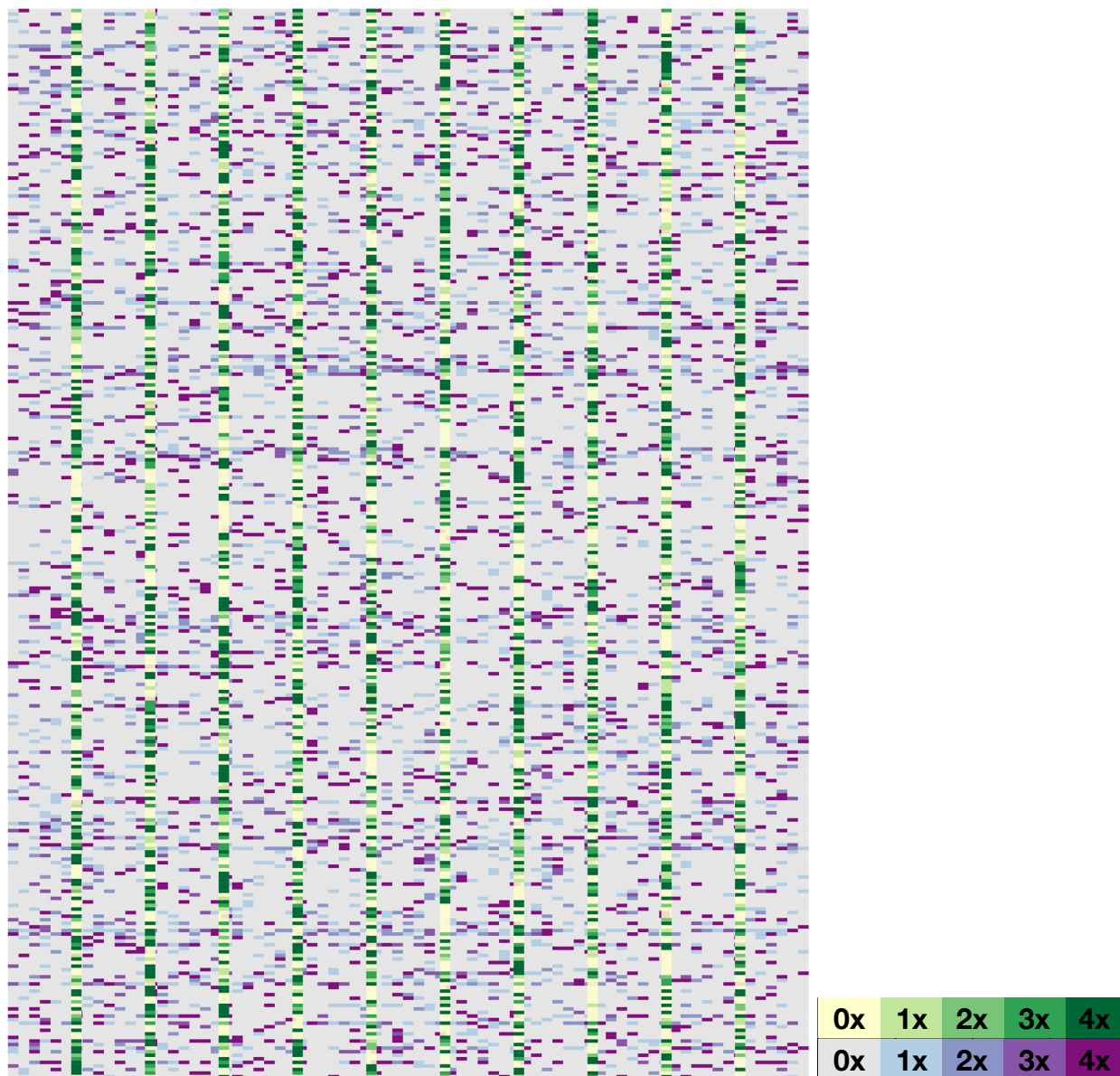


Figure 4.4: **Optimal personalized dose scheduling for each of the 300 virtual patients.** Dose size presented as a multiple of the standard dose with immunotherapy in shades of purple, and virotherapy in shades of green. The n th horizontal row corresponds to the n th virtual patient, while the m -th vertical column corresponds to the dose administered on day m .

virotherapy serves mainly to maintain immune recruitment [Aitken et al., 2017]. To test this hypothesis, we defined Maintenance Therapy to be the administration of virotherapy once every 14 days with immunotherapy administered evenly throughout on days 3, 6, 9, and 12 of each virotherapy treatment cycle. Dose size was calculated based on the cumulative expected weekly dose of immunotherapy (8 doses over 14 days) from the optimized

Day _{<i>i</i>}	-3	-2	-1	Start of Cycle	1	2	3
$P_I(\text{Day}_i)$	0.2043	0.2020	0.2037	0.2027	0.2200	0.2047	0.2057
$P_I(1 \text{Day}_i)$	0.3719	0.3762	0.3519	0.3799	0.3803	0.3583	0.3387
$P_I(2 \text{Day}_i)$	0.1599	0.1419	0.1702	0.1694	0.1439	0.1482	0.1929
$P_I(3 \text{Day}_i)$	0.1550	0.1733	0.1637	0.1217	0.1348	0.1678	0.1378
$P_I(4 \text{Day}_i)$	0.3132	0.3086	0.3142	0.3289	0.3409	0.3257	0.3306

Table 4.1: **Inferred probability distribution for GM-CSF scheduling.** The probability of administering immunotherapy ($P_I(\text{Day}_i)$) in each day of the treatment cycle and the conditional probability $P_I(n|\text{Day}_i)$ of administering n doses of immunotherapy for $n = 1, 2, 3, 4$.

regimen. Two doses of immunotherapy were therefore administered on days 3, 6, 9, and 12 to replicate the total expected immunotherapy dose. The same procedure was used to determine virotherapy doses.

$P_V(\text{Day}_7)$	0.5487
$P_V(1 \text{Day}_7)$	0.1592
$P_V(2 \text{Day}_7)$	0.1200
$P_V(3 \text{Day}_7)$	0.1597
$P_V(4 \text{Day}_7)$	0.5611

Table 4.2: **Inferred probability distribution for T-VEC scheduling.** The probability of administering virotherapy on each 7th day of the treatment cycle ($P_V(\text{Day}_7)$) and the conditional probability $P_V(n|\text{Day}_7)$ of administering n doses of virotherapy for $n = 1, 2, 3, 4$.

Maintenance and predictive combination therapies improve virtual patient survival

Despite the shorter treatment period, both the maintenance and probabilistic combination immuno- and oncolytic virotherapies improved overall survival times as compared to the simulated OPTiM trial (Fig. 4.5). Maintenance therapy similarly significantly increased mean survival time against mono-virotherapy (47.5 months vs. 35.36 months, two-sided t-test p-value of 1.02×10^{-6}). The maintenance therapy and optimal dosing regimens also outperformed the standard combination therapy: on average, the mean survival time for patients receiving standard combination therapy was 26.1 months, while patients receiving the maintenance therapy or probabilistic dosing survived for 47.5 or 46.6 months respectively (two-sided t-test p-values of $p < 0.001$ in both cases). The hypothesis that the two treatments were equally efficacious was rejected with $p < 0.001$ using a logrank test.

To improve therapy tolerability, an additional criterion for regimen optimality is the minimization of the number of treatment days. In the standard combination schedule,

patients received 2 administrations of virotherapy and 14 doses of immunotherapy per 28 day cycle, thus requiring 15 total days of drug administration per 28 day cycle with one simultaneous dose of virotherapy and immunotherapy. The maintenance therapy schedule required a total of 11 treatment days per 28 day cycle (9 administrations of immunotherapy and 2 administrations of virotherapy), whereas patients given the optimized treatment schedule were administered an expected 5 immunotherapy doses and 2 virotherapy doses per 28 day cycle, for a total of 9 expected treatment days.

Crucially, the results of the individualized therapy can be translated into a clinically-actionable therapeutic strategy that significantly improves simulated clinical outcomes (maintenance schedule). Mean survival times between patients receiving the maintenance therapy and the probabilistic therapy were not significantly different (47.9 months vs 46.7 months, two-sided t-test p-value of 0.754). This is unsurprising, given that the maintenance therapy was defined directly from the personalized regimens using the “naïve” constraint that immunotherapy be equally spread throughout each virotherapy cycle. While, for a given patient, it may be unsurprising that an optimized and individualized dose predict improved outcomes, leveraging the insights gained from the individualized cohort to produce population-wide improvements on a new cohort is a compelling achievement of our approach.

In summary, in terms of both end-points and dosing burden, immune maintenance therapy outperforms the standard-of-care combination therapy. The equivalency in mean survival times between the maintenance and probabilistic schedules also further motivates the rationalization of therapy scheduling via *in silico* clinical trials to better ascertain the key mechanisms regulating to treatment success prior to clinical trial enrolment.

DISCUSSION

Improving patient end-points and decreasing the drug burden during anti-cancer treatment are crucial components of cancer care. The introduction of new and advanced therapy modalities is critical to this goal. The approval of T-VEC, the first FDA approved, genetically modified oncolytic virus, was an important step forward for the treatment of late-stage melanoma that significantly improved patient survival over mono-immunotherapy GM-CSF administration. However, the question of whether combined immunotherapy and virotherapy will provide further benefits for patients and, if so, the optimal strategy for such combination therapy, remains. Running clinical trials is an expensive and onerous process. Trial failures are disappointing for patients, clinicians, and researchers, and contribute to overall attrition along the drug development pipeline. Here we have outlined a

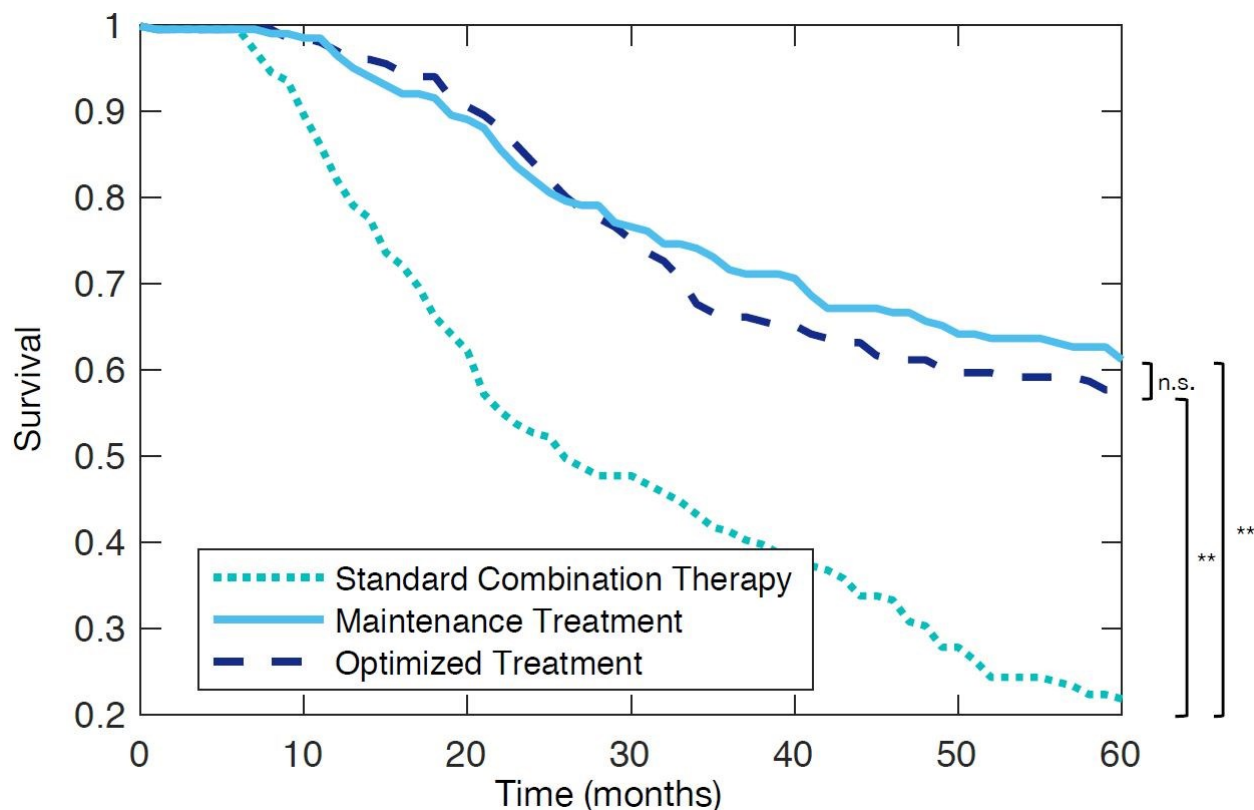


Figure 4.5: *In silico* clinical trial predicts improved outcomes for both probabilistic dosing strategies and maintenance therapy versus standard combination therapy. Kaplan-Meier curves for Arm 1: patients receiving Standard Combination Therapy (dotted turquoise line), Arm 2: Maintenance Treatment (solid light blue line), Arm 3: Probabilistic dosing regimen determined through the *in silico* clinical trial (dashed dark blue line).

rational approach to therapy optimization that has significant consequences for how we effectively design and implement clinical trials to maximize their success, and how we treat melanoma with combined immuno- and virotherapy.

Leveraging our previous computational biology model, we developed an *in silico* clinical trial by creating virtual individuals based on a realistic distribution of model parameter values. Each generated individual was cloned and assigned to different trial cohorts. This innovative strategy enabled us to analyze the effects of distinct therapy procedures on the *same* person, something which is clearly infeasible in the real world. Personalization of treatment regimens was achieved by simultaneously minimizing cumulative tumour and drug burdens. A probabilistic dosing regimen was subsequently defined based on the resulting personalized treatment schedules. Incorporating clinical realities, we determined

that standard combination therapy was improved upon by both a maintenance strategy (where immunotherapy is administered evenly throughout each virotherapy cycle) and this probabilistic dosing strategy. It is worth noting that the maintenance type therapy performed equivalently in terms of endpoints than the optimized scheduling, illustrating the utility of model-based optimization techniques in identifying and developing improved, clinically-actionable therapeutic strategies.

There are differences between the OPTiM trial and our *in silico* trial. First, while we can broadly recreate the number of individuals in each stage of disease, we cannot identically recreate the underlying distribution of patients. Accordingly, our results are highly dependent on the virtual patients selected for participation based on their tumour doubling time, and would be improved through the incorporation of detailed staging and patient distribution data. Second, the administration of an oncolytic virus can lead to an anti-viral adaptive immune responses and a decrease in treatment efficacy that is currently not accounted for in the model. Last, our computational model simplifies tumour-immune interactions by consolidating all immune cells into a single phagocyte population. We also considered a single cytokine as a cipher for all pro-inflammatory responses induced by tumour-immune communication. We believe that these considerations do not significantly impact on our general results, but they should be addressed in future work to increase the precision of the predicted personalized regimens. Ideally, empirically determined distributions for the model's parameter values would be available to strengthen the model's predictions. Fortunately, notwithstanding the general unavailability of such data, our parameterization successfully recapitulated the OPTiM trial results.

Despite these limitations, our results underline the contribution of computational biology to understanding the determinants of improved clinical care and support continued efforts towards rational therapy design. Significantly, this computational biology study suggests promising avenues of investigation towards tailored combination immunotherapy/oncolytic virotherapy for patients with late-stage melanoma.

SUPPORTING INFORMATION

S1 Supplementary Information

S1 Fig. Parameter fitting results. A and B) Data (red circles) from [Dingli et al. \[2009\]](#) for tumour growth in immunocompromised mice compared to model predictions (solid black lines). C) Comparisons of model predictions (solid black lines) and the [Toda et al. \[2000\]](#) data (red circles) for the number of viable cells following the administration of T-VEC.

S2 Fig. Local parameter sensitivity analysis. Left: dependence of tumour burden on the parameters shown on the y-axis. Right: dependence of tumour doubling time on the parameters shown on the y-axis. In both cases, parameters were varied by $\pm 10\%$. Tumour doubling times of 0 indicate that the tumour did not reach twice the initial size.

S1 Table Mean parameter estimates. The vector \mathbf{p} (see main section *Generation of in-silico individuals and patient cohorts*) with biological interpretations. See [Cassidy and Humphries \[2019\]](#) for detailed descriptions of each parameter.

ACKNOWLEDGMENTS

Part of this work was performed while TC attended the *Mathematical Biology* thematic research program organized by the Mittag-Leffler Institute. TC and MC thank Tony Humphries for discussions regarding this work.

BIBLIOGRAPHY

- Agur, Z. (2010). From the evolution of toxin resistance to virtual clinical trials: the role of mathematical models in oncology. *Futur. Oncol.*, 6(6):917–927.
- Aitken, A., Roy, D., and Bourgeois-Daigneault, M.-C. (2017). Taking a Stab at Cancer; Oncolytic Virus-Mediated Anti-Cancer Vaccination Strategies. *Biomedicines*, 5(4):3.
- Allen, R. J., Rieger, T. R., and Musante, C. J. (2016). Efficient Generation and Selection of Virtual Populations in Quantitative Systems Pharmacology Models. *CPT Pharmacometrics Syst. Pharmacol.*, 5(3):140–146.
- Andtbacka, R. H. I., Kaufman, H. L., Collichio, F., Amatruda, T., Senzer, N., Chesney, J., Delman, K. A., Spitler, L. E., Puzanov, I., Agarwala, S. S., Milhem, M., Cranmer, L., Curti, B., Lewis, K., Ross, M., Guthrie, T., Linette, G. P., Daniels, G. A., Harrington, K., Middleton, M. R., Miller, W. H., Zager, J. S., Ye, Y., Yao, B., Li, A., Doleman, S., Van Der Walde, A., Gansert, J., and Coffin, R. S. (2015). Talimogene laherparepvec improves durable response rate in patients with advanced melanoma. *J. Clin. Oncol.*, 33(25):2780–2788.
- Bell, J. and McFadden, G. (2014). Viruses for tumor therapy. *Cell Host Microbe*, 15(3):260–265.

- Bentele, M., Lavrik, I., Ulrich, M., Stößer, S., Heermann, D., Kalthoff, H., Krammer, P., and Eils, R. (2004). Mathematical modeling reveals threshold mechanism in CD95-induced apoptosis. *J. Cell Biol.*, 166(6):839–851.
- Bommareddy, P. K., Patel, A., Hossain, S., and Kaufman, H. L. (2017). Talimogene Laherparepvec (T-VEC) and Other Oncolytic Viruses for the Treatment of Melanoma. *Am. J. Clin. Dermatol.*, 18(1):1–15.
- Breitbach, C. J., Lichty, B. D., and Bell, J. C. (2016). Oncolytic viruses: Therapeutics with an identity crisis. *EBioMedicine*, 9:31–36.
- Carlson, J. A. (2003). Tumor doubling time of cutaneous melanoma and its metastasis. *Am. J. Dermatopathol.*, 25(4):291–299.
- Cassady, K., Haworth, K., Jackson, J., Markert, J., and Cripe, T. (2016). To infection and beyond: The multi-pronged anti-cancer mechanisms of oncolytic viruses. *Viruses*, 8(2):43.
- Cassidy, T. and Humphries, A. R. (2019). A mathematical model of viral oncology as an immuno-oncology instigator. *Math. Med. Biol. A J. IMA*, To appear.
- Chaurasiya, S., Chen, N. G., and Fong, Y. (2018). Oncolytic viruses and immunity. *Curr. Opin. Immunol.*, 51:83–90.
- Chesney, J., Puzanov, I., Collichio, F., Singh, P., Milhem, M. M., Glaspy, J., Hamid, O., Ross, M., Friedlander, P., Garbe, C., Logan, T. F., Hauschild, A., Lebbé, C., Chen, L., Kim, J. J., Gansert, J., Andtbacka, R. H., and Kaufman, H. L. (2018). Randomized, Open-Label Phase II Study Evaluating the Efficacy and Safety of Talimogene Laherparepvec in Combination With Ipilimumab Versus Ipilimumab Alone in Patients With Advanced, Unresectable Melanoma. *J. Clin. Oncol.*, 36(17):1658–1667.
- Chiocca, E. A. and Rabkin, S. D. (2015). Oncolytic viruses and their application to cancer immunotherapy. *Cancer Immunol. Res.*, 2(4):295–300.
- Collins, V. P., Loeffler, R. K., and Tivey, H. (1956). Observations on growth rates of human tumors. *Amer. J. Roentgenol.*, 76:988–1000.
- Craig, M., Humphries, A. R., and Mackey, M. C. (2016). A mathematical model of granulopoiesis incorporating the negative feedback dynamics and kinetics of G-CSF/neutrophil binding and internalization. *Bull. Math. Biol.*, 78(12):2304–2357.

- Dingli, D., Chalub, F. A. C. C., Santos, F. C., Van Segbroeck, S., and Pacheco, J. M. (2009). Cancer phenotype as the outcome of an evolutionary game between normal and malignant cells. *Br. J. Cancer*, 101(7):1130–1136.
- Fukuhara, H., Ino, Y., and Todo, T. (2016). Oncolytic virus therapy: A new era of cancer treatment at dawn. *Cancer Sci.*, 107(10):1373–1379.
- Gatenby, R. A., Silva, A. S., Gillies, R. J., and Frieden, B. R. (2009). Adaptive Therapy. *Cancer Res.*, 69(11):4894–4903.
- Guo, Z. S. and Bartlett, D. L. (2014). Oncolytic viruses as platform for multimodal cancer therapeutics: a promising land. *Cancer Gene Ther.*, 21(7):261–263.
- Holland, J. (1975). *Adaptation in natural and artificial systems: An introductory analysis with applications to biology, control, and artificial intelligence*. The MIT Press, Cambridge, Massachusetts, 1 edition.
- Holland, J. (1992). Genetic Algorithms. *Sci. Am.*, (July).
- Hoster, H. A., Zanes, R. P., and von Hamm, E. (1949). The Association of “Viral” Hepatitis and Hodgkin’s Disease. *Cancer Res.*, 9(8):473–480.
- Klasse, P. (2015). Molecular Determinants of the Ratio of Inert to Infectious Virus Particles. volume 118, pages 285–326.
- Lawler, S. E. and Chiocca, E. A. (2015). Oncolytic virus-mediated immunotherapy: A combinatorial approach for cancer treatment. *J. Clin. Oncol.*, 33(25):2812–2814.
- Love, S. B., Brown, S., Weir, C. J., Harbron, C., Yap, C., Gaschler-Markefski, B., Matcham, J., Caffrey, L., McKevitt, C., Clive, S., Craddock, C., Spicer, J., and Cornelius, V. (2017). Embracing model-based designs for dose-finding trials. *Br. J. Cancer*, 117(3):332–339.
- Marelli, G., Howells, A., Lemoine, N. R., and Wang, Y. (2018). Oncolytic Viral Therapy and the Immune System: A Double-Edged Sword Against Cancer. *Front. Immunol.*, 9(APR):1–8.
- Martin, N. T. and Bell, J. C. (2018). Oncolytic Virus Combination Therapy: Killing One Bird with Two Stones. *Mol. Ther.*, 26(6):1414–1422.
- MATLAB (2017). *R2017a*. The MathWorks Inc., Natick, Massachusetts.
- McCall, J. (2005). Genetic algorithms for modelling and optimisation. *J. Comput. Appl. Math.*, 184(1):205–222.

- Mellman, I., Coukos, G., and Dranoff, G. (2011). Cancer immunotherapy comes of age. *Nature*, 480(7378):480–489.
- Mostafa, A., Meyers, D., Thirukkumaran, C., Liu, P., Gratton, K., Spurrell, J., Shi, Q., Thakur, S., and Morris, D. (2018). Oncolytic Reovirus and Immune Checkpoint Inhibition as a Novel Immunotherapeutic Strategy for Breast Cancer. *Cancers (Basel)*, 10(6):205.
- Randazzo, B. P., Bhat, M. G., Kesari, S., Fraser, N. W., and Brown, S. M. (1997). Treatment of experimental subcutaneous human melanoma with a replication-restricted herpes simplex virus mutant. *J. Invest. Dermatol.*, 108(6):933–937.
- Rehman, H., Silk, A. W., Kane, M. P., and Kaufman, H. L. (2016). Into the clinic: Talimogene laherparepvec (T-VEC), a first-in-class intratumoral oncolytic viral therapy. *J. Immunother. Cancer*, 4(1):1–8.
- Russell, S. J., Peng, K.-W., and Bell, J. C. (2012). Oncolytic virotherapy. *Nat. Biotechnol.*, 30(7):658–670.
- Sato, S., Rancourt, A., Sato, Y., and Satoh, M. S. (2016). Single-cell lineage tracking analysis reveals that an established cell line comprises putative cancer stem cells and their heterogeneous progeny. *Sci. Rep.*, 6(1):23328.
- Schmidt, B. J., Casey, F. P., Paterson, T., and Chan, J. R. (2013). Alternate virtual populations elucidate the type I interferon signature predictive of the response to rituximab in rheumatoid arthritis. *BMC Bioinformatics*, 14(1):221.
- Schwartz, M. (1961). A biomathematical approach to clinical tumor growth. *Cancer*, 14(6):1272–1294.
- Stadler, R., Luger, T., Bieber, T., Köhler, U., Linse, R., Technau, K., Schubert, R., Schroth, K., Vakilzadeh, F., Volkenandt, M., Gollnick, H., Von Eick, H., Thoren, F., and Strannegård, Ö. (2006). Long-term survival benefit after adjuvant treatment of cutaneous melanoma with dacarbazine and low dose natural interferon alpha: A controlled, randomised multicentre trial. *Acta Oncol. (Madr)*, 45(4):389–399.
- Toda, M., Martuza, R. L., and Rabkin, S. D. (2000). Tumor Growth Inhibition by Intratumoral Inoculation of Defective Herpes Simplex Virus Vectors Expressing Granulocyte-Macrophage Colony-Stimulating Factor. *Mol. Ther.*, 2(4):324–329.

Wang, H., Milberg, O., Bartelink, I. H., Vicini, P., Wang, B., Narwal, R., Roskos, L., Santa-Maria, C. A., and Popel, A. S. (2019). In silico simulation of a clinical trial with anti-CTLA-4 and anti-PD-L1 immunotherapies in metastatic breast cancer using a systems pharmacology model. *R. Soc. Open Sci.*, 6(5):190366.

Zhang, J., Cunningham, J. J., Brown, J. S., and Gatenby, R. A. (2017). Integrating evolutionary dynamics into treatment of metastatic castrate-resistant prostate cancer. *Nat. Commun.*, 8(1):1816.

SUPPLEMENTARY INFORMATION

Determinants of combination GM-CSF immunotherapy and oncolytic virotherapy success identified through *in silico* treatment personalization

Tyler Cassidy, Morgan Craig

The computational biology model (described textually in Eq. (4.1)) was based on the model of Cassidy and Humphries [2019] and explicitly included heterogeneity in tumour cell reproduction velocity and tumour-immune interactions via a distributed delay differential equation. The model describes both quiescent and G_1 phase tumour cell populations while modelling the remainder of mitosis as a delayed process, and incorporates a phagocyte population and a proinflammatory cytokine that drives the tumour-immune interaction through increased phagocyte recruitment.

Let $Q(t)$ and $G_1(t)$ denote the quiescent and proliferative phase susceptible tumour cells, respectively, $C(t)$ denote the concentration of GM-CSF, $P(t)$ the phagocyte concentration in the tumour microenvironment, $V(t)$ the concentration of oncolytic virions, and $I(t)$ the number of infected tumour cells. Infection of susceptible tumour cells occurred at rate η , while tumour-immune interactions took place with rate $\psi_{Q,G}$.

To account for immune selection, we included a resistant strain of tumour cells undetectable to the immune system (represented by $Q_R(t)$, $G_{1,R}(t)$, analogous to the susceptible population). We assumed that tumour cells successfully completing mitosis could randomly mutate into the immune resistant strain with probability $\mu = 1 \times 10^{-10}$, and we assumed that the mutated strain of cancer cells reproduced identically to the non-mutated strain.

$$\left. \begin{aligned}
\frac{d}{dt}Q(t) &= \text{Mitotic Output} - \text{Transit to active phase} \\
&\quad - \text{Apoptosis} - \text{Immune Death} \\
\frac{d}{dt}G_1(t) &= \text{Transit from quiescence} - \text{Transit to Mitosis} \\
&\quad - \text{Apoptosis} - \text{Viral Infection} - \text{Immune Death} \\
\frac{d}{dt}I(t) &= \text{Viral infection} - \text{Death of infected cells} \\
\frac{d}{dt}V(t) &= \text{Dose}_V(t) + \text{Lysis} - \text{Viral infection} - \text{Virion death} \\
\frac{d}{dt}P(t) &= \text{Immune recruitment} - \text{Phagocyte death} \\
\frac{d}{dt}C(t) &= \text{Dose}_C(t) + \text{Cytokine Production} - \text{Renal clearance} \\
\frac{d}{dt}Q_R(t) &= \text{Development of Resistance} + \text{Mitotic Output} \\
&\quad - \text{Transit to active phase} - \text{Apoptosis} \\
\frac{d}{dt}G_{1,R}(t) &= \text{Transit from quiescence} - \text{Transit to Mitosis} \\
&\quad - \text{Apoptosis} - \text{Viral Infection.}
\end{aligned} \right\} \quad (4.1)$$

The differential equations describing the progression of disease are

$$\left. \begin{aligned}
\frac{d}{dt}Q(t) &= 2(1 - \mu) \int_{-\infty}^t \exp \left[- \int_{\sigma}^t \hat{d}_K + \eta(U(x)) + \psi_G(U(x)) dx \right] a_2 G_1(\sigma) K(t - \sigma) d\sigma \\
&\quad - a_1 Q(t) - d_1 Q(t) - \psi_Q(U(t)) Q(t) \\
\frac{d}{dt}G_1(t) &= a_1 Q(t) - a_2 G_1(t) - d_2 G_1(t) - \eta(U(t)) G_1(t) - \psi_G(U(t)) G_1(t) \\
\frac{d}{dt}Q_R(t) &= 2\mu \int_{-\infty}^t \exp \left[- \int_{\sigma}^t \hat{d}_K + \eta(U(x)) + \psi_G(U(x)) dx \right] a_2 G_1(\sigma) K(t - \sigma) d\sigma \\
&\quad - a_1 Q_R(t) - d_1 Q_R(t) \\
&\quad + 2 \int_{-\infty}^t \exp \left[- \int_{\sigma}^t \hat{d}_K + \eta(U(x)) dx \right] a_2 G_{1,R}(\sigma) K(t - \sigma) d\sigma \\
\frac{d}{dt}G_{1,R}(t) &= a_1 Q_R(t) - a_2 G_{1,R}(t) - d_2 G_{1,R}(t) - \eta(U(t)) G_{1,R}(t) \\
\frac{d}{dt}I(t) &= \eta(U(t)) [G_1(t) + G_{1,R}(t) + N(t)] - \delta I(t) \\
\frac{d}{dt}V(t) &= \text{Dose}_V(t) - \eta(U(t)) [G_1(t) + G_{1,R}(t) + N(t)] + \alpha[\delta I(t)] - \omega V(t) \\
\frac{d}{dt}C(t) &= \text{Dose}_C(t) + C_{prod}(U(t)) - k_{elim} C(t) \\
\frac{d}{dt}P(t) &= \varphi(C(t)) - \gamma_p P(t).
\end{aligned} \right\} \quad (4.2)$$

The total number of cells in the cell cycle is given by

$$N(t) = \int_0^{\infty} a_2 \exp \left[- \int_{t-\xi}^t \hat{d}_K + \eta(U(x)) dx \right] \left(1 - \int_0^{\xi} K(\sigma) d\sigma \right)$$

$$\times \left(G_1(t - \xi) \exp \left[- \int_{t-\xi}^t \psi_G(U(x)) dx \right] + G_{1,R}(t - \xi) \right) d\xi.$$

We modelled the subcutaneous administration of N doses of GM-CSF similar to [Craig et al. \[2016\]](#) by

$$\text{Dose}_C(t) = \sum_{i=1}^N \frac{k_a^c F_c \text{Admin}_i^c(t)}{\text{Vol}} \exp[-k_a^c(t - t_i)], \quad (4.3)$$

where the amount of GM-CSF administered at time t_i is Dose_i^c and

$$\text{Admin}_i^c(t) = \begin{cases} 0 & \text{if } t < t_i \\ \text{Dose}_i^c & \text{if } t \geq t_i. \end{cases}$$

The parameter k_a^c denotes the absorption rate of GM-CSF, and F the bioavailable fraction of GM-CSF. Similarly, the intralesion administration of oncolytic viruses [[Andtbacka et al., 2015](#); [Bommareddy et al., 2017](#); [Johnson et al., 2015](#)] was modelled as

$$\text{Dose}_V(t) = \sum_{j=1}^N \frac{k_a^v F_v \text{Admin}_j^v(t)}{\text{Vol}} \exp[-k_a^v(t - t_j)] \quad (4.4)$$

where Dose_j^v is the amount of virus administered at time $t = t_j$ and

$$\text{Admin}_j^v(t) = \begin{cases} 0 & \text{if } t < t_j \\ \text{Dose}_j^v & \text{if } t \geq t_j. \end{cases}$$

As we considered intralesional administration, $F_V = 1$. Further, absorption into the tumour was assumed to be much faster than cytokine absorption, so that $k_a^v \gg k_a^c$. Model predictions were obtained using the stiff ODE solver *ode15s* in Matlab [[MATLAB, 2017](#)] after reduction to a finite dimensional system of ODEs obtained using the technique

previously developed [Cassidy and Humphries, 2019]

$$\begin{aligned}
 \frac{d}{dt}Q(t) &= 2(1 - \mu)k_{tr}A_j(t) - a_1Q(t) - d_1Q - \psi_Q(U(t))Q(t) \\
 \frac{d}{dt}G_1(t) &= a_1Q(t) - a_2G_1(t) - d_2G_1(t) - \psi_G(U(t))G_1(t) - \eta(U(t))G_1(t) \\
 \frac{d}{dt}A_1(t) &= a_2G_1(t) - k_{tr}A_1(t) - [\hat{d}_g + \eta(U(t)) + \psi_G(U(t))]A_1(t) \\
 \frac{d}{dt}A_i(t) &= k_{tr}(A_{i-1}(t) - A_i(t)) - [\hat{d}_g + \eta(U(t)) + \psi_G(U(t))]A_i(t) \quad \text{for } i = 2, 3, \dots, j \\
 \frac{d}{dt}Q_R(t) &= 2\mu k_{tr}A_j(t) + 2k_{tr}A_{j,R}(t) - a_1Q_R(t) - d_1Q_R(t) \\
 \frac{d}{dt}G_{1,R}(t) &= a_1Q_R(t) - a_2G_{1,R}(t) - d_2G_{1,R}(t) - \eta(U(t))G_{1,R}(t) \\
 \frac{d}{dt}A_{1,R}(t) &= a_2G_{1,R}(t) - k_{tr}A_{1,R}(t) - [\hat{d}_g + \eta(U(t)) + \psi_G(U(t))]A_{1,R}(t) \\
 \frac{d}{dt}A_{i,R}(t) &= k_{tr}(A_{i-1,R}(t) - A_{i,R}(t)) - [\hat{d}_g + \eta(U(t)) + \psi_G(U(t))]A_{i,R}(t) \quad \text{for } i = 2, 3, \dots, j \\
 \frac{d}{dt}I(t) &= -\delta I(t) + \eta(U(t)) [G_1(t) + N(t)] \\
 \frac{d}{dt}V(t) &= \alpha\delta I(t) - \omega V(t) - \eta(U(t)) [G_1(t) + N(t)] \\
 \frac{d}{dt}C(t) &= C_{prod}(U(t)) - k_{elim}C(t) \\
 \frac{d}{dt}P(t) &= \varphi(C(t)) - \gamma_p P(t)
 \end{aligned} \tag{4.5}$$

Model parametrization

To begin, we converted tumour volumes to cell numbers by assuming that $1\text{mm}^3 = 1 \times 10^6$ cells [Dingli et al., 2009]. To accurately account for the heterogeneity in cell cycle time, we integrated the intermitotic time of cervical cancer cells measured by Sato et al. [2016]. There, the intermitotic time was determined by calculating the division time of a HeLa parent cell and then tracking the two daughter cells until their division. For each daughter cell, the intermitotic time was given by the time difference between birth and division, with a mean duration of 1.40 (standard deviation of $s = 0.28$ days). This measurement also includes the G_1 phase of the cell cycle. In (4.2), cells that divide spend, on average, $1/a_2$ days in G_1 . Thus, the mean of the delay kernel in (4.2), τ , satisfied

$$\tau = 1.40 - 1/a_2, \tag{4.6}$$

which provided a lower bound on the value of a_2 . The gamma distribution has a density given by

$$g_{k_{tr}}^j(t) = \frac{k_{tr}^j}{\Gamma(j)} t^{j-1} \exp[-k_{tr}t]$$

with mean $\tilde{x} = j/k_{tr}$ and standard deviation $s^2 = \tau^2/j$. Thus, for a given value of a_2 , we parametrized the delay kernel in (4.2) by

$$j = \tau^2/s^2,$$

and

$$k_{tr} = j/\tau.$$

To use the linear chain technique [Cassidy and Humphries, 2019], we enforced that $j \in \mathbb{N}$.

Dingli et al. [2009] administered myeloma cells to 6 week old irradiated and severely immunocompromised mice and measured the increase in tumour volume over 40+ days. We digitized the data from their Figure 1 and used tumour growth in the absence of immune pressure to fit the tumour growth parameters a_1 , a_2 and d_2 . To reduce the number of parameters to be estimated, we fixed the apoptosis rate of quiescent cells to be $d_1 = 0$. Since the mice in the Dingli et al. [2009] study were immunocompromised and no viral therapy was administered, we only considered the reduced system of $Q(t)$, $S(t)$ and $N(t)$, and then calculated the distribution parameters using (4.6) and $b = j/\tau$. As only the initial number of tumour cells (and not their distribution across the cell cycle) is known for each mouse, we distributed the initial inoculum of tumour cells across quiescent and the active portions of the cell cycle according to the proportion of time spent in each phase. Then, for each parameter set, we simulated the reduced mathematical model and minimized the least-squares error

$$err = \sum_{i=1}^N (y_i - \hat{y}_i)^2$$

between model predictions (y_i) and the data (\hat{y}_i) from Figures 1 (a) and (c) in Dingli et al. using the *fmincon* function in Matlab (Fig. S1 A and B).

Viral and infected cell kinetic parameters were determined using *in vitro* and *in vivo* studies of T-VEC kinetics and data from Toda et al. [2000]. In their study, Toda et al. injected murine melanoma cells into mice and waited for the tumours reached 5 mm in size. At that point, defective HSV virus encoding for GM-CSF was injected into the tumour. The increase in tumour volume as compared with untreated control mice was measured over 15 days. To fit this data, we fixed the tumour growth parameters a_1 , a_2 , d_1 and d_2 from the Dingli et al. estimates and simulated tumour growth during 15 days. Then, for fixed parameter set $[\kappa, \eta_{1/2}, \omega, \delta, \alpha]$, we simulated the administration of one dose of oncolytic virus (supplied in 1 mL vials with a concentration of 1×10^6 pfu/mL or 1×10^8 pfu/mL). We then normalized the treated simulation against the control simulation.

To reduce identifiability issues, we also integrated data from Randazzo et al. [1997].

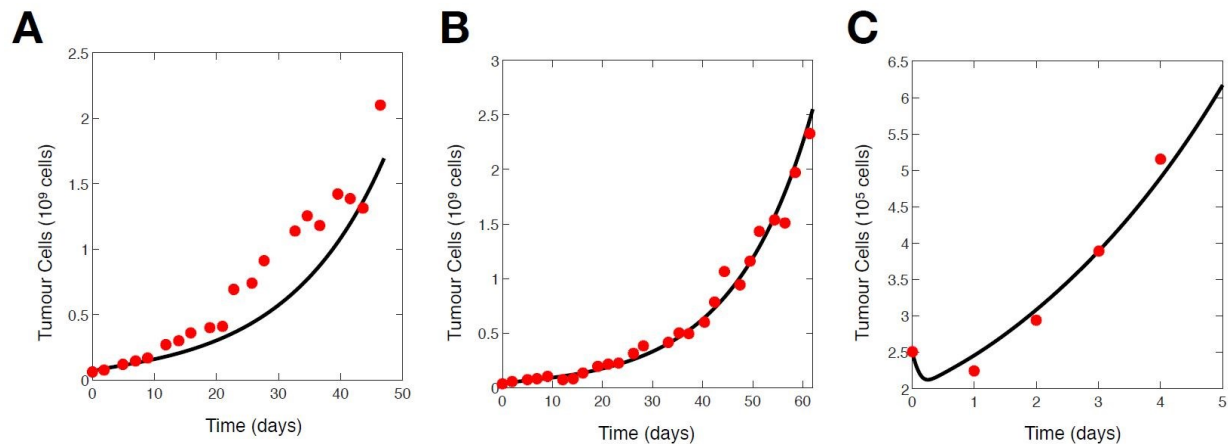


Figure 4.6: **Parameter fitting results.** A and B) Data (red circles) from [Dingli et al. \[2009\]](#) for tumour growth in immunocompromised mice compared to model predictions (solid black lines). C) Comparisons of model predictions (solid black lines) and the [Toda et al. \[2000\]](#) data (red circles) for the number of viable cells following the administration of T-VEC.

There, an oncolytic HSV virus was mixed with tumour cells *in vitro* and the proportion of viable cells was studied for different multiplicities of infection. As before, we fixed the tumour growth parameters and, for fixed parameter set $[\kappa, \eta_{1/2}, \omega, \delta, \alpha]$, simulated infection and calculated the percentage of viable (non-infected) cells. For each of the Toda et al. and Randazzo et al. datasets, we calculated the least-squares error between simulations and data and minimized the sums of their errors ([Fig. S1 C](#)).

Due to the lack of PopPK/semi-mechanistic models of GM-CSF, we adapted a model [[Craig et al., 2016](#)] for granulocyte colony stimulating factor (G-CSF), a similar protein, that includes both neutrophil mediated and renal clearance of circulating G-CSF. Since we were primarily interested in immune cells that do not have a G-CSF receptor (macrophages and T-cells), we did not consider neutrophil mediated clearance and fixed $k_{elim} = 0.16139$ 1/day. The basal concentration of GM-CSF in healthy patients is 2.43 pg/mL [[Lee et al., 2008](#)], given by

$$C^* = \frac{C_{prod}^*}{k_{elim}},$$

at homeostasis. Thus,

$$C_{prod}^* = k_{elim} C^* = 0.00039863 \text{ng/mL/day}.$$

To calculate the maximal cytokine production, C_{prod}^{max} , we considered experimental data

from Liu [2013] from the injection of carcinoma cells into mice. Therein, different MOIs of oncolytic HSV virus expressing GM-CSF was administered after a period of initial tumour growth. Throughout, circulating GM-CSF was measured through ELISA. To replicate the experimental set up, we simulated the administration of oncolytic virus in and minimized the least-squares error between the simulation and the experimental data for fixed parameter values $[C_{prod}^{max}, C_{1/2}]$, while holding the tumour growth and viral dynamics at their previously estimated values.

The parametrization of the immune compartment was based on Barish et al. [2017], where a mathematical model of murine tumour growth in the presence of a competent immune system and dendritic cell vaccine was developed. The structure of the Barish et al. model of immune dynamics is quite similar to our differential equation for $P(t)$. There, the rate of conversion from dendritic cell activation to recruitment of active anti tumour T-cells was given by $\chi_X = 4.6754$, which we adopted directly ($k_{cp} = \chi_X = 4.6754$). We also set the clearance rate of phagocytes to be the same as the clearance rate of T-cells, so $\gamma_p = \delta_T = 0.35$. The remaining immune involvement parameters, k_p and $k_q = k_s$, were set to ensure that the average patient had a tumour doubling time that fell near the center of the range found in patients with late stage melanoma [Carlson, 2003]. Parameters values for an average patient (see main section *Generation of In Silico Individuals and Patient Cohorts*) are provided in Table 4.3.

Virtual population patient distribution and history function derivation

The distribution of disease stage in the OPTiM trial was a crucial component for considering the overall survival statistics given the decreased 5 year survival rate for patients with more advanced disease. The original trial registered patients with not surgically resectable stage IIIB to IV melanoma. In the T-VEC cohort, 30% of patients had stage 3 melanoma. The median progression time from first treatment to lymph metastases was 18 months, while the median time to distant metastases was 24 months [Meier et al., 2002]. To reproduce this distribution of disease stage in our virtual population, for each of the 30% of virtual patients with stage 3 melanoma, we assumed that initial treatment was discontinued sometime s_0 in the past, where s_0 was sampled uniformly from $[16, 20]$. Similarly, for the 70% of virtual patients with stage 4 melanoma, we sampled s_0 uniformly from $[22, 26]$.

To set the history function ϕ_G for (4.2), we assumed that there was a tumour of size $T_0 > 0$ at cessation of the initial therapy. We began by modelling untreated tumour growth by

$$\frac{d}{dt} [Q(s) + G_1(s)] \approx \frac{d}{dt} T(s) = [2a_2 \exp[-d_3\tau] - a_2 - d_2] T(s), \quad s \in [s_0, 0].$$

Parameter	Value	Biological Interpretation (Unit)
a_1	1.183	Quiescent to interphase rate (1/day)
d_1	0	Quiescent death rate (1/day)
a_2	1.758	Interphase to active phase rate (1/day)
d_2	0.539	Interphase death rate (1/day)
d_3	0.539	Active phase death rate (1/day)
\hat{d}_g	0.167	Active phase death rate (1/day)
κ	3.53	Virion contact rate (1/day)
$\eta_{1/2}$	0.51	Virion half effect concentration (virions)
δ	4.96	Lysis rate (1/day)
α	0.00829	Lytic virion release rate (virions/cell)
ω	9.686	Virion death rate (1/day)
k_{cp}	4.675	Maximal phagocyte production rate (10^{10} cells/day)
$C_{1/2}$	0.739	Phagocyte production half effect (ng/mL/day)
$\Psi_{1/2}$	5	Cytokine production half effect (10^{10} cells/day)
γ_p	0.35	Phagocyte death rate (1/day)
C_{prod}^*	3.98×10^{-4}	Homeostatic cytokine production rate (ng/mL/day)
C_{prod}^{max}	1.429	Maximal cytokine production rate (ng/mL/day)
k_{elim}	0.16139	Cytokine elimination rate (1/day)
k_p	0.05	Phagocyte-tumour cell contact rate (1/day)
$k_{q,s}$	10	Phagocyte cell digestion constant
τ	0.8354	Expected cell cycle duration (day)
k_{tr}	10.77	Transit rate in (4.5) (1/day)
j	9	Number of Compartments in (4.5)

Table 4.3: **Mean parameter estimates.** The vector \mathbf{p} (see main section *Generation of in-silico individuals and patient cohorts*) with biological interpretations. See [Cassidy and Humphries \[2019\]](#) for detailed descriptions of each parameter.

Thus, at the beginning of treatment, the total number of tumour cells for each patient was

$$T_0 \exp [(2a_2 \exp[-d_3\tau] - a_2 - d_2) s_0].$$

We distributed these tumour cells across the quiescent, G_1 , and mitotic populations according to the expected fraction of time spent in each population.

Local sensitivity analysis

Particularly important physiological processes in disease dynamics were identified by performing a sensitivity analysis on the mathematical model's parameters. Each parameter was varied one-by-one by 10%. The influence of each of these variations was measured by comparing the predicted tumour doubling time and the tumour burden after 15 months to

the model's predictions without any parameter changes according to

$$\% \text{ change in tumour burden} = 100\% \times \frac{\text{Tumour burden with parameter change}}{\text{Tumour burden without parameter change}}$$

The parameters controlling the dynamics of mitotic cells were the most sensitive, with the 10% change accounting for drastic changes in disease burden. For example, increasing the rate at which G_1 cells enter into mitosis results in a 60-fold increase in tumour burden, while decreasing this rate decreased the tumour burden by a factor of 33 (Figure 4.7), indicating that interventions that inhibit the specific transition from G_1 into mitosis may offer consequential therapeutic benefits.

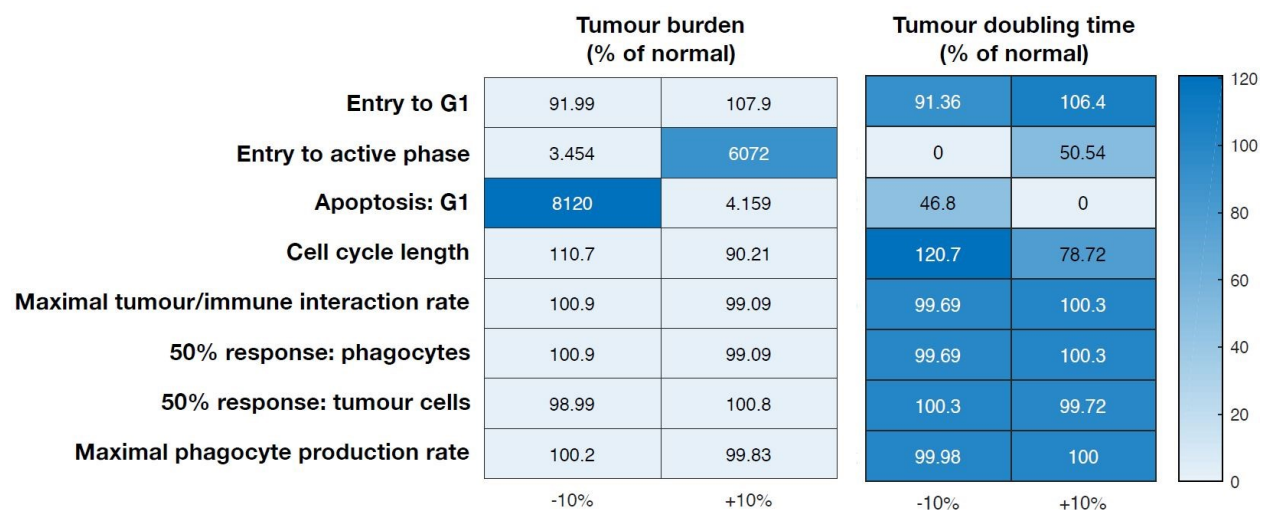


Figure 4.7: **Local parameter sensitivity analysis.** Left: dependence of tumour burden on the parameters shown on the y-axis. Right: dependence of tumour doubling time on the parameters shown on the y-axis. In both cases, parameters were varied by $\pm 10\%$. Tumour doubling times of 0 indicate that the tumour did not reach twice the initial size.

Bibliography

- Andtbacka, R. H. I., Kaufman, H. L., Collichio, F., Amatruda, T., Senzer, N., Chesney, J., Delman, K. A., Spitler, L. E., Puzanov, I., Agarwala, S. S., Milhem, M., Cranmer, L., Curti, B., Lewis, K., Ross, M., Guthrie, T., Linette, G. P., Daniels, G. A., Harrington, K., Middleton, M. R., Miller, W. H., Zager, J. S., Ye, Y., Yao, B., Li, A., Doleman, S., Van Der Walde, A., Gansert, J., and Coffin, R. S. (2015). Talimogene laherparepvec improves durable response rate in patients with advanced melanoma. *J. Clin. Oncol.*, 33(25):2780–2788.
- Barish, S., Ochs, M. F., Sontag, E. D., and Gevertz, J. L. (2017). Evaluating optimal therapy robustness by virtual expansion of a sample population, with a case study in cancer immunotherapy. *Proc. Natl. Acad. Sci.*, 114(31):E6277–E6286.
- Bommareddy, P. K., Patel, A., Hossain, S., and Kaufman, H. L. (2017). Talimogene Laherparepvec (T-VEC) and Other Oncolytic Viruses for the Treatment of Melanoma. *Am. J. Clin. Dermatol.*, 18(1):1–15.
- Carlson, J. A. (2003). Tumor doubling time of cutaneous melanoma and its metastasis. *Am. J. Dermatopathol.*, 25(4):291–299.
- Cassidy, T. and Humphries, A. R. (2019). A mathematical model of viral oncology as an immuno-oncology instigator. *Math. Med. Biol. A J. IMA*, To appear.
- Craig, M., Humphries, A. R., and Mackey, M. C. (2016). A mathematical model of granulopoiesis incorporating the negative feedback dynamics and kinetics of G-CSF/neutrophil binding and internalization. *Bull. Math. Biol.*, 78(12):2304–2357.
- Dingli, D., Offord, C., Myers, R., Peng, K. W., Carr, T. W., Josic, K., Russell, S. J., and Bajzer, Z. (2009). Dynamics of multiple myeloma tumor therapy with a recombinant measles virus. *Cancer Gene Ther.*, 16(12):873–882.
- Johnson, D. B., Puzanov, I., and Kelley, M. C. (2015). Talimogene laherparepvec (T-VEC) for the treatment of advanced melanoma. *Immunotherapy*, 7(6):611–619.
- Lee, J., Kim, Y., Lim, J., Kim, M., and Han, K. (2008). G-CSF and GM-CSF concentrations and receptor expression in peripheral blood leukemic cells from patients with chronic myelogenous leukemia. *Ann. Clin. Lab. Sci.*, 38(4):331–337.
- Liu, H. (2013). Preclinical evaluation of herpes simplex virus armed with granulocyte-macrophage colony-stimulating factor in pancreatic carcinoma. *World J. Gastroenterol.*, 19(31):5138.

- MATLAB (2017). *R2017a*. The MathWorks Inc., Natick, Massachusetts.
- Meier, F., Will, S., Ellwanger, U., Schlagenhauff, B., Schitteck, B., Rassner, G., and Garbe, C. (2002). Metastatic pathways and time courses in the orderly progression of cutaneous melanoma. *Br. J. Dermatol.*, 147(1):62–70.
- Randazzo, B. P., Bhat, M. G., Kesari, S., Fraser, N. W., and Brown, S. M. (1997). Treatment of experimental subcutaneous human melanoma with a replication-restricted herpes simplex virus mutant. *J. Invest. Dermatol.*, 108(6):933–937.
- Sato, S., Rancourt, A., Sato, Y., and Satoh, M. S. (2016). Single-cell lineage tracking analysis reveals that an established cell line comprises putative cancer stem cells and their heterogeneous progeny. *Sci. Rep.*, 6(1):23328.
- Toda, M., Martuza, R. L., and Rabkin, S. D. (2000). Tumor Growth Inhibition by Intratumoral Inoculation of Defective Herpes Simplex Virus Vectors Expressing Granulocyte - Macrophage Colony-Stimulating Factor. *Mol. Ther.*, 2(4):324–329.

CONCLUSION

As we have seen in the preceding chapters, time delays in human physiology are both heterogeneous in length and often subject to external control. This dissertation has described the development of mathematical models that explicitly incorporate both of these characteristics. Here, we summarise the main contributions of the thesis and indicate avenues of future work.

Chapter 2 provided the analytical framework necessary to derive a (possibly) state dependent distributed DDE from an underlying ageing or maturation process. The resulting distributed DDE preserves non-negativity of initial conditions and we demonstrated how to linearise the system about an equilibrium point. By choosing specific delay kernels, we recovered state dependent discrete DDEs, uniformly distributed DDEs and gamma distributed DDEs from the general distributed DDE framework. In fact, we reduced both the uniform and gamma distributed DDEs to formulations that are amenable to numerical simulation. In the case of the gamma distributed DDE, we derived a linear chain technique that incorporates variable ageing rates between successive compartments. To demonstrate the utility of this linear chain technique, we considered two ODE models of hematopoietic cell production used in the pharmaceutical sciences. We showed how to use these ODE models to derive an equivalent state dependent distributed DDE and, by using the equivalent DDE formulation, analysed the models. This linear chain technique is also amenable to models displaying a cyclic formulation.

Future work along this axis could include formalising the relationship between cyclic systems and possibly state dependent distributed DDEs. Moreover, numerical implementation of distributed DDEs requires the evaluation of a convolution integral which, currently, must be handled on a model-by-model case as there is no general purpose method available. To facilitate the use of state dependent distributed DDEs, an all-purpose numerical solver could be developed to simulate distributed DDEs for arbitrary delay kernels.

Next, in Chapter 3, we leveraged this understanding of heterogeneous reproductive processes to study cellular reproduction in malignant tumours. We developed a mathematical model of tumour-immune interactions and explicitly incorporated reproductive time heterogeneity. Analysis of the mathematical model indicated that immune recognition and killing of tumour cells acts to stabilize the disease free state. Further, we illustrated the role

of reproductive time heterogeneity in driving disease progression. By using the Erlang distribution to model cell cycle duration, we reduced the infinite dimensional distributed DDE to a finite dimensional system of ODEs. We demonstrated equivalence between these formulations by explicitly constructing a suitable history function for given ODE initial conditions—the first such direct construction to our knowledge. By incorporating oncolytic viral therapy, we showed that the level of immune involvement determines the long term success or failure of therapy.

However, the mathematical model developed in Chapter 3 drastically simplified the nuances of anti-tumour immune responses. In our model, immune cells interact with tumour cells without regard for the spatial distribution of immune and tumour cells, pro- and anti-inflammatory cytokine gradients and other aspects of the tumour microenvironment. Incorporating spatial effects into the model is a possible extension of this work that would naturally lead to the development of an agent-based model more appropriate to study extinction events. Moreover, the model did not incorporate the impact of anti-inflammatory cytokines which are critical for the modulation of the anti-tumour immune response.

Finally, we turned to the question of understanding and optimising combination viral and immunotherapy scheduling in Chapter 4. Using the previously derived mathematical model, we proposed a logical and rational approach to *in silico* clinical trials aimed at addressing some issues faced by clinicians. We began by generating virtual patients that reproduced clinically relevant aspects of late stage melanoma and cloned these patients into a number of distinct treatment arms. In this way, we studied disease progression under a number of different therapies in precisely the same virtual patient, which is clinically infeasible. Next, we used the mathematical model to individualize treatment strategies for each virtual patient. However, these treatment strategies are individualized and optimized for the patient in question. To translate these optimized schedules to new patients, we created a probabilistic dosing regimen with the expected dosing frequency of the optimized strategy that is unlikely to reach the clinic. To avoid the ethical considerations of the proposed optimized strategy, we studied the underlying principles of the optimized therapeutic strategies and identified the mechanisms by which immunotherapy can support oncolytic viral therapy. We designed a maintenance type regimen that uses the administration of pro-inflammatory cytokines to maintain an immune response between doses of viral therapy. By performing a second *in silico* clinical trial, we demonstrated that both the maintenance and probabilistic therapeutic strategies outperform the current standard of care while there is no significant difference between the probabilistic and maintenance type strategies.

The virtual clinical trial in Chapter 4 provided a framework to utilize mathematical

models to inform clinical treatment strategies. However, there are a number of important questions raised by our work. Specific to oncolytic viruses, we did not incorporate an anti-viral adaptive immune response, nor the development of viral resistance due to exposure to numerous viral cycles. Both of these adaptive responses would function to decrease viral infectivity and treatment efficacy, which may explain the discrepancies between our virtual trial and the OPTiM trial [[Andtbacka et al., 2015](#)]. Future work should address these shortcomings and study the possibility of alternating between different oncolytic viruses to avoid the development of anti-viral effects.

In summary, this dissertation has addressed the issue of heterogeneity in ageing processes through the development of mathematical models incorporating distributed DDEs. The analytical and numerical results of this work indicate that incorporating distributions of delays in mathematical models can drastically impact model predictions. It follows that including delay time heterogeneity is crucial when developing mathematical models of physiological systems.

BIBLIOGRAPHY

- Agur, Z. (2010). From the evolution of toxin resistance to virtual clinical trials: the role of mathematical models in oncology. *Futur. Oncol.*, 6(6):917–927.
- Aitken, A., Roy, D., and Bourgeois-Daigneault, M.-C. (2017). Taking a Stab at Cancer; Oncolytic Virus-Mediated Anti-Cancer Vaccination Strategies. *Biomedicines*, 5(4):3.
- Allen, R. J., Rieger, T. R., and Musante, C. J. (2016). Efficient Generation and Selection of Virtual Populations in Quantitative Systems Pharmacology Models. *CPT Pharmacometrics Syst. Pharmacol.*, 5(3):140–146.
- Andtbacka, R. H. I., Kaufman, H. L., Collichio, F., Amatruda, T., Senzer, N., Chesney, J., Delman, K. A., Spitler, L. E., Puzanov, I., Agarwala, S. S., Milhem, M., Cranmer, L., Curti, B., Lewis, K., Ross, M., Guthrie, T., Linette, G. P., Daniels, G. A., Harrington, K., Middleton, M. R., Miller, W. H., Zager, J. S., Ye, Y., Yao, B., Li, A., Doleman, S., Van Der Walde, A., Gansert, J., and Coffin, R. S. (2015). Talimogene laherparepvec improves durable response rate in patients with advanced melanoma. *J. Clin. Oncol.*, 33(25):2780–2788.
- Barish, S., Ochs, M. F., Sontag, E. D., and Gevertz, J. L. (2017). Evaluating optimal therapy robustness by virtual expansion of a sample population, with a case study in cancer immunotherapy. *Proc. Natl. Acad. Sci.*, 114(31):E6277–E6286.
- Bartlett, D. L., Liu, Z., Sathaiah, M., Ravindranathan, R., Guo, Z., He, Y., and Guo, Z. S. (2013). Oncolytic viruses as therapeutic cancer vaccines. *Mol. Cancer*, 12(1):103.
- Bélair, J., Mackey, M. C., and Mahaffy, J. M. (1994). Age-structured and two-delay models for erythropoiesis. *Math. Biosci.*, 128(1-2):317–46.
- Bell, J. and McFadden, G. (2014). Viruses for tumor therapy. *Cell Host Microbe*, 15(3):260–265.
- Bentele, M., Lavrik, I., Ulrich, M., Stößer, S., Heermann, D., Kalthoff, H., Krammer, P., and Eils, R. (2004). Mathematical modeling reveals threshold mechanism in CD95-induced apoptosis. *J. Cell Biol.*, 166(6):839–851.

- Bernard, S. (2016). Moving the boundaries of granulopoiesis modelling. *Bull. Math. Biol.*, 78(12):2358–2363.
- Bernard, S., Bélair, J., and Mackey, M. C. (2003). Oscillations in cyclical neutropenia: new evidence based on mathematical modeling. *J. Theor. Biol.*, 223:283–298.
- Bhatia, A. and Kumar, Y. (2011). Cancer-immune equilibrium: Questions unanswered. *Cancer Microenviron.*, 4(2):209–217.
- Bommareddy, P. K., Patel, A., Hossain, S., and Kaufman, H. L. (2017). Talimogene Laherparepvec (T-VEC) and Other Oncolytic Viruses for the Treatment of Melanoma. *Am. J. Clin. Dermatol.*, 18(1):1–15.
- Bourgeois-Daigneault, M. C., Roy, D. G., Falls, T., Twumasi-Boateng, K., St-Germain, L. E., Marguerie, M., Garcia, V., Selman, M., Jennings, V. A., Pettigrew, J., Amos, S., Diallo, J. S., Nelson, B., and Bell, J. C. (2016). Oncolytic vesicular stomatitis virus expressing interferon-gamma has enhanced therapeutic activity. *Mol. Ther. - Oncolytics*, 3:16001.
- Breitbach, C. J., Lichty, B. D., and Bell, J. C. (2016). Oncolytic viruses: Therapeutics with an identity crisis. *EBioMedicine*, 9:31–36.
- Buczacki, S. J., Popova, S., Biggs, E., Koukorava, C., Buzzelli, J., Vermeulen, L., Hazelwood, L., Francies, H., Garnett, M. J., and Winton, D. J. (2018). Itraconazole targets cell cycle heterogeneity in colorectal cancer. *J. Exp. Med.*, 215(7):jem.20171385.
- Burns, F. J. and Tannock, J. F. (1970). On the existence of a G₀-phase in the cell cycle. *Cell Tissue Kinet.*, 3(4):321–334.
- Câmara De Souza, D., Craig, M., Cassidy, T., Li, J., Nekka, F., Bélair, J., and Humphries, A. R. (2018). Transit and lifespan in neutrophil production: implications for drug intervention. *J. Pharmacokinet. Pharmacodyn.*, 45(1):59–77.
- Campbell, S. A. and Jessop, R. (2009). Approximating the Stability Region for a Differential Equation with a Distributed Delay. *Math. Model. Nat. Phenom.*, 4(2):1–27.
- Carlson, J. A. (2003). Tumor doubling time of cutaneous melanoma and its metastasis. *Am. J. Dermatopathol.*, 25(4):291–299.
- Cassady, K., Haworth, K., Jackson, J., Markert, J., and Cripe, T. (2016). To infection and beyond: The multi-pronged anti-cancer mechanisms of oncolytic viruses. *Viruses*, 8(2):43.

- Cassidy, T. and Humphries, A. R. (2019). A mathematical model of viral oncology as an immuno-oncology instigator. *Math. Med. Biol. A J. IMA*, To appear.
- Chaurasiya, S., Chen, N. G., and Fong, Y. (2018). Oncolytic viruses and immunity. *Curr. Opin. Immunol.*, 51:83–90.
- Chesney, J., Puzanov, I., Collichio, F., Singh, P., Milhem, M. M., Glaspy, J., Hamid, O., Ross, M., Friedlander, P., Garbe, C., Logan, T. F., Hauschild, A., Lebbé, C., Chen, L., Kim, J. J., Gansert, J., Andtbacka, R. H., and Kaufman, H. L. (2018). Randomized, Open-Label Phase II Study Evaluating the Efficacy and Safety of Talimogene Laherparepvec in Combination With Ipilimumab Versus Ipilimumab Alone in Patients With Advanced, Unresectable Melanoma. *J. Clin. Oncol.*, 36(17):1658–1667.
- Chiocca, E. A. and Rabkin, S. D. (2015). Oncolytic viruses and their application to cancer immunotherapy. *Cancer Immunol. Res.*, 2(4):295–300.
- Colao, I., Pennisi, R., Venuti, A., Nygårdas, M., Heikkilä, O., Hukkanen, V., and Sciortino, M. T. (2017). The ERK-1 function is required for HSV-1-mediated G1/S progression in HEP-2 cells and contributes to virus growth. *Sci. Rep.*, 7(1):9176.
- Colijn, C. and Mackey, M. (2005a). A mathematical model of hematopoiesis - I. Periodic chronic myelogenous leukemia. *J. Theor. Biol.*, 237(2):117–132.
- Colijn, C. and Mackey, M. (2005b). A mathematical model of hematopoiesis: II. Cyclical neutropenia. *J. Theor. Biol.*, 237:133–46.
- Collins, V. P., Loeffler, R. K., and Tivey, H. (1956). Observations on growth rates of human tumors. *Amer. J. Roentgenol.*, 76:988–1000.
- Cooke, K. and Huang, W. (1996). On the Problem of Linearization for State-Dependent Delay Differential Equations. *Proc. Am. Math. Soc.*, 124(5):1417–1426.
- Cooke, K. L. and Grossman, Z. (1982). Discrete delay, distributed delay and stability switches. *J. Math. Anal. Appl.*, 86(2):592–627.
- Cox, D. R. (1972). Regression models and life-tables. *J. R. Stat. Soc.*, 34(2):187–220.
- Craig, M., Humphries, A. R., and Mackey, M. C. (2016). A mathematical model of granulopoiesis incorporating the negative feedback dynamics and kinetics of G-CSF/neutrophil binding and internalization. *Bull. Math. Biol.*, 78(12):2304–2357.

- Craig, M., Humphries, A. R., Nekka, F., Bélair, J., Li, J., and Mackey, M. C. (2015). Neutrophil dynamics during concurrent chemotherapy and G-CSF : Mathematical modelling guides dose optimisation to minimize neutropenia. *J. Theor. Biol.*, 385:77–89.
- Crauste, F. and Adimy, M. (2007). Modeling and asymptotic stability of a growth factor-dependent stem cell dynamics model with distributed delay. *Discret. Contin. Dyn. Syst. - Ser. B*, 8(1):19–38.
- Crivelli, J. J., Földes, J., Kim, P. S., and Wares, J. R. (2012). A mathematical model for cell cycle-specific cancer virotherapy. *J. Biol. Dyn.*, 6(sup1):104–120.
- Dale, D. and Mackey, M. (2015). Understanding, Treating and Avoiding Hematological Disease: Better Medicine Through Mathematics? *Bull. Math. Biol.*, 77(5):739–757.
- Diekmann, O., Gyllenberg, M., and Metz, J. A. J. (2018). Finite dimensional state representation of linear and nonlinear delay systems. *J. Dyn. Differ. Equations*, 30(4):1439–1467.
- Dingli, D., Offord, C., Myers, R., Peng, K. W., Carr, T. W., Josic, K., Russell, S. J., and Bajzer, Z. (2009). Dynamics of multiple myeloma tumor therapy with a recombinant measles virus. *Cancer Gene Ther.*, 16(12):873–882.
- Dranoff, G. (2004). Cytokines in cancer pathogenesis and cancer therapy. *Nat. Rev. Cancer*, 4(1):11–22.
- Dunn, G. P., Bruce, A. T., Ikeda, H., Old, L. J., and Schreiber, R. D. (2002). Cancer immunoeediting: From immunosurveillance to tumor escape. *Nat. Immunol.*, 3(11):991–998.
- Dunn, G. P., Old, L. J., and Schreiber, R. D. (2004). The Three Es of Cancer Immunoeediting. *Annu. Rev. Immunol.*, 22(1):329–360.
- Eftimie, R. and Eftimie, G. (2018). Tumour-associated macrophages and oncolytic virotherapies: a mathematical investigation into a complex dynamics. *Lett. Biomath.*, 5:S6–S35.
- Eissa, I., Bustos-Villalobos, I., Ichinose, T., Matsumura, S., Naoe, Y., Miyajima, N., Morimoto, D., Mukoyama, N., Zhiwen, W., Tanaka, M., Hasegawa, H., Sumigama, S., Aleksic, B., Koder, Y., and Kasuya, H. (2018). The Current Status and Future Prospects of Oncolytic Viruses in Clinical Trials against Melanoma, Glioma, Pancreatic, and Breast Cancers. *Cancers (Basel)*, 10(10):356.
- Fredrickson, A. G., Ramkrishna, D., and Tsuchya, H. M. (1967). Statistics and Dynamics of Procaryotic Cell Populations. *Math. Biosci.*, 1:327–374.

- Friberg, L. E., Henningsson, A., Maas, H., Nguyen, L., and Karlsson, M. O. (2002). Model of chemotherapy-induced myelosuppression with parameter consistency across drugs. *J. Clin. Oncol.*, 20(24):4713–4721.
- Fukuhara, H., Ino, Y., and Todo, T. (2016). Oncolytic virus therapy: A new era of cancer treatment at dawn. *Cancer Sci.*, 107(10):1373–1379.
- Ganesh, K. and Massagué, J. (2018). TGF- β Inhibition and Immunotherapy: Checkmate. *Immunity*, 48(4):626–628.
- Gatenby, R. A., Silva, A. S., Gillies, R. J., and Frieden, B. R. (2009). Adaptive Therapy. *Cancer Res.*, 69(11):4894–4903.
- Glass, L. (2015). Dynamical disease: Challenges for nonlinear dynamics and medicine. *Chaos An Interdiscip. J. Nonlinear Sci.*, 25(9):097603.
- Golubev, A. (2016). Applications and implications of the exponentially modified gamma distribution as a model for time variabilities related to cell proliferation and gene expression. *J. Theor. Biol.*, 393:203–217.
- Goodwin, B. C. (1965). Oscillatory behavior in enzymatic control processes. *Adv. Enzyme Regul.*, 3:425–437.
- Grivennikov, S. I. and Karin, M. (2011). Inflammatory cytokines in cancer: tumour necrosis factor and interleukin 6 take the stage. *Ann. Rheum. Dis.*, 70(Suppl 1):i104–i108.
- Grzywa, T. M., Paskal, W., and Włodarski, P. K. (2017). Intratumor and Intertumor Heterogeneity in Melanoma. *Transl. Oncol.*, 10(6):956–975.
- Guo, Z. S. and Bartlett, D. L. (2014). Oncolytic viruses as platform for multimodal cancer therapeutics: a promising land. *Cancer Gene Ther.*, 21(7):261–263.
- Gurney, W., Nisbet, R., and Blythe, S. (1986). The systematic formulation of models of stage-structured populations. In Metz, J. A. J. and Diekmann, O., editors, *Dyn. Physiol. Struct. Popul.*, chapter 11, pages 474–493. Springer Berlin Heidelberg, Berlin, Heidelberg, 3 edition.
- Gyllenberg, M. (2007). Mathematical aspects of physiologically structured populations: the contributions of J. A. J. Metz. *J. Biol. Dyn.*, 1(1):3–44.
- Hale, J. K. and Verduyn Lunel, S. M. (1993). *Introduction to Functional Differential Equations*, volume 99 of *Applied Mathematical Sciences*. Springer New York, New York, NY.

- Hallam, S., Escorcio-Correia, M., Soper, R., and Schultheiss, A. (2009). Activated macrophages in the tumour microenvironment - dancing to the tune of TLR and NF- κ B. *J. Pathol.*, 219(2):143–152.
- Hartung, F., Krisztin, T., Walther, H.-O., and Wu, J. (2006). Chapter 5 Functional Differential Equations with State-Dependent Delays: Theory and Applications. In Canada, A., Drabek, P., and Fonda, A., editors, *Handb. Differ. Equations*, chapter 5, pages 435–545. Elsevier, North Holland 2004, 3rd edition.
- Hearn, T., Haurie, C., and Mackey, M. (1998a). Cyclical neutropenia and the peripheral control of white blood cell production. *J. Theor. Biol.*, 192(2):167–81.
- Hearn, T., Haurie, C., and Mackey, M. C. (1998b). Cyclical neutropenia and the peripheral control of white blood cell production. *J. Theor. Biol.*, 192:167–181.
- Hillen, T., Enderling, H., and Hahnfeldt, P. (2013). The tumor growth paradox and immune system-mediated selection for cancer stem cells. *Bull. Math. Biol.*, 75(1):161–184.
- Hino, Y., Murakami, S., and Naito, T. (1991). *Functional Differential Equations with Infinite Delay*, volume 1473 of *Lecture Notes in Mathematics*. Springer Berlin Heidelberg, Berlin, Heidelberg.
- Holland, J. (1975). *Adaptation in natural and artificial systems: An introductory analysis with applications to biology, control, and artificial intelligence*. The MIT Press, Cambridge, Massachusetts, 1 edition.
- Holland, J. (1992). Genetic Algorithms. *Sci. Am.*, (July).
- Hoos, A., Britten, C. M., Huber, C., and O'Donnell-Tormey, J. (2011). A methodological framework to enhance the clinical success of cancer immunotherapy. *Nat. Biotechnol.*, 29(10):867–870.
- Hoster, H. A., Zanes, R. P., and von Hamm, E. (1949). The Association of “Viral” Hepatitis and Hodgkin’s Disease. *Cancer Res.*, 9(8):473–480.
- Hu, J. C., Coffin, R. S., Davis, C. J., Graham, N. J., Groves, N., Guest, P. J., Harrington, K. J., James, N. D., Love, C. A., McNeish, I., Medley, L. C., Michael, A., Nutting, C. M., Pandha, H. S., Shorrock, C. A., Simpson, J., Steiner, J., Steven, N. M., Wright, D., and Coombes, R. C. (2006). A Phase I Study of OncoVEXGM-CSF, a Second-Generation Oncolytic Herpes Simplex Virus Expressing Granulocyte Macrophage Colony-Stimulating Factor. *Clin. Cancer Res.*, 12(22):6737–6747.

- Hu, S., Dunlavey, M., Guzy, S., and Teuscher, N. (2018). A distributed delay approach for modeling delayed outcomes in pharmacokinetics and pharmacodynamics studies. *J. Pharmacokinet. Pharmacodyn.*, 45(2):1–24.
- Idema, S., Dirven, C. M. F., van Beusechem, V., Carette, J., Planqué, R., Noske, D. P., Lamfers, M. L. M., and Vandertop, W. P. (2010). Objective determination of the oncolytic potency of conditionally-replicating adenoviruses using mathematical modeling. *J. Gene Med.*, 12(7):564–571.
- Imran, M. and Smith, H. L. (2007). The dynamics of bacterial infection, innate immune response, and antibiotic treatment. *Discret. Contin. Dyn. Syst. B*, 8(1):127–143.
- Jenner, A. L., Yun, C. O., Kim, P. S., and Coster, A. C. (2018). Mathematical Modelling of the Interaction Between Cancer Cells and an Oncolytic Virus: Insights into the Effects of Treatment Protocols. *Bull. Math. Biol.*, 80(6):1615–1629.
- Johnson, D. B., Puzanov, I., and Kelley, M. C. (2015). Talimogene laherparepvec (T-VEC) for the treatment of advanced melanoma. *Immunotherapy*, 7(6):611–619.
- Kaplan, E. L. and Meier, P. (1958). Nonparametric estimation from incomplete observations. *J. Am. Stat. Assoc.*, 53(282):457.
- Kaufman, H., Lilley, C., Ponce, R., Hughes, T., and Coffin, R. (2014). Critical analysis of an oncolytic herpesvirus encoding granulocyte-macrophage colony stimulating factor for the treatment of malignant melanoma. *Oncolytic Virotherapy*, 3:11–20.
- Kim, P. S., Crivelli, J. J., Choi, I., Yun, C., and Wares, J. R. (2015). Quantitative impact of immunomodulation versus oncolysis with cytokine-expressing virus therapeutics. *Math. Biosciences Eng.*, 12(4):841–58.
- Kirschner, D. and Panetta, J. C. (1998). Modeling immunotherapy of the tumor - immune interaction. *J. Math. Biol.*, 37(3):235–252.
- Klasse, P. (2015). Molecular Determinants of the Ratio of Inert to Infectious Virus Particles. volume 118, pages 285–326.
- Krzyzanski, W. (2011). Interpretation of transit compartments pharmacodynamic models as lifespan based indirect response models. *J. Pharmacokinet. Pharmacodyn.*, 38(2):179–204.
- Krzyzanski, W., Wiczling, P., Lowe, P., Pigeolet, E., Fink, M., Berghout, A., and Balsler, S. (2010). Population modeling of filgrastim PK-PD in healthy adults following intravenous and subcutaneous administrations. *J. Clin. Pharmacol.*, 50(S9):101S–112S.

- Kuznetsov, V. A., Makalkin, I. A., Taylor, M. A., and Perelson, A. S. (1994). Nonlinear dynamics of immunogenic tumors: Parameter estimation and global bifurcation analysis. *Bull. Math. Biol.*, 56(2):295–321.
- Lawler, S. E. and Chiocca, E. A. (2015). Oncolytic virus-mediated immunotherapy: A combinatorial approach for cancer treatment. *J. Clin. Oncol.*, 33(25):2812–2814.
- Lawrence, M. S., Stojanov, P., Polak, P., Kryukov, G. V., Cibulskis, K., Sivachenko, A., Carter, S. L., Stewart, C., Mermel, C. H., Roberts, S. A., Kiezun, A., Hammerman, P. S., McKenna, A., Drier, Y., Zou, L., Ramos, A. H., Pugh, T. J., Stransky, N., Helman, E., Kim, J., Sougnez, C., Ambrogio, L., Nickerson, E., Shefler, E., Cortés, M. L., Auclair, D., Saksena, G., Voet, D., Noble, M., DiCara, D., Lin, P., Lichtenstein, L., Heiman, D. I., Fennell, T., Imielinski, M., Hernandez, B., Hodis, E., Baca, S., Dulak, A. M., Lohr, J., Landau, D.-A., Wu, C. J., Melendez-Zajgla, J., Hidalgo-Miranda, A., Koren, A., McCarroll, S. A., Mora, J., Lee, R. S., Crompton, B., Onofrio, R., Parkin, M., Winckler, W., Ardlie, K., Gabriel, S. B., Roberts, C. W. M., Biegel, J. A., Stegmaier, K., Bass, A. J., Garraway, L. A., Meyerson, M., Golub, T. R., Gordenin, D. A., Sunyaev, S., Lander, E. S., and Getz, G. (2013). Mutational heterogeneity in cancer and the search for new cancer-associated genes. *Nature*, 499(7457):214–218.
- Lee, J., Kim, Y., Lim, J., Kim, M., and Han, K. (2008). G-CSF and GM-CSF concentrations and receptor expression in peripheral blood leukemic cells from patients with chronic myelogenous leukemia. *Ann. Clin. Lab. Sci.*, 38(4):331–337.
- Lichty, B. D., Breitbach, C. J., Stojdl, D. F., and Bell, J. C. (2014). Going viral with cancer immunotherapy. *Nat. Rev. Cancer*, 14(8):559–567.
- Liu, H. (2013). Preclinical evaluation of herpes simplex virus armed with granulocyte-macrophage colony-stimulating factor in pancreatic carcinoma. *World J. Gastroenterol.*, 19(31):5138.
- Liu, W., Hillen, T., and Freedman, H. I. (2007). A mathematical model for M-phase specific chemotherapy including the G0-phase and immunoresponse. *Math. Biosci. Eng.*, 4(2):239–59.
- Love, S. B., Brown, S., Weir, C. J., Harbron, C., Yap, C., Gaschler-Markefski, B., Matcham, J., Caffrey, L., McKevitt, C., Clive, S., Craddock, C., Spicer, J., and Cornelius, V. (2017). Embracing model-based designs for dose-finding trials. *Br. J. Cancer*, 117(3):332–339.
- MacDonald, N. (1978). *Time Lags in Biological Models*. Springer, Berlin, 1 edition.

- Mackey, M. C. (1978). Unified hypothesis for the origin of aplastic anemia and periodic hematopoiesis. *Blood*, 51(5):941–956.
- Mackey, M. C. and Glass, L. (1977). Oscillation and chaos in physiological control systems. *Science (80-.)*, 197(4300):287–289.
- MacNamara, C. and Eftimie, R. (2015). Memory versus effector immune responses in oncolytic virotherapies. *J. Theor. Biol.*, 377:1–9.
- Mahaffy, J. M., Bélair, J., and Mackey, M. C. (1998). Hematopoietic model with moving boundary condition and state dependent delay: application in erythropoiesis. *J. Theor. Biol.*, 190(2):135–146.
- Mahasa, K. J., Eladdadi, A., de Pillis, L., and Ouifki, R. (2017). Oncolytic potency and reduced virus tumor- specificity in oncolytic virotherapy. A mathematical modelling approach. *PLoS One*, 12(9):1–25.
- Mahoney, K. M., Freeman, G. J., and McDermott, D. F. (2015). The next immune-checkpoint inhibitors: Pd-1/pd-l1 blockade in melanoma. *Clin. Ther.*, 37(4):764–782.
- Malinzi, J., Eladdadi, A., and Sibanda, P. (2017). Modelling the spatiotemporal dynamics of chemovirotherapy cancer treatment. *J. Biol. Dyn.*, 11(1):244–274.
- Marelli, G., Howells, A., Lemoine, N. R., and Wang, Y. (2018). Oncolytic Viral Therapy and the Immune System: A Double-Edged Sword Against Cancer. *Front. Immunol.*, 9(APR):1–8.
- Martin, N. T. and Bell, J. C. (2018). Oncolytic Virus Combination Therapy: Killing One Bird with Two Stones. *Mol. Ther.*, 26(6):1414–1422.
- MATLAB (2017). *R2017a*. The MathWorks Inc., Natick, Massachusetts.
- McCall, J. (2005). Genetic algorithms for modelling and optimisation. *J. Comput. Appl. Math.*, 184(1):205–222.
- McKendrick, A. G. (1925). Applications of mathematics to medical problems. *Proc. Edinburgh Math. Soc.*, 44:98–130.
- Meier, F., Will, S., Ellwanger, U., Schlagenhauff, B., Schitteck, B., Rassner, G., and Garbe, C. (2002). Metastatic pathways and time courses in the orderly progression of cutaneous melanoma. *Br. J. Dermatol.*, 147(1):62–70.

- Mellman, I., Coukos, G., and Dranoff, G. (2011). Cancer immunotherapy comes of age. *Nature*, 480(7378):480–489.
- Metz, J. and Diekmann, O., editors (1986). *The Dynamics of Physiologically Structured Populations*, volume 68 of *Lecture Notes in Biomathematics*. Springer Berlin Heidelberg, Berlin, Heidelberg, 3 edition.
- Mittal, D., Gubin, M. M., Schreiber, R. D., and Smyth, M. J. (2014). New insights into cancer immunoediting and its three component phases—elimination, equilibrium and escape. *Curr. Opin. Immunol.*, 27:16–25.
- Mosser, D. M. (2003). The many faces of macrophage activation. *J. Leukoc. Biol.*, 73(2):209–212.
- Mostafa, A., Meyers, D., Thirukkumaran, C., Liu, P., Gratton, K., Spurrell, J., Shi, Q., Thakur, S., and Morris, D. (2018). Oncolytic Reovirus and Immune Checkpoint Inhibition as a Novel Immunotherapeutic Strategy for Breast Cancer. *Cancers (Basel)*, 10(6):205.
- Otto, A. and Radons, G. (2017). Transformations from variable delays to constant delays with applications in engineering and biology. In Insperger, T., Ersal, T., and Orosz, G., editors, *Time Delay Syst.*, volume 7 of *Advances in Delays and Dynamics*, pages 169–183. Springer International Publishing, Cham.
- Palm, M. M., Elemans, M., and Beltman, J. B. (2018). Heritable tumor cell division rate heterogeneity induces clonal dominance. *PLOS Comput. Biol.*, 14(2):e1005954.
- Pauksen, K., Elfman, L., Ulfgren, A., and Venge, P. (1994). Serum levels of granulocyte-colony stimulating factor (G-CSF) in bacterial and viral infections, and in atypical pneumonia. *Br J Haematol*, 88(2):256–260.
- Pérez-Ruixo, J. J., Krzyzanski, W., and Hing, J. (2008). Pharmacodynamic analysis of recombinant human erythropoietin effect on reticulocyte production rate and age distribution in healthy subjects. *Clin. Pharmacokinet.*, 47(6):399–415.
- Piscitelli, S., Reiss, W., Figg, W., and Petros, W. (1997). Pharmacokinetic studies with recombinant cytokines. Scientific issues and practical considerations. *Clin. Pharmacokinet.*, 32(5):368–81.
- Pol, J., Kroemer, G., and Galluzzi, L. (2016). First oncolytic virus approved for melanoma immunotherapy. *Oncoimmunology*, 5(1):e1115641.

- Quartino, A. L., Karlsson, M. O., Lindman, H., and Friberg, L. E. (2014). Characterization of endogenous G-CSF and the inverse correlation to chemotherapy-induced neutropenia in patients with breast cancer using population modeling. *Pharm. Res.*, 31(12):3390–3403.
- Randazzo, B. P., Bhat, M. G., Kesari, S., Fraser, N. W., and Brown, S. M. (1997). Treatment of experimental subcutaneous human melanoma with a replication-restricted herpes simplex virus mutant. *J. Invest. Dermatol.*, 108(6):933–937.
- Rehman, H., Silk, A. W., Kane, M. P., and Kaufman, H. L. (2016). Into the clinic: Talimogene laherparepvec (T-VEC), a first-in-class intratumoral oncolytic viral therapy. *J. Immunother. Cancer*, 4(1):1–8.
- Roberts, A. (2005). G-CSF: A key regulator of neutrophil production, but that's not all! *Growth Factors*, 23(1):33–41.
- Roskos, L. K., Lum, P., Lockbaum, P., Schwab, G., and Yang, B.-B. (2006). Pharmacokinetic/pharmacodynamic modeling of pegfilgrastim in healthy subjects. *J. Clin. Pharmacol.*, 46(7):747–757.
- Rowshanravan, B., Halliday, N., and Sansom, D. M. (2017). CTLA-4: a moving target in immunotherapy. *Blood*, 131(1):blood-2017-06-741033.
- Rubinow, S. and Lebowitz, J. (1975). A mathematical model of neutrophil production and control in normal man. *J. Math. Biol.*, 225:187–225.
- Russell, S. J., Peng, K.-W., and Bell, J. C. (2012). Oncolytic virotherapy. *Nat. Biotechnol.*, 30(7):658–670.
- Sandler, O., Mizrahi, S. P., Weiss, N., Agam, O., Simon, I., and Balaban, N. Q. (2015). Lineage correlations of single cell division time as a probe of cell-cycle dynamics. *Nature*, 519(7544):468–471.
- Santiago, D. N., Heidbuechel, J. P. W., Kandell, W. M., Walker, R., Djeu, J., Engeland, C. E., Abate-Daga, D., and Enderling, H. (2017). Fighting cancer with mathematics and viruses. *Viruses*, 9(9):1–26.
- Sato, S., Rancourt, A., Sato, Y., and Satoh, M. S. (2016). Single-cell lineage tracking analysis reveals that an established cell line comprises putative cancer stem cells and their heterogeneous progeny. *Sci. Rep.*, 6(1):23328.

- Schirm, S., Ahnert, P., Wienhold, S., Mueller-Redetzky, H., Nouailles-Kursar, G., Loeffler, M., Witzentrath, M., and Scholz, M. (2016). A biomathematical model of pneumococcal lung infection and antibiotic treatment in mice. *PLoS One*, 11(5):1–22.
- Schmidt, B. J., Casey, F. P., Paterson, T., and Chan, J. R. (2013). Alternate virtual populations elucidate the type I interferon signature predictive of the response to rituximab in rheumatoid arthritis. *BMC Bioinformatics*, 14(1):221.
- Schwartz, M. (1961). A biomathematical approach to clinical tumor growth. *Cancer*, 14(6):1272–1294.
- Seidel, J. A., Otsuka, A., and Kabashima, K. (2018). Anti-PD-1 and Anti-CTLA-4 Therapies in Cancer: Mechanisms of Action, Efficacy, and Limitations. *Front. Oncol.*, 8(March):1–14.
- Shochat, E., Rom-Kedar, V., and Segel, L. (2007). G-CSF control of neutrophils dynamics in the blood. *Bull. Math. Biol.*, 69:299–338.
- Sinko, J. W. and Streifer, W. (1967). A New Model For Age-Size Structure of a Population. *Ecology*, 48(6):910–918.
- Sinko, J. W. and Streifer, W. (1971). A Model for Population Reproducing by Fission. *Ecology*, 52(2):330–335.
- Smith, H. (2011). *An Introduction to Delay Differential Equations with Applications to the Life Sciences*, volume 57 of *Texts in Applied Mathematics*. Springer New York, New York, NY.
- Smith, H. L. (1993). Reduction of structured population models to threshold-type delay equations and functional differential equations: a case study. *Math. Biosci.*, 113(1):1–23.
- Stadler, R., Luger, T., Bieber, T., Köhler, U., Linse, R., Technau, K., Schubert, R., Schroth, K., Vakilzadeh, F., Volkenandt, M., Gollnick, H., Von Eick, H., Thoren, F., and Strannegård, Ö. (2006). Long-term survival benefit after adjuvant treatment of cutaneous melanoma with dacarbazine and low dose natural interferon alpha: A controlled, randomised multicentre trial. *Acta Oncol. (Madr.)*, 45(4):389–399.
- Sunshine, J. and Taube, J. M. (2015). PD-1/PD-L1 inhibitors. *Curr. Opin. Pharmacol.*, 23:32–38.
- Swann, J. B. and Smyth, M. J. (2007). Immune surveillance of tumors. *J. Clin. Invest.*, 117(5):1137–1146.

- Teslya, A. (2015). *Predator-Prey Models With Distributed Time Delay*. Doctoral dissertation, McMaster University.
- Toda, M., Martuza, R. L., and Rabkin, S. D. (2000). Tumor Growth Inhibition by Intratumoral Inoculation of Defective Herpes Simplex Virus Vectors Expressing Granulocyte-Macrophage Colony-Stimulating Factor. *Mol. Ther.*, 2(4):324–329.
- Trucco, E. (1965). Mathematical models for cellular systems. The Von Foerster equation. Part II. *Bull. Math. Biophys.*, 27(4):449–471.
- Villasana, M. and Radunskaya, A. (2003). A delay differential equation model for tumor growth. *J. Math. Biol.*, 47(3):270–294.
- Vogel, T. (1961). Systèmes Déferlants, Systèmes Héritaires, Systèmes Dynamiques. In *Proc. Int. Symp. Nonlinear Vib.*, pages 123–130, Kiev. Academy of Sciences USSR.
- von Schulthess, G. and Mazer, N. (1982). Cyclic neutropenia (CN): A clue to the control of granulopoiesis. *Blood*, 59:27–37.
- Walker, R. and Enderling, H. (2016). From concept to clinic: Mathematically informed immunotherapy. *Curr. Probl. Cancer*, 40(1):68–83.
- Wang, H., Milberg, O., Bartelink, I. H., Vicini, P., Wang, B., Narwal, R., Roskos, L., Santa-Maria, C. A., and Popel, A. S. (2019). In silico simulation of a clinical trial with anti-CTLA-4 and anti-PD-L1 immunotherapies in metastatic breast cancer using a systems pharmacology model. *R. Soc. Open Sci.*, 6(5):190366.
- Wodarz, D. (2016). Computational modeling approaches to the dynamics of oncolytic viruses. *Wiley Interdiscip. Rev. Syst. Biol. Med.*, 8(3):242–252.
- Yamashita, M. and Emerman, M. (2006). Retroviral infection of non-dividing cells: Old and new perspectives. *Virology*, 344(1):88–93.
- Yates, C. A., Ford, M. J., and Mort, R. L. (2017). A Multi-stage Representation of Cell Proliferation as a Markov Process. *Bull. Math. Biol.*, 79(12):2905–2928.
- Yildirim, N., Santillán, M., Horike, D., and Mackey, M. C. (2004). Dynamics and bistability in a reduced model of the lac operon. *Chaos An Interdiscip. J. Nonlinear Sci.*, 14(2):279–292.
- Yuan, Y. and Bélair, J. (2011). Stability and Hopf Bifurcation Analysis for Functional Differential Equation with Distributed Delay. *SIAM J. Appl. Dyn. Syst.*, 10(2):551–581.

Zhang, J., Cunningham, J. J., Brown, J. S., and Gatenby, R. A. (2017). Integrating evolutionary dynamics into treatment of metastatic castrate-resistant prostate cancer. *Nat. Commun.*, 8(1):1816.